

## Nonclassical gasdynamics

### theory and experiments on nonlinear wave propagation in BZT fluids

Chandrasekaran, N.B.

**DOI**

[10.4233/uuid:65d578ce-b904-466f-a57e-4086dbee4a98](https://doi.org/10.4233/uuid:65d578ce-b904-466f-a57e-4086dbee4a98)

**Publication date**

2023

**Document Version**

Final published version

**Citation (APA)**

Chandrasekaran, N. B. (2023). *Nonclassical gasdynamics: theory and experiments on nonlinear wave propagation in BZT fluids*. [Dissertation (TU Delft), Delft University of Technology]. <https://doi.org/10.4233/uuid:65d578ce-b904-466f-a57e-4086dbee4a98>

**Important note**

To cite this publication, please use the final published version (if applicable). Please check the document version above.

**Copyright**

Other than for strictly personal use, it is not permitted to download, forward or distribute the text or part of it, without the consent of the author(s) and/or copyright holder(s), unless the work is under an open content license such as Creative Commons.

**Takedown policy**

Please contact us and provide details if you believe this document breaches copyrights. We will remove access to the work immediately and investigate your claim.

**Nonclassical gasdynamics: theory and  
experiments on nonlinear wave  
propagation in BZT fluids**



# **Nonclassical gasdynamics: theory and experiments on nonlinear wave propagation in BZT fluids**

## **Dissertation**

for the purpose of obtaining the degree of doctor  
at Delft University of Technology  
by the authority of the Rector Magnificus prof.dr.ir. T.H.J.J. van der Hagen,  
chair of the Board of Doctorates,  
to be defended publicly on  
Monday 6 November 2023 at 10:00 hours

by

**Nitish Barathwaj CHANDRASEKARAN**

Master of Science in Aerospace Engineering,  
Delft University of Technology, Delft, the Netherlands,  
born in Chennai, India.

This dissertation has been approved by the promotor.

Composition of the doctoral committee:

Rector Magnificus, Prof. dr. ir. P. Colonna di Paliano,	Chairperson Delft University of Technology, <i>promotor</i>
Dr. ir. B. H. Mercier,	Université de Poitiers, <i>co-promotor</i>

*Independent members:*

Prof. dr. D.J.E.M. Roekaerts,	Delft University of Technology
Prof. Dr. Dipl.-Ing. S. Kenjereš,	Delft University of Technology
Prof. Dr.-Ing. R. Span,	Ruhr-Universität Bochum
Dr. ir. A. Spinelli,	Politecnico di Milano

*Overige leden:*

Dr.ir. T. Michelis,	Delft University of Technology
---------------------	--------------------------------



**SIEMENS**



This research has been supported by the Engineering Sciences Division (TTW) of the Dutch Organization for Scientific Research (NWO), Technology Program of the Ministry of Economic Affairs, Grant No. 15837.

*Keywords:* rarefaction shock wave, BZT fluids, shock tube, thermodynamic modelling

*Printed by:* Ridderprint | <http://www.ridderprint.nl/>

*Front & Back:* Artist's impression of waves in a flow. Designed by Vignesh Prakash.

Copyright © 2023 by N. B. Chandrasekaran

ISBN 978-94-6384-496-3

An electronic version of this dissertation is available at  
<http://repository.tudelft.nl/>.

ஒருமைக்கண் தான் கற்ற கல்வி ஒருவற்கு எழுமையும் ஏமாப்  
புடைத்து  
— திருவள்ளுவர்

*The learning, which a person has acquired in one birth, will yield them  
pleasure during seven births.*

— Thiruvalluvar, Sangam Tamil poet



# Contents

<b>Summary</b>	<b>xi</b>
<b>Samenvatting</b>	<b>xv</b>
<b>1 Introduction</b>	<b>1</b>
1.1 A primer in nonclassical gasdynamics . . . . .	1
1.2 Motivation and thesis outline . . . . .	5
<b>2 Nonlinear waves in Bethe-Zel'dovich-Thompson fluids</b>	<b>11</b>
2.1 Theory of wave propagation . . . . .	11
2.1.1 Linear Wave Equation . . . . .	12
2.1.2 Origin of nonlinearities. . . . .	13
2.1.3 Nonlinear Wave Equation . . . . .	16
2.2 Nonlinear distortion and shock formation . . . . .	18
2.3 Shock jump conditions and admissibility criterion . . . . .	18
2.4 Admissibility of compression shocks in BZT fluids. . . . .	24
2.5 Admissibility of rarefaction shocks in BZT fluids . . . . .	24
<b>3 Nonclassical gasdynamics experiments</b>	<b>33</b>
3.1 Review of experimental options . . . . .	34
3.1.1 Steady Experiments . . . . .	34
3.1.2 Unsteady Experiments . . . . .	38
3.1.3 Choice of experimental technique . . . . .	42
3.2 Past Experiments with shock and Ludwig tubes . . . . .	44
3.3 Flexible Asymmetric Shock Tube (FAST) facility . . . . .	45
3.3.1 Description of the setup . . . . .	46
3.3.2 Fast Opening Valve . . . . .	47
3.3.3 Improvements to the FAST and lessons learned . . . . .	51
3.3.4 Temperature inhomogeneities along the charge tube . . . . .	55
3.4 Concluding Remarks . . . . .	57
<b>4 Nonlinear Waves in inhomogeneous BZT fluids</b>	<b>67</b>
4.1 Introduction . . . . .	67
4.2 Modelling nonlinear wave propagation in thermoviscous fluids . . . . .	70
4.2.1 Wavefront Expansion Technique. . . . .	70
4.2.2 Westervelt Equation Model . . . . .	71

4.3	Evolution of initial disturbance and shock formation . . . . .	72
4.3.1	Uniform Temperature . . . . .	72
4.3.2	Non-uniform Temperature . . . . .	73
4.3.3	Analysis based on the Westervelt Equation . . . . .	75
4.4	Effect of temperature gradients on shock formation distance . . . . .	80
4.5	Conclusions . . . . .	88
<b>5</b>	<b>A new setup and first experiments</b>	<b>93</b>
5.1	Introduction . . . . .	93
5.2	Design and working principle . . . . .	94
5.2.1	Diaphragm and rupture mechanism . . . . .	96
5.2.2	Instrumentation, data acquisition and control . . . . .	98
5.3	Experiments . . . . .	101
5.3.1	Leak-tightness Characterization . . . . .	101
5.3.2	Working Fluid Preparation . . . . .	102
5.3.3	Start-up Procedure . . . . .	103
5.3.4	Finite-amplitude Wave Speed Measurements . . . . .	105
5.3.5	Estimation of $\Gamma$ . . . . .	115
5.3.6	Sound speed measurements . . . . .	118
5.4	Conclusions . . . . .	123
<b>6</b>	<b>Organic Vapour Acoustic Resonator</b>	<b>131</b>
6.1	Introduction . . . . .	131
6.2	The acoustic resonator . . . . .	135
6.2.1	General layout . . . . .	135
6.2.2	Instrumentation . . . . .	136
6.2.3	Acoustic excitation . . . . .	138
6.2.4	Thermal control . . . . .	138
6.3	Experimental method . . . . .	140
6.3.1	Fluid characteristics and purification . . . . .	140
6.3.2	Measurement procedure . . . . .	141
6.3.3	Estimation of the speed of sound . . . . .	142
6.3.4	Calibration of the resonator . . . . .	146
6.3.5	Estimation of the density . . . . .	148
6.4	Measurements . . . . .	150
6.4.1	Thermodynamic states . . . . .	150
6.4.2	Comparison with sound speed and density values computed by means of a cubic equation of state . . . . .	150
6.5	Conclusions . . . . .	153
<b>7</b>	<b>Conclusions and recommendations</b>	<b>163</b>
7.1	Key findings . . . . .	163
7.2	Recommendations . . . . .	166

---

<b>A</b>	<b>Rarefaction experiments in the ASTER</b>	<b>171</b>
A.1	Test 1: $P_0 = 2.66$ bar, $T_0 = 349.8$ °C, $\Gamma_{\text{model}} = 0.87$ . . . . .	171
A.2	Test 2: $P_0 = 2.89$ bar, $T_0 = 300.3$ °C, $\Gamma_{\text{model}} = 0.74$ . . . . .	175
A.3	Test 3: $P_0 = 5.85$ bar, $T_0 = 357.6$ °C, $\Gamma_{\text{model}} = 0.58$ . . . . .	178
A.4	Test 4: $P_0 = 8.87$ bar, $T_0 = 370.9$ °C, $\Gamma_{\text{model}} = 0.096$ . . . . .	181
A.5	Test 5: $P_0 = 8.96$ bar, $T_0 = 369.6$ °C, $\Gamma_{\text{model}} = -0.052$ . . . . .	184
A.6	Test 6: $P_0 = 9.33$ bar, $T_0 = 372.1$ °C, $\Gamma_{\text{model}} = -0.013$ . . . . .	187
A.7	Test 7: $P_0 = 9.37$ bar, $T_0 = 370.7$ °C, $\Gamma_{\text{model}} = 6$ . . . . .	190
A.8	Test 8: $P_0 = 9.4$ bar, $T_0 = 372$ °C, $\Gamma_{\text{model}} = 0.023$ . . . . .	193
	<b>Acknowledgements</b>	<b>197</b>
	<b>Curriculum Vitæ</b>	<b>199</b>
	<b>List of Publications</b>	<b>201</b>



# Summary

The study of compressible fluid dynamics has traditionally focused on flows of gases whose thermodynamic properties are related according to the ideal-gas law. In this context, for a long time, it has been demonstrated that shock waves in gases are exclusively of the compressive type, characterized by a discontinuity across which the fluid pressure rapidly increases. However, in the 1940s, world-renowned scientists such as Bethe and Zel'dovich put forth the theoretical possibility of the formation of rarefaction shock waves (RSWs) if the fluid is a high molecular complexity compound and its thermodynamic state is that of a dense vapour. Across such a RSW, the flow experiences an abrupt drop in pressure. The theoretical concept of RSWs became more known and gained widespread acceptance when further investigations were conducted in the 1970s by Thompson and his colleagues. They introduced the fundamental derivative of gasdynamics  $\Gamma$ , the caloric fluid property that determines the nature of shock waves that can occur in a flow depending on the molecular complexity of the fluid and its thermodynamic state. To acknowledge the significant contributions of the aforementioned scientists to this field of fluid mechanics, fluids that possess the unique characteristic of theoretically admitting RSWs due to the occurrence of thermodynamic states featuring  $\Gamma < 0$  in the dense-vapour phase are referred to as BZT fluids. The branch of fluid dynamics dealing with fluid flows that might display characteristics that are radically different or even opposite to those of classical gas dynamics is aptly called *nonclassical gasdynamics*.

Despite extensive theoretical knowledge of nonclassical gas dynamics, which includes rarefaction shock waves (RSWs), there is still a lack of compelling experimental evidence supporting their existence. The motivation for the research documented in this dissertation is two-fold: firstly, it is crucial to conduct experiments that can provide empirical validation of nonclassical gas dynamics, with a specific focus on observing RSWs, which have proven elusive in previous attempts. Secondly, performing accurate measurements of fluid properties in the dense-vapour thermodynamic regime has the potential to improve the thermodynamic models of BZT fluids or fluids made of complex organic molecules in general. This in turn can contribute to a more accurate characterisation of flows in practical applications that involve these fluids, such as turbine flows in Organic Rankine Cycle (ORC) systems or compressors in high temperature heat pumps.

This research work aimed to provide conclusive experimental evidence for

the existence of nonclassical expansion shock waves in the flows of a candidate BZT fluid, siloxane D<sub>6</sub>. Relevant theoretical studies were performed to complement the experimental observation of nonclassical effects. In addition, novel measurements of fluid properties in the nonclassical gasdynamic region of the candidate BZT fluid were executed, the outcomes of which are useful for the improvement and the optimisation of thermodynamic models for this fluid. For this purpose, two novel test facilities namely the Asymmetric Shock Tube for Experiments on Rarefaction Waves (ASTER) and the Organic Vapour Acoustic Resonator (OVAR) have been conceived, developed, designed, built and commissioned at TU Delft.

This dissertation begins with a brief review of the theory on nonclassical gasdynamics (Chapter 2). Here, starting from the fundamental conservation equations, it is discussed how nonlinearities arising from both the fluid properties and the wave propagation itself can result in the formation of shock waves. The chapter also examines the criteria for the admissibility of rarefaction shock waves (RSWs) in BZT fluids. Moving forward, Chapter 3 explores various experimental techniques suitable to demonstrate the existence of nonclassical RSWs. In particular, the previous experimental attempts to generate and measure a RSW with the Flexible Asymmetric Shock Tube (FAST) facility, which was commissioned at TU Delft in 2010 before the development of the ASTER, is discussed. Unfortunately, these initial experiments proved unsuccessful due to the complex nature of the FAST facility and the challenges associated with attaining and maintaining the required thermodynamic conditions. Furthermore, the presence of significant axial temperature variations along the charge tube of the FAST hindered meaningful measurements even if the initial thermodynamic state of the working fluid is possibly one featuring negative  $\Gamma$ .

The measurement of axial temperature variations along the charge tube of the FAST prompted a theoretical and numerical study on the effect of such gradients on nonlinear wave propagation in BZT fluids. Previous studies on nonlinear wave propagation assumed homogeneous thermodynamic conditions of the fluid, but the few experimental efforts aimed at generating and measuring rarefaction shock waves were hindered by the challenge of maintaining a constant temperature in the medium. This is because the nonclassical effects due to negative nonlinearity wave propagation may occur with the fluid in a state that spans a narrow range of pressures and temperatures, and even small change of the fluid thermodynamic state may cause nonclassical gasdynamic flows to become impossible. Chapter 4 presents a comprehensive analysis of the study on the evolution and steepening of a wavefront propagating through a BZT fluid with axial temperature gradients. This study employed both analytical and numerical approaches to examine the effects of temperature gradients on wave behavior. The results of this study highlighted for some

conditions variations in the temperature along the direction of propagation of the wave might actually enhance nonlinear effects provided such variations have a wavelength much smaller than that of the wave.

To overcome the challenges encountered with the FAST facility, the ASTER was developed with the primary objective of successfully generating and measuring a rarefaction shock wave in  $D_6$ . The design features and the working principle of this new facility are described in detail in Chapter 5. The ASTER shares a similar layout with the FAST but is smaller, simpler, and easier to operate. Using the ASTER, a series of rarefaction tests were conducted with  $D_6$  at different initial thermodynamic conditions in the vapor phase, spanning from 2.66 bar and 350 °C in the mildly non-ideal gasdynamic region to 9.4 bar and 372 °C in the highly non-ideal and the predicted nonclassical states. Notably, measurements of wavespeeds during the dense-vapour tests indicated the presence of strong non-ideal effects in the flow. Furthermore, some of the tests even showcased features that could be explained as the propagation of a rarefaction shock wave, however the repetition of more experiments and a more accurate determination of the thermodynamic state of the fluid will be needed to conclude that the existence of nonclassical gas dynamics is proven.

This thesis also reports about measurements of the speed of sound of  $D_6$  performed with the fluid in dense vapour thermodynamic states. These measurements are particularly challenging given the high temperature at which the fluid must be kept and crucial both for the development of more accurate thermodynamic models of the fluid and for the validation of rarefaction shock wave experiments. To address this challenge, a new setup called the Organic Vapour Acoustic Resonator (OVAR) was conceived, designed and realized. The OVAR, as presented in Chapter 6, is capable of measuring speeds of sound in organic molecules at temperatures and pressures of up to 400 °C and 15 bar, respectively. Measurements of both the sound speed and density of  $D_6$  were taken along eight isotherms between 282 °C and 372 °C with estimated relative uncertainties of 0.14% for the sound speed and between  $0.2 \text{ kg}\cdot\text{m}^{-3}$  and  $1.2 \text{ kg}\cdot\text{m}^{-3}$  for the density. Such measurements are the first-of-its-kind in case of  $D_6$  and possibly for any complex organic molecule. Chapter 7 provides concluding remarks and recommendations for future work.



# Samenvatting

De studie van samendrukbare fluidodynamica heeft traditioneel gefocust op de stroming van gassen waarvan de thermodynamische eigenschappen volgens de ideale gaswet zijn. In deze context is al lange tijd aangetoond dat schokgolven in gassen uitsluitend van het compressieve type zijn, gekenmerkt door een discontinuïteit waarbij de vloeistofdruk snel toeneemt. Echter, in de jaren 1940 stelden wereldberoemde wetenschappers zoals Bethe en Zel'dovich de theoretische mogelijkheid voor van de vorming van expansie schokgolven (ESW's) als de vloeistof een verbinding is met een hoge moleculaire complexiteit en de thermodynamische toestand ervan die van een dichte dampfase is. Over zo'n ESW ervaart de stroming een abrupte drukdaling. Het theoretische concept van ESW's werd bekender en kreeg brede acceptatie toen er in de jaren 1970 verder onderzoek werd gedaan door Thompson en zijn collega's. Zij introduceerden de fundamentele afgeleide van gasdynamica  $\Gamma$ , de calorische eigenschap van een vloeistof die het karakter van schokgolven bepaalt die kunnen optreden in een stroming afhankelijk van de moleculaire complexiteit van de vloeistof en de thermodynamische toestand ervan. Ter erkenning van de belangrijke bijdragen van de eerder genoemde wetenschappers aan dit vakgebied van de fluidomechanica, worden vloeistoffen die de unieke eigenschap bezitten om theoretisch ESW's toe te laten vanwege thermodynamische toestanden met  $\Gamma < 0$  in de dichte dampfase aangeduid als BZT-vloeistoffen. De tak van de fluidodynamica die zich bezighoudt met stromingen die kenmerken kunnen vertonen die radicaal verschillend of zelfs tegengesteld zijn aan die van de klassieke gasdynamica, wordt toepasselijk aangeduid als *niet-klassieke gasdynamica*.

Ondanks uitgebreide theoretische kennis van niet-klassieke gasdynamica, inclusief expansie schokgolven (ESW's), ontbreekt het nog steeds aan overtuigend experimenteel bewijs voor hun bestaan. De motivatie voor het onderzoek dat in deze dissertatie wordt beschreven, is tweeledig: ten eerste is het cruciaal om experimenten uit te voeren die empirische validatie van niet-klassieke gasdynamica kunnen bieden, met speciale aandacht voor het waarnemen van ESW's, die in eerdere pogingen moeilijk te observeren waren. Ten tweede kan het nauwkeurig meten van vloeistofeigenschappen in het dichte-damp thermodynamische regime bijdragen aan verbetering van thermodynamische modellen voor BZT-vloeistoffen of vloeistoffen die bestaan uit complexe organische moleculen in het algemeen. Dit is met name relevant voor de efficiënte ontwerp en werking van industriële processen waarbij dergelijke stromingen wor-

den aangetroffen, zoals turbine-stromingen van Organic Rankine Cycle (ORC) systemen..

Het onderzoek had als doel om overtuigend experimenteel bewijs te leveren voor het bestaan van niet-klassieke expansie schokgolven in de stromingen van een potentiële BZT-vloeistof, siloxaan  $D_6$ . Er werden relevante theoretische studies uitgevoerd om de experimentele waarneming van niet-klassieke effecten aan te vullen. Bovendien werden nieuwe metingen van vloeistofeigenschappen in het niet-klassieke gasdynamische gebied van de potentiële BZT-vloeistof uitgevoerd, waarvan de resultaten nuttig zijn voor de verbetering en optimalisatie van thermodynamische modellen voor deze vloeistof. Hiervoor werden twee nieuwe testfaciliteiten ontwikkeld, namelijk de Asymmetrische Schokbuis voor Experimenten met Expansiegolven (ASTER) en de Organische Damp Akoestische Resonator (OVAR), die zijn bedacht, ontwikkeld, ontworpen, gebouwd en in gebruik genomen aan de Technische Universiteit Delft (TU Delft).

Deze dissertatie begint met een beknopte bespreking van de theorie over niet-klassieke gasdynamica (Chapter 2). Hier wordt, uitgaande van de fundamentele behoudsvergelijkingen, besproken hoe niet-lineariteiten die voortkomen uit zowel de vloeistofeigenschappen als de golfvoortplanting zelf, kunnen leiden tot de vorming van schokgolven. Het hoofdstuk onderzoekt ook de criteria voor de toelaatbaarheid van expansie schokgolven (ESW's) in BZT-vloeistoffen. Vervolgens worden in Chapter 3 verschillende experimentele technieken besproken die geschikt zijn om het bestaan van niet-klassieke ESW's aan te tonen. In het bijzonder wordt ingegaan op eerdere experimentele pogingen om een ESW te genereren en meten met de Flexibele Asymmetrische Schokbuis (FAST)-faciliteit, die in 2010 in gebruik werd genomen aan de TU Delft voordat de ASTER werd ontwikkeld. Helaas waren deze eerste experimenten onsuccesvol vanwege de complexe aard van de FAST-faciliteit en de uitdagingen die gepaard gaan met het bereiken en handhaven van de vereiste thermodynamische omstandigheden. Bovendien belemmerde de aanwezigheid van aanzienlijke axiale temperatuurvariaties langs de laadbuis van de FAST zinvolle metingen, zelfs als de aanvankelijke thermodynamische toestand van de werkende vloeistof mogelijk een negatieve  $\Gamma$  had.

De meting van axiale temperatuurvariaties langs de laadbuis van de FAST leidde tot een theoretische en numerieke studie naar het effect van dergelijke gradiënten op niet-lineaire golfvoortplanting in BZT-vloeistoffen. Eerdere studies naar niet-lineaire golfvoortplanting gingen uit van homogene omstandigheden, en eerdere experimentele inspanningen gericht op het genereren en meten van verdunningsschokgolven werden gehinderd door de uitdaging om een constante temperatuur in het medium te handhaven. Dit komt omdat het negatieve niet-lineariteitsgebied een smalle range van drukken en temperaturen beslaat en zelfs kleine temperatuur-inhomogeniteiten de thermody-

namische toestand van de vloeistof kunnen veranderen, waardoor niet-klassieke stromingen onmogelijk worden. Chapter 4 presenteert een uitgebreide analyse van de studie naar de evolutie en versterking van een golffront dat zich voortplant door een BZT-vloeistof met axiale temperatuurgradiënten. Deze studie maakte gebruik van zowel analytische als numerieke benaderingen om de effecten van temperatuurgradiënten op het golfgedrag te onderzoeken. De resultaten van deze studie lieten zien dat variaties in temperatuur langs de voortplantingsrichting van de golf in sommige gevallen daadwerkelijk niet-lineaire effecten kunnen versterken, mits dergelijke variaties een golflengte hebben die veel kleiner is dan die van de golf.

Om de uitdagingen van de FAST-faciliteit te overwinnen, werd de ASTER ontwikkeld met als belangrijkste doel het succesvol genereren en meten van een expansie schokgolf in  $D_6$ . Het ontwerp en het werkingsprincipe van deze nieuwe faciliteit worden uitvoerig beschreven in Chapter 5. De ASTER heeft een vergelijkbare opstelling als de FAST, maar is kleiner, eenvoudiger en gemakkelijker te bedienen. Met behulp van de ASTER werden een reeks expansietests uitgevoerd met  $D_6$  bij verschillende aanvangs thermodynamische condities in de dampfase, variërend van 2,66 bar en 350 °C in het licht niet-ideale gasdynamische gebied tot 9,4 bar en 372°C in het sterk niet-ideale en voorspelde niet-klassieke toestanden. Opmerkelijk genoeg wezen metingen van golfsnelheden tijdens de dichte-damp tests op de aanwezigheid van sterke niet-ideale effecten in de stroming. Bovendien vertoonden sommige tests zelfs kenmerken die verklaard konden worden als de voortplanting van een expansie schokgolf, maar herhaling van meer experimenten en een nauwkeurigere bepaling van de thermodynamische toestand van de vloeistof zijn nodig om te concluderen dat het bestaan van niet-klassieke gasdynamica bewezen is.

Deze proefschrift rapporteert ook metingen van de geluidssnelheid van  $D_6$  die zijn uitgevoerd met behulp van de OVAR in een bredere thermodynamische toestand, waarvan de resultaten worden besproken in Chapter 6. De OVAR is een niet-geometrisch begrensde resonator die is ontworpen om zowel de longitudinale als de transversale geluidssnelheid in dampen en gassen te meten. De metingen van de geluidssnelheid van  $D_6$  in een breed scala aan drukken en temperaturen maakten het mogelijk om de thermodynamische eigenschappen van  $D_6$  in het niet-klassieke gasdynamische gebied te karakteriseren. Deze resultaten dragen bij aan het begrip van de vloeistofeigenschappen van  $D_6$  en kunnen worden gebruikt om bestaande thermodynamische modellen te verbeteren en te valideren.

Ten slotte geeft Chapter 7 een samenvatting van de belangrijkste bevindingen van het onderzoek en bespreekt het de mogelijke implicaties en toekomstige richtingen. Hoewel er geen definitief bewijs is geleverd voor het bestaan van expansie schokgolven in  $D_6$ , hebben de experimentele inspanningen in deze scriptie belangrijke inzichten opgeleverd in niet-klassieke gasdynamica

en de meettechnieken die kunnen worden gebruikt om dergelijke fenomenen te onderzoeken. Het onderzoek heeft ook bijgedragen aan een beter begrip van de thermodynamische eigenschappen van  $D_6$  in het niet-klassieke gasdynamische regime, wat relevant is voor toepassingen waarin deze vloeistof wordt gebruikt. Verdere experimenten en verbeterde meettechnieken kunnen leiden tot de definitieve bevestiging van niet-klassieke expansie schokgolven en een beter begrip van niet-klassieke gasdynamica in het algemeen.

# 1

## Introduction

### 1.1. A primer in nonclassical gasdynamics

*Compressible Fluid Dynamics*, or *Gasdynamics*, is the study of fluid flows where the change in fluid density is significant. Such flows occur in several natural and technological processes, e.g., the life-cycle of stars, the exhaust of aircraft engines, turbomachinery flows, etc.

In general, most compressible flows can be assumed to obey the ideal gas equation of state (EoS). However, it is well known that substances in the vapour phase exhibit an appreciable departure from ideal-gas behaviour even at moderate pressures and temperatures. This effect is particularly pronounced if the thermodynamic conditions are in the dense-vapour region close to the critical point or the saturation curve. In such cases, the ideal-gas law completely fails to describe the behaviour of the substance [1].

The deviation in the behaviour of a specific gas from that predicted by the ideal-gas law can be measured using the empirical quantity called the *Compressibility Factor*,  $Z$ , defined as,

$$Z = \frac{Pv}{RT}, \quad (1.1)$$

where  $P$ ,  $v$ ,  $R$  and  $T$  are the pressure, specific volume, specific gas constant and temperature respectively. A gas behaves ideally when  $Z = 1$ . The extent to which it exhibits dense-vapour characteristics is the extent to which  $Z$  deviates from 1, as seen for Nitrogen ( $N_2$ ) in Fig. 1.1.

As a result, the study of dense vapours requires the use of equations of state that account for non-ideal gas effects arising from intermolecular forces

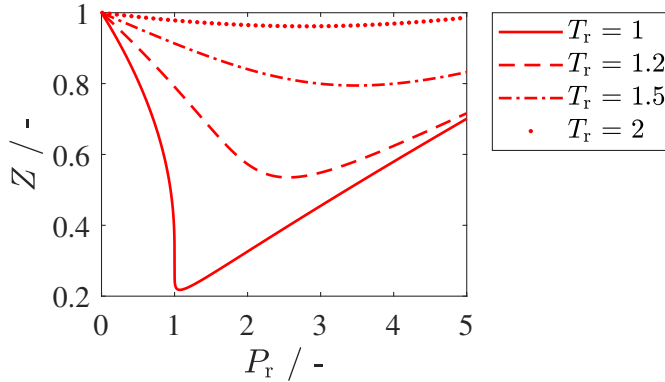


Figure 1.1: Variation of  $Z$  with reduced quantities  $P_r$  and  $T_r$  for Nitrogen. A value of 1 denotes ideal-gas behaviour.

of attraction and repulsion. The effect of these forces was first identified by Johannes Diderik van der Waals, who in his PhD thesis, conceived the best known and the simplest form of the cubic equation of state, now known as the van der Waals (vdW) EoS, written as,

$$P = \frac{RT}{v - b} - \frac{a}{v^2}, \quad (1.2)$$

where  $a$  and  $b$  are constants derived from the critical properties of the substance being considered. In Eq. (1.2), the first term on the right-hand side expresses the effect of repulsive forces between molecules while the second term models the attractive vdW forces [2], [3]. Despite its simplicity, the vdW EoS correctly (at least qualitatively) models the  $P-v-T$  relation of substances in the liquid and the gaseous states.

Even with such simple equations of state that consider non-ideal gas effects, several studies have shown that substances made up of polyatomic molecules may exhibit gasdynamic features that are markedly different from their ideal-gas counterparts in a narrow region in the  $P-v$  thermodynamic plane. These flow characteristics include rarefaction shockwaves, which are forbidden in the ideal-gas region due to their violation of the second law of thermodynamics, double sonic shocks, compression fans, etc.[4]–[6]

Considering the case of shock waves, Bethe [7] showed that the entropy

increase across a shock wave is given by,

$$\Delta s = - \left( \frac{\partial^2 p}{\partial v^2} \right)_s \frac{(\Delta v)^3}{12T}, \quad (1.3)$$

where the term,  $(\partial^2 p / \partial v^2)_s$ , is a measure of the curvature of an isentrope in the  $P-v$  plane. Thus, to satisfy the 2nd law of thermodynamics (i.e.,  $\Delta s > 0$ ), a necessary condition for the formation of a compressive ( $\Delta V = V_2 - V_1 < 0$ ) shock wave is that

$$\left( \frac{\partial^2 p}{\partial v^2} \right)_s > 0 \quad (1.4)$$

which is generally satisfied by most substances in the single-phase region. Naturally, since  $\Delta V$  is positive for a rarefaction wave, Eq. (1.3) is not satisfied and hence, RSWs are not thermodynamically admissible. Anticipating the discussions to be followed in Chapter 2, the derivative in Eq. (1.4) can be written in the non-dimensional form as ([8], [9]),

$$\Gamma \equiv 1 + \frac{\rho}{c} \left( \frac{\partial c}{\partial \rho} \right)_s = \frac{v^3}{2c^2} \left( \frac{\partial^2 p}{\partial v^2} \right)_s. \quad (1.5)$$

Thompson [4] referred to this thermodynamic property  $\Gamma$  as the fundamental derivative of gasdynamics due to its importance to compressible gasdynamic phenomena including shock-wave theory, Raleigh and Fanno flows, etc. For an ideal gas, Eq. (1.5) reduces to  $\Gamma = (\gamma + 1)/2$ , where  $\gamma$  is the ratio of the specific heat capacities, i.e.,  $\gamma = c_p/c_v$ , and therefore  $\Gamma > 1$ . However, there is no fundamental reason for  $\Gamma$  to be only positive for all fluids in every thermodynamic state. It has already been shown both theoretically and experimentally that for certain fluids,  $\Gamma$  can assume values lower than 1 in the dense-vapour thermodynamic region [4], [10]. The study of fluid flows occurring in such conditions is referred to as Non-Ideal Compressible Fluid Dynamics (NICFD). It has been further theorized that for fluids of sufficient molecular complexity,  $\Gamma$  can even change sign and become negative owing to a finite region of concavity of the isentropes in the  $P-v$  plane. In such conditions, Eqs. (1.3) and (1.4) are satisfied, thereby enabling the admissibility of rarefaction shock waves, compression fans, etc. The study of flows occurring in conditions where  $\Gamma < 0$  is called *nonclassical gasdynamics*.

The concavity of the isentropes, and the resulting negative values of  $\Gamma$ ,

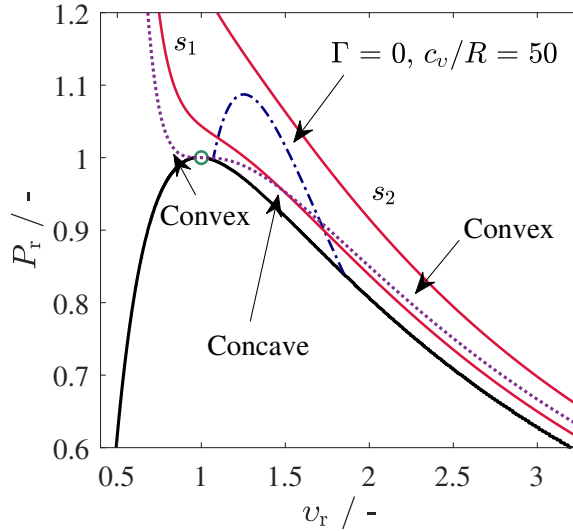


Figure 1.2:  $P-v$  plane of an exemplary vdW fluid;  $\Gamma < 0$  region for  $c_v/R = 50$  is shown. The critical point (○), the critical isotherm (⋯), and two isentropes ( $s_1$ ) and go over ( $s_2$ ) the  $\Gamma < 0$  region are shown.

can be explained by examining the behaviour of the critical isotherm in the  $P-v$  plane. It is known that, for the critical isotherm, both  $(\partial P/\partial v)_T$  and  $(\partial^2 P/\partial v^2)_T$  are zero at the critical point and that it is convex in the ideal gas limit where  $v \rightarrow \infty$  [11]. Therefore, the isotherm must display a concave curvature in a limited range between the critical point and the ideal gas region, as shown in Fig. 1.2. For substances comprising of sufficiently complex molecules, the behaviour of the isentropes is similar to the isotherms due to their high isochoric heat capacities, and therefore, feature a region of concavity.

Bethe showed that vdW gases can indeed exhibit a region of negative concavity ( $(\partial^2 P/\partial v^2)_s < 0$ ) in the general vicinity of the critical point given that ratio of the isochoric heat capacity  $C_v$  to the universal gas constant  $R$  is larger than 17.5. However, he dismissed this value as being physically impossible. Zeldovich [12] also independently arrived at this value for  $C_v/R$  but speculated that such a value for a vdW gas might be possible. Thompson *et al.* [13] and Lambrakis *et al.* [14] further went on to provide substantial theoretical evidence for the existence of such fluids with an embedded  $\Gamma < 0$  region. Owing to the pioneering work and contribution of Bethe, Zeldovich and Thompson to the field of nonclassical gasdynamics, substances that exhibit a  $\Gamma < 0$  region in the single-phase dense-gas regime are collectively known

as the Bethe-Zel'dovich-Thompson (BZT) fluids, and the phenomena that are observed in this thermodynamic region are referred to as BZT effects.

## 1.2. Motivation and thesis outline

Despite such well-established theories for the existence of nonclassical gasdynamics, no successful experimental observations of BZT effects in a gas exist to date. To the author's knowledge, only three such experiments to demonstrate BZT effects in the single-phase thermodynamic region of dense gases have been attempted, and that too have produced inconclusive results. The first of these experiments was conducted by Borisov *et al.* [15] using Freon-13 (trifluorochloromethane,  $\text{CClF}_3$ ) as the test fluid. The authors claimed to have observed a propagating rarefaction shock wave in the single-phase region. However, this result has been refuted by Fergason [16], stating that the model EoS for Freon-13 doesn't predict a  $\Gamma < 0$  region in the dense-gas thermodynamic regime. Fergason also showed using numerical simulations that, since the initial conditions of the experiment conducted by Borisov were at the critical point, the observed expansion wave potentially displayed critical-point phenomena and two-phase effects. The second experiment was conducted by Fergason and is documented in his PhD thesis [16]. This attempt too did not produce conclusive results due to the thermal decomposition of the test fluid, a perfluorocarbon, at the high experimental initial conditions.

The most recent attempt to measure a RSW in the single-phase dense-gas region was performed by Mathijssen [17] using the Flexible Asymmetric Shock Tube (FAST) facility at TU Delft. He reported performing several measurements in the predicted  $\Gamma < 0$  region of siloxane  $\text{D}_6$  and documented evidence of the possibility of RSWs existing in the flow. However, anticipating the results of Section 3.3.4, it is possible that Mathijssen was observing mixed waves evolving in the two-phase region due to the large longitudinal temperature gradients in the FAST. The setup also used a fast opening valve (FOV) as a barrier element, as opposed to the conventional diaphragm, and delays in the opening of the valve can also affect the steepening behaviour of the rarefaction wave.

Experimental evidence of nonclassical gasdynamic effects is needed in general for further progress in the field of compressible fluid dynamics. One challenge in improving our understanding of nonclassical flows is the relatively poor accuracy of the existing thermodynamic models for BZT fluids. In general, it is the case that the more complex an organic molecule is, the more challenging it is to perform measurements to characterize its behaviour. While technical equations of state have been developed for several of these fluids, their accuracy is limited when compared to other classes of substances due to the lack of experimental data sets.

The scarcity of experimental data for flows in the nonclassical gasdynamic region is rather the result of the difficulties in performing experiments in these conditions than a lack of scientific interest. Fluids that commonly exhibit nonclassical behaviour are liquids at standard room temperature and pressure. However, the predicted  $\Gamma < 0$  region lies close to the critical point, which typically is in the range of 10-20 bar in pressure and 300-400 °C in temperature [18], [19]. Achieving these conditions in a test facility is both complicated and expensive. Furthermore, such conditions are also close to the thermal stability limit of the BZT fluids, and the presence of moisture or air in the setup can lead to thermal decomposition [20]. Measurement procedures are more complex owing to the high fluid temperatures and there is also the risk of local condensation in cold spots or pneumatic lines. Additionally, the  $\Gamma < 0$  region spans a narrow range of pressures and temperatures and any temperature gradient in the setup can alter the experimental outcome.

This research aims to provide the first-of-its-kind experimental evidence for the existence of nonclassical gasdynamic effects by demonstrating the formation of a rarefaction shock wave in the dense-vapours of a BZT candidate fluid, siloxane D<sub>6</sub>. To achieve this goal, a new shock tube facility has been designed, developed, built and commissioned. Additionally, thermodynamic measurements of sound speed and density have also been recorded to improve the technical equations of state for the aforementioned fluid. Finally, relevant theory describing the propagation of RSWs in fluids that are subjected to axial temperature gradients has been developed.

This thesis is organized as follows: in Chapter 2, the theory governing nonclassical gasdynamics is outlined. Starting from the propagation of waves in general, the origin of nonlinearities and the admissibility criteria for the formation of nonclassical rarefaction shockwaves are discussed. Chapter 3 provides a brief overview of the experimental options that can be employed to generate RSWs in a BZT fluid. It also discusses the experiments that have been performed in the past to prove the existence of nonclassical gasdynamic effects. In particular, this chapter discusses the design and functioning of the FAST, along with the various issues faced in the setup and the modifications that were made to improve its operability. One of the issues encountered in the FAST was the inhomogeneity in the axial temperature of the setup. Given the sensitivity of  $\Gamma$  to temperature, this can hinder the formation of an RSW in the setup. To understand the impact of such temperature inhomogeneities on nonlinear wave steepening and shock formation, a numerical study using analytical equations and 1D wave equation models was performed. The details of this study are presented in Chapter 4.

Building upon the experiences gained with the FAST, a novel Ludwig-type shock tube was designed and constructed at the Propulsion & Power Group at TU Delft for the purpose of creating and detecting RSWs. The design of this

new setup, called the Asymmetric Shock Tube for Experiments on Rarefaction Waves (ASTER), is described in Chapter 5. This chapter also presents the results of rarefaction experiments performed in both the mildly non-ideal and the dense-gas thermodynamic regions of the working fluid siloxane  $D_6$ , along with sound speed measurements at different pressures and temperatures. The speed of sound in  $D_6$  was also measured using the Organic Vapour Acoustic Resonator (OVAR), a square-cylindrical resonator that was specifically built for performing such measurements in the dense-gas region of the working fluid. The design of the OVAR, its commissioning, and the experimental results are discussed in detail in Chapter 6. Finally, in Chapter 7, the conclusions and recommendations for future research activities are summarized.



# Bibliography

- [1] P. A. Thompson, *Compressible Fluid Dynamics (advanced engineering series)*, Third. McGraw-Hill Inc., US, 1988.
- [2] G. Soave, "Improvement of the Van Der Waals equation of state," *Chemical Engineering Science*, vol. 39, no. 2, pp. 357–369, 1984. DOI: [10.1016/0009-2509\(84\)80034-2](https://doi.org/10.1016/0009-2509(84)80034-2).
- [3] G. M. Kontogeorgis, R. Privat, and J.-N. Jaubert, "Taking Another Look at the van der Waals Equation of State - Almost 150 Years Later," *Journal of Chemical & Engineering Data*, vol. 64, no. 11, pp. 4619–4637, Aug. 2019. DOI: [10.1021/acs.jced.9b00264](https://doi.org/10.1021/acs.jced.9b00264).
- [4] P. A. Thompson, "A Fundamental Derivative in Gasdynamics," *Physics of Fluids*, vol. 14, no. 9, p. 1843, 1971. DOI: [10.1063/1.1693693](https://doi.org/10.1063/1.1693693).
- [5] A. Kluwick, in *Handbook of Shock Waves*. Elsevier, 2001, ch. Rarefaction Shockwaves, pp. 339–411. DOI: [10.1016/b978-012086430-0/50008-7](https://doi.org/10.1016/b978-012086430-0/50008-7).
- [6] N. R. Nannan, "Advancements in nonclassical gas dynamics," Ph.D. dissertation, TU Delft, 2009.
- [7] H. A. Bethe, "On the Theory of Shock Waves for an Arbitrary Equation of State," in *Classic Papers in Shock Compression Science*, Springer New York, 1998, pp. 421–495. DOI: [10.1007/978-1-4612-2218-7\\_11](https://doi.org/10.1007/978-1-4612-2218-7_11).
- [8] W. D. Hayes, in *Fundamentals of gasdynamics*. Princeton Univeristy Press, 1958, vol. 3, ch. The basic theory of gas dynamic discontinuities, p. 426.
- [9] L. D. Landau and E. M. Lifschitz, "Fluid Mechanics," in Addison-Wesley, 1959, p. 373.
- [10] A. Spinelli, G. Cammi, S. Gallarini, *et al.*, "Experimental evidence of non-ideal compressible effects in expanding flow of a high molecular complexity vapor," *Experiments in Fluids*, vol. 59, no. 8, Jul. 2018. DOI: [10.1007/s00348-018-2578-0](https://doi.org/10.1007/s00348-018-2578-0).
- [11] J. J. Martin and Y.-C. Hou, "Development of an equation of state for gases," *AIChE Journal*, vol. 1, no. 2, pp. 142–151, Jun. 1955. DOI: [10.1002/aic.690010203](https://doi.org/10.1002/aic.690010203).

- [12] Y. B. Zeldovich, “14. On the Possibility of Rarefaction Shock Waves,” in *Selected Works of Yakov Borisovich Zeldovich, Volume I*, Princeton University Press, Dec. 1992, pp. 152–154. DOI: [10.1515/9781400862979.152](https://doi.org/10.1515/9781400862979.152).
- [13] P. A. Thompson and K. C. Lambrakis, “Negative shock waves,” *Journal of Fluid Mechanics*, vol. 60, no. 1, pp. 187–208, Aug. 1973. DOI: [10.1017/s002211207300011x](https://doi.org/10.1017/s002211207300011x).
- [14] K. C. Lambrakis and P. A. Thompson, “Existence of Real Fluids with a Negative Fundamental Derivative  $\Gamma$ ,” *Physics of Fluids*, vol. 15, p. 933, 1972. DOI: <https://doi.org/10.1063/1.1694004>.
- [15] A. A. Borisov, A. A. Borisov, S. S. Kutateladze, and V. E. Nakoryakov, “Rarefaction shock wave near the critical liquid–vapour point,” *Journal of Fluid Mechanics*, vol. 126, pp. 59–73, Jan. 1983. DOI: [10.1017/s002211208300004x](https://doi.org/10.1017/s002211208300004x).
- [16] S. H. Ferguson, “Dense gas shock tube: Design and analysis,” Ph.D. dissertation, University of Colorado at Boulder, 2001.
- [17] T. Mathijssen, “Experimental Observation of Non-Ideal Compressible Fluid Dynamics with application in Organic Rankine Cycle Power Systems,” Ph.D. dissertation, TU Delft, 2017.
- [18] P. Colonna, A. Guardone, and N. R. Nannan, “Siloxanes: A new class of candidate Bethe-Zel’dovich-Thompson fluids,” *Physics of Fluids*, vol. 19, no. 8, p. 086102, Aug. 2007. DOI: [10.1063/1.2759533](https://doi.org/10.1063/1.2759533).
- [19] C. Zamfirescu and I. Dincer, “Performance investigation of high-temperature heat pumps with various BZT working fluids,” *Thermochimica Acta*, vol. 488, no. 1-2, pp. 66–77, May 2009. DOI: [10.1016/j.tca.2009.01.028](https://doi.org/10.1016/j.tca.2009.01.028).
- [20] S. Chen, C. Liu, Q. Li, Y. Liu, L. Xin, and W. Yu, “A ReaxFF-based molecular dynamics study of the pyrolysis mechanism of hexamethyldisiloxane,” *Journal of Molecular Liquids*, vol. 356, p. 119026, Jun. 2022. DOI: [10.1016/j.molliq.2022.119026](https://doi.org/10.1016/j.molliq.2022.119026).

# 2

## Nonlinear waves in Bethe-Zel'dovich-Thompson fluids

### 2.1. Theory of wave propagation

A wave is a transfer of energy through a medium from one point to another. In fluids, waves typically manifest in the form of a disturbance in the local pressure (such as in acoustic waves), temperature or density. The basic equations that govern wave propagation in a thermoviscous fluid are the conservation principles of mass, momentum and energy, and these must be complemented by a model of the material in which the wave propagates. This model is based on an equation of state (EoS) for the fluid. These equations are of the form

$$\frac{\partial \rho}{\partial t} + \nabla \cdot (\rho \mathbf{v}) = 0 \quad (2.1a)$$

$$\rho \left[ \frac{\partial \mathbf{v}}{\partial t} + (\mathbf{v} \cdot \nabla) \mathbf{v} \right] = -\nabla p + \nabla \cdot \bar{\bar{\tau}} + \rho \mathbf{f} \quad (2.1b)$$

$$\rho \left[ \frac{\partial h}{\partial t} + \nabla \cdot (h \mathbf{v}) \right] = \frac{Dp}{Dt} + \nabla \cdot (k \nabla T) + \phi \quad (2.1c)$$

with  $\rho$  being the density,  $p$  the pressure,  $T$  the temperature,  $\mathbf{v}$  the velocity vector,  $\mathbf{f}$  the body force vector,  $\bar{\bar{\tau}}$  the viscous stress tensor,  $h$  the enthalpy,  $k$

the thermal conductivity and  $\phi$  the dissipation function [1]. Equations (2.1a) and (2.1b) are collectively known as the Navier-Stokes equations. The viscous stress tensor is expressed as

2

$$\bar{\tau}_{ij} = \mu \left( \frac{\partial v_i}{\partial x_j} + \frac{\partial v_j}{\partial x_i} - \frac{2}{3} (\nabla \cdot \mathbf{v}) \delta_{ij} \right), \quad (2.2)$$

in which  $\mu$  is the coefficient of shear viscosity and  $\delta_{ij}$  is the Kronecker-Delta operator that is 1 if  $i = j$  and zero otherwise. The dissipation function represents the work done against viscous forces, one that is irreversibly converted into internal energy, and is written as

$$\phi = \bar{\tau}_{ij} \frac{\partial v_i}{\partial x_j}. \quad (2.3)$$

Equation (2.1) can be simplified by neglecting the viscous and thermal conductivity terms giving rise to the Euler equations, here written for a 1D flow with a constant cross-sectional area as

$$\begin{aligned} \frac{\partial \rho}{\partial t} + \rho \frac{\partial u}{\partial x} + u \frac{\partial \rho}{\partial x} &= 0 \\ \frac{\partial u}{\partial t} + u \frac{\partial u}{\partial x} + \frac{1}{\rho} \frac{\partial p}{\partial x} &= 0 \end{aligned} \quad (2.4)$$

where  $x$  represents the spatial coordinate.

The equation required to close the set of Eq. (2.1) is the material EoS that relates the fluid properties such as  $p$ ,  $T$ ,  $\rho$ ,  $c$ , etc., which in general, can be written in the form of

$$p = p(\rho, s) \quad (2.5)$$

where  $s$  is the specific entropy [2]. These equations range from the simple ideal-gas law to complex technical equations such as the Helmholtz EoS that can describe both the ideal and real gas properties of substances.

### 2.1.1. Linear Wave Equation

Equation (2.1) are inherently complex, nonlinear and normally, exact solutions do not exist. One approach to simplify these equations and obtain analytical solutions is to consider small perturbations of the relevant quantities about

the equilibrium [3]. Considering the case of a local pressure disturbance  $\Delta p$ , the conditions to assume that the amplitude of a wave is *small* are:

- the amplitude of the perturbation  $\Delta p$  is smaller than the average pressure  $\bar{p}$  of the medium
- the displacement of a fluid element in the medium is smaller when compared to its wavelength  $\lambda$  and,
- the wavelength  $\lambda$  is itself smaller than the length scale  $L$  over which  $\bar{p}$  changes

The advantage of studying small-amplitude waves is that the nonlinear terms in Eq. (2.1) can be expressed as linear functions of the displacement field. The simplest equation describing wave propagation in one-dimension in an inviscid medium with constant properties is the 1D wave equation in pressure

$$\frac{\partial^2 p}{\partial x^2} - \frac{1}{c_0^2} \frac{\partial^2 p}{\partial t^2} = 0, \quad (2.6)$$

where  $x$  is the spatial co-ordinate [4]. It describes how the pressure evolves in space and time as a small-amplitude wave propagates through the medium. However, linear theory fails to correctly characterize the behaviour of the wave if its amplitude increases or if the propagation distances are long with sufficiently low damping. In these cases, nonlinear phenomena unknown in linear acoustics such as the formation of shockwaves can occur [5]. Waves with large enough amplitude to exhibit nonlinear propagation effects are called as *finite-amplitude* waves.

### 2.1.2. Origin of nonlinearities

Waves propagating in an acoustic medium may experience nonlinear effects through two mechanisms. The first arises from the inherent nonlinearity in the relation between the properties of the medium. The second is due to the distortion of the waveform caused by the propagation of the wave itself through the medium [5], [6]. Nonlinearities in a medium are present even in the simple case of an ideal gas since it obeys the isentropic equation

$$pv^\gamma = \text{constant}, \quad (2.7)$$

where  $\gamma = c_p/c_v$  is the ratio of the specific heat at constant pressure  $c_p$  to that at constant volume  $c_v$ . One way of writing a pressure-explicit EoS is to

develop a Taylor series expansion in terms of density  $\rho$  and entropy  $s$  about the equilibrium state. Assuming small deviations of pressure  $p$  over the ambient pressure  $p_0$ , this equation can be written as:

$$p = p_0 + \left( \frac{\partial p}{\partial \rho} \right)_s (\rho - \rho_0) + \frac{1}{2!} \left( \frac{\partial^2 p}{\partial \rho^2} \right)_s (\rho - \rho_0)^2 + \frac{1}{3!} \left( \frac{\partial^3 p}{\partial \rho^3} \right)_s (\rho - \rho_0)^3 + \dots \quad (2.8)$$

or,

$$p = p_0 + A \left( \frac{\rho - \rho_0}{\rho_0} \right) + \frac{B}{2} \left( \frac{\rho - \rho_0}{\rho_0} \right)^2 + \frac{C}{6} \left( \frac{\rho - \rho_0}{\rho_0} \right)^3 + \dots \quad (2.9)$$

Here,

$$A = \rho_0 \left( \frac{\partial p}{\partial \rho} \right)_s = \rho_0 c_0^2; \quad B = \rho_0^2 \left( \frac{\partial^2 p}{\partial \rho^2} \right)_s; \quad C = \rho_0^3 \left( \frac{\partial^3 p}{\partial \rho^3} \right)_s, \quad (2.10)$$

and  $\rho_0$  and  $c_0$  are the ambient density and the small-signal adiabatic sound speed respectively. The higher order terms in Eq. (2.8) can generally be neglected. The ratio of the coefficient of the second-order term  $B$  to the linear coefficient  $A$  provides a measure of the strength of the nonlinearity in the medium and is called the *nonlinearity parameter*. Using Eq. (2.10), this can be expressed as,

$$\frac{B}{A} = \frac{\rho_0}{c_0^2} \left( \frac{\partial^2 p}{\partial \rho^2} \right)_s \quad (2.11)$$

This ratio is common in the field of acoustics and has been measured and reported for a wide range of fluids [7]–[10].  $B/A$  has a strong influence on the speed of sound  $c$ . Since  $c^2 = (\partial p / \partial \rho)_s$ , Eq. (2.9) can be rearranged in terms of the sound speed as

$$\left( \frac{c}{c_0} \right)^2 = 1 + \frac{B}{A} \left( \frac{\rho - \rho_0}{\rho_0} \right) + \frac{C}{2A} \left( \frac{\rho - \rho_0}{\rho_0} \right)^2 + \dots, \quad (2.12)$$

which can be further expanded and written as

$$\frac{c}{c_0} = 1 + \frac{B}{2A} \left( \frac{\rho - \rho_0}{\rho_0} \right) + \frac{1}{4} \left[ \frac{C}{A} - \frac{1}{2} \left( \frac{B}{A} \right)^2 \right] \left( \frac{\rho - \rho_0}{\rho_0} \right)^2 + \dots, \quad (2.13)$$

which shows that the leading-order correction to  $c_0$  depends on  $B/A$  [11], [12]. For a small-amplitude plane wave propagating in the + x-direction, the speed of propagation at any point along the wave is given as

$$\frac{dx}{dt} = c_0. \quad (2.14)$$

However, in the case of a finite amplitude wave, different points along the wave travel at different speeds. This primarily arises due to the fact that a propagating wave sets up a longitudinal velocity field  $u$  in the fluid through which it travels. Since the moving fluid also helps to convect the wave along, the propagation speed at any point in the wave with respect to a fixed observer is now

$$\frac{dx}{dt} = c + u = w, \quad (2.15)$$

where  $w$  is the phase velocity of the wave [6]. The longitudinal velocity  $u$  of the fluid, also known as the particle velocity, can be written using Eq. (2.12) as

$$u = c_0 \left( \frac{\rho - \rho_0}{\rho_0} \right). \quad (2.16)$$

Substituting the above equation into Eq. (2.13) and neglecting the higher-order terms yields

$$c = c_0 + \frac{B}{2A} u, \quad (2.17)$$

The phase velocity  $w$  then becomes

$$w = c_0 + \beta u, \quad (2.18)$$

where  $\beta$ , called the *coefficient of nonlinearity*, is given by [13]

$$\beta = 1 + \frac{B}{2A}. \quad (2.19)$$

2

Equation (2.18) clearly shows the two distinct effects that give rise to nonlinear behaviour: one, the inherent nonlinearity of the medium in the  $B/A$  term and the other due to convection. This nonlinearity due to the convective term would exist even if the medium itself is devoid of nonlinearities, i.e.,  $B/A = 0$ . This implies that a truly linear wave propagation does not exist except for infinitely small values of  $u$ , i.e., waves of infinitely small amplitudes. It also shows that the nonlinear distortion of the wave is cumulative, depending on the time and distance travelled by the wave [14].

Equation (2.11) shows that the ratio  $B/A$  is also a measure of the curvature of an isentrope,  $(\partial^2 p / \partial v^2)_s$ , like  $\Gamma$ . In fact, Eq. (1.5) for  $\Gamma$  can be rewritten in terms of  $\rho$  as

$$\begin{aligned} \Gamma &= \frac{v^3}{2c^2} \left( \frac{\partial^2 p}{\partial v^2} \right)_s = 1 + \frac{\rho}{2c^2} \left( \frac{\partial^2 p}{\partial \rho^2} \right)_s \\ &= 1 + \frac{B}{2A} = \beta. \end{aligned} \quad (2.20)$$

Thus, like  $\beta$ ,  $\Gamma$  is related to the distortion of finite-amplitude waves that propagate through nonlinear mediums. In acoustics,  $\beta$  is always positive and usually much larger than 1. However, in the case of non-ideal gasdynamics,  $\Gamma$  can also assume values less than 1 or even be negative.

### 2.1.3. Nonlinear Wave Equation

The linear wave equation, Eq. (2.6), cannot be used to accurately describe the propagation of waves in the presence of nonlinearities. To get an accurate representation of nonlinear wave propagation, it is necessary to solve the full Navier-Stokes system of equations (Equation (2.1)). However, finding an analytical solution to this set of equations is difficult, and normally not possible, due to its complexity. In order to facilitate obtaining solutions that are more mathematically amenable, it is common in the study of nonlinear acoustics to consider only equations that take into account quadratic nonlinear terms. Such simplified equations are referred to as *weakly nonlinear wave equations* [2].

Several models of such weakly nonlinear equations have been proposed and studied in literature [15], [16]. The most widely used equation in nonlinear

acoustics is the Kuznetsov equation, written as

$$c_0^2 \frac{\partial^2 \phi}{\partial x^2} - \frac{\partial^2 \phi}{\partial t^2} + \delta \frac{\partial^3 \phi}{\partial^2 x \partial t} = \frac{\partial}{\partial t} \left[ \left( \frac{\partial \phi}{\partial t} \right)^2 + \frac{\beta - 1}{c_0^2} \left( \frac{\partial \phi}{\partial t} \right)^2 \right], \quad (2.21)$$

where  $\phi$  is the velocity potential, and  $\delta$  is the diffusivity of sound given by [17], [18]

$$\delta = \nu \left[ \frac{4}{3} + \frac{\mu_B}{\mu} + \frac{\gamma - 1}{Pr} \right], \quad (2.22)$$

in which  $\mu$ ,  $\mu_B$  and  $\nu$  ( $=\mu/\rho_0$ ) are the shear, bulk and kinematic viscosities respectively,  $\gamma$  is the ratio of specific heats and  $Pr = \nu/\kappa$  is the Prandtl number where  $\kappa$  is the thermal diffusivity. The Kuznetsov equation is a general nonlinear wave equation that describes wave propagation in a thermoviscous fluid. It is seen that in the absence of viscosity, and in a medium without nonlinearities, i.e., for  $\delta = 0$  and  $\beta = 1$ , Eq. (2.21) reduces to the linear wave equation (Eq. (2.6)). A somewhat simpler equation in terms of mathematical treatment is the Westervelt Equation [19], [20], which is a simplification of Eq. (2.21) and is written as

$$c_0^2 \frac{\partial^2 \phi}{\partial x^2} - \frac{\partial^2 \phi}{\partial t^2} + \frac{\delta}{c_0^2} \frac{\partial^3 \phi}{\partial t^3} = \frac{\beta}{c_0^2} \frac{\partial}{\partial t} \left( \frac{\partial \phi}{\partial t} \right)^2. \quad (2.23)$$

Equation (2.23) is valid for finite-amplitude waves that propagate in a medium with homogeneous conditions. This equation can be further extended to include wave propagation in mediums with axially varying properties. Rewriting in terms of the pressure, and replacing  $\beta$  with  $\Gamma$  [21], [22], the Westervelt equation becomes

$$\frac{\partial^2 p}{\partial x^2} - \frac{1}{c_0^2} \frac{\partial^2 p}{\partial t^2} - \frac{1}{\rho_0} \frac{\partial \rho}{\partial x} \frac{\partial p}{\partial x} + \frac{\delta}{c_0^4} \frac{\partial^3 p}{\partial t^3} + \frac{\Gamma}{\rho_0 c_0^4} \frac{\partial^2 p^2}{\partial t^2} = 0, \quad (2.24)$$

wherein, similar to Eq. (2.23), the first two terms make up the 1D linear wave equation describing the lossless propagation of a wave at the small-signal sound speed  $c_0$ . The third term accounts for the inhomogeneity in the medium through the gradients in density, the fourth term models the losses due to thermal and viscous effects and the fifth term defines the nonlinear distortion that arises from finite-amplitude effects.

## 2.2. Nonlinear distortion and shock formation

A consequence of the varying propagation speed  $w$  across a wave is the nonlinear distortion of the wave profile as it travels in a medium. Rewriting Eq. (2.18) in terms of  $p$  and  $\Gamma$  gives

$$w = c_0 + \Gamma \left( \frac{p - p_0}{\rho_0 c_0} \right), \quad (2.25)$$

where  $p - p_0$  is the *acoustic pressure*, and the expression  $\rho_0 c_0$  is called the *acoustic impedance*.

Figure 2.1 shows the propagation of a weak pressure wave generated by the actuation of a piston in a tube containing a BZT fluid. Figure 2.1a displays the profile of a compression wave propagating in the fluid. Such a compression is generated by advancing the piston in the tube. Assuming that the fluid is in a state featuring  $\Gamma > 0$ , and since the acoustic pressure is always positive ( $p > p_0$ ) in a compression, from Eq. (2.25),  $w$  progressively increases in the direction of increasing pressure, i.e., from the head to the tail of the wave. Thus, the tail of the wave would accelerate during propagation thereby distorting the wavefront. If the wave is of sufficient amplitude, this acceleration would result in the tail catching up with the head thereby creating a discontinuity, which in this case, is called a *compression shock wave* (CSW).

Instead of advancing the piston, if it is withdrawn as shown in Fig. 2.1b, an expansion wave is generated in the tube. Across an expansion, the acoustic pressure is negative ( $p < p_0$ ). In the classical sense, according to Eq. (2.25), this would cause the wavespeed to decrease from the head to the tail of the wave, resulting in an isentropic expansion fan. However, if the fluid is also assumed to be in a state that features  $\Gamma < 0$ , then  $w$  would increase from the head to the tail of the wave, as in the case of a compression. The tail would therefore accelerate during propagation, eventually catching up with the head. This leads to the formation of the so-called *rarefaction shock wave* (RSW).

## 2.3. Shock jump conditions and admissibility criterion

The flow of matter across a shock wave must satisfy the conservation equations of mass, momentum, and energy (Eq. (2.1)). Once a shock is formed, nonlinear models such as Eqs. (2.21) and (2.24) are no longer valid and the flow-field can only be described through a balance of the flow properties across the shock.

The conservation equations can be applied to an arbitrarily thin control volume that encloses the shock wave and moves with the same velocity  $W$ . The control volume is chosen such that both viscous stresses and the heat flux

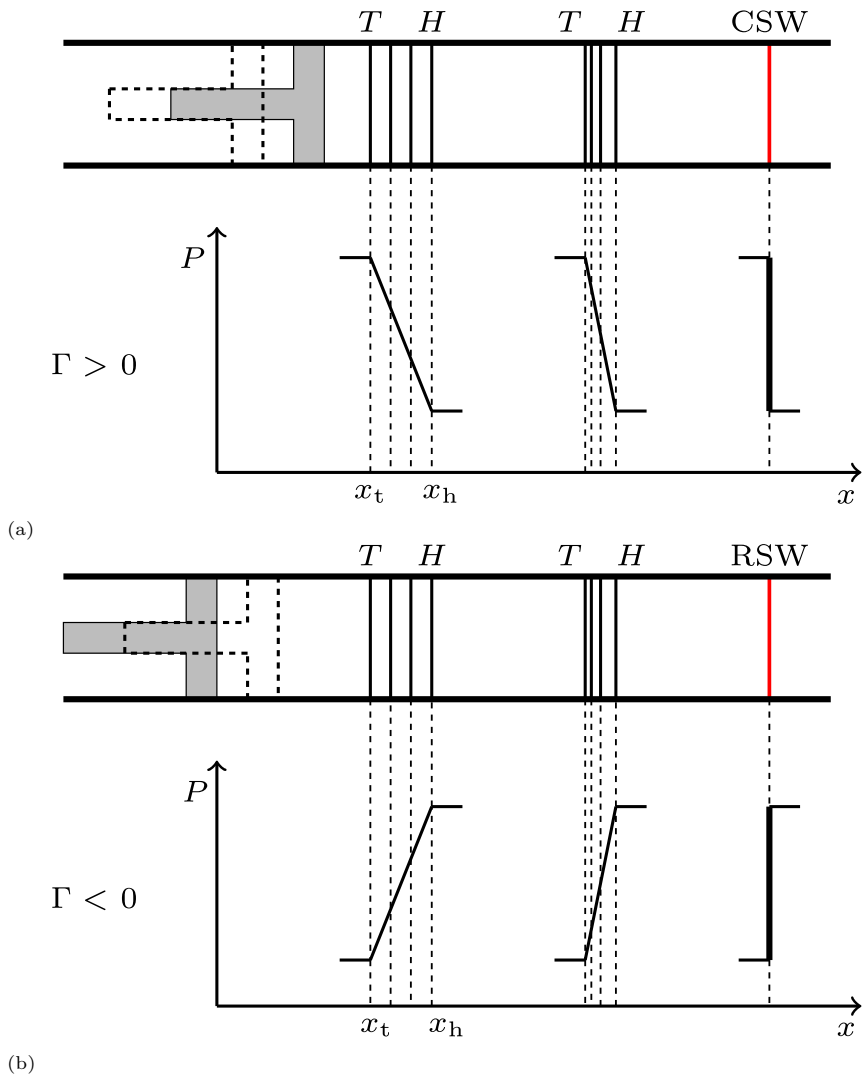


Figure 2.1: Nonlinear distortion of (a) compression and (b) expansion waves propagating in mediums featuring  $\Gamma > 0$  and  $\Gamma < 0$ .  $H$  and  $T$  denote the head and the tail of the wave.

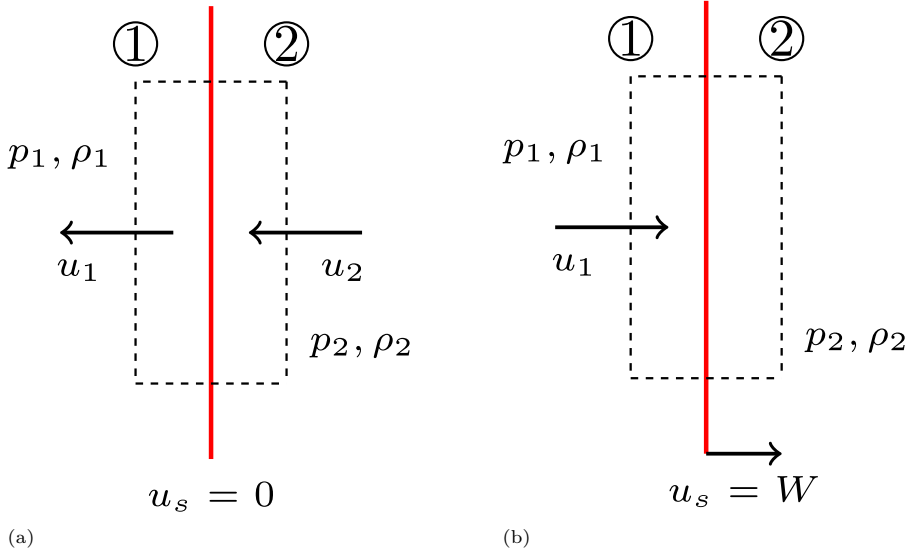


Figure 2.2: Control volume around a travelling shock wave in (a) Laboratory frame and (b) Shock frame of reference.

within it can be neglected. This results in a set of simple equations called the *shock conditions* that relate the thermodynamic state 1 upstream of the shock wave to the downstream state 2 (see Fig. 2.2). These conditions are written as

$$\rho_1 u_1 = \rho_2 u_2 = J \quad (2.26a)$$

$$p_1 + \rho_1 u_1^2 = p_2 + \rho_2 u_2^2 \quad (2.26b)$$

$$h_2 + \frac{1}{2} u_2^2 = h_1 + \frac{1}{2} u_1^2 \quad (2.26c)$$

where  $J$  is the mass flux, which is determined by the upstream flow. In Eq. (2.26), it is assumed that the heat flux and viscous losses are negligible at the control surface. Combining Eqs. (2.26a) and (2.26b) and multiplying both the left- and the right-hand sides by  $\rho_1 \rho_2$  gives,

$$J^2 = \frac{P_2 - P_1}{v_1 - v_2}. \quad (2.27)$$

This equation represents a straight line, with a slope of  $-J^2$ , in the  $P - v$  plane that connects the pre- and post-shock states. It is referred to as the

*Rayleigh line.* Equation (2.27) can also be rearranged in terms of  $P$  and  $v$  to give

$$h_2 - h_1 = \frac{1}{2}(P_2 - P_1)(v_2 + v_1). \quad (2.28)$$

This equation, called the Rankine-Hugoniot (RH) *shock adiabat*, was independently derived by Rankine [23] and Hugoniot [24] and is applicable to shock discontinuities in general. It mathematically connects the pre- and post-shock states only by means of thermodynamic properties and is independent of the reference frame. For a given pre-shock state 1, the solution of the equation gives a locus of all the possible post-shock thermodynamic states, which can be drawn, for example, in a  $P - v$  plot.

In this analysis, the control volume is chosen such that the shock wave can be treated as a discontinuity without considering its structure. As such, dissipative effects are neglected within this volume. This simplifies the mathematical treatment of the discontinuous change in properties across the shock wave. However, the thermodynamic and fluid dynamic properties across the shock wave change rather abruptly, and this sudden change brings about large temperature and velocity gradients, thereby making the process from state 1 to 2 irreversible. This implies that, in addition to the conservation laws, the entropy must also increase across the shock wave, i.e.,

$$[s] \geq 0, \quad (2.29)$$

where the square brackets represent the jump in the quantity across the shock wave, i.e.,  $[\cdot] = (\cdot)_2 - (\cdot)_1$ . The entropy jump across a shock can be obtained by performing a Taylor series expansion of the RH equation in terms of pressure, yielding

$$[s] = \frac{1}{6} \frac{\Gamma_1 c_1^2}{T_1} \Pi^3 + \mathcal{O}(\Pi^4), \quad (2.30)$$

where  $\Pi = [P]/\rho_1 c_1^2$  is the non-dimensional pressure jump which is positive for a compression wave and negative for rarefactions. Since  $[s] \geq 0$ , and  $c$  and  $T$  can only be positive, Eq. (2.30) is satisfied only if  $\Pi$  and  $\Gamma$  are of the same sign. Thus, it is immediately evident that weak compression shocks are possible only when  $\Gamma > 0$  and weak expansion shocks only when  $\Gamma < 0$ . It can also be readily demonstrated that, since  $[s] \propto [P]^3$ , there is a negligible change in entropy as  $[P] \rightarrow 0$ , i.e., the entropy jump across a weak shock is negligibly small. This result allows the treatment of weak shock waves as isentropic [25].

Moreover, as shown by Lax [26] and Oleinik [27], a fifth condition called the mechanical stability criterion or the speed-ordering condition needs to be satisfied for admissible shock waves. This condition states that the pre-shock Mach number  $M_1 = u_1/c_1$  must be greater than or at least equal to unity and that the post-shock Mach number  $M_2 = u_2/c_2$  must be less than or at most equal to unity. Thus, a shock wave must satisfy the following conditions to be admissible:

$$[\rho u] = 0, \quad (2.31a)$$

$$[P + \rho u] = 0, \quad (2.31b)$$

$$\left[h + \frac{1}{2}u^2\right] = 0, \quad (2.31c)$$

$$[s] \geq 0, \quad (2.31d)$$

$$Ma_1 \geq 1 \geq Ma_2, \quad (2.31e)$$

Unlike the conservation equations, the entropy (Eq. (2.31d)) and the speed-ordering conditions (Eq. (2.31e)) impose a direction in which a flow process can occur across a shock wave.

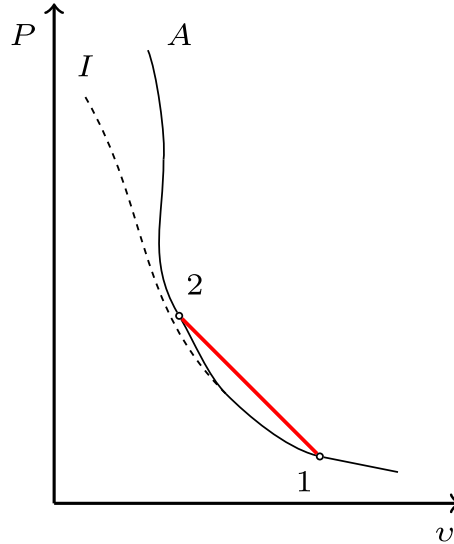


Figure 2.3: Shock adiabat ( $A$ ) and isentrope ( $I$ ) in the  $P-v$  plane. Rayleigh line connecting upstream state 1 with downstream state 2 is shown in red.

Figure 2.3 shows a schematic of a shock-adiabat and an isentrope in the

$P - v$  thermodynamic plane and a hypothetical compression shock jump from state 1 to state 2. At state 1, the slope of the isentrope is

$$\left(\frac{\partial p}{\partial v}\right)_1 = -\frac{1}{v^2} \frac{\partial^2 p}{\partial v^2} \Big|_1 = -\rho_1^2 c_1^2, \quad (2.32)$$

while the slope of the line connecting upstream state 1 with downstream state 2 is  $-J^2$ , as shown in Eq. (2.27). Dividing the two expressions for the slope and applying the speed-ordering criterion yields

$$\frac{-J^2}{\left(\frac{\partial p}{\partial v}\right)_1} = \left(\frac{u_1}{c_1}\right)^2 = M_1^2 \geq 1. \quad (2.33)$$

A similar equation can be derived for the downstream state 2. The equivalent expression for the mechanical stability criterion then becomes

$$\left(\frac{\partial p}{\partial v}\right)_1 \geq \left[\frac{P}{v}\right]_{1 \rightarrow 2} \geq \left(\frac{\partial p}{\partial v}\right)_2. \quad (2.34)$$

Thus, for a shock wave to be admissible, the slope of the shock adiabat evaluated at state 1 must be greater than or at least equal to the slope of the Rayleigh line connecting states 1 and 2, which itself must be greater than or at least equal to the slope of the shock adiabat evaluated at state 2. Also, by combining Gibb's relation,

$$Tds = de + pdv, \quad (2.35)$$

with Eqs. (2.31c) and (2.31d) yields

$$\int_{v_1}^{v_2} Tds = \int_{v_1}^{v_2} pdv - \frac{P_2 + P_1}{2} [v] = S_A - S_R, \quad (2.36)$$

where  $S_A$  and  $S_R$  denote the areas subtended by the adiabat and the Rayleigh line respectively in the  $P - v$  plane. Equations (2.34) and (2.36) together imply that the Rayleigh line cannot intersect the adiabat at any interior point and must lie completely above (if convex) or below (if concave) the adiabat connecting states 1 and 2 for a shock to be admissible. The mechanical stability criterion is the most restrictive condition for the admissibility of a shock wave, and a shock that satisfies this condition automatically satisfies Eq. (2.31d).

## 2.4. Admissibility of compression shocks in BZT fluids

A necessary condition for the admissibility of compression shock waves is that  $\Gamma$  be locally positive. However, theoretical studies have shown that, given the appropriate pre-shock and post-shock conditions, it is possible that compression shocks can also occur in the  $\Gamma < 0$  thermodynamic region [28]. Figure 2.4 shows a hypothetical shock adiabat that passes through the  $\Gamma < 0$  region in the  $P-v$  plane. As expected, the adiabat is concave in the region where  $\Gamma < 0$  and convex outside of this domain. The pre-shock state 1 is arbitrarily chosen in the  $\Gamma > 0$  region just below the  $\Gamma = 0$  boundary.

Starting from state 1, the first process leading to state 2 lies entirely within the  $\Gamma > 0$  region. The Rayleigh line is also completely above the adiabat. This process would therefore be admissible and can be determined using Eq. (2.31). Similarly, a compression shock would be admissible between states 1 & 3 even though state 3 lies in the negative  $\Gamma$  region. A special case occurs for the shock jump from state 1 to 4 since at state 4, the Rayleigh line is tangent to the adiabat. Thus, the entropy is at a maximum and the post-shock state features a sonic speed (see Eq. (2.34)) giving rise to a *post-sonic shock wave*.

A shock wave leading to state 5 would be inadmissible since the Rayleigh line would then intersect the adiabat at an interior point thereby violating the speed-ordering criterion. In fact, all possible post-shock states between states 4 and 6 are inadmissible because of this reason. The shock from state 1 to 6 is a composite wave, made-up of a post-sonic shock from state 1 to 4 and a *pre-sonic shock* from state 4 to 6. For the Rayleigh line connecting states 1 and 7, a single compression shock wave is admissible that is neither pre-sonic nor post-sonic but one that just passes through the  $\Gamma < 0$  region.

It is still possible to achieve post-shock states that are lower in pressure than state 6, e.g., states 8 and 9, through a composite wave. A compression from state 1 to 9 would initially begin as a post-sonic shock from state 1 to 4. From state 4 to state 8, both being in the BZT region, a nonclassical isentropic compression fan is formed. At state 8, the isentrope is tangent to the adiabat and thus, a pre-sonic shock connects state 8 to state 9.

## 2.5. Admissibility of rarefaction shocks in BZT fluids

The admissibility criterion for RSWs can be treated similarly to that of compression waves. Unlike a compression shock, however, the thermodynamic states related to a RSW are restricted to a narrow range of pressures and temperatures in which the isentrope exhibits a negative curvature. Figure 2.5 shows a hypothetical shock adiabat passing through the  $\Gamma < 0$  region in the  $P-v$  plane. The initial state 1 is chosen arbitrarily to lie within the BZT region.

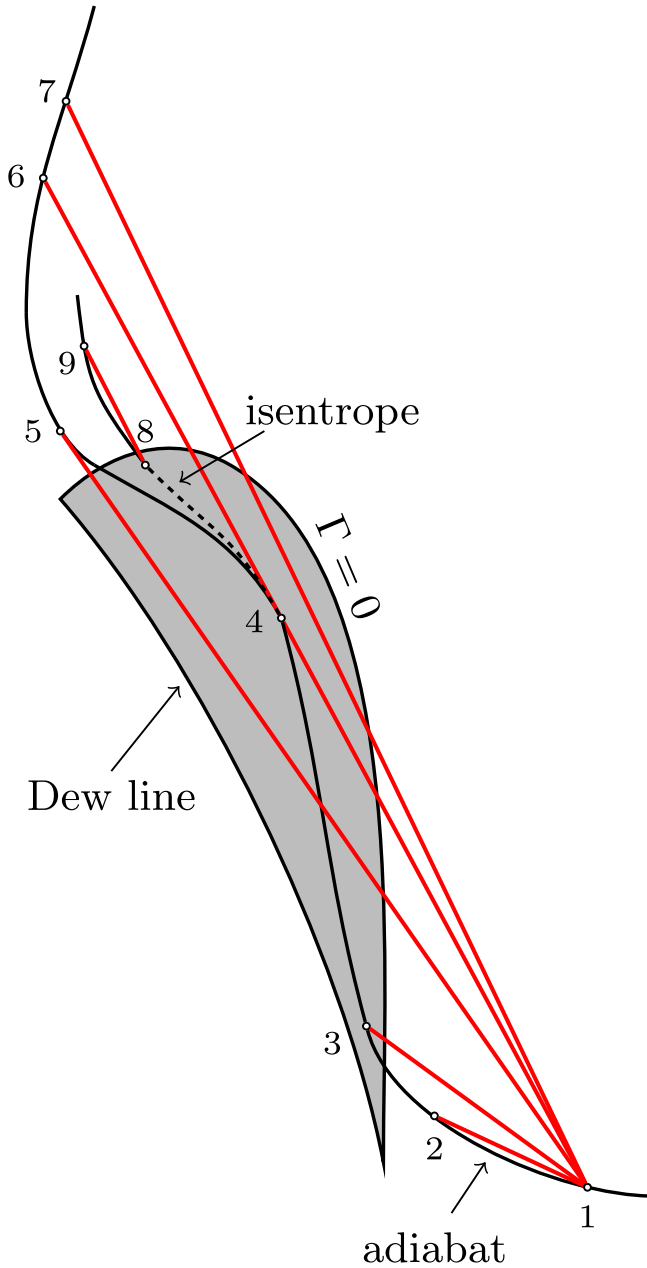


Figure 2.4: Representation of thermodynamic process across a compression shock wave from a state outside of the BZT region. Rayleigh lines connecting the pre-shock state to possible post-shock states are shown in red.

2

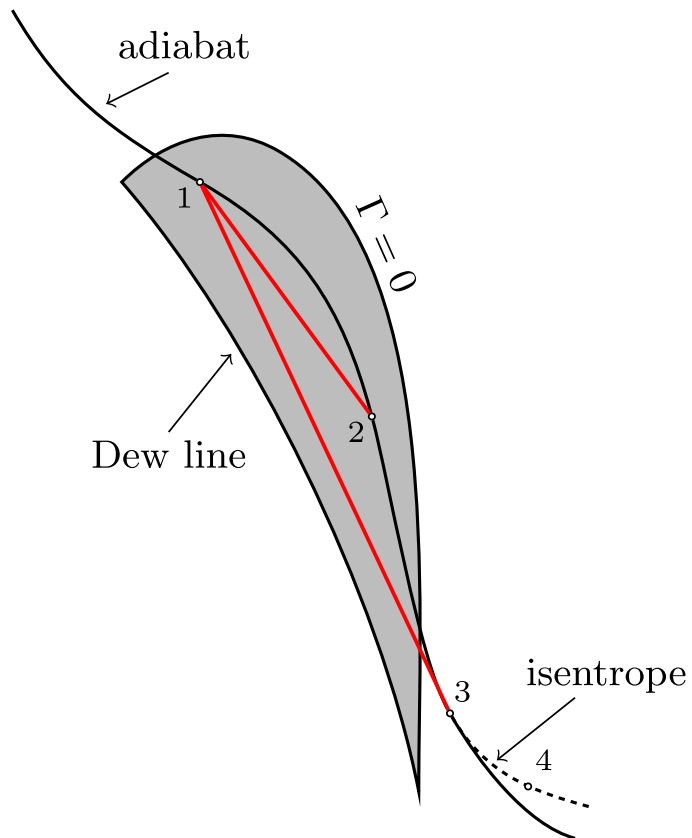


Figure 2.5: Representation of the thermodynamic process across an expansion shock wave from a state within the BZT region. Rayleigh lines connecting the pre-shock state to possible post-shock states are shown in red.

The shock adiabat is fully concave in this thermodynamic region. Thus, for all post-shock states for which  $\Gamma < 0$ , the Rayleigh line would lie completely below the adiabat thus admitting the formation of a RSW. Even for post-shock states that lie outside of the  $\Gamma < 0$  region, a RSW is still admissible as long as the Rayleigh line does not cross the adiabat. In Fig. 2.5, this is possible till state 3 at which point the Rayleigh line is tangential to the adiabat. Thus, any shock that connects state 1 with 3 would feature a post-sonic flow. Past state 3, any expansion must happen isentropically, for example, to state 4.

RSWs can form even if the pre-shock state lies outside but close to the BZT region. Figure 2.6 shows possible rarefaction shock jumps starting from state 1. For post-shock state 1' that lies in the  $\Gamma > 0$  region, only shocks of the compressive type are admissible. Consequently, an expansion between these states takes the form of an isentropic expansion fan. The isentrope at state 1' is however tangential to the adiabat at this state. Thus, any further expansion to state 1'' that lies within the  $\Gamma < 0$  region occurs through a *pre-sonic RSW*.

For states featuring pressures lower than 1'' in the BZT region, the Rayleigh line gets steeper and the initial pressure at which a pre-sonic shock can occur increases. For example, for a shock connecting states 1 and 2, the Rayleigh line is tangent to the adiabat at state 1 thus giving rise to a pre-sonic shock. A limiting case occurs if the post-shock state reaches state 3 in which case the Rayleigh line is tangent to the adiabat at both states 1 and 3. This results in a *double-sonic shock wave* in which the flow has sonic conditions both before and after the shock wave. This double-sonic RSW is the maximum possible pressure difference that can occur across a RSW on a given adiabat [28], [29]. By connecting all the pre-and post-shock states that can result in a double-sonic shock, the *double-sonic locus* (DSL) is obtained (see Fig. 2.6). The area contained within the DSL and the dew line is the region in which RSWs are admissible, and is referred to as the *rarefaction shock region* (RSR). Since state 4 lies outside both the RSR and the BZT region, expansion to this post-shock state can no longer occur through a RSW but rather via an isentropic expansion fan.

2

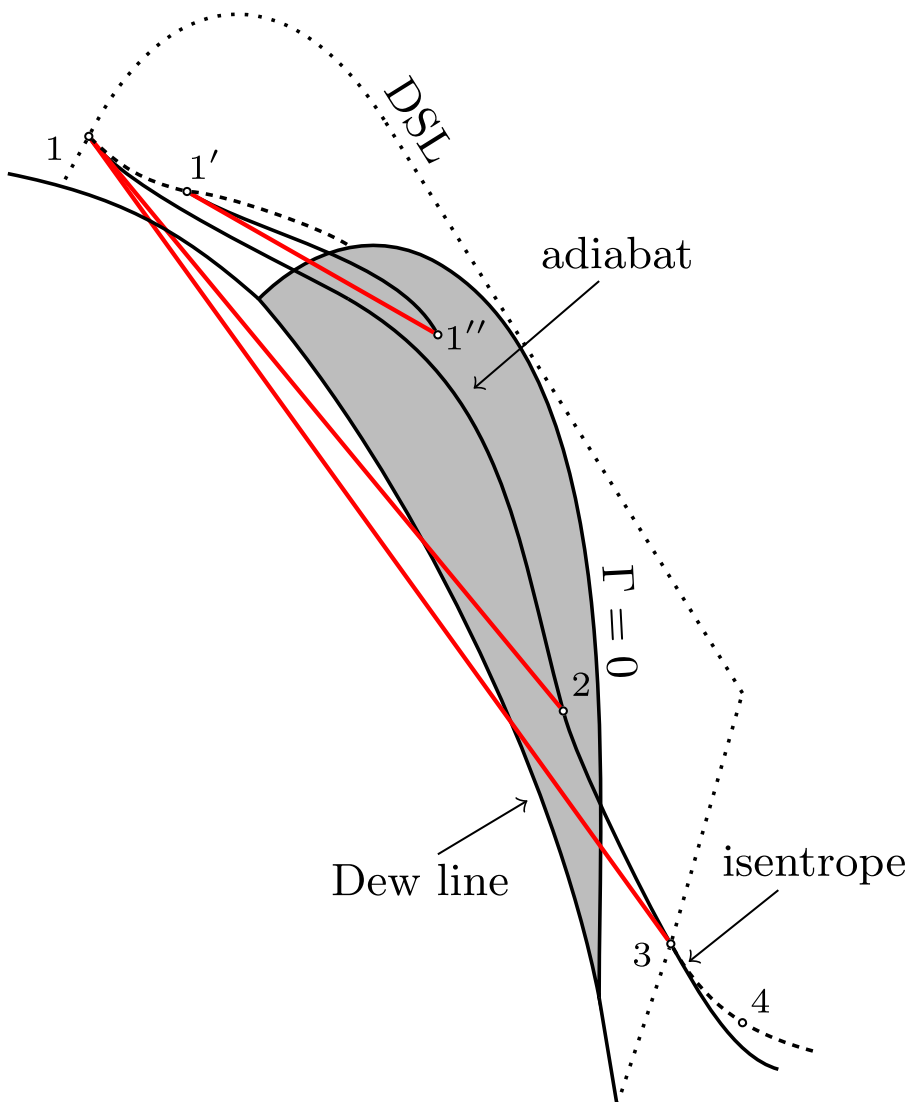


Figure 2.6: Representation of the thermodynamic process across an expansion shock wave from a state outside the BZT region. Rayleigh lines connecting the pre-shock state to possible post-shock states are shown in red.

# Bibliography

- [1] M. Kaltenbacher, “Fundamental Equations of Acoustics,” in *Computational Acoustics*, Springer International Publishing, Jul. 2017, pp. 1–33. DOI: [10.1007/978-3-319-59038-7\\_1](https://doi.org/10.1007/978-3-319-59038-7_1).
- [2] A. R. Rasmussen, “Thermoviscous Model Equations in Nonlinear Acoustics: Analytical and Numerical Studies of Shocks and Rarefaction Waves,” Ph.D. dissertation, Technical University of Denmark, 2009.
- [3] A. Achterberg, “Small Amplitude Waves: Basic Theory,” in *Gas Dynamics*, Atlantis Press, 2016, pp. 125–156. DOI: [10.2991/978-94-6239-195-6\\_7](https://doi.org/10.2991/978-94-6239-195-6_7).
- [4] E. Skudrzyk, “The One-Dimensional Wave Equation and Its Solutions,” in *The Foundations of Acoustics*, Springer Vienna, 1971, pp. 284–294. DOI: [10.1007/978-3-7091-8255-0\\_15](https://doi.org/10.1007/978-3-7091-8255-0_15).
- [5] W. Lauterborn, T. Kurz, and I. Akhatov, “Nonlinear Acoustics in Fluids,” in *Springer Handbook of Acoustics*, Springer New York, 2007, pp. 257–297. DOI: [10.1007/978-0-387-30425-0\\_8](https://doi.org/10.1007/978-0-387-30425-0_8).
- [6] D. T. Blackstock and M. J. Crocker, “Nonlinear Acoustics and Cavitation,” in *Encyclopedia of Acoustics*, John Wiley & Sons, Inc., Dec. 2007, pp. 191–195. DOI: [10.1002/9780470172513.ch17](https://doi.org/10.1002/9780470172513.ch17).
- [7] L. Adler and E. A. Hiedemann, “Determination of the Nonlinearity Parameter  $B/A$  for Water and  $m$ -Xylene,” *The Journal of the Acoustical Society of America*, vol. 34, no. 4, pp. 410–412, Apr. 1962. DOI: [10.1121/1.1918142](https://doi.org/10.1121/1.1918142).
- [8] W. N. Cobb, “Finite amplitude method for the determination of the acoustic nonlinearity parameter  $B/A$ ,” *The Journal of the Acoustical Society of America*, vol. 73, no. 5, pp. 1525–1531, May 1983. DOI: [10.1121/1.389413](https://doi.org/10.1121/1.389413).
- [9] Z. Zhu, M. S. Roos, W. N. Cobb, and K. Jensen, “Determination of the acoustic nonlinearity parameter  $B/A$  from phase measurements,” *The Journal of the Acoustical Society of America*, vol. 74, no. 5, pp. 1518–1521, Nov. 1983. DOI: [10.1121/1.390154](https://doi.org/10.1121/1.390154).
- [10] A. Panfilova, R. J. G. van Sloun, H. Wijkstra, O. A. Sapozhnikov, and M. Mischi, “A review on  $B/A$  measurement methods with a clinical perspective,” *The Journal of the Acoustical Society of America*, vol. 149, no. 4, pp. 2200–2237, Apr. 2021. DOI: [10.1121/10.0003627](https://doi.org/10.1121/10.0003627).

- [11] R. T. Beyer, “Nonlinear Acoustics,” *American Journal of Physics*, vol. 41, no. 9, pp. 1060–1067, Sep. 1973. DOI: [10.1119/1.1987473](https://doi.org/10.1119/1.1987473).
- [12] M. F. Hamilton and D. T. Blackstock, *Nonlinear Acoustics*. Academic Press, 1998.
- [13] —, “On the coefficient of nonlinearity  $\beta$  in nonlinear acoustics,” *The Journal of the Acoustical Society of America*, vol. 83, no. 1, pp. 74–77, Jan. 1988. DOI: [10.1121/1.396187](https://doi.org/10.1121/1.396187).
- [14] E. C. Everbach, “Parameters of Nonlinearity of Acoustic Media,” in *Encyclopedia of Acoustics*, John Wiley & Sons, Inc., Dec. 2007, pp. 219–226. DOI: [10.1002/9780470172513.ch20](https://doi.org/10.1002/9780470172513.ch20).
- [15] D. T. Blackstock, “Some Model Equations of Nonlinear Acoustics,” in *Encyclopedia of Acoustics*, John Wiley & Sons, Inc., Dec. 2007, pp. 197–202. DOI: [10.1002/9780470172513.ch18](https://doi.org/10.1002/9780470172513.ch18).
- [16] P. M. Jordan, “A survey of weakly-nonlinear acoustic models: 1910–2009,” *Mechanics Research Communications*, vol. 73, pp. 127–139, Apr. 2016. DOI: [10.1016/j.mechrescom.2016.02.014](https://doi.org/10.1016/j.mechrescom.2016.02.014).
- [17] A. Dekkers, A. Rozanova-Pierrat, and V. Khodygo, “Models of nonlinear acoustics viewed as approximations of the Kuznetsov equation,” *Discrete & Continuous Dynamical Systems - A*, vol. 40, no. 7, pp. 4231–4258, 2020. DOI: [10.3934/dcds.2020179](https://doi.org/10.3934/dcds.2020179).
- [18] P. M. Jordan, “An analytical study of Kuznetsov’s equation: diffusive solitons, shock formation, and solution bifurcation,” *Physics Letters A*, vol. 326, no. 1-2, pp. 77–84, May 2004. DOI: [10.1016/j.physleta.2004.03.067](https://doi.org/10.1016/j.physleta.2004.03.067).
- [19] P. J. Westervelt, “Parametric Acoustic Array,” *The Journal of the Acoustical Society of America*, vol. 35, no. 4, pp. 535–537, Apr. 1963. DOI: [10.1121/1.1918525](https://doi.org/10.1121/1.1918525).
- [20] I. Shevchenko and B. Kaltenbacher, “Absorbing boundary conditions for nonlinear acoustics: The Westervelt equation,” *Journal of Computational Physics*, vol. 302, pp. 200–221, Dec. 2015. DOI: [10.1016/j.jcp.2015.08.051](https://doi.org/10.1016/j.jcp.2015.08.051).
- [21] I. M. Hallaj, R. O. Cleveland, and K. Hynynen, “Simulations of the thermo-acoustic lens effect during focused ultrasound surgery,” *The Journal of the Acoustical Society of America*, vol. 109, no. 5, pp. 2245–2253, May 2001. DOI: [10.1121/1.1360239](https://doi.org/10.1121/1.1360239).
- [22] G. Pinton, J. Dahl, S. Rosenzweig, and G. Trahey, “A heterogeneous nonlinear attenuating full-wave model of ultrasound,” *IEEE Transactions on Ultrasonics, Ferroelectrics and Frequency Control*, vol. 56, no. 3, pp. 474–488, Mar. 2009. DOI: [10.1109/tuffc.2009.1066](https://doi.org/10.1109/tuffc.2009.1066).

- [23] W. J. M. Rankine, “XV. On the thermodynamic theory of waves of finite longitudinal disturbance,” *Philosophical Transactions of the Royal Society of London*, vol. 160, pp. 277–288, Dec. 1870. DOI: [10.1098/rstl.1870.0015](https://doi.org/10.1098/rstl.1870.0015).
- [24] P. H. Hugoniot, “Sur la propagation du mouvement dans les corps et spécialement dans les gaz parfaits (On the propagation of the movement of bodies, and especially of the perfect gas),” *Journal de l’Ecole Polytechnique*, vol. 57, no. 1, p. 59, 1887.
- [25] P. A. Thompson and G. S. Beavers, “Compressible-Fluid Dynamics,” *Journal of Applied Mechanics*, vol. 39, no. 2, pp. 366–366, Jun. 1972. DOI: [10.1115/1.3422684](https://doi.org/10.1115/1.3422684).
- [26] P. D. Lax, “Hyperbolic systems of conservation laws II,” *Communications on Pure and Applied Mathematics*, vol. 10, no. 4, pp. 537–566, 1957. DOI: [10.1002/cpa.3160100406](https://doi.org/10.1002/cpa.3160100406).
- [27] O. A. Oleinik, “Uniqueness and stability of the generalized solution of the Cauchy problem for a quasi-linear equation,” *Uspekhi Matematicheskikh Nauk*, vol. 14, no. 2, pp. 165–170, 1959.
- [28] C. Zamfirescu, A. Guardone, and P. Colonna, “Admissibility region for rarefaction shock waves in dense gases,” *Journal of Fluid Mechanics*, vol. 599, pp. 363–381, Mar. 2008. DOI: [10.1017/s0022112008000207](https://doi.org/10.1017/s0022112008000207).
- [29] A. Guardone, C. Zamfirescu, and P. Colonna, “Maximum intensity of rarefaction shock waves for dense gases,” *Journal of Fluid Mechanics*, vol. 642, pp. 127–146, Dec. 2009. DOI: [10.1017/s0022112009991716](https://doi.org/10.1017/s0022112009991716).



# 3

## The experimental detection of nonclassical flow phenomena

Chapter 2 treats in detail the theory of nonclassical gasdynamics and the relevant aspects of nonlinear wave propagation in vapours in which portions of the fluid feature thermodynamic states for which the fundamental derivative of gasdynamics  $\Gamma$  is negative. These fluids are collectively referred to as Bethe-Zel'dovich-Thompson (BZT) fluids. Nonclassical gasdynamic phenomena differ from their classical counterparts in multiple aspects, and many flow characteristics are “reversed” to a certain extent [1]. For example, rarefaction shocks and compression fans are possible, as opposed to compression shocks and expansion fans. Though the observation of any such phenomenon would provide conclusive evidence for the existence of nonclassical gasdynamics, hence of fluids for which a finite thermodynamic region of dense vapour states feature  $\Gamma < 0$ , the nonclassical phenomenon that has been at the focus of flow experiments in the perspective of BZT fluids is the rarefaction shock wave (RSW), perhaps because of its exotic nature and novelty. Also, the admissibility region of a RSW in terms of the range in pressures and temperatures is larger when compared to that of a compression fan; therefore, it is comparatively simpler to choose and achieve initial conditions for experiments that aim to generate nonclassical shock waves [2], [3].

Another motivation for focussing on the generation of a rarefaction shock is that there have already been three experiments in different laboratories around the world that have attempted to create and detect a RSW. However, none of the attempted experiments has been able to conclusively settle the debate as

to the existence of nonclassical gasdynamics. The claims resulting from the first attempt by Borisov *et al.* [4] in 1983 have been disputed by Ferguson [5], whose own experiment in 2001 suffered from many technical difficulties, the thermal decomposition of the working fluid being one of them (see Section 3.2). More recently, experiments performed with the Flexible Asymmetric Shock Tube (FAST) at TU Delft seemed to have managed to produce rarefaction waves in the supposed nonclassical region of a BZT fluid [6], siloxane D<sub>6</sub>, but, anticipating the results of Section 3.3.4, even these results can be contested due to the difficulty in maintaining homogeneous initial conditions.

There are a variety of experimental options available for the investigation of nonclassical gasdynamic phenomena. A detailed description of several of these techniques can be found in Chaps. 4-6 of Zamfirescu *et al.* [7]. In Section 3.1, a brief discussion on the different options, and the motivation for using a shock tube as the experimental technique of choice are presented. Section 3.2 discusses the previous experimental attempts at generating a nonclassical RSW that are based on the shock tube design, followed by Section 3.3 that particularly focusses on the Flexible Asymmetric Shock Tube (FAST) setup that was designed and commissioned at TU Delft. The FAST facility is a modular (hence, in principle, flexible), variable cross-sectional area shock tube based on a Ludwig-tube design that makes use of a Fast Opening Valve (FOV) as a barrier element [8]. Preliminary rarefaction tests were performed in air to test the functioning of the FAST and the FOV. Such tests highlighted several issues related to the mechanical action of the FOV, especially at elevated temperatures of operation. Several improvements to the setup were proposed and implemented, the details of which are discussed in Section 3.3.3.

### 3.1. Review of experimental options

There are several methods which could be adopted for generating both classical and nonclassical shockwaves. These experimental methods can be broadly categorized into either *steady* or *unsteady* experiments.

#### 3.1.1. Steady Experiments

Steady experiments are classified as those in which the flow-field is steady and the nonclassical phenomenon that is being studied remains unchanged with respect to the laboratory frame [3]. Experiments that feature such steady flows include the generation of a nonclassical supersonic flow through a nozzle and the generation of a nonclassical flow-field by turning a supersonic flow over an edge or a body. Wind tunnels or so-called blow-down facilities such as a Ludwig tube can be used to generate steady flows in the test section.

### Stationary RSWs in a nozzle

Nonclassical flows of a BZT fluid through a converging-diverging (CD) nozzle and the occurrence of a rarefaction shock have been numerically investigated by Chandrasekar *et al.* [9], Kluwick [10], and Cramer *et al.* [11]. Provided the upstream and downstream conditions are suitable, a steady RSW should form at the throat of a CD nozzle, as shown in Fig. 3.1.

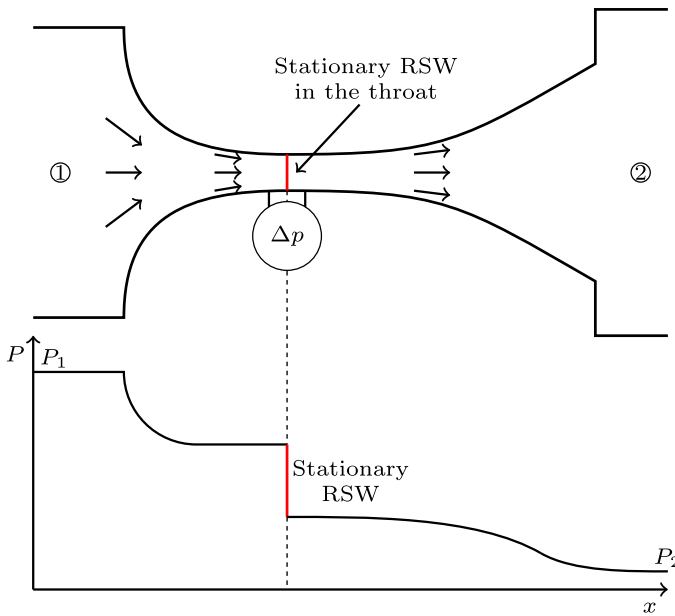


Figure 3.1: Schematic cross-section of a two-dimensional nozzle test section to generate a nonclassical shock wave in a de Laval nozzle. The nozzle may be equipped with pressure measurement sensors and optical access for shock wave visualization. The chart shows the expected qualitative trend of the static pressure ( $P$ ) vs the axial co-ordinate ( $x$ ).

The rarefaction shock may, in principle, be identified by the uniquely characteristic sharp pressure drop across the wave which could be measured by means of static pressure taps on either side of the nozzle throat and visualized by means of schlieren imaging. It is possible that oblique rarefaction shocks, or compression fans, would also appear further downstream, depending on the inlet and discharge conditions. These additional flow features could also be visualized with schlieren imaging. However, the flow-field in the nozzle is quite complex and sensitive to both the upstream and the downstream conditions and is prone to flow instabilities. In fact, the simulations of Cramer [11] show that for a given upstream condition, up to three shock waves of both compressive and expansive types can appear depending on the thermodynamic

state of the reservoir. Since such different discontinuities can all occur in the same flow-field, expansion experiments in nozzles are not suitable for providing incontrovertible experimental evidence for the existence of nonclassical gasdynamic phenomena.

### Stationary RSWs in supersonic flows over corners

The turning of nonclassical flows over corners and wedges has been extensively studied, both theoretically and numerically [12]–[16]. Considering the example of an ideal gas flow, if a fluid passes over a concave corner at supersonic velocity, a classical compression shock wave (CSW) is formed stemming from the corner. Conversely, if the same flow passes over a convex corner, the fluid expands isentropically through a centred expansion fan (EF). As with other nonclassical phenomena, this flow behaviour too is reversed in a flow featuring  $\Gamma < 0$  upstream of the corner, with RSWs forming in correspondence with a concave corner and an isentropic compression fan (CF) in correspondence with a convex corner (see Fig. 3.2) [1]. Depending on the thermodynamic states of the fluid downstream of the wave, these systems can either be “pure” RSWs and compression fans or composite waves like expansion fans-shocks or fans-shocks-fans.

To prove the existence of nonclassical gasdynamics, an experiment aimed at either creating and detecting a pure oblique RSW or a centred compression fan in a supersonic flow over a corner can be carried out. This can, for example, be performed using a Ludwieg tube in order to achieve a constant supersonic flow over the corner. A Ludwieg tube is a facility that is capable of providing steady supersonic flows on timescales of a few to tens of milliseconds [17]–[19]. It is commonly employed for short-duration experiments such as supersonic flows over two- or three-dimensional bodies, etc.

A schematic of a Ludwieg tube setup is shown in Fig. 3.3. It consists of four main components: a long charge tube called the Ludwieg tube that holds the high-pressure fluid, a nozzle, a reservoir that is maintained at a low pressure and a diaphragm element separating the high and low-pressure sections of the setup. When the diaphragm is ruptured, the high-pressure fluid empties into the reservoir and an expansion wave propagates into the charge tube. The high-pressure fluid is accelerated by the expansion wave and achieves a constant temperature and Mach number at the nozzle inlet. In the case of classical flows, this expansion is isentropic; thus, the total pressure is equal to the reservoir pressure downstream of the expansion. The temperature and the Mach number are, however, set by the area ratio of the nozzle throat through isentropic flow relations. These conditions can be held constant for the duration of the test, which is the time taken for the expansion wave to reach the end wall and for the reflections to reach the nozzle. The flow at the outlet of the nozzle is steady and supersonic; an oblique shock wave or

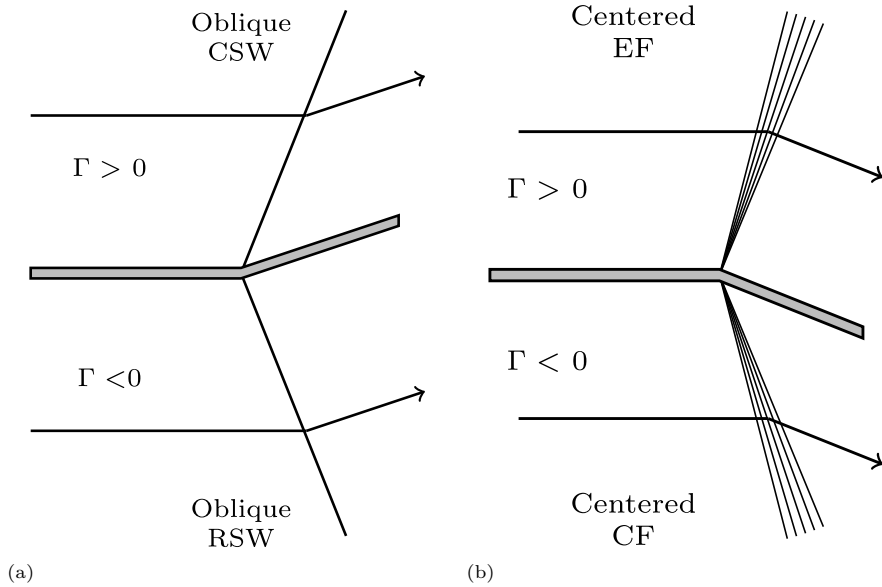


Figure 3.2: (a) Formation of an oblique shock wave over an expansion corner in classical and nonclassical flows (b) Formation of a centred Prandtl-Meyer fan over a compression corner in classical and nonclassical flows.

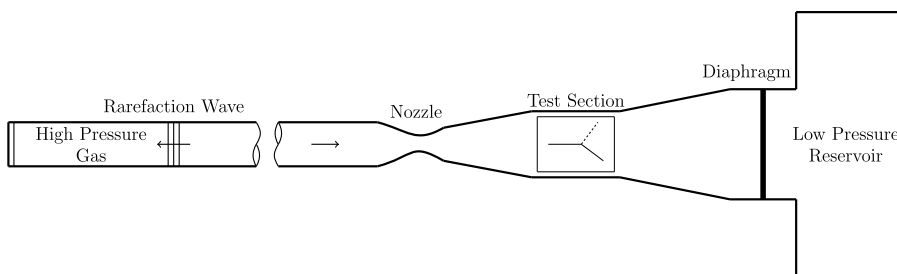


Figure 3.3: Schematic of a Ludwieg tube showing a test section with visual access, where a supersonic flow turns over a corner.

an expansion can, therefore, be obtained by placing a body in this portion of the tube. The discontinuity can be analyzed with the help of a visualization technique such as shadowgraphy or schlieren imaging.

### 3.1.2. Unsteady Experiments

Unsteady experiments involve propagating shock waves or isentropic fans through the dense vapours of the BZT fluid of interest. There are several methods to generate and detect both classical and nonclassical shock waves. For example, spherical shocks can be generated with local (point-like) explosions, while finite amplitude waves can be generated using shock tubes.

#### Non-classical spherical waves resulting from laser-induced point explosions

It is possible to initiate a breakdown of the molecules by focussing a pulsed laser beam on a point-like small spot in a gas or vapour. If the strength of the electromagnetic field generated by the incident laser beam exceeds a threshold value, then ions are generated. These ions have a much larger absorption cross-section than that of neutral atoms and absorb photons that result from the free-free transitions of electrons in the ion field. As energy is absorbed, more ion pairs are generated, further increasing the absorption coefficient of the fluid. This results in a cascade phenomenon which substantially increases the absorption of the energy of the laser pulse, thereby forming a hot plasma that rapidly expands in the fluid.

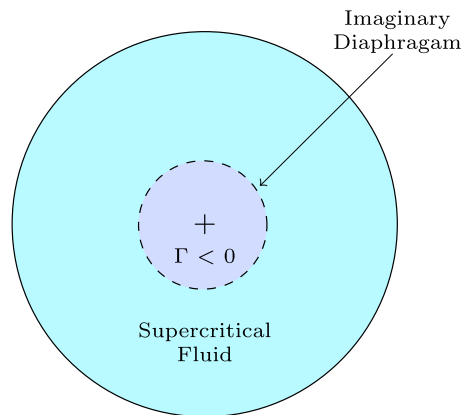


Figure 3.4: Model of a point explosion. The imaginary diaphragm disappears instantaneously at  $t = 0$ .

With reference to Fig. 3.4, Guardone *et al.* [20] numerically investigated the possibility of using such an experimental method for providing the proof

of the existence of nonclassical gasdynamics, and in particular of nonclassical compression waves. To model the phenomenon, the authors simulated the formation of such finite-amplitude acoustic waves starting from the localized explosion of a small quantity of pressurized siloxane  $D_6$  contained in a small sphere, separated from the outside fluid by an imaginary diaphragm. The initial conditions were chosen such that the fluid within the sphere is in a  $\Gamma < 0$  thermodynamic state, while that contained in the outer sphere was slightly supercritical.

The authors found that while a compression wave arising from the explosion indeed propagates as an isentropic compression fan, rarefaction waves do not coalesce to form a rarefaction shock wave. They also showed using numerically simulated schlieren images that it was not possible to visually detect this compression fan using an optical arrangement. The spreading of the compression fan, therefore, could be measured only using pressure probes located at known distances from the point explosion, whose presence can in turn disturb the flow-field. Also, it is possible that the fluid undergoes thermal decomposition due to a highly localized energy input. Though this doesn't affect the propagating compression wave, the fluid would have to be changed after each trial or in a few trials. This can potentially be an issue if the working fluid is not easily available, if it's expensive, or both [3].

### Nonclassical wave propagation in a shock tube

A shock tube is a conventional device used to generate one-dimensional planar wave-fields at high pressures and temperatures mainly for the study of chemical kinetics ([21]–[23]), and combustion ([24]–[26]). A typical shock tube is a pipe of constant cross-section that is separated into high pressure (driver side) and low pressure (driven side) sections by a diaphragm (see Fig. 3.5). Diaphragms can open within a few microseconds [27], and therefore, arguably provide the best approximation of an instantaneous rupture. In the context of classical flows, when the diaphragm is ruptured, a jet of high pressure gas flows into the driven side giving rise to a series of compression waves that eventually coalesce to form a compression shock wave (CSW). This shock wave moves at supersonic speed with respect to the quiescent fluid in the driven section. The expansion wave, on the other hand, spreads out in time forming a rarefaction fan (RF) as it travels in the high-pressure section. Also, a contact surface (CS) between the fluid past the shock wave and the driven gas is generated, across which the velocity and pressure are constant. A schematic of such a shock tube flow is shown in Fig. 3.5b.

If the fluid flow can exhibit nonclassical gas dynamic behaviour, and the initial states of the driver and the driven sections are chosen such that the expansion occurs with the fluid thermodynamic states featuring  $\Gamma < 0$ , then the expansion wave can steepen into a rarefaction shock wave (RSW). Such a

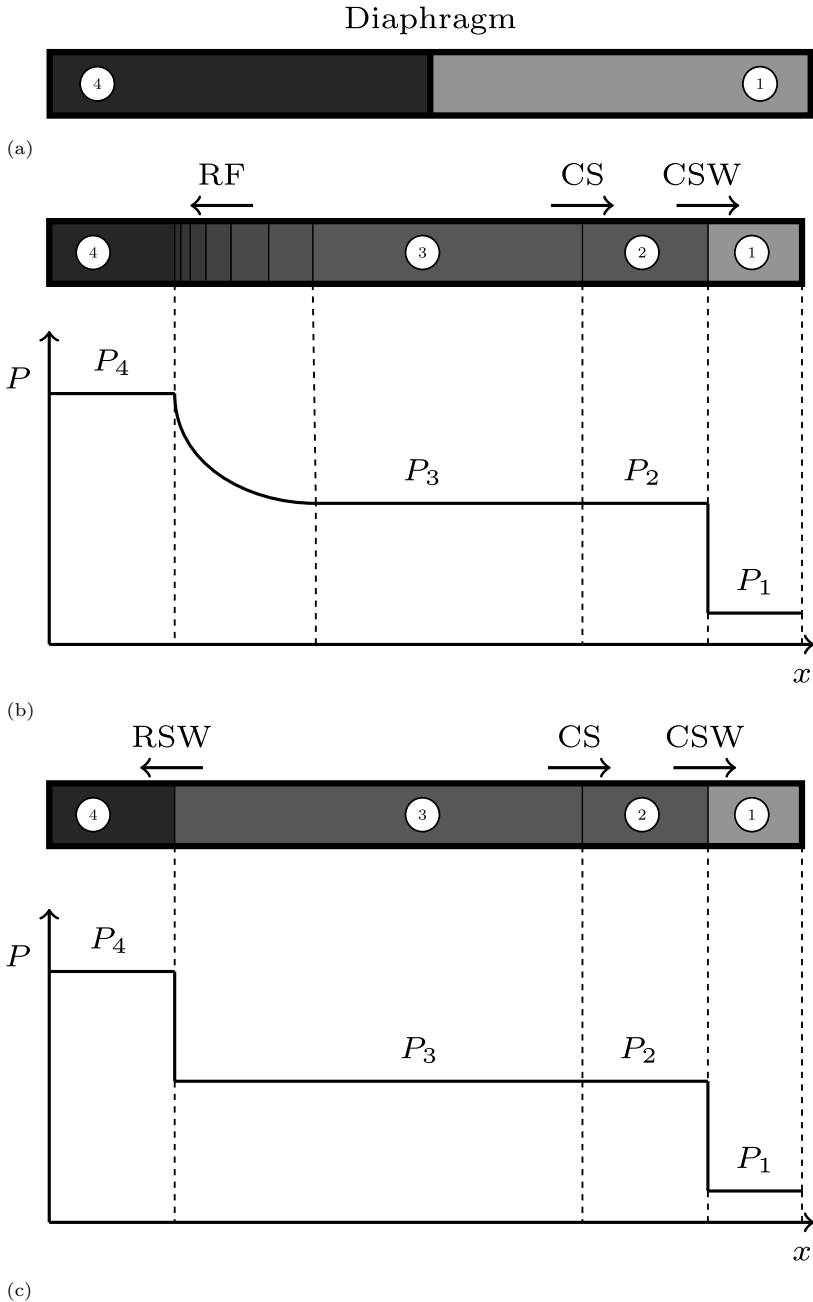


Figure 3.5: (a) A conventional shock tube with high (4) and low pressure (1) sections separated by a diaphragm. (b) Shock tube test in a classical fluid.  $P-x$  chart shows the formation of a CSW and a RF. (c) Shock tube test featuring nonclassical wave fields.  $P-x$  chart shows triple discontinuities of right-running CSW and CS and left-running RSW [3].

shock tube experiment in which three discontinuities are generated is called a *triple discontinuity experiment* and was proposed by Ferguson *et al.* [28] (see Fig. 3.5c). A propagating RSW can be identified by estimating the upstream Mach number ( $M_4$ ) of the wave, defined as,

$$M_4 = \frac{u_4}{c_4} \quad (3.1)$$

where  $u$  and  $c$  are the flow velocity and the speed of sound in the stationary fluid (State 4 in Fig. 3.5c), respectively. The local sound speed in the medium can be determined either through an on-site measurement or from predictions based on pressure and temperature measurements using an accurate thermodynamic model. The speed of propagation of the shock can be estimated using a time-of-flight method by measuring the time ( $\Delta t$ ) it takes for the RSW to travel between two pressure transducers placed at a known distance ( $\Delta x$ ) from each other.

Operational drawbacks of the conventional shock tube, especially if adopted for nonclassical gas dynamics experiments, arise from the choice of the barrier element, i.e., the diaphragm. Though still one of the quickest methods to remove the barrier between the driver and driven sections, the diaphragm may not open completely, thereby causing a constriction of the cross-sectional area of the tube. An imperfect opening of the diaphragm may also cause complex flow-fields and increase the distance needed for the waves to coalesce to form a shock wave. In fact, numerical simulations of shock tube flows past partially opened diaphragms show that the intensity of the leading shock is influenced by the ratio of the diameter of the opened portion of the diaphragm  $d$ , to the diameter of the tube  $D$ , with the strength of the leading shock decreasing with decreasing  $d/D$  [29], [30]. Moreover, diaphragms have to be changed between consecutive runs, which implies that the inner surfaces of the shock tube are exposed to the atmosphere in the mean time. Impurities and humidity may therefore adhere to the surfaces and contaminate the test fluid. Furthermore, a diaphragm often does not rupture according to a predictable pattern, thereby making the repeatability of experiments difficult or impossible.

To overcome such issues with a diaphragm, several diaphragmless versions of a shock tube have been developed, a common alternative being the fast opening valve (FOV), see Refs. [31]–[35]. Using a FOV, though, implies that the cross-section of the tube can no longer be constant – the cross-section of the tube must be locally increased to both accommodate the valve and to create additional space for the flow so as to compensate for that occupied by the valve. Variable area shock tubes have been widely studied and employed in several investigations [36]–[38]. When the valve is opened, the flow-field is similar to that occurring in a constant cross-section area shock tube with a diaphragm. In case nonclassical gasdynamics is of interest, a CSW propagates

in the driven side, and a CS and a RSW are generated in the driver side, provided that a BZT fluid is used as test fluid and that the conditions are chosen appropriately. However, the CSW is also partly reflected by the valve into the driver section and the reflection may disturb the formation of the RSW due to the relatively higher propagation speed of the CSW if compared to the RSW. A detailed analysis on the effect of the opening mechanism of a FOV on the flow-field can be found in Zamfirescu *et al.* [7]. Also, since the flow area increases close to the valve, this can generate local expansion waves that coalesce into an expansion fan (or a RSW, provided the conditions are favorable), that travels into the driver section and can also affect the experiment. One way to avoid all these reflections from travelling upstream towards the RSW or anyway the nonclassical expansion waves is to include a nozzle upstream of the valve opening. The purpose of the nozzle, which must be designed to be chocked during the experiment, is to block any possible waves generated either in the valve or in the low-pressure tank from travelling upstream and interfering with the formation of the RSW. In this arrangement, the shock tube becomes a Ludwieg tube.

### 3.1.3. Choice of experimental technique

To successfully generate a RSW and verify nonclassical gasdynamic effects, the most appropriate experimental technique must be selected based on several criteria. These include the complexity of the flow field in the setup, the intrusiveness of the measurement techniques, and the repeatability of the results.

In order to distinguish non-classical gasdynamic phenomena from underlying flow-fields, it is important to keep the observed flow-field in a setup as uncomplicated as possible. This simplifies measurements and avoids confusion between the observed and measured phenomena [7], thereby simplifying the design process of the setup. For example, a shock tube can be designed using 1D analytical solutions or inviscid CFD simulations. On the other hand, the design of a convergent-divergent nozzle for steady state nozzle experiments needs the solution of boundary layer equations or the full Navier-Stokes equation.

The choice of measurement technique also plays a crucial role in the successful outcome of a nonclassical gasdynamic experiment. Given the very short range of operating conditions that allow for nonclassical behaviour, a less intrusive measurement technique would keep disturbances in the flow as low as possible. Three different measurement types are commonly employed in such experiments, namely, static pressure measurement on the setup walls (e.g., in a shock/Ludwieg tube), total pressure measurements in the flow (e.g., choked flow in convergent-divergent nozzles, laser-induced point explosions)

and flow-visualization techniques (e.g., schlieren imaging in Ludwieg tubes for supersonic flow over corners, laser-induced point explosions, etc.). Of these three, the least intrusive technique is the measurement of the static pressure of the flow. The pressure sensors are flush-mounted onto the setup walls; thus, they have a negligible effect on the flow-field.

Total pressure measurements, on the other hand, need to be performed using pitot tubes that protrude into the flow-field. The probe then has a non-negligible impact on the flow characteristics. For example, in the case of a supersonic flow, a bow shock can be expected in front of the probe's head. The total pressure measured by the sensor would then be different from the pressure that would be recorded at that location in the absence of the sensor. The pressure measurement is also affected by the orientation of the pitot to the flow, which cannot always be easily adjusted given that the sensor is in a high-temperature, sealed environment and might not be directly accessible. Moreover, given the narrow range in which nonclassical effects can be encountered, any disturbance induced by the sensor can alter the local conditions to an extent that such effects cannot exist in the flow-field.

In the case of flow visualization techniques, an optical access to the flow-field such as a transparent window in the setup is required. Given that the fundamental derivative of gasdynamics  $\Gamma$  is highly sensitive to the temperature, maintaining the surface of the test-section as constant and uniform as possible is crucial to the success of an experiment. The presence of a window, however, can induce a local gradient in the temperature. This not only alters the flow-field in the setup but the cooler window can also act as a site of local condensation of the flow, thus obscuring the view of the flow-field. Moreover, setups for laser-based measurements such as Particle Image Velocimetry (PIV) can be expensive to setup and operate.

It is also important for the experiment to be repeatable, since differences between runs could introduce large uncertainties in the results and reduce their accuracy. A more detailed analysis on the assessment of the different experimental techniques based on suitably defined criteria can be found in Zamfirescu *et al.* [7].

After comparing the various experimental techniques discussed in Section 3.1, it can be concluded that the shock tube design is the most favorable technique for measuring nonclassical gasdynamic flows. This is due to its simple design and flow field, as well as other advantages, including the ability to use non-intrusive measurement techniques, the repeatability of experiments, and ease of construction.

### 3.2. Past Experiments with shock and Ludwig tubes

There has been, till date, a limited amount of experimental work related to the observation of rarefaction shock waves. This is, primarily, the result of the technical difficulties in performing such an experiment [39], [40]. The first experimental attempt at generating and measuring a RSW was made in the former USSR by Borisov *et al.* [4] who performed a shock tube experiment using Freon-13 (trifluorochloromethane,  $\text{CClF}_3$ ) as the test fluid. A rarefaction wave with a width of approximately 3 cm propagating with minimal distortion was indeed recorded, which the authors claimed was a RSW in the single-phase region of the test fluid. These results have, however, been confuted by several authors (see [3], [28], [39], [41]–[43]) who have proposed an alternate explanation for the observed expansion wave based on critical-point phenomena and two-phase effects. Remarkably, Freon-13 is not a retrograde fluid which implies that its specific heat is not large enough for nonclassical phenomena to occur. Ferguson *et al.* [28] also showed using numerical simulations that the expansion wave witnessed by Borisov *et al.* [4] lied completely below the spinodal curve in the  $P - v$  plane, indicating that the fluid must have been in two-phase states. The experiments of Borisov, therefore, might not have featured a single-phase RSW.

A second shock-tube experiment was conducted at the University of Colorado at Boulder, aiming to generate a nonclassical shock wave in the fluid PP10 (perfluorofluorene,  $\text{C}_{13}\text{F}_{22}$ ) [39], [44]. The RSW would have been identified by comparing the wave propagation speed with the local soundspeed in the fluid at the experimental initial conditions; a RSW would travel at supersonic speeds while a classical rarefaction propagates at the speed of sound. This experiment too was unfortunately unsuccessful due to the thermal decomposition of the working fluid at the operating temperature ( $\approx 300^\circ\text{C}$ ) [39]. There was also a lack of accurate information on the thermophysical properties of the fluid which would have prevented the estimation of the soundspeed with sufficient accuracy to claim that the observed expansion was indeed supersonic [45].

The third and most recent attempt at producing a RSW was carried out using the Flexible Asymmetric Shock Tube (FAST) facility that was conceived and commissioned by the Propulsion & Power Group at TU Delft in the Netherlands. Unlike the other two setups that used a diaphragm to separate the high and low-pressure sections of the tube, the FAST employed a fast opening valve (FOV) which offered the advantage of the precise opening of the barrier element and of performing consecutive tests without the need to open the setup to replace the diaphragm. Siloxane  $\text{D}_6$  (dodecamethylcyclohexasiloxane,  $\text{C}_{12}\text{H}_{36}\text{O}_6\text{Si}_6$ ) was chosen as the working fluid due to its high thermal stability and the predicted range of its nonclassical region in terms of pressure and temperature [46].

### 3.3. Flexible Asymmetric Shock Tube (FAST) facility

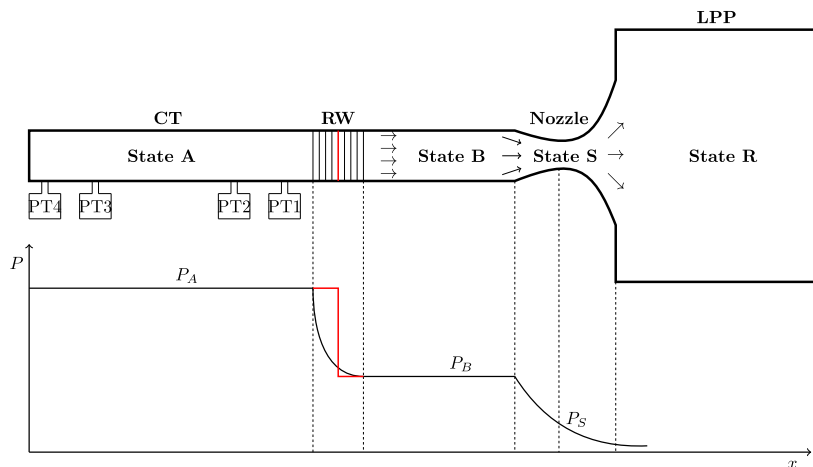


Figure 3.6: Schematic of a rarefaction wave experiment in a Ludwieg-tube-like shock tube. The lower chart shows the qualitative pressure profile along the tube. A propagating rarefaction shock wave is shown in red.

The Flexible Asymmetric Shock Tube was a Ludwieg-tube type setup that consists of a high-pressure section called the charge tube (CT) and a low-pressure reservoir called the low-pressure plenum (LPP) [3], [6], [7], [47]. A schematic of the FAST and the qualitative pressure profile pertaining to a rarefaction experiment are shown in Fig. 3.6. The CT and the LPP are connected to each other via a FOV. The fluid is initially at rest everywhere and the temperature of the setup is maintained using a temperature-control system. The experiment starts when the FOV is opened, thereby allowing the fluid in the CT to expand into the LPP. If the initial conditions (State A) in the CT are suitable, then a RSW is expected to form and propagate into the high-pressure section. This RSW accelerates the fluid from rest State A to post-shock condition State B. The fluid then flows through the nozzle which is designed to operate under choked conditions (sonic State S). This serves the purpose of preventing reflections from travelling upstream into the CT. Four dynamic pressure transducers, flush mounted on the CT wall, are used in pairs to measure the wave propagation speed based on the time-of-flight (ToF) technique: if the speed is greater than the local speed of sound in State A, then the wave is indeed a rarefaction shock wave. Figure 3.7 shows an overview of the FAST setup with its major components.

The working fluid chosen for the experiment is dodecamethylcyclohexsiloxane ( $D_6, C_{12}H_{36}O_6Si_6$ ) due to its relatively high thermal stability at elevated

temperatures and the size, in terms of the range of pressures and temperatures, of the nonclassical gasdynamic region according to state-of-the-art thermodynamic models [48]. Pre- and post-shock states can be chosen so as to maximize the shock wave Mach number as presented by Guardone *et al.* [45].

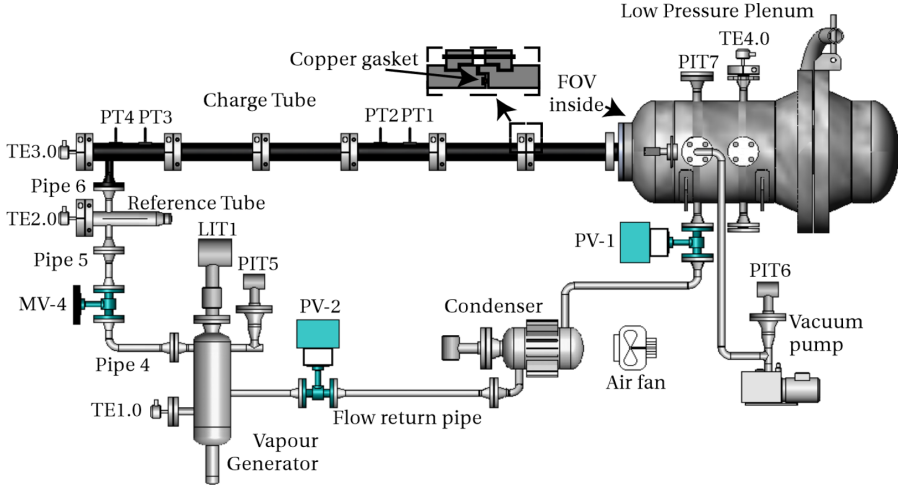


Figure 3.7: Overview of the FAST setup [6].

A detailed description of the FAST setup and its components can be found in Refs. [3], [6], [49]. Here, only a brief overview of its design is presented. A more detailed description of the design and functioning of the FOV, arguably the most complex component in the FAST, is reported Section 3.3.2

### 3.3.1. Description of the setup

The FAST consists of five main components each made of stainless steel (316Ti). These are, clockwise from the bottom left of Fig. 3.7, the Vapour Generator or the Heated Fluid Tank (HFT), the reference tube (RT), the charge tube (CT), the fast opening valve (FOV) and the Low Pressure Plenum (LPP).

The HFT is a custom-built vessel with a 5.9 liter capacity designed to heat the working fluid isochorically to the desired temperature and pressure. A 1.5 kW ceramic band heater, located at the bottom section of the HFT, supplies the thermal energy required for this process. The RT is a 500 mm long tube with a thickness and diameter of 15 mm and 40 mm, respectively, identical to those of the CT. It serves as a reference temperature for the control of the CT. The outer wall temperature of the CT is regulated to follow that of the RT. The temperature of the RT itself is controlled such that the measurement of

the PT100, which protrudes into the RT, matches the setpoint temperature. This temperature is always slightly higher than that of the HFT, which is the boiling temperature of the fluid. This strategy enables the control of the superheating of the vapor in the RT, and consequently, of the CT. A 335 W heater supplies the thermal energy to the RT.

The CT comprises six pipe segments each of length 1520 mm, held together by a coupling. The total CT assembly is 9 m long and is placed on sliding supports to allow for its thermal expansion, which can be up to 55 mm at 400 °C. Each segment is fitted with a 950 W Tyco glass-silk heating jacket while the couplings are heated by a 180 W Joule electric heating wire. The gaps between the couplings and the blankets are insulated with rockwool. The temperature of each segment is controlled via a thermocouple whose hot and cold junctions are fixed to the outer walls of the CT and the RT respectively. This setup is that of a differential thermometer; the setpoint of the control system is 0 K to ensure a match between the RT and the CT temperatures.

Four high-temperature dynamic pressure transducers (PT01-PT04), with a measurement accuracy of 0.5% of the full range of 21 bar, are flush mounted on the CT walls at distances of 4, 4.3, 8.4 and 8.7 m from the FOV respectively. The sensors are placed in pairs so as to be able to measure the wavespeed using the time-of-flight method at two different locations along the CT.

At the end of the CT is the LPP, a 113 liter cylindrically shaped vessel with an outer diameter of 406.4 mm and a thickness of 9.53 mm at room temperature. The FOV that connects the CT and the LPP is contained within the tank. A lid with a 648 mm diameter flange provides access to the interior of the vessel for the installation of the FOV. The heating of the LPP is achieved with 4 custom-built heaters with powers of 1.45 kW, 425 W, 960 W and 490 W.

### 3.3.2. Fast Opening Valve

The Fast Opening Valve used in the FAST is a custom-designed stainless steel valve with a design opening time of 4 ms and intended to be operable at temperatures of up to 400 °C without the need for lubrication to avoid contamination of the working fluid. A schematic of the FOV is shown in Fig. 3.8. The valve is placed inside the LPP and is operated remotely to keep the entire facility hermetically sealed between successive experiments. In the open position, the fluid can expand from the CT into the LPP via venting holes located in the inner and outer bodies of the FOV in the radial direction. In the closed position, a sliding cylinder is pushed between these bodies, blocking the flow through the venting holes. The sliding cylinder pushes onto a Kalrez compound sealing pad placed on the flange to ensure sealing. A Kalrez O-ring placed between the sliding cylinder and the inner body offers sealing on the

other side.

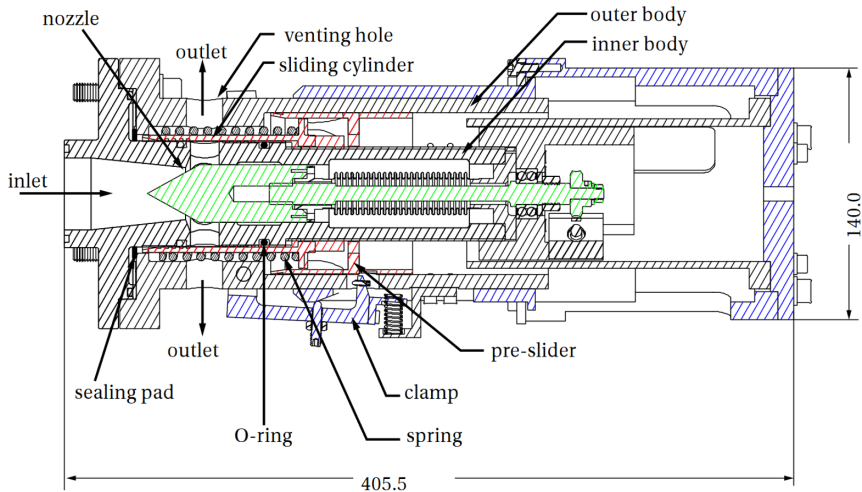


Figure 3.8: Schematic of the Fast Opening Valve used in the FAST [6].

The opening sequence of the FOV is shown in the photographs of Fig. 3.9. An Inconel steel spring is initially held compressed by a pre-slider which itself is locked in place by three radial clamps. To open the valve, the clamps are disengaged by an actuation system, allowing the spring to push the pre-slider and the sliding cylinder away, thereby opening the venting holes. A nozzle insert creates a throat area in order to choke the flow, thus preventing flow disturbances from travelling upstream. This insert can be moved longitudinally to vary the throat area in order to regulate the strength of the rarefaction waves.

### Effect of FOV opening on expansion waves

During the commissioning of the FOV, a series of rarefaction tests were performed using air as the test fluid at different CT and LPP pressures in order to characterize its behaviour. The expansion is obtained by pressurizing the CT while maintaining the LPP at a lower pressure. Once the FOV is opened, air expands into the LPP, and a rarefaction wave travels into the CT expanding the gas from State A to State B before the fluid enters the nozzle, where sonic conditions are achieved (see Fig. 3.6).

Figure 3.10 shows the pressure measurement signals in time acquired during an air expansion test with an initial pressure of 6 bar in the CT and 2 bar in the LPP. It is seen that even before the large drop in pressure that is brought about by the expansion wave, two smaller expansions propagate into

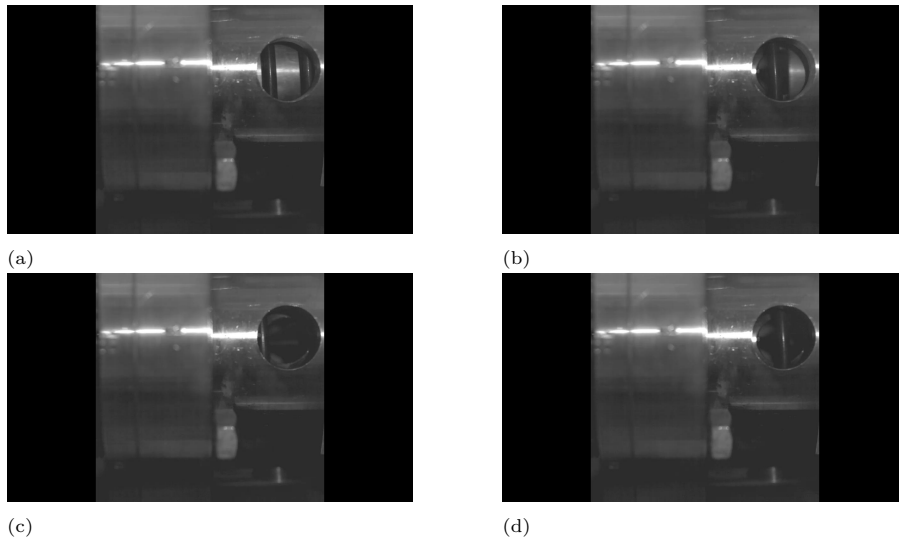


Figure 3.9: Photographs taken with a high-speed camera of a view of the venting holes during the opening sequence of the FOV. (a) FOV in closed position with the sliding cylinder blocking the venting holes; the spring is compressed; (b) sliding cylinder in motion with partially opened venting holes; (c) FOV in full open position; (d) rebound of the Inconel spring partially blocking the venting hole.

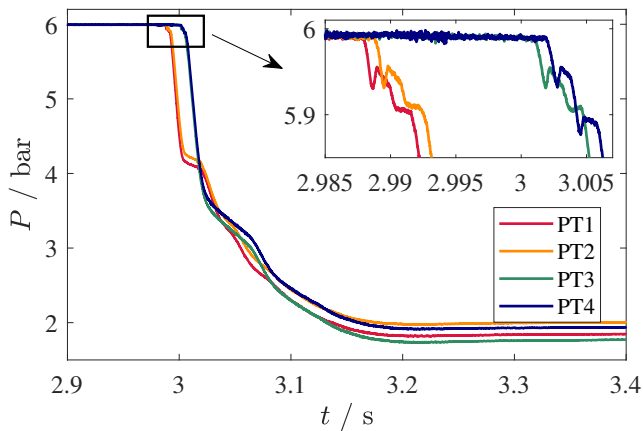


Figure 3.10: Pressure signals recorded by the sensors PT1 to PT4 during a rarefaction test using air as the test fluid. The drop in pressure due to the opening of the FOV, from 5.9 bar to about 4 bar, is preceded by two smaller drops attributed to the FOV opening process.

the CT. Mathijssen [6] reasoned that these waves were a result of the opening process of the FOV. As soon as the clamps are released, the spring pushes the sliding cylinder creating a small gap between the cylinder and the seal. This becomes a choke-point for the leaking flow creating the initial drop of 0.05 bar seen in Fig. 3.10. As the slider moves further away from the seal, the point of minimum cross-section moves to a location between the slider and the inner body which is marginally larger than the initial choke-point. This leads to the second small drop of another 0.05 bar. Only when the venting holes are completely unblocked does the nozzle choke which corresponds to the large drop in pressure from 5.9 bar to approximately 4 bar.

The impact that this initial drop has on rarefaction experiments in BZT fluids would depend on the thermodynamic state of the fluid. If the initial conditions are such that the local value of  $\Gamma$  is large and negative, then this initial drop itself can steepen into a rarefaction shock wave thereby increasing the chances of successfully identifying one in the experiment. However, if the conditions are such that the fluid would already only exhibit weak negative nonlinearity, then this initial expansion can alter the fluid's thermodynamic state such that it is no longer in the  $\Gamma < 0$  region, thus preventing the formation of a RSW.

Since this initial pressure drop is a small-amplitude wave, such a signal is suitable for estimating the local speed of sound of the fluid in State A in the CT. Considering the sensor pair PT1 & PT2, the time delay in the wave reaching these sensors is estimated through cross-correlation. The speed of sound can then be computed using the time-of-flight (ToF) method as,

$$c = \frac{\Delta l}{\Delta t} \quad (3.2)$$

where  $\Delta l$  is the distance between the two sensors, which is 0.3 m for PT1 & PT2. Sensors PT3 & PT4 are not considered for this analysis as they are placed too close to the end wall and therefore are affected by reflections. Figure 3.11 shows the estimated soundspeeds as a function of the pressure ratio for the air rarefaction tests performed with the FAST. Almost all the estimated values of  $c$  are seen to lie within one standard deviation of the mean value  $\bar{c}$  computed using the ideal-gas law. Anticipating the results of Chapters 5 and 6, this method serves as an alternative for providing an accurate measure of the local speed of sound in the CT at conditions where even the best thermodynamic models suffer from large uncertainties.

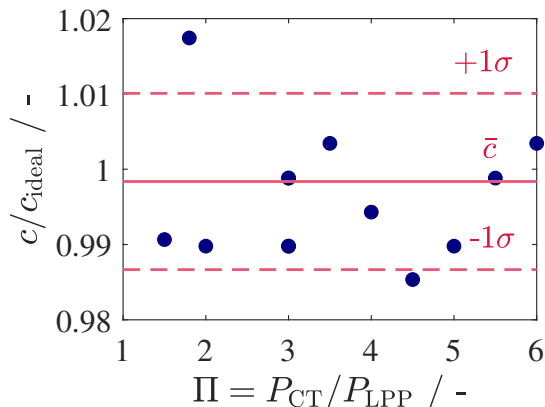


Figure 3.11: Speed of sound values of air in CT estimated using ToF method. The mean and standard deviations of the measurements are also shown.

### 3.3.3. Improvements to the FAST and lessons learned

#### Issues with FOV

Though designed to be operated at temperatures of up to 400 °C and still be able to open within 4 ms, the FOV suffered from several issues when repeatedly operated in those conditions. Most of these issues were caused by the excessive thermal expansion of the seals. Despite protective coatings to reduce friction, the O-ring between the inner body and the sliding cylinder was often dislodged from its groove because of the sliding motion (see Fig. 3.8). The O-ring close to the venting holes was also getting damaged, sometimes even severed, probably due to being pinched between by the sliding cylinder and the flange when the FOV was being closed (see Fig. 3.12). This resulted in the O-ring jamming the sliding cylinder, thereby preventing the FOV from either closing or opening completely. Though Kalrez 7075, the compound used for the O-rings, is capable of withstanding a continuous exposure to temperatures of up to 330 °C [50], and the temperature of the FOV was never measured to go over 250 °C, the O-rings were better suited for static rather than dynamic applications and thus could not handle the motion of the sliding cylinder properly and repetitively. Thus, even after a single shot, the FOV would leak making it difficult to maintain constant conditions in the CT. In such instances, the FOV had to be taken out of the LPP and new seals had to be replaced before further testing could continue.

To overcome this issue, initially, it was decided to replace the O-rings with seals better suited for dynamic applications, namely, the Spring Energized Seals (SES) [51]. A simple SES consists of two components: a polymer-based



Figure 3.12: A damaged O-ring close to the venting holes in the FOV, possibly cut when pinched by the sliding cylinder when the valve was closed.

seal jacket made from high-performance fluouropastics such as polytetrafluoroethylene (PTFE) or polyetheretherketone (PEEK) chosen primarily for their low-friction and favorable temperature resistance, and the spring. The seal jacket is typically machined in the shape of a “U” and the spring is placed within the jacket, as shown in Fig. 3.13. The SES is typically installed such that the open section of the seal faces the system pressure. At low pressure conditions, the radial tension created and maintained by the spring ensures that the sealing jacket remains in contact with the surfaces, thus providing good sealability. When system pressure is applied, the spring action is intensified — the force from the pressure “energizes” the seal and expands the sealing jacket thereby pressing them onto the counter surfaces and creating a gas-tight seal [52], [53].

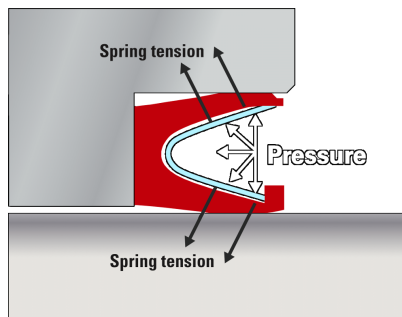


Figure 3.13: Working principle of Spring Energized Seals [54].

Figure 3.14 shows a schematic of the FOV with the SES installed in place of the Kalrez O-rings. Both the seals are positioned facing the venting holes which is the direction in which the system pressure is applied. Testing the FOV equipped with the SES showed that though they improved the sealing

characteristics of the FOV, the effect of temperature was too severe for the SESs to maintain their operability over consecutive runs. The SES installed downstream of venting holes was less susceptible to thermal expansion as it was always in contact with the inner body and the sliding cylinder, even when the FOV was in the open position. However, the SES on the inlet side was dislodged from the groove every time the FOV was opened since there was no longer a bounding surface at the top. Also, the seal's open section now faced the sliding cylinder which meant that when the valve was closed again, the slider would damage the interior of the seal, or, in the worst case, cut it altogether instead of sliding over the sealing jacket. This once again jammed the FOV making it impossible to open or close it again, a problem similar to that encountered with the Kalrez O-rings.

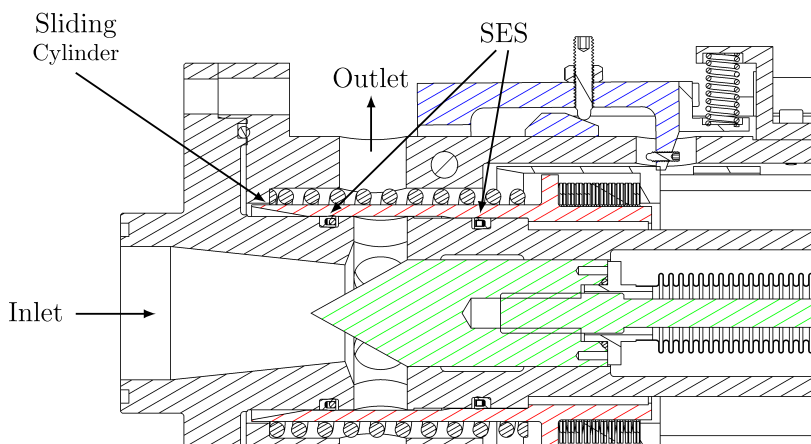


Figure 3.14: Schematic of the FOV with the Spring Energized Seals installed in place of the O-rings.

### FOV Redesign

With both the O-rings and the SES, the seal placed upstream of the venting holes proved to be problematic due to it always being dislodged from the groove. It was therefore decided to redesign the FOV such that a need for a seal in this location can altogether be avoided. The modified design of the FOV is shown in Fig. 3.15.

In this design, the venting holes on the outer body were sealed off and new vents were created further downstream of the valve. This removes the need for a seal close to the flange as in the old design. Since the old venting holes were no longer needed to be blocked when the FOV was closed, a new,

shorter sliding cylinder was designed. An advantage of a lighter slider is its lower inertia which can lead to a possible reduction in the opening time. The SES downstream of the old venting holes, between the sliding cylinder and the inner body, was retained for sealing. Though the SES can expand out of its groove when the shorter sliding cylinder moves away, the open end of the cylinder faces away from the sliding cylinder. This not only prevents the seal from being damaged by the cylinder, but also helps to push the seal back into the groove when the FOV is closed. A new Kalrez O-ring was placed between the slider and the outer body close to the new venting slits. Unlike the previous design, the O-ring is completely static thus preventing damage due to friction.

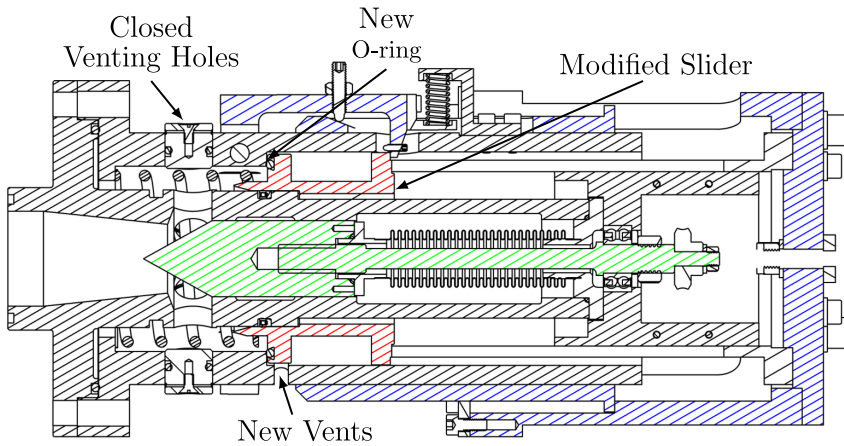


Figure 3.15: Modified design of the FOV with new venting holes placed further downstream of the valve.

Multiple tests conducted in the FAST with the modified FOV showed that several sealing issues that had plagued the old design existed in the new design as well. For example, some expansion of the SES was expected at the operating conditions of the FAST, but this was not deemed to be an issue since the design of the SES jacket would ensure that the seal is pushed back into the groove by the sliding cylinder when closing the FOV. However, the SES expanded so much that it was severely damaged by the slider as it moved over the seal. Within a few tests, the slider was so completely jammed by the broken seal that the FOV was inoperable. Moreover, the new O-ring between the outer body and the slider also expanded outside of its groove thus preventing the slider from properly pressing onto the outer body to ensure a good seal. After multiple tests and redesigns, it was found that irrespective of the location or the type of seal used, the mechanical action of the sliding cylinder coupled with

the high operating temperatures of the setup resulted in the failure of the seals which in turn prevented the FOV from functioning properly. Since the FOV is crucial for performing the envisaged non-classical gas dynamics experiments, this meant that no meaningful tests could be conducted with the FAST if the FOV was the adopted device to initiate the flow. It was, therefore, decided that the FOV was unsuitable to achieve the goals of the experiments and a new barrier element needed to be conceived and designed to make progress in the experimental investigation.

### 3.3.4. Temperature inhomogeneities along the charge tube

The initial conditions for nonclassical experiments with candidate BZT fluids are chosen such that the fluid state is in the  $\Gamma < 0$  thermodynamic region. It is of utmost importance that the fluid conditions, especially the temperature, are maintained as uniformly as possible. This is because, one, the region of negative nonlinearity spans a narrow range of pressures and temperatures, and two,  $\Gamma$  is very sensitive to changes in temperature, particularly close to the critical point and to the vapour-liquid saturation curve. Thus, even a small inhomogeneity in the temperature can alter the thermodynamic state of the fluid, and can even cause  $\Gamma$  to become positive, thereby nullifying the possibility of generating nonclassical flows.

The temperature control system of the FAST was designed keeping these constraints in consideration. Since the CT was long, it was impossible to accurately measure the temperature of the vapour within it without multiple sensors immersed in the vapour at different locations. Such a setup can in turn disturb the flow field complicating the analysis of the experimental results. This justified the control strategy based on the reference tube temperature mentioned in Section 3.3.1.

Often when performing rarefaction wave tests using  $D_6$  as the working fluid temperature fluctuations in the RT were observed during the heating phase. Since the control of the CT is dependent on the stability of RT temperature, these fluctuations in turn caused the CT temperature to oscillate. This greatly increased the time needed by the control system to stabilize the temperatures of the CT and the RT at the setpoint conditions. These fluctuations in the RT were most likely caused by liquid  $D_6$  which condensed at some cold spots within the CT. The CT was intentionally placed at a slight slope so that any condensed fluid would flow back into the HFT, via pipes 5 & 6 as shown in Fig. 3.7, where it would be vaporized again. This liquid, being considerably colder than the  $D_6$  vapour in the RT, would then lead to a sudden drop in the temperature measured by the Pt-100 in the RT, thereby destabilizing the entire control system.

In order to identify the cold spots in the CT that resulted in such local con-

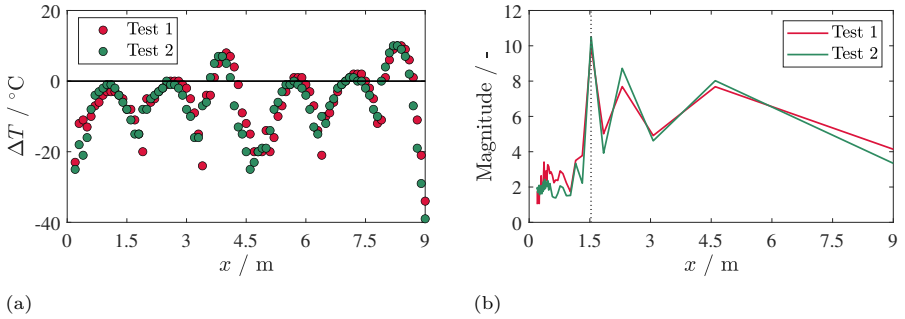


Figure 3.16: (a) Difference between the internal wall temperature of the CT and the thermal control system setpoint, measured at 10 cm intervals. (b) Fast Fourier Transform of  $\Delta T$  measurements showing the period of the signals.

densation, the internal wall temperature ( $T_{\text{int}}$ ) of the CT was measured under atmospheric conditions at two setpoint temperatures of  $T_{\text{SP1}} = 175^\circ\text{C}$  and  $T_{\text{SP2}} = 190^\circ\text{C}$ . A 10 m thermocouple was slid into the CT through the LPP and  $T_{\text{int}}$  was recorded at intervals of 10 cm. The measurements were taken 3 hours and 24 hours after reaching setpoint values  $T_{\text{SP1}}$  and  $T_{\text{SP2}}$  respectively to ensure that steady-state temperatures were achieved. Figure 3.16a shows the difference  $\Delta T$  between  $T_{\text{int}}$  and the temperature setpoint of the control system along the length of the CT.

In the majority of the CT locations,  $T_{\text{int}}$  remained well below the setpoint, only reaching the setpoint value at periodic intervals. It was also evident that the duration of the heating has a negligible effect on the temperature distribution. Since  $T_{\text{int}}$  varied periodically and resembled a sinusoid, a simple Fourier Transform was performed to identify the period of the oscillation, as shown in Fig. 3.16b. The period of the signals was found to be 1.5 m, which is the length of a single segment of the CT. Since the first temperature measurement point was in contact with a flange, this implied that the coldest points along tube were close to the locations of the flange with the desired setpoint value in temperature being achieved only at the midpoint of a segment where the thermocouples were actually attached. Thus, every coupling is a location for local condensation of the fluid, and this cold fluid disrupts the control system as it flows through the RT into HFT.

The reason for such cold-spots at the segment coupling location (flange) is three-fold: i) the heating blankets used in the FAST are designed in such a manner that a 2-3 cm portion of the blankets on either end is devoid of any heating coil to make space for the internal circuitry, thus the sections of the CT segment close to the couplings are unheated; ii) the couplings themselves are heated by a much less powerful 180 W heating wire compared to the 950 W heater applied to the the segments. The energy supplied by the heating wire

must also travel a larger distance to reach the interior of the CT, due to the larger thickness of the couplings; iii) the larger area of the couplings implies a higher heat loss rate, further decreasing the temperature at this location. In addition, the thermal conductivity of stainless steel itself is not sufficient enough to homogenize the temperature across the segment.

One solution to address this issue is to use several smaller thermal blankets, each with its own PID controller and thermocouple for independent control. This, combined with using more powerful thermal blankets for the segments, can help ensure a uniform temperature distribution in the CT. However, implementing this approach would result in an extremely complex thermal control system, and the cost of purchasing and maintaining numerous thermal blankets would also be high.

A simpler solution to achieve temperature homogeneity without altering the existing control system would be to compensate for the lower thermal conductivity of stainless steel by adding outer shells made of a metal with high thermal conductivity, such as aluminum, to the CT. Sleeves made of aluminum would ensure uniform and efficient heat transfer along the segment, due to aluminum's nearly ten times higher thermal conductivity when compared to stainless steel 316Ti. Meanwhile, stainless steel would provide the necessary structural support to handle the mechanical stress caused by the pressurized fluid.

A Finite Volume Modelling (FVM) simulation of the heat transfer in a FAST segment was performed to evaluate the effects of adding aluminium shells to the stainless steel tube. The results, presented in Fig. 3.17, demonstrate that adding 5 mm thick aluminium sleeves can reduce the temperature difference between the ends and middle of the CT segment from 20 °C to less than 2 °C. This was determined to be the maximum thickness possible while still allowing for the use of existing thermal blankets. Moreover, the simulation indicated that the temperature can nearly be made uniform by slightly overheating the couplings, i.e., by providing a setpoint temperature that is  $\approx 1\%$  over the desired experimental initial temperature. Thus, combining the use of Al sleeves with a slight overheating of the couplings can ensure a homogeneous temperature distribution in the CT, preventing not only fluid condensation, but also any part of the tube from reaching decomposition temperatures.

### 3.4. Concluding Remarks

This chapter provides an overview of the experimental procedure for the generation of nonclassical wave fields. Though the generation of both rarefaction shock waves (RSW) and isentropic compression fans can provide evidence of the existence of nonclassical gasdynamics, the novelty of the phenomenon, the relative ease in generating and identifying a RSW owing to a larger admis-

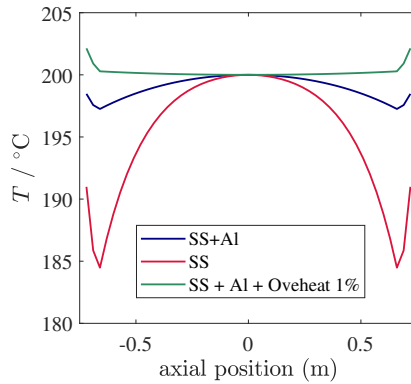


Figure 3.17: Comparison of internal wall temperatures in a CT segment with different configurations: stainless steel tube (SS —), stainless steel tube fitted with Al shells (—) and the stainless steel tube fitted with Al shells and a 1% overheating applied to the couplings (—); axial position of 0 denotes the midpoint location of a segment with a coupling at either end.

sibility region, and the availability of previous experimental knowledge make it the primary goal of a nonclassical gasdynamic experiment. Several experimental options are available to achieve this goal, from a classical nozzle setup to novel methods such as laser-induced point explosion within a dense organic vapour control volume. A Ludwig-type shock tube, however, was considered to be the most suitable option due to its simplicity and the ability to generate a variety of wave fields in a controlled manner.

The novel, Ludwig-tube based Flexible Asymmetric Shock Tube (FAST) facility at TU Delft is presented. The FAST was designed to operate at conditions of up to 400 °C and 10 bar pressure and used a Fast Opening Valve (FOV) as a barrier element to separate the high and low-pressure sections of the tube. The FOV, the most complex component of the FAST, was a custom-made valve that was specifically designed to be operated at the extreme conditions of the experiment without the need for lubrication in order to avoid contamination of the working fluid. However, the FOV suffered from numerous mechanical failures in its sealing components, primarily because of temperature expansion effects. Several redesigns and modifications of the FOV failed to mitigate the issues and it was therefore decided not to proceed with experiments using the FOV. Moreover, the FAST also suffered from temperature homogeneity issues due to the presence of multiple flanges which acted as cold spots at which the hot vapours underwent condensation. This in turn caused instabilities in the temperature control system when the cold fluid flowed over temperature sensors that were used as references in the control.

Based on the experiences gained by operating the FAST, it was concluded that the setup was not suitable for performing experiments with the test fluid in a thermodynamic state within the so-called BZT region to provide evidence for the existence of negative  $\Gamma$  effects. A new setup would be required, one that must be designed to mitigate the problems encountered with the FAST. However, given the weakly nonlinear feature of the RSW, any new setup would also be of considerable length and thereby make temperature homogeneity, one of the chief issues with the FAST, a challenge. It is therefore necessary that, before any new experimental activity is undertaken, the effect of temperature gradients on a propagating RSW in a BZT fluid is clearly understood. The next chapter presents the results of such a study conducted as a part of this research project.



# Bibliography

- [1] P. A. Thompson, “A Fundamental Derivative in Gasdynamics,” *Physics of Fluids*, vol. 14, no. 9, p. 1843, 1971. DOI: [10.1063/1.1693693](https://doi.org/10.1063/1.1693693).
- [2] C. Zamfirescu, A. Guardone, and P. Colonna, “Admissibility region for rarefaction shock waves in dense gases,” *Journal of Fluid Mechanics*, vol. 599, pp. 363–381, Mar. 2008. DOI: [10.1017/s0022112008000207](https://doi.org/10.1017/s0022112008000207).
- [3] N. R. Nannan, “Advancements in nonclassical gas dynamics,” Ph.D. dissertation, TU Delft, 2009.
- [4] A. A. Borisov, A. A. Borisov, S. S. Kutateladze, and V. E. Nakoryakov, “Rarefaction shock wave near the critical liquid–vapour point,” *Journal of Fluid Mechanics*, vol. 126, pp. 59–73, Jan. 1983. DOI: [10.1017/s002211208300004x](https://doi.org/10.1017/s002211208300004x).
- [5] S. H. Ferguson, “Dense gas shock tube: Design and analysis,” Ph.D. dissertation, University of Colorado at Boulder, 2001.
- [6] T. Mathijssen, “Experimental Observation of Non-Ideal Compressible Fluid Dynamics with application in Organic Rankine Cycle Power Systems,” Ph.D. dissertation, TU Delft, 2017.
- [7] C. Zamfirescu, P. Colonna, N. R. Nannan, and A. Guardone, “Experiment Options to Investigate *BZTE* effects in Dense Gases,” TU Delft, Tech. Rep., Jan. 2005.
- [8] C. Zamfirescu, A. Guardone, and P. Colonna, “Preliminary Design of the FAST Dense Gas Ludwig Tube,” in *9th AIAA/ASME Joint Thermophysics and Heat Transfer Conference*, American Institute of Aeronautics and Astronautics, Jun. 2006. DOI: [10.2514/6.2006-3249](https://doi.org/10.2514/6.2006-3249).
- [9] D. Chandrasekar and P. Prasad, “Transonic flow of a fluid with positive and negative nonlinearity through a nozzle,” *Physics of Fluids A: Fluid Dynamics*, vol. 3, no. 3, pp. 427–438, Mar. 1991. DOI: [10.1063/1.858099](https://doi.org/10.1063/1.858099).
- [10] A. Kluwick, “Transonic nozzle flow of dense gases,” *Journal of Fluid Mechanics*, vol. 247, pp. 661–688, Feb. 1993. DOI: [10.1017/s0022112093000618](https://doi.org/10.1017/s0022112093000618).
- [11] M. S. Cramer and R. N. Fry, “Nozzle flows of dense gases,” *Physics of Fluids A: Fluid Dynamics*, vol. 5, no. 5, pp. 1246–1259, May 1993. DOI: [10.1063/1.858610](https://doi.org/10.1063/1.858610).

- [12] P. A. Thompson, *Compressible Fluid Dynamics (advanced engineering series)*, Third. McGraw-Hill Inc., US, 1988.
- [13] B. P. Brown and B. M. Argrow, “Nonclassical Dense Gas Flows for Simple Geometries,” *AIAA Journal*, vol. 36, no. 10, pp. 1842–1847, Oct. 1998. DOI: [10.2514/2.276](https://doi.org/10.2514/2.276).
- [14] V. Elling and T.-P. Liu, “Supersonic flow onto a solid wedge,” *Communications on Pure and Applied Mathematics*, vol. 61, no. 10, pp. 1347–1448, Oct. 2008. DOI: [10.1002/cpa.20231](https://doi.org/10.1002/cpa.20231).
- [15] D. Vimercati, A. Kluwick, and A. Guardone, “Oblique waves in steady supersonic flows of Bethe–Zel’dovich–Thompson fluids,” *Journal of Fluid Mechanics*, vol. 855, pp. 445–468, Sep. 2018. DOI: [10.1017/jfm.2018.633](https://doi.org/10.1017/jfm.2018.633).
- [16] S. D’Angelo, D. Vimercati, and A. Guardone, “A unified description of oblique waves in ideal and non-ideal steady supersonic flows around compressive and rarefactive corners,” *Acta Mechanica*, vol. 229, no. 6, pp. 2585–2595, Feb. 2018. DOI: [10.1007/s00707-018-2130-6](https://doi.org/10.1007/s00707-018-2130-6).
- [17] T. J. Juliano, S. P. Schneider, S. Aradag, and D. Knight, “Quiet-Flow Ludwig Tube for Hypersonic Transition Research,” *AIAA Journal*, vol. 46, no. 7, pp. 1757–1763, Jul. 2008. DOI: [10.2514/1.34640](https://doi.org/10.2514/1.34640).
- [18] F. F. J. Schrijer and W. J. Bannink, “Description and Flow Assessment of the Delft Hypersonic Ludwig Tube,” *Journal of Spacecraft and Rockets*, vol. 47, no. 1, pp. 125–133, Jan. 2010. DOI: [10.2514/1.40773](https://doi.org/10.2514/1.40773).
- [19] R. Cummings and T. McLaughlin, “Hypersonic Ludwig Tube Design and Future Usage at the US Air Force Academy,” in *50th AIAA Aerospace Sciences Meeting including the New Horizons Forum and Aerospace Exposition*, American Institute of Aeronautics and Astronautics, Jan. 2012. DOI: [10.2514/6.2012-734](https://doi.org/10.2514/6.2012-734).
- [20] A. Guardone and P. Colonna, “Point Explosions in Dense Gases,” in *9th AIAA/ASME Joint Thermophysics and Heat Transfer Conference*, American Institute of Aeronautics and Astronautics, Jun. 2006. DOI: [10.2514/6.2006-3391](https://doi.org/10.2514/6.2006-3391).
- [21] K. Yasunaga, T. Mikajiri, S. M. Sarathy, *et al.*, “A shock tube and chemical kinetic modeling study of the pyrolysis and oxidation of butanols,” *Combustion and Flame*, vol. 159, no. 6, pp. 2009–2027, Jun. 2012. DOI: [10.1016/j.combustflame.2012.02.008](https://doi.org/10.1016/j.combustflame.2012.02.008).
- [22] X. Han, J. M. Mehta, and K. Brezinsky, “Temperature approximations in chemical kinetics studies using single pulse shock tubes,” *Combustion and Flame*, vol. 209, pp. 1–12, Nov. 2019. DOI: [10.1016/j.combustflame.2019.07.022](https://doi.org/10.1016/j.combustflame.2019.07.022).

- [23] K. Grogan and M. Ihme, “StanShock: A gas-dynamic model for shock tube simulations with non-ideal effects and chemical kinetics,” *Shock Waves*, vol. 30, no. 4, pp. 425–438, Jan. 2020. DOI: [10.1007/s00193-019-00935-x](https://doi.org/10.1007/s00193-019-00935-x).
- [24] J. F. Bott and N. Cohen, “A shock tube study of the reactions of the hydroxyl radical with several combustion species,” *International Journal of Chemical Kinetics*, vol. 23, no. 12, pp. 1075–1094, Dec. 1991. DOI: [10.1002/kin.550231203](https://doi.org/10.1002/kin.550231203).
- [25] S. Saxena, M. S. P. Kahandawala, and S. S. Sidhu, “A shock tube study of ignition delay in the combustion of ethylene,” *Combustion and Flame*, vol. 158, no. 6, pp. 1019–1031, Jun. 2011. DOI: [10.1016/j.combustflame.2010.10.011](https://doi.org/10.1016/j.combustflame.2010.10.011).
- [26] A. Burcat, E. Olchanski, and C. Sokolinski, “Kinetics of Hexane Combustion in a Shock Tube,” *Israel Journal of Chemistry*, vol. 36, no. 3, pp. 313–320, 1996. DOI: [10.1002/ijch.199600043](https://doi.org/10.1002/ijch.199600043).
- [27] J. E. Drewry and Z. A. Walenta, “Determination of diaphragm opening-times and use of diaphragm particle traps in a hypersonic shock tube,” National Aeronautics and Space Administration (NASA), Tech. Rep., Jun. 1965.
- [28] S. H. Ferguson, T. L. Ho, B. M. Argrow, and G. Emanuel, “Theory for producing a single-phase rarefaction shock wave in a shock tube,” *Journal of Fluid Mechanics*, vol. 445, pp. 37–54, Oct. 2001. DOI: [10.1017/s0022112001005444](https://doi.org/10.1017/s0022112001005444).
- [29] P. Gaetani, A. Guardone, and G. Persico, “Shock tube flows past partially opened diaphragms,” *Journal of Fluid Mechanics*, vol. 602, pp. 267–286, Apr. 2008. DOI: [10.1017/s0022112008000815](https://doi.org/10.1017/s0022112008000815).
- [30] M. M. Alves and C. T. Johansen, “Modeling shock-wave strength near a partially opened diaphragm in a shock tube,” *Shock Waves*, vol. 31, no. 5, pp. 499–508, Jul. 2021. DOI: [10.1007/s00193-021-01028-4](https://doi.org/10.1007/s00193-021-01028-4).
- [31] A. Svete and J. Kutin, “Characterization of a newly developed diaphragmless shock tube for the primary dynamic calibration of pressure meters,” *Metrologia*, vol. 57, no. 5, p. 055 009, Sep. 2020. DOI: [10.1088/1681-7575/ab8f79](https://doi.org/10.1088/1681-7575/ab8f79).
- [32] R. S. Tranter and B. R. Giri, “A diaphragmless shock tube for high temperature kinetic studies,” *Review of Scientific Instruments*, vol. 79, no. 9, p. 094 103, 2008. DOI: [10.1063/1.2976671](https://doi.org/10.1063/1.2976671).
- [33] Y. Takano and T. Akamatsu, “A diaphragmless shock tube,” *Journal of Physics E: Scientific Instruments*, vol. 17, no. 8, pp. 644–646, Aug. 1984. DOI: [10.1088/0022-3735/17/8/005](https://doi.org/10.1088/0022-3735/17/8/005).

- [34] M. S. Downey, T. J. Cloete, and A. D. B. Yates, "A rapid opening sleeve valve for a diaphragmless shock tube," *Shock Waves*, vol. 21, no. 4, pp. 315–319, Mar. 2011. DOI: [10.1007/s00193-011-0310-6](https://doi.org/10.1007/s00193-011-0310-6).
- [35] R. Mejia-Alvarez, B. Wilson, M. C. Leftwich, A. A. Martinez, and K. P. Prestridge, "Design of a fast diaphragmless shock tube driver," *Shock Waves*, vol. 25, no. 6, pp. 635–650, Jul. 2015. DOI: [10.1007/s00193-015-0579-y](https://doi.org/10.1007/s00193-015-0579-y).
- [36] I. Stotz, G. Lamanna, and B. Weigand, "Fluid disintegration studies in a specialized shock tube," in *Progress in Propulsion Physics*, EDP Sciences, 2011. DOI: [10.1051/eucass/201102165](https://doi.org/10.1051/eucass/201102165).
- [37] J. J. Keller, "Nonlinear acoustic resonances in shock tubes with varying cross-sectional area," *Zeitschrift für angewandte Mathematik und Physik*, vol. 28, no. 1, pp. 107–122, Jan. 1977. DOI: [10.1007/bf01590712](https://doi.org/10.1007/bf01590712).
- [38] L. Z. Dumitrescu, "An Attenuation-Free Shock Tube," *Physics of Fluids*, vol. 15, no. 1, p. 207, 1972. DOI: [10.1063/1.1693742](https://doi.org/10.1063/1.1693742).
- [39] S. Ferguson, A. Guardone, and B. Argrow, "Construction and Validation of a Dense Gas Shock Tube," *Journal of Thermophysics and Heat Transfer*, vol. 17, no. 3, pp. 326–333, Jul. 2003. DOI: [10.2514/2.6789](https://doi.org/10.2514/2.6789).
- [40] P. Colonna, A. Guardone, N. R. Nannan, and C. Zamfirescu, "Design of the Dense Gas Flexible Asymmetric Shock Tube," *Journal of Fluids Engineering*, vol. 130, no. 3, Mar. 2008. DOI: [10.1115/1.2844585](https://doi.org/10.1115/1.2844585).
- [41] M. S. Cramer and R. Sen, "Shock formation in fluids having embedded regions of negative nonlinearity," *Physics of Fluids*, vol. 29, no. 7, p. 2181, 1986. DOI: [10.1063/1.865555](https://doi.org/10.1063/1.865555).
- [42] S. S. Kutateladze, V. E. Nakoryakov, and A. A. Borisov, "Rarefaction Waves in Liquid and Gas-Liquid Media," *Annual Review of Fluid Mechanics*, vol. 19, no. 1, pp. 577–600, Jan. 1987. DOI: [10.1146/annurev.fl.19.010187.003045](https://doi.org/10.1146/annurev.fl.19.010187.003045).
- [43] P. A. Thompson, "Liquid-Vapor Adiabatic Phase Changes and Related Phenomena," in *Nonlinear Waves in Real Fluids*, Springer Vienna, 1991, pp. 147–213. DOI: [10.1007/978-3-7091-2608-0\\_6](https://doi.org/10.1007/978-3-7091-2608-0_6).
- [44] A. Guardone, "Three-dimensional shock tube flows for dense gases," *Journal of Fluid Mechanics*, vol. 583, pp. 423–442, Jul. 2007. DOI: [10.1017/s0022112007006313](https://doi.org/10.1017/s0022112007006313).
- [45] A. Guardone, C. Zamfirescu, and P. Colonna, "Maximum intensity of rarefaction shock waves for dense gases," *Journal of Fluid Mechanics*, vol. 642, pp. 127–146, Dec. 2009. DOI: [10.1017/s0022112009991716](https://doi.org/10.1017/s0022112009991716).

- [46] P. Colonna and P. Silva, “Dense Gas Thermodynamic Properties of Single and Multicomponent Fluids for Fluid Dynamics Simulations,” *Journal of Fluids Engineering*, vol. 125, no. 3, pp. 414–427, May 2003. DOI: [10.1115/1.1567306](https://doi.org/10.1115/1.1567306).
- [47] T. Mathijssen, M. Gallo, E. Casati, *et al.*, “The flexible asymmetric shock tube (FAST): a Ludwig tube facility for wave propagation measurements in high-temperature vapours of organic fluids,” *Experiments in Fluids*, vol. 56, no. 10, Oct. 2015. DOI: [10.1007/s00348-015-2060-1](https://doi.org/10.1007/s00348-015-2060-1).
- [48] P. Colonna, A. Guardone, and N. R. Nannan, “Siloxanes: A new class of candidate Bethe-Zel’dovich-Thompson fluids,” *Physics of Fluids*, vol. 19, no. 8, p. 086102, Aug. 2007. DOI: [10.1063/1.2759533](https://doi.org/10.1063/1.2759533).
- [49] E. I. M. Casati, “New concepts for organic Rankine cycle power systems,” Ph.D. dissertation, TU Delft, Sep. 2014.
- [50] *DuPont™ Kalrez® Spectrum™ 7075*, Jul. 2010.
- [51] Saint-Gobain, *Omniseal® Spring-Energized Seals: Polymer Seals with Metal Springs*, <https://www.omniseal-solutions.com/components/omniseal-polymers/omniseal-spring-energized-seals>, Accessed: 16-09-2022, 2022.
- [52] I. Hajzer, *Understanding Spring Energized Seals and When to Use Them*, <https://blog.chesterton.com/sealing/understanding-spring-energized-seals/>, Accessed: 17-09-2022.
- [53] E. E. Inc., *How Spring Energized Seals Are Made (And Why You Need One)*, <https://eclipseseal.com/blog/seals/spring-energized-seals-made-need-one/>, Accessed: 17-09-2022.
- [54] S. S. Gaskets, *Spring Energized Seals*, <https://www.sigmasalsgaskets.com/products/spring-energized-seals/>, 16-09-2022, 2022.



# 4

## Nonlinear Wave Propagation in BZT Fluids with Temperature Gradients

From:

N. B. Chandrasekaran *et al.*, “Nonlinear wave propagation in dense vapor of Bethe–Zel’dovich–Thompson fluids subjected to temperature gradients,” *Physics of Fluids*, vol. 33, no. 10, p. 107109, Oct. 2021. DOI: [10.1063/5.0063226](https://doi.org/10.1063/5.0063226)

### 4.1. Introduction

Experiments conducted till date in the NICFD region of BZT fluids have always strived to maintain as homogeneous a temperature distribution as possible across the test setups. This is because the temperature window is the single major restriction to observe BZT effects in nonclassical experiments. There are two reasons as to why the temperature control of any BZT experiment should be tight: one, to avoid local condensation in the CT, which, if occurring close to the location of the pressure sensors can complicate the interpretation of the results, and two, just a few degrees of difference in the temperature can decide whether nonclassical effects are permitted in the flow or not.

Measurements of the internal wall temperature of the FAST, as discussed in Chapter 3, already showed that despite very tight temperature controls

and numerous precautions adopted to maintain uniform temperature of the fluid, the vapours were always subjected to gradients of temperature in the longitudinal direction. In fact, the gradients in the FAST were large enough to cause local condensation of  $D_6$  thereby destabilizing the temperature control system. This also suggested that the experiments conducted by Mathijssen [2] were far from the nonclassical thermodynamic region. For example, assuming the same temperature distribution at a setpoint temperature of  $369\text{ }^\circ\text{C}$  as was observed at the steady-state case of  $190\text{ }^\circ\text{C}$  (see Chap. 3.3.4), and that there is no condensation in the CT (which is a weak assumption), the variation of  $\Gamma$  in  $D_6$  is displayed in Fig. 4.1. It is seen that the fluid exists in the classical ( $\Gamma \approx 1$ ), the non-ideal ( $0 < \Gamma < 1$ ), and the nonclassical ( $\Gamma < 0$ ) thermodynamic states in the CT.

4

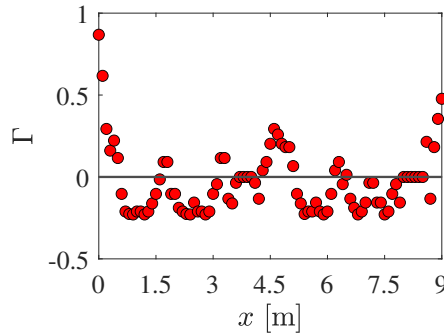


Figure 4.1: Expected variation of  $\Gamma$  in the CT of the FAST at  $369\text{ }^\circ\text{C}$  assuming temperature gradients similar to that observed at  $190\text{ }^\circ\text{C}$  and no condensation.

Such a large variation in  $\Gamma$  is expected to have a profound impact on the formation and the propagation of a RSW. Given the already weak nature of RSWs, temperature gradients can therefore prevent any steepening of a propagating wavefront, at least to the extent in which it cannot be measured with sufficient confidence. It is therefore of great interest to investigate the effect of such temperature variations on the formation of RSWs in BZT fluids in order to improve the interpretation of envisaged experiments.

Several studies have investigated the propagation of nonlinear waves in ideal gases subjected to non-uniform temperature distributions [3]–[5]. Lin *et al.* [6] developed an analytical criterion for computing the shock formation distance and time using the wavefront expansion technique [7] for a finite-amplitude wave travelling in a medium with smoothly varying entropy. The effect of temperature gradients on shock waves in BZT fluids was first dealt with by Cramer *et al.* [8] who analysed the propagation of waves in a single-phase fluid whose properties were close to the transition region between positive and negative  $\Gamma$ . This study was subsequently extended to investigate

the formation of one-dimensional shock waves in van der Waals (vdW) fluids which feature an embedded  $\Gamma < 0$  region by Cramer *et al.* [9]. More recently, Muralidharan *et al.* [10] derived an analytical solution for the steepening of a wavefront propagating in a medium with both positive and negative nonlinearity using the wavefront expansion technique. Though developed for a vdW's gas, the solution is valid for any equation of state (EoS) in the near-critical thermodynamic region.

Given that temperature inhomogeneities in facilities of the scale of the FAST and the ASTER are largely inevitable, understanding the effect of gradients in temperature can help predict the behaviour of non-ideal waves in BZT fluids and also assist in adjusting the initial conditions of the experiment in order to ensure the successful formation of RSWs. In this chapter, such a study is carried out analytically using the wavefront expansion technique and numerically using the Westervelt equation. To achieve the highest accuracy in terms of fluid properties, the fluid of interest D<sub>6</sub> is modelled using the state-of-the-art multiparameter EoS [11]. The effect such gradients can have on the shock formation distance of both the compressive and expansive types are studied.

In the study documented here, the analytical solution obtained with the so-called wavefront expansion technique was employed to investigate the propagation of finite-amplitude waves in BZT fluids with axial temperature variations. This investigation is motivated by observations made by the authors while trying to improve the FAST [12] that in any shock tube setup developed to study RSWs, temperature gradients along the tube are inevitable. Moreover, in this study multiparameter equation of state were employed to model fluid properties [13] in order to achieve the highest accuracy. The validity of the inviscid analysis is tested against viscous effects by comparing with the solution of the one-dimensional Westervelt equation. In addition, the effect of such gradients on shock formation distances were also computed.

This chapter is structured as follows: in Section 4.2.1, the analytical model used to describe the nonlinear steepening of a wave propagating in a thermoviscous medium subjected to temperature gradients is introduced. This is followed by Section 4.2.2 that describes the Westervelt equation and the numerical method used to solve it. Section 4.3 provides the results obtained from applying the aforementioned methods on the evolution of an initial disturbance till a shock is formed. The effect that temperature gradients in a medium can have on the shock formation distance is analysed in Section 4.3. Concluding remarks are summarized in Section 4.5.

## 4.2. Modelling nonlinear wave propagation in thermoviscous fluids

### 4.2.1. Wavefront Expansion Technique

If a finite-amplitude rarefaction wave travels in a homogeneous medium featuring a thermodynamic state with negative  $\Gamma$ , accepted theory prescribes that it steepens as a result of the nonlinearity. Given sufficient amplitude of the initial disturbance, the steepening of the wave can eventually result in the formation of a rarefaction shockwave (RSW). Numerically, the formation of a RSW can be identified by tracking the rate of steepening of the leading edge of the disturbance till the slope becomes infinity. According to Muralidharan *et al.* [10], the evolution of the leading edge of a finite-amplitude wave propagating in a stationary vapor in the presence of entropy gradients is

$$\frac{1}{u_1(x)} = \frac{F(0)}{F(x)u_1(0)} + \frac{1}{F(x)} \int_0^x \frac{F(\hat{x})\Gamma_0(\hat{x})}{c_0(\hat{x})} d\hat{x}, \quad (4.1)$$

where  $u$  is the particle velocity and

$$u_1(x) = \frac{d}{dx}[u(x)], \quad (4.2)$$

$$F(x) = c_0(x)^{-3/2} \rho_0(x)^{-1/2}, \quad \text{and} \quad x = X(t), \quad (4.3)$$

with  $u_1(0)$  being the initial slope of the wave,  $X(t)$  the location of the leading edge of the wave at time  $t$ , and  $c_0$  and  $\rho_0$  the local soundspeed and density of the undisturbed medium. It is convenient to think of the strength of the wave in terms of the magnitude of  $u_1(0)$ . Higher the value of  $u_1(0)$ , lower is its inverse, and thus steeper is the initial wavefront. A steeper initial wave is closer to forming a shock than a shallow one, and thus, the former can be considered stronger than the latter. A shock is formed if  $u_1(x) \rightarrow \infty$  (thus,  $1/u_1 \rightarrow 0$ ). The local rate of change of  $1/u_1$ , which is a measure of the curvature of the wavefront, can be derived from Eq. (4.1) and is written as

$$\frac{d}{dx} \left( \frac{1}{u_1} \right) = \frac{\Gamma}{c} - \frac{1}{u_1} \left[ \frac{1}{F(x)} \frac{d}{dx} [F(x)] \right]. \quad (4.4)$$

This numerical method provides a closed-form solution which is at the foundation of the study on the effect of temperature variations on wave steepening. Equation (4.1) provides the wave slope only at the leading edge and therefore does not capture shocks formed elsewhere along the wave. This is however

consistent with the current study which also focuses on the steepening at the leading edge of the wave.

The wavefront expansion method is used to investigate the propagation of waves in the dense vapor of dodecamethylcyclohexasiloxane,  $D_6$ , a complex organic molecule considered in recent theoretical, numerical and experimental studies on nonclassical gas dynamics [14] including the FAST. The properties of the fluid are computed using a Span-Wagner multiparameter equation of state model [13], [15] implemented in an in-house software library for the computation of fluid thermophysical properties.[16] Since the pressure of the medium is assumed constant, the variation of the temperature alone can completely describe the thermodynamic state of the fluid.

#### 4.2.2. Westervelt Equation Model

The Westervelt equation used for modelling nonlinear waves in thermoviscous fluids was already introduced in Chapter 2. Written in terms of  $\Gamma$ , and assuming that the disturbances in the fluid properties are of small amplitude relative to the medium at rest, and that the wave propagates in a fluid in which the length scale of the inhomogeneity is larger than the wavelength of the wave, the propagation of finite amplitude disturbances in a thermoviscous fluid is given by [17], [18]

$$\nabla^2 p - \frac{1}{c_0^2} \frac{\partial^2 p}{\partial t^2} - \frac{1}{\rho_0 \nabla \rho_0 \nabla p} + \frac{\delta}{c_0^4} \frac{\partial^3 p}{\partial t^3} + \frac{\Gamma}{\rho_0 c_0^4} \frac{\partial^2 p^2}{\partial t^2} = 0, \quad (4.5)$$

where  $p$  is the acoustic pressure,  $c_0$  and  $\rho_0$  are the soundspeed and density of the quiescent fluid,  $\delta$  is the diffusivity of sound and  $\Gamma$  is the fundamental derivative of gasdynamics.

#### Solving the Westervelt Equation

The Westervelt equation does not have a known analytical solution and is therefore solved using numerical methods. Spatial and temporal derivatives in Eq. (4.5) are approximated with discrete differences using the Finite Difference Time Domain (FDTD) method [19]. The  $x$  spatial dimension is divided into  $N_x$  elements, equally spaced by  $\Delta x$  and indexed with  $i$ . Absorbing boundary conditions are imposed to prevent wave reflections that are numerical artefacts from affecting the results. The spatial derivative is computed using second-

order-accurate central differences as

$$\frac{\partial p}{\partial x} \approx \frac{1}{2\Delta x} (p_i^{n+1} - p_i^{n-1}), \quad (4.6a)$$

$$\frac{\partial^2 p}{\partial x^2} \approx \frac{1}{\Delta x^2} (p_{i+1}^n - 2p_i^n + p_{i-1}^n). \quad (4.6b)$$

Similarly, the temporal dimension is discretized into  $N_t$  elements, divided into equal intervals  $\Delta t$  and indexed with  $n$ . The time derivative in the second term of Eq. (4.5) is computed using second-order-accurate central differences while the nonlinear and absorption terms are expanded using backward differencing, resulting in

$$\frac{\partial^2 p}{\partial t^2} \approx \frac{1}{(\Delta t)^2} (p_i^{n+1} - 2p_i^n + p_i^{n-1}), \quad (4.7a)$$

$$\frac{\partial^3 p}{\partial t^3} \approx \frac{1}{(2\Delta t)^3} (5p_i^n - 18p_i^{n-1} + 24p_i^{n-2} - 14p_i^{n-3} + 3p_i^{n-4}), \quad (4.7b)$$

$$\frac{\partial^2 p^2}{\partial t^2} \approx 2 \left[ \left( \frac{3p_i^n - 4p_i^{n-1} + p_i^{n-2}}{2\Delta t} \right)^2 + \frac{2p_i^n - 5p_i^{n-1} + 4p_i^{n-2} - p_i^{n-3}}{\Delta t^2} \right]. \quad (4.7c)$$

Equations (4.6) and (4.7) are substituted into Eq. (4.5) and solved for  $p_i^{n+1}$ .

### 4.3. Evolution of initial disturbance and shock formation

The treatment of the evolution of an initial disturbance propagating in a medium subjected to temperature gradients is simplified by the adoption of the non-dimensional parameters

$$x^* = x/L_0 \quad \text{and} \quad \eta = x - X(t),$$

where  $L_0$  ( $= 10$  m) and  $\eta$  are the domain length and the distance from the leading edge at time  $t$ , respectively.

#### 4.3.1. Uniform Temperature

The baseline case is that of a finite-amplitude wave travelling in a medium with a uniform temperature distribution. In this case,  $F(0) = F(x)$  everywhere,

and Eq. (4.1) reduces to the form

$$\frac{1}{u_1} = \frac{1}{u_1(0)} + \Gamma_0 t, \quad (4.8)$$

where  $\Gamma = \Gamma_0$  is the fundamental derivative evaluated for the thermodynamic state of the medium, and is therefore constant. The local rate of change of the wavefront slope  $(1/u_1)'$  given by Eq. (4.4) also simplifies to

$$\frac{d}{dx} \left( \frac{1}{u_1} \right) = \frac{\Gamma_0}{c_0}. \quad (4.9)$$

Equation (4.8) is an equation for a straight line with a slope of  $\Gamma_0/c$ . Thus, a wave travelling in a medium with constant temperature would continuously steepen till it forms a shock wave, provided it is of sufficient initial strength  $u_1(0)$ . Consequently, the sign and magnitude of  $\Gamma$  dictate the nature and rate of steepening of the wave in this case. Equation (4.9) also shows that any traveling wave, irrespective of whether it is of the compressive or the expansive type, would necessarily undergo distortion, apart from the exceptional case of  $\Gamma = 0$ , entailing therefore linear propagation.

#### 4.3.2. Non-uniform Temperature

For this study, the behaviour of a propagating nonlinear wave in  $D_6$  subjected to different temperature distributions was analysed. First, a linear temperature profile was considered: the fluid temperature was varied from 369 °C to 373 °C over a length of 10 m and the ambient pressure was kept at 9 bar. The choice of temperature and pressure were motivated by the initial conditions of nonclassical gas dynamic experiments by means of a shock tube documented in the literature and planned within this research project for the near future [12]. However, the validity of the results does not depend on these values or fluid and a different fluid and similar reduced thermodynamic properties would lead to similar results. The variation in  $T$ , and the corresponding variation in  $\Gamma$ , as a function of the non-dimensional tube length is shown in Fig. 4.2. For these fluid thermodynamic conditions,  $\Gamma$  transitions from negative values at lower temperature to positive values at higher temperature. It can therefore be expected that a rarefaction wave travelling in this medium would initially steepen for all locations within the tube in which  $\Gamma$  is negative and then relax further downstream. This is indeed what is observed in Fig. 4.3, which shows the evolution of  $1/u_1$  of rarefaction waves for different inverse initial slopes  $1/u_1(0)$ . The global trend for all rarefaction waves propagating in the fluid subjected to the temperature gradient shown in Fig. 4.2 is to initially steepen in portions of the flow domain in which the thermodynamic state features

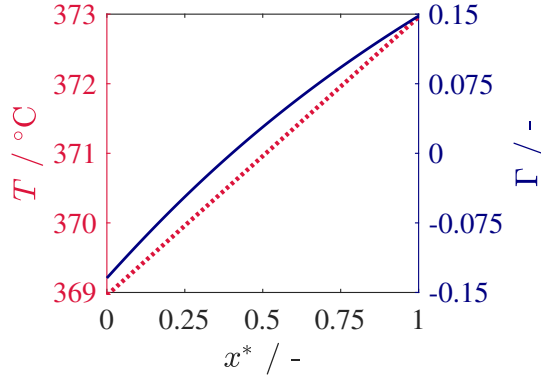


Figure 4.2: Variation of  $T$  (····) and  $\Gamma$  (—) as a function of the non-dimensional coordinate  $x^*$  related to the evolution of rarefaction waves in a one-dimensional flow domain ( $x = 0 - 10$  m) formed by dense vapor of siloxane  $D_6$  at  $p = 9$  bar and subjected to a linearly increasing temperature change.

$\Gamma < 0$  followed by a relaxation in the portions featuring the  $\Gamma > 0$  thermodynamic state. The value of  $1/u_1$  reaches a minimum at the location where the steepening behaviour of the wavefront reverses. As the initial strength of the wave increases (decreasing  $1/u_1(0)$ ), this minimum value of  $1/u_1$  gradually approaches zero until eventually when  $\min(1/u_1)$  reaches zero indicating the formation of a shockwave. The corresponding initial strength of the wave  $\tilde{u}_1(0)$  is defined such that any wave with an initial slope larger than  $\tilde{u}_1(0)$  can steepen to form a shock wave while a wave with  $u_1(0) < \tilde{u}_1(0)$  cannot steepen sufficiently to form a shock wave in the medium.

Fig. 4.3 also shows the line connecting the points of minimum of  $1/u_1$  in the flow domain, denoted as  $x_{\min\{1/u_1\}}$ , for different  $u_1(0)$  and where the thermodynamic state of the fluid features  $\Gamma = 0$ , denoted as  $x_{\Gamma=0}$ . In a fluid affected by temperature gradients, a rarefaction wavefront might be expected to steepen as long as the thermodynamic state implies that  $\Gamma < 0$  and to relax if  $\Gamma > 0$ . The transition to the opposite steepening behaviour of the wave would occur at the location where  $\Gamma$  is zero. However, as shown in Fig. 4.3, for all the initial wave strengths characterized by a value of the initial wave slope lower than  $\tilde{u}_1(0)$ ,  $x_{\min\{1/u_1\}}$  precedes  $x_{\Gamma=0}$  along the  $x$  coordinate. Thus, the wave ceases to steepen and starts relaxing even if the thermodynamic state of the fluid features negative  $\Gamma$ . The value of  $\Gamma$  at the position where  $x_{\min\{1/u_1\}}$  can be found from Eq. (4.4) as

$$\Gamma(x_{\min\{1/u_1\}}) = \frac{c}{u_1} \left[ \frac{1}{F(x)} \frac{d}{dx} [F(x)] \right] \Big|_{x_{\min\{1/u_1\}}} . \quad (4.10)$$

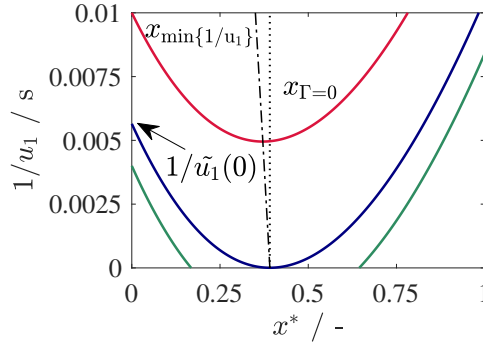


Figure 4.3: Evolution of the inverse of the leading edge slope of rarefaction waves propagating along  $x^*$ , starting at  $x^* = 0$  and  $t = 0$  with different values of  $u_1(0)$ , in dense vapor of siloxane  $D_6$  at  $p = 9$  bar and subjected to a linearly increasing temperature change. (---): locus of the positions in the flow domain where the wave features minimum  $1/u_1$ . (.....): locus of the positions in the flow domain for which the thermodynamic state of the fluid features  $\Gamma = 0$ .

Note that  $F(x)$  defined in Eq. (4.3) has a finite value and  $dF/dx$  cannot be zero in a flow domain featuring gradients in fluid properties. Therefore, for  $\Gamma$  to be zero at  $x_{\min\{1/u_1\}}$ ,  $1/u_1$  must be necessarily zero at that location in a fluid subject to a temperature gradient, thereby indicating the formation of a shock wave. This leads to definition of the critical initial slope condition  $\tilde{u}_1(0)$ .

The evolution of compression wavefronts propagating in a medium in which  $\Gamma$  changes from positive to negative was also studied. In this case, the temperature of the fluid decreases linearly from 373 °C to 369 °C. The variation of  $\Gamma$  and  $1/u_1$  along the flow domain is shown in Figs. 4.4 and 4.5. Initially, the wave steepens as expected since  $\Gamma > 0$ , but the rate of steepening decreases as  $\Gamma$  approaches zero. Unlike the case of a medium subjected to a linearly increasing temperature,  $x_{\min\{1/u_1\}}$  is greater than  $x_{\Gamma=0}$  for all initial wave strengths  $u_1(0) < \tilde{u}_1(0)$ . Therefore, compression waves continue to steepen even if the local thermodynamic state of the fluid features negative  $\Gamma$  before starting to relax. Again, there exists a critical initial strength  $\tilde{u}_1(0)$  for which  $1/u_1$  is tangential to the  $x$ -axis. This highlights the fact that the observed behaviour is a general physical characteristic of nonlinear waves in the region close to  $\Gamma = 0$  regardless of its sign.

### 4.3.3. Analysis based on the Westervelt Equation

Unlike the analytical solution of the one dimensional wave propagation problem that can be derived from the 1D Euler equations, the Westervelt equation

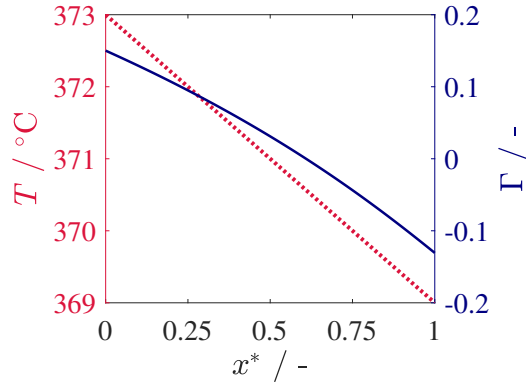


Figure 4.4: Variation of  $T$  (····) and  $\Gamma$  (-·-·) as a function of the non-dimensional coordinate  $x^*$  related to the evolution of compression waves in a one-dimensional flow domain ( $x = 0 - 10$  m) formed by dense vapor of siloxane  $D_6$  at  $p = 9$  bar and subjected to a linearly decreasing temperature change.

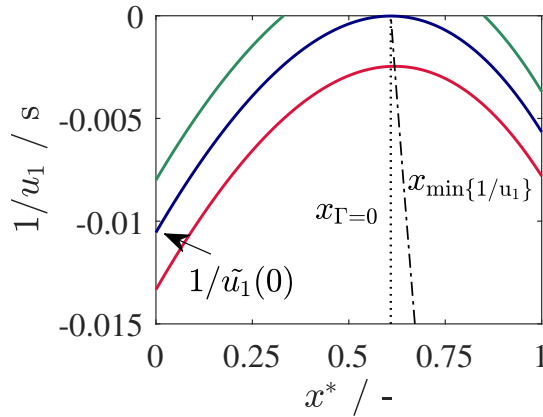


Figure 4.5: Evolution of the inverse of the slope of the leading edge of compression waves propagating along  $x^*$ , starting at  $x^* = 0$  and  $t = 0$  s with different values of  $u_1(0)$ , in dense vapor of siloxane  $D_6$  at  $p = 9$  bar and subjected to a linearly decreasing temperature change. (-·-·): locus of the positions in the flow domain where the wave features minimum  $1/u_1$ . (····): locus of the positions in the flow domain for which the thermodynamic state of the fluid features  $\Gamma = 0$ .

accounts for the effect of viscosity. The effect this has on wave propagation can be assessed by comparing the numerical solution of the Westervelt equation model to the analytical solution of the Euler equations.

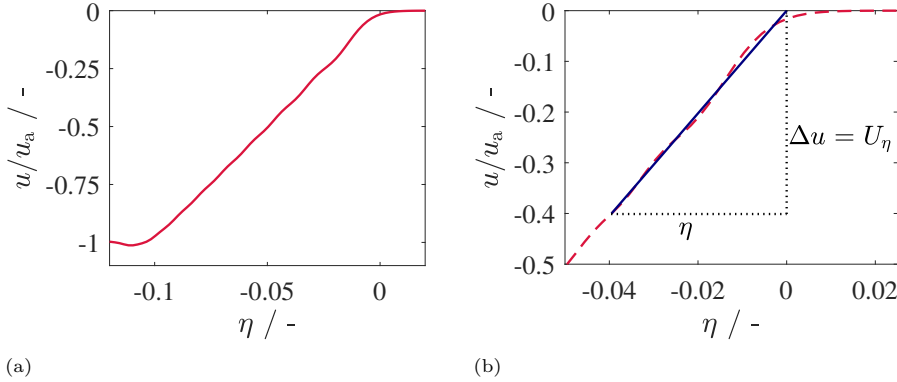


Figure 4.6: (a) Variation in acoustic velocity as a function of  $\eta = x - X(t)$  along the wavefront of a rarefaction wave propagating in dense vapor of isothermal  $D_6$  at  $p = 9$  bar. (b) Closeup of the leading edge location showing the numerical dissipation and the method of estimation of the leading edge slope.

Fig. 4.6a shows the wavefront of a rarefaction wave, defined as a ramp in pressure and expressed in terms of acoustic velocity, at a given time instant while propagating in quiescent isothermal  $D_6$ . The particle velocity increases linearly from  $u = 0$  m/s at the wavefront ( $\eta = 0$  m) till it reaches a maximum value of  $u_a$  at the tail of the wave, defined as

$$u_a = \frac{\Delta p}{\rho_0 \cdot c_0}, \quad (4.11)$$

where  $\Delta p$  is the pressure difference across the wave and  $\rho_0$  and  $c_0$  are the density and soundspeed in the quiescent medium. Minor undulations can be observed along the wavefront, which result from the Gibb's oscillations forming at the two edges of the wavefront.

Fig. 4.6b shows a closeup of the wavefront between the leading edge point ( $\eta = 0$  m) and a location downstream of the wavefront. Though  $1/u_1$  is calculated at the leading edge in the analytical solution, this does not yield accurate values in the simulation since it suffers from numerical dissipation at this location. This can be observed clearly at  $\eta = 0$  m where the leading edge of the wavefront is smoothed due to dissipation. This has the tendency to artificially reduce the slope of the wavefront. To overcome this effect, the leading edge of the wavefront is reconstructed by calculating the actual leading edge location in the absence of numerical dissipation. This can be readily

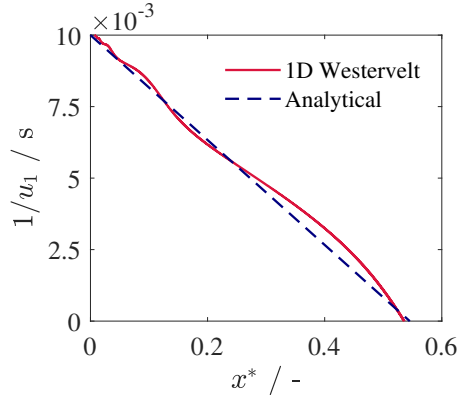


Figure 4.7: Evolution of the inverse of the wavefront slope in isothermal  $D_6$  at  $p = 9$  bar propagating along  $x^*$ , starting at  $x^* = 0$  and  $t = 0$  s calculated using the analytical solution of the Euler equations and the solution of the Westervelt equation.

estimated owing to the fact that the leading edge is unaffected by nonlinear effects and propagates only at the local soundspeed. Thus, the leading edge location at any timestep  $n$  is

$$X(n) = X(n-1) + c(n-1) \cdot dt. \quad (4.12)$$

The slope between the leading edge point and a location at  $\eta$  along the wavefront is calculated as

$$u_1|_{\text{numr.}} = \frac{u(\eta)}{\eta}. \quad (4.13)$$

The calculation of  $u_1$  in this study is performed numerically at a location where  $u(\eta) = 0.1u_a$ . The sensitivity of  $u_1$  to the choice of  $u(\eta)$  was analyzed and was found to be small. Figure 4.7 compares the evolution of  $1/u_1$  calculated using the analytical solution of the 1D Euler equations and the numerical solution of the Westervelt equation. As expected, both models predict a monotonous steepening of the wavefront until a shock wave is formed and the results are very similar, except for the fluctuations affecting the solution of the Westervelt equation arising from the Gibb's oscillations shown in Fig. 4.6a.

Figure 4.8a shows the variation in the particle velocity along the wavefront at three different time instances for a rarefaction wave propagating in the dense vapor of  $D_6$  subjected to linearly increasing temperature as shown in Fig. 4.2. The profile of the wavefront during the initial stage of propagation in the medium is shown for  $t = 0.005$  s. The particle velocity varies linearly from  $u = 0$  at the leading edge to  $u = u_a$  at the tail of the wave and the wavefront

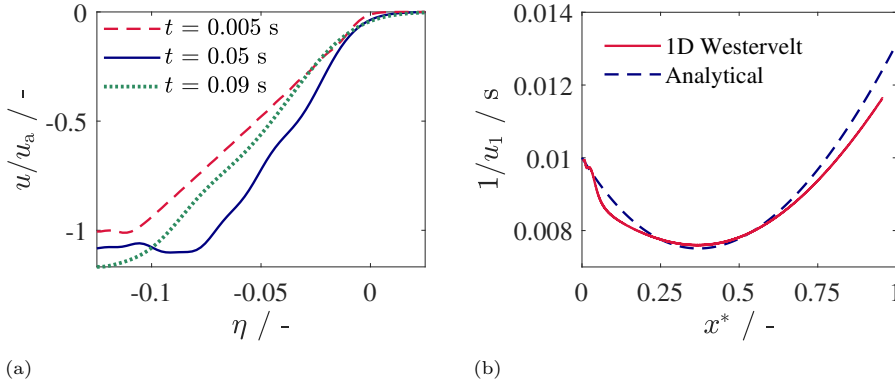


Figure 4.8: (a) Particle velocity  $u$  vs.  $\eta$  ( $= x - X(t)$ ) along a rarefaction wave propagating in  $D_6$  subjected to linearly increasing temperature at three different time instances. (b) Comparison of evolution of  $1/u_1$  between analytical solution to 1D Euler equations and the solution of the Westervelt equation.

is largely devoid of any numerical oscillation. Since  $\Gamma < 0$  in the fluid in this thermodynamic state, the wave steepens as it propagates. This steepening can be observed in the wavefront profile shown at  $t = 0.1$  s with the tail of the wave lying closer to  $\eta = 0$  m than at  $t = 0.005$  s. At this time instant, the wave is close to the location of  $x_{\min\{1/u_1\}}$  in Fig. 4.3. After this time, the fluid thermodynamic state features  $\Gamma > 0$  and thus the wave relaxes during propagation. This is seen at  $t = 0.15$  s in Fig. 4.8a. Once again, the tail of the wave moves farther from  $\eta = 0$  m indicating that the wave is relaxing as it travels in the medium.

Another observation that can be deduced from Fig. 4.8a is related to the magnitude of  $u$  at the tail of the wave. Since the wave travels in a medium in which the temperature varies, the acoustic impedance  $\mathcal{Z}$  of the medium also varies with location. This results in a continuous reflection of a part of the incident wave in the upstream direction. Thus, the particle velocity at the tail end of the wave is higher than  $u_a$  as the wave progresses and increases steadily from  $t = 0.005$  s to  $t = 0.15$  s. Figure 4.8b shows the evolution of  $1/u_1$  calculated using both the analytical solution to the 1D Euler equation and the Westervelt equation. The steepening of the wavefront computed using the Westervelt equation is seen to match closely with the analytical solution and captures the behaviour accurately. Once again, numerical oscillations seen in Fig. 4.8a affect  $1/u_1$  and the numerical slope fluctuates about the analytical solution.

It can therefore be concluded that the variation of temperature significantly affects the steepening characteristics of finite-amplitude waves propagating in

dense vapors of fluids made of complex molecules. If the fluid is in a thermodynamic state close to states for which  $\Gamma = 0$ , the effect of soundspeed and density variation can alter the steepening of the wave in a way that is opposite to that dictated by the local value of  $\Gamma$ . Unless the wave features a critical initial strength  $\tilde{u}_1(0)$ , then it is shown that a rarefaction wave can relax even if it propagates through a fluid for which the thermodynamic state features  $\Gamma < 0$  and vice-versa for a compression wave. In addition, numerical simulations of wave propagation show that viscosity has a negligible effect on wave steepening even if the wave propagates in a fluid whose thermodynamic state features  $\Gamma$  close to zero.

#### 4.4. Effect of temperature gradients on shock formation distance

Apart from the scientific interest of understanding how temperature variations influence the propagation of waves in dense vapors, the results of this investigation are of particular relevance regarding experiments aimed at generating and proving the formation of a rarefaction shock with a shock tube experiment. In such an experiment, one is interested in obtaining the shortest shock formation distance to keep the length of the shock tube as short as possible.

As an example relevant to the experimental study of nonclassical gasdynamics, the propagation of a rarefaction wave in a tube containing dense vapor of siloxane  $D_6$  and subjected to a sinusoidal fluctuation of temperature around a mean value along its length was numerically investigated. This type of temperature perturbation allows to study the effect of both the amplitude and wavelength of the disturbance on wave evolution. The temperature perturbation is therefore

$$T = T_0 + \Delta T \cdot \sin\left(\frac{2\pi x}{\lambda_T} + \phi\right), \quad (4.14)$$

where  $T_0$  is the temperature of the quiescent fluid in  $^{\circ}\text{C}$ ,  $\Delta T$  is the amplitude of temperature variation in  $^{\circ}\text{C}$ ,  $\lambda_T$  is the wavelength of the temperature variation in meters and  $\phi \in [-\pi, \pi]$  is the phase of the sinusoidal disturbance. The evolution of the wavefront is analysed for  $M$  values of  $\lambda_T$  and  $N$  values of  $\phi$ , linearly distributed over their range and indexed as  $\lambda_{T,i}$  ( $i = 1, 2, \dots, M$ ) and  $\phi_j$  ( $j = 1, 2, \dots, N$ ), and the corresponding shock formation distances  $x_{\text{sh}}$  are calculated. To remove the effect of the initial phase of the disturbance, mean shock distances  $\bar{x}_{\text{sh}}$  rather than a single shock distance  $x_{\text{sh}}$  dependent on the initial phase are compared. The mean shock distances are therefore computed

as

$$\bar{x}_{\text{sh}}(i) = \frac{\sum_{j=1}^N x_{\text{sh}}(\lambda_{T,i}, \phi_j)}{N}, \quad (4.15)$$

and are compared with the shock distance  $x_{\text{sh,homog}}$  that is computed for the case in which the properties of the medium are homogeneous, with temperature equal to the mean temperature of the sinusoidal profile. The non-dimensional parameters

$$\lambda^* = \lambda_T/L_0, \quad x^* = x/L_0,$$

and

$$x_{\text{sh}}^* = x_{\text{sh}}/x_{\text{sh,homog}}, \quad \bar{x}_{\text{sh}}^* = \bar{x}_{\text{sh}}/x_{\text{sh,homog}}$$

facilitate the analysis of the results. In these definitions,  $L_0$  ( $= 10$  m) and  $x_{\text{sh,homog}}$  are the fluid domain length and the shock formation distance in a homogeneous fluid, respectively.

### Rarefaction Waves

The fluid thermodynamic state chosen for this analysis is such that  $\Gamma < 0$  everywhere in the domain. Rarefaction waves with different initial waveslopes  $u_1(0)$  were simulated to propagate in dense vapor of  $\text{D}_6$  at 9 bar and subjected to a sinusoidal temperature disturbance defined by Eq. (4.14) with  $T = 369$  °C,  $\Delta T = 0.5$  °C,  $M = 10$  and  $N = 200$ . In this thermodynamic state, the mean value of  $\Gamma$  is  $-0.14$ .

Fig. 4.9 shows the variation of the mean shock formation distance  $\bar{x}_{\text{sh}}^*$  as a function of  $\lambda^*$  for pressure waves with different values of  $u_1(0)$ . Figure 4.9a highlights that  $\bar{x}_{\text{sh}}^*$  is between 0.96 and 0.99 for  $\lambda^* \leq 0.1$  for all values of  $u_1(0)$ . This implies that the shock formation distance is only weakly dependent on the initial wave slope for  $\lambda^* < 0.1$ . It can also be observed that, though  $\bar{x}_{\text{sh}}^* < 1$ , the spread in the mean shock distance increases with increasing  $\lambda^*$ . Figure 4.9b puts into evidence that, for  $\lambda^* > 0.1$ , the mean shock formation distance increases with increasing  $\lambda^*$ , eventually reaching a value greater than 1. Also, the variation of  $\bar{x}_{\text{sh}}^*$  with  $\lambda^*$  exhibits a stronger dependency on  $u_1(0)$ : as the initial slope of the wave increases, the minimum wavelength at which  $\bar{x}_{\text{sh}}^*$  starts increasing towards 1 decreases.

Fig. 4.10 compares the evolution of  $1/u_1$  in a fluid affected by a sinusoidal temperature variation with  $\lambda^* = 0.05$  and  $\phi = \pi/2$  with the evolution of  $1/u_1$  for a wave that propagates in a homogeneous medium. The choice of the

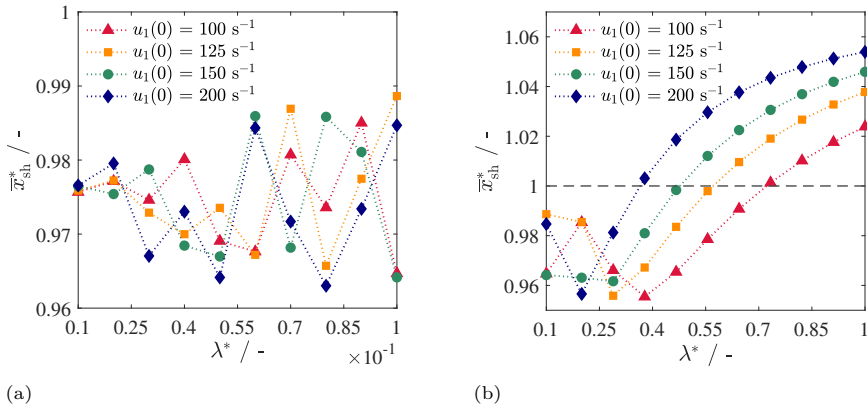


Figure 4.9: Variation of  $\bar{x}_{sh}$  as a function of  $\lambda^*$  for rarefaction waves with different values of initial slope  $u_1(0)$  evolving in dense vapors of  $D_6$  at  $p = 9$  bar and subjected to a sinusoidally varying temperature. (a)  $\lambda^* < 0.1$ . (b)  $\lambda^*$  between 0.1 and 1.

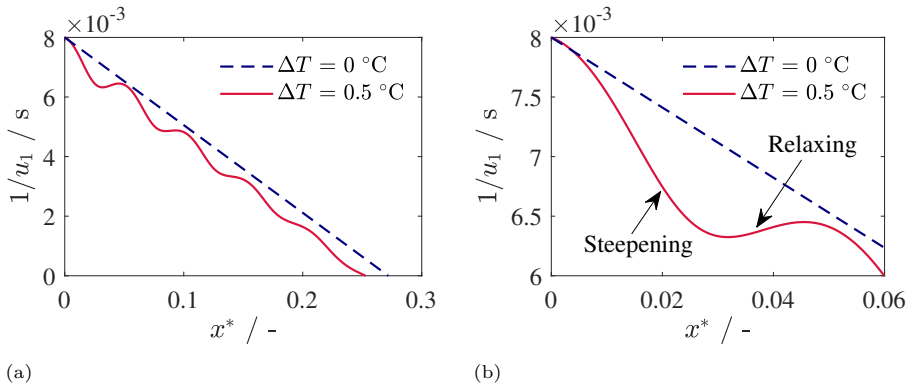


Figure 4.10: Variation of relevant quantities as a function of the non-dimensional coordinate  $x^*$  related to the evolution of rarefaction waves in a one-dimensional flow domain ( $x = 0 - 10$  m) formed by dense vapor of siloxane  $D_6$  at  $p = 9$  bar and subjected to a sinusoidal temperature change (see Eq. (4.14)) with  $\lambda^* = 0.05$  and  $\phi = \pi/2$ . (a) Evolution of  $1/u_1$  of the rarefaction wave propagating along  $x^*$ , starting at  $x^* = 0$  and  $t = 0$  s, till  $x^* = x_{sh}^*$ . (b) Closeup of evolution of  $1/u_1$  from  $x^* = 0$  to 0.06 for better clarity.

values of  $\lambda^*$  and  $\phi$  was made to highlight the effect of the temperature gradient on wave evolution and has no impact on the previous observations. Similar to what is displayed in Figs. 4.3 and 4.5, the rarefaction wave steepens if the fluid is in a thermodynamic state featuring negative  $\Gamma$  and relaxes if  $\Gamma > 0$ . The undulations in the slope of the evolving wavefront in Fig. 4.10a are caused by the periodic oscillation of the local temperature, and therefore of  $\Gamma$ . It can be seen in Fig. 4.10b, which is a close-up of Fig. 4.10 and shows the early evolution of the wave, that the steepening phase of the wave is more prominent than the relaxing phase. This observation can be explained by means of Eq. (4.4), rewritten here for better clarity, as

$$\frac{d}{dx} \left( \frac{1}{u_1} \right) = \frac{\Gamma}{c} - \frac{\kappa}{u_1}, \quad (4.16)$$

where

$$\kappa \equiv \left[ \frac{1}{F(x)} \frac{d}{dx} [F(x)] \right],$$

which shows that  $(1/u_1)'$  depends on both the local values of  $\Gamma$  and  $c$  as well as on the gradient of soundspeed and density.

Fig. 4.11 displays the variation of the two terms constituting Eq. (4.16) for two different values of  $\lambda^*$ . The first term,  $\Gamma/c$ , is directly determined by the local temperature in the medium, and therefore, shows a similar sinusoidal oscillation. Since the fluid is in a state in which  $\Gamma < 0$ , this term is negative everywhere in the fluid. The second term,  $\kappa/u_1$ , is also determined by the initial conditions of the medium. However,  $\kappa$  can either be positive or negative depending on whether the location is on the increasing or the decreasing branch of the sinusoidal temperature gradient. If  $\kappa < 0$ , the cumulative effect of the negative contributions of both terms enhances the nonclassical steepening of the rarefaction wave. However, if  $\kappa$  is positive, the contributions have opposite sign and the relaxing of the wave is mitigated. This explains why a shorter shock formation distance is calculated in a wave propagating through a medium with temperature gradients when compared to a medium with homogeneous temperature distribution.

In Eq. (4.16),  $\kappa$  is modulated by the local inverse slope of the wavefront  $1/u_1$ , therefore the magnitude of  $\kappa/u_1$  reduces as the wave steepens ( $1/u_1 \rightarrow 0$ ) to form a shock. Since the magnitude of  $\Gamma/c$  is smaller than  $\kappa/u_1$  (see Fig. 4.11), the undulations are dampened as the wave steepens during propagation, as seen in Fig. 4.10. Figure 4.11 also highlights the effect of the change in the wavelength of the temperature distribution on  $\Gamma/c$  and  $\kappa/u_1$ . As the wavelength increases, the magnitude of  $\Gamma/c$  remains constant but the value of  $\kappa$  decreases significantly owing to the smaller gradients in soundspeed

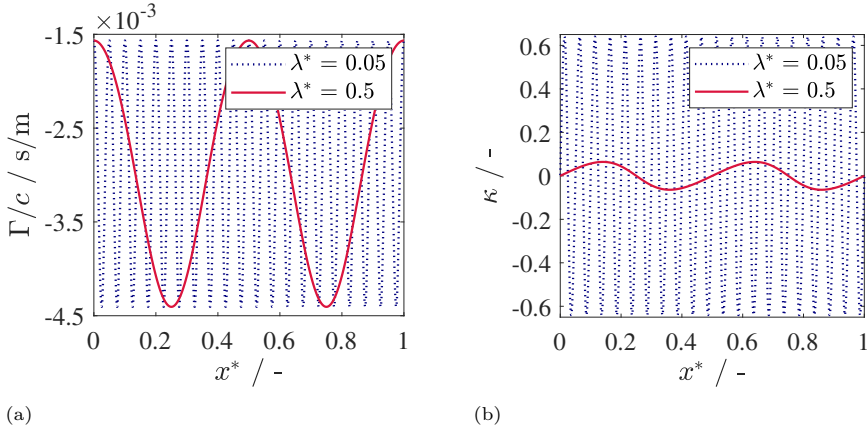


Figure 4.11: Variation of relevant quantities constituting Eq. (4.16) as a function of the non-dimensional coordinate  $x^*$  in dense vapor of siloxane  $D_6$  at  $p = 9$  bar and subjected to a sinusoidal temperature change with  $\Delta T = 0.5$  °C and for  $\lambda^* = 0.05$  & 0.5. (a) Variation of  $\Gamma/c$ . (b) Variation of  $\kappa$ .

and density in a fluid whose temperature varies less sharply. Thus, at higher  $\lambda^*$ , the enhancement of nonlinear steepening caused by  $\kappa$  decreases. This also explains the inverse dependence among  $\bar{x}_{sh}^*$  and  $u_1(0)$  for  $\lambda^* > 0.1$ : the contribution of  $\kappa/u_1$ , which is already lower at higher  $\lambda^*$ , is further reduced due to smaller  $1/u_1$  (higher  $u_1(0)$ ) leading to the behaviour observed in Fig. 4.9b.

Fig. 4.12 shows the variation of the shock formation distance  $x_{sh}^*$  as a function of  $\phi$  for  $\lambda^*$  equal to 0.05 and to 0.5 for two initial wave slopes of  $100 \text{ s}^{-1}$  and  $200 \text{ s}^{-1}$ . The enhancement of the nonlinear steepening of the wave by the gradients in soundspeed and density can be observed in the lines showing the variation of  $x_s^*$  with  $\phi$  for  $\lambda^* = 0.05$ . For both cases of  $u_1(0)$ , the variation of  $x_{sh}^*$  with  $\lambda^*$  is similar and superimpose each other highlighting the independence of  $x_{sh}^*$  from  $u_1(0)$  as observed in Fig. 4.9. Also,  $x_{sh}^*$  is close to 1 or lower than 1 for both  $u_1(0)$ , indicating that the gradients in soundspeed and density ensure that the wave in this medium almost always shocks earlier than in a homogeneous medium. For  $\lambda^* = 0.5$ , the variation in  $x_s^*$  with  $\phi$  is more significant due to the smaller gradients in soundspeed and density associated with this temperature variation. For both the initial wave slope cases,  $x_s^*$  is greater than 1 for certain  $\phi$ . This effect is stronger for  $u_1(0) = 200 \text{ s}^{-1}$  where, in addition to the smaller value of  $\kappa$ , the contribution of the  $\kappa/u_1$  term in Eq. (4.16) is also smaller owing to the lower value of  $1/u_1(0)$ . Thus, the shock formation distance is more susceptible to the phase of the sinusoidal temperature distribution as the wavelength of this variation increases.

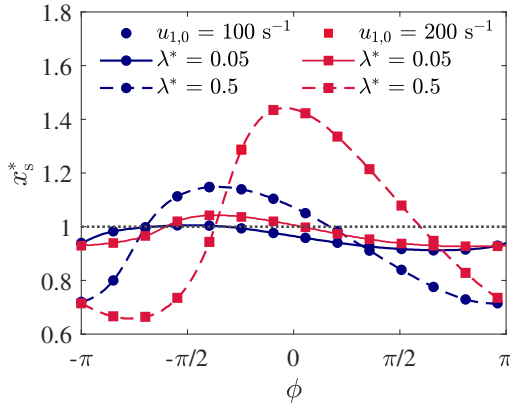


Figure 4.12: Variation of shock formation distance  $x_{\text{sh}}^*$  as a function of the phase of the sinusoidal temperature gradient  $\phi$  for rarefaction waves with different  $u_1(0)$  evolving in dense vapor of  $\text{D}_6$  at  $p = 9$  bar and subjected to a temperature distribution give by Eq. (4.14) for different  $\lambda^*$ .

The results presented here indicate that, contrary to the intuition that a temperature gradient in an experimental setup aimed at generating a rarefaction shock wave would be detrimental with respect to nonlinear steepening, a temperature variation can help enhance the steepening of a propagating finite-amplitude wave and can in fact cause the wave to steepen into a shock at a shorter distance from the wave origin if compared to the wave propagation in a homogeneous medium. This outcome has a significant impact on rarefaction shock wave experiments using shock tubes, because inevitable fluctuations of the temperature along the tube can be controlled to cause a shorter shock formation distance. The results also show that the shock formation distance is the lowest when the wave initially encounters a  $\Gamma < 0$  region during propagation in an inhomogeneous fluid. Thus, even in experiments without inherent temperature gradients, or in situations where maintaining one across the setup is not feasible, the shock formation distance can be reduced by simply altering the conditions in the region close to the wave origin to obtain a value of  $\Gamma$  that is lower than elsewhere.

### Compression Waves

The fluid thermodynamic state chosen for this analysis is such that  $\Gamma > 0$  everywhere in the fluid domain. Compression waves with different initial wave-lopes  $u_1(0)$  were simulated to propagate in dense vapor of  $\text{D}_6$  at 9 bar and subjected to a sinusoidal temperature disturbance defined by Eq. (4.14) with  $T = 373$  °C,  $\Delta T = 0.5$  °C,  $M = 10$  and  $N = 200$ . In this thermodynamic

state, the mean value of  $\Gamma$  is 0.11.

Fig. 4.13 shows the variation in mean shock formation distance  $\bar{x}_{\text{sh}}^*$  for different  $\lambda^*$ . It is seen that for all  $\lambda^*$ , the mean shock distance is greater than the homogeneous shock formation distance  $x_{\text{sh,homog}}$ . The variation of  $\bar{x}_{\text{sh}}^*$  with  $\lambda^*$ , however, is similar to what can be observed in Fig. 4.9, wherein  $\bar{x}_{\text{sh}}^*$  remains fairly constant for  $\lambda^* < 0.1$  and then increases depending on  $u_1(0)$  for  $\lambda^* > 0.1$ . It can also be noticed that the variations in  $\bar{x}_{\text{sh}}^*$  in this case are not more than 1.5% in the considered range of  $\lambda^*$  which is significantly lower than the observed variations in  $\bar{x}_{\text{sh}}^*$  seen in Fig. 4.9.

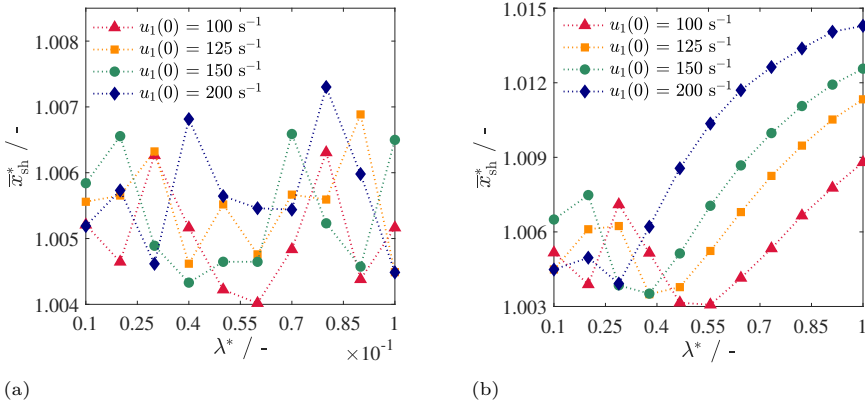


Figure 4.13: Variation of  $\bar{x}_{\text{sh}}$  as a function of  $\lambda^*$  for compression waves with different values of initial slope  $u_1(0)$  evolving in dense vapors of D<sub>6</sub> at  $p = 9$  bar and subjected to a sinusoidally varying temperature. (a)  $\lambda^* < 0.1$ . (b)  $\lambda^*$  between 0.1 and 1.

Fig. 4.14 shows the comparison of the evolution of the compression wavefront in a fluid affected by sinusoidal temperature variation with  $\lambda^* = 0.05$  and  $\phi = \pi/2$  with the evolution of  $1/u_1$  for a wave that propagates in a homogeneous medium. Unlike what can be seen in Fig. 4.10, the rate of steepening of the wavefront is nearly constant with only minor undulations. For this combination of  $\phi$  and  $\lambda^*$ , the shock formation distance in the fluid affected temperature gradients is only marginally smaller than that in the fluid subjected to uniform gradients. Similar to what is observed in Fig. 4.10a, the undulations in the evolution of  $1/u_1$  are dampened in this case also as the wave approaches shock formation.

The reason for the dampened response of  $1/u_1$  to the variation in  $\Gamma$  and  $\kappa$  can be attributed to the lower sensitivity of  $\Gamma$ ,  $\rho$  &  $c$  to temperature variations in this thermodynamic region. Figure 4.15 depicts the variation in  $(\partial\Gamma/\partial T)_P$  and  $(\partial F/\partial T)_P$  with the reduced temperature  $T_r$  along the isotherm at  $P_r = 0.94$  in the range of temperatures related to the cases presented in Section 4.3.2

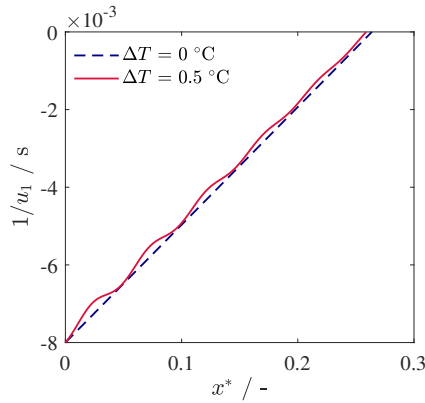


Figure 4.14: Evolution of  $1/u_1$  of a compression wave propagating along  $x^*$ , starting at  $x^* = 0$  and  $t = 0$  s, till  $x^* = x^*_{sh}$  in a one-dimensional flow domain ( $x = 0 - 10$  m) formed by dense vapor of siloxane  $D_6$  at  $p = 9$  bar and subjected to a sinusoidal temperature change (see Eq. (4.14)) with  $\lambda^* = 0.05$  and  $\phi = \pi/2$ .

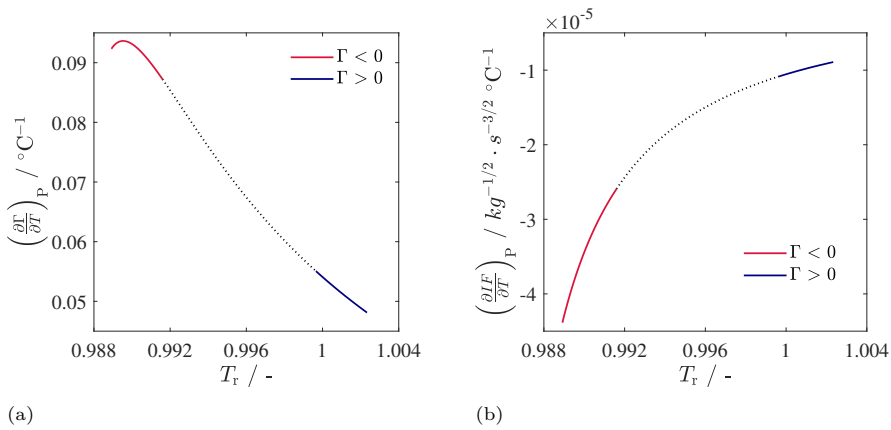


Figure 4.15: Variation in (a)  $(\frac{\partial \Gamma}{\partial T})_P$  and (b)  $(\frac{\partial F}{\partial T})_P$  vs.  $T_r$  along the isobar  $P_r = 0.94$ . Values of the gradients in the range of temperatures observed in Fig. 4.9 and 4.13 in the  $\Gamma < 0$  and  $\Gamma > 0$  thermodynamic regions are highlighted.

and Section 4.3.3, in the  $\Gamma < 0$  and  $\Gamma > 0$  domains. It is seen that the gradients in  $\Gamma$  are approximately twice as large in  $\Gamma < 0$  region (Fig. 4.15a), while the gradients in  $F$  are three times larger in the same regime (see Fig. 4.15b) when compared to those in the  $\Gamma > 0$  region. Thus, the impact of the variations in medium properties on  $(1/u_1)'$  and  $(1/u_1)$  are much smaller in the  $\Gamma > 0$  region when compared with those in the  $\Gamma < 0$  region. This results in a smaller perturbation of the propagating wave, resulting in similar or longer shock formation distances than those calculated for the case of homogeneous medium.

## 4.5. Conclusions

### 4

This chapter presented the results of an analytical and numerical investigation on the effect of axial temperature gradients on the propagation of finite amplitude waves in the dense vapor of BZT fluids, therefore in the case of non-classical gasdynamics. The evolution and the steepening of the wavefront was studied analytically by means of a closed form solution of the one dimensional governing equation. A model based on the Westervelt equation was developed in order to simulate wave propagation and visualize simulation results. The analysis was performed by assuming that the dense vapor is that of siloxane  $D_6$ , initially isobaric conditions. Different temperature variations along the physical domain were considered.

The model allowed to demonstrate analytically that, if the wave propagates nonclassically, there exists a minimum initial value of the slope of a finite-amplitude wave which allows the wave to steepen into a shock, if the fluid is subjected to a variation of temperature along the flow domain. While  $\Gamma$  determines the nature of the steepening of propagating disturbances for the most part, there exists a small region close to  $\Gamma = 0$  in which the gradients in soundspeed and density overcome the effect of nonlinearity on the distortion of the wave. If the state of the fluid lies in this thermodynamic region, a rarefaction wave can relax even if  $\Gamma < 0$  and a compression wave can steepen even if  $\Gamma > 0$ .

The effect of gradients in soundspeed and density are also shown to significantly influence the location of the shock formation. Results show that rarefaction waves evolving in a fluid for which  $\Gamma < 0$  and subjected to temperature gradients tend to shock at a shorter distance from the wave origin if compared to the case in which the fluid is at uniform temperature. Furthermore, this effect of enhanced nonlinear steepening is shown to decrease with increasing initial wave slopes. Compression waves evolving in a fluid for which  $\Gamma > 0$  are seen to be less influenced by the gradients of the medium properties owing to the lower sensitivity of these properties to temperature variations in this thermodynamic region.

The results of this study indicate that, contrary to intuition that temperature gradients can negatively impact nonclassical gasdynamic experiments aimed at measuring rarefaction shockwaves (RSW), a non-uniform temperature distribution can in fact enhance nonlinear steepening of the wavefront helping achieve a shorter shock formation distance. This is especially favorable for experimental setups such as shock tubes where maintaining a constant temperature can be difficult owing to the size of the system.



# Bibliography

- [1] N. B. Chandrasekaran, B. Mercier, and P. Colonna, “Nonlinear wave propagation in dense vapor of Bethe–Zel’dovich–Thompson fluids subjected to temperature gradients,” *Physics of Fluids*, vol. 33, no. 10, p. 107 109, Oct. 2021. DOI: [10.1063/5.0063226](https://doi.org/10.1063/5.0063226).
- [2] T. Mathijssen, “Experimental Observation of Non-Ideal Compressible Fluid Dynamics with application in Organic Rankine Cycle Power Systems,” Ph.D. dissertation, TU Delft, 2017.
- [3] R. F. Chisnell, “The normal motion of a shock wave through a non-uniform one-dimensional medium,” *Proceedings of the Royal Society of London. Series A. Mathematical and Physical Sciences*, vol. 232, no. 1190, pp. 350–370, Nov. 1955. DOI: [10.1098/rspa.1955.0223](https://doi.org/10.1098/rspa.1955.0223).
- [4] V. S. Soukkhominov, V. Y. Kolosov, V. A. Sheverev, and M. V. Ötügen, “Formation and propagation of a shock wave in a gas with temperature gradients,” *Journal of Fluid Mechanics*, vol. 473, pp. 245–264, Dec. 2002. DOI: [10.1017/s0022112002002380](https://doi.org/10.1017/s0022112002002380).
- [5] R. I. Sujith, G. A. Waldherr, and B. T. Zinn, “An exact solution for one-dimensional acoustic fields in ducts with an axial temperature gradient,” *Journal of Sound and Vibration*, vol. 184, no. 3, pp. 389–402, Jul. 1995. DOI: [10.1006/jsvi.1995.0323](https://doi.org/10.1006/jsvi.1995.0323).
- [6] H. Lin and A. J. Szeri, “Shock formation in the presence of entropy gradients,” *Journal of Fluid Mechanics*, vol. 431, pp. 161–188, Mar. 2001. DOI: [10.1017/s0022112000003104](https://doi.org/10.1017/s0022112000003104).
- [7] G. Russo, “Generalized wavefront expansion properties and limitations,” *Meccanica*, vol. 21, no. 4, pp. 191–199, Dec. 1986. DOI: [10.1007/bf01556485](https://doi.org/10.1007/bf01556485).
- [8] M. S. Cramer and A. Kluwick, “On the propagation of waves exhibiting both positive and negative nonlinearity,” *Journal of Fluid Mechanics*, vol. 142, pp. 9–37, May 1984. DOI: [10.1017/s0022112084000975](https://doi.org/10.1017/s0022112084000975).
- [9] M. S. Cramer and R. Sen, “Shock formation in fluids having embedded regions of negative nonlinearity,” *Physics of Fluids*, vol. 29, no. 7, p. 2181, 1986. DOI: [10.1063/1.865555](https://doi.org/10.1063/1.865555).

- [10] S. Muralidharan and R. I. Sujith, “Shock formation in the presence of entropy gradients in fluids exhibiting mixed nonlinearity,” *Physics of Fluids*, vol. 16, no. 11, pp. 4121–4128, Nov. 2004. DOI: [10.1063/1.1795272](https://doi.org/10.1063/1.1795272).
- [11] P. Colonna, N. R. Nannan, A. Guardone, and E. W. Lemmon, “Multiparameter equations of state for selected siloxanes,” *Fluid Phase Equilibria*, p. 19, 2006. DOI: [10.1016/j.fluid.2006.04.015](https://doi.org/10.1016/j.fluid.2006.04.015).
- [12] T. Mathijssen, M. Gallo, E. Casati, *et al.*, “The flexible asymmetric shock tube (FAST): a Ludwig tube facility for wave propagation measurements in high-temperature vapours of organic fluids,” *Experiments in Fluids*, vol. 56, no. 10, Oct. 2015. DOI: [10.1007/s00348-015-2060-1](https://doi.org/10.1007/s00348-015-2060-1).
- [13] P. Colonna, N. R. Nannan, and A. Guardone, “Multiparameter equations of state for siloxanes:  $[(\text{CH}_3)_3\text{Si-O}1/2]_2\text{-[O-Si-(CH}_3)_2]_i$ ,  $i=1,\dots,3$ , and  $[\text{O-Si-(CH}_3)_2]_6$ ,” *Fluid Phase Equilibria*, vol. 263, no. 2, pp. 115–130, Feb. 2008. DOI: [10.1016/j.fluid.2007.10.001](https://doi.org/10.1016/j.fluid.2007.10.001).
- [14] P. Colonna, A. Guardone, and N. R. Nannan, “Siloxanes: A new class of candidate Bethe-Zel’dovich-Thompson fluids,” *Physics of Fluids*, vol. 19, no. 8, p. 086 102, Aug. 2007. DOI: [10.1063/1.2759533](https://doi.org/10.1063/1.2759533).
- [15] R. Span, *Multiparameter Equations of State*. Springer Berlin Heidelberg, 2000. DOI: [10.1007/978-3-662-04092-8](https://doi.org/10.1007/978-3-662-04092-8).
- [16] P. Colonna, T. P. van der Stelt, and A. Guardone, *FluidProp (Version 3.1): A program for the estimation of thermophysical properties of fluids*, A computer program since 2004, 2019.
- [17] Y. Jing, T. Wang, and G. T. Clement, “A k-Space Method for Moderately Nonlinear Wave Propagation,” *IEEE Transactions on Ultrasonics, Ferroelectrics, and Frequency Control*, vol. 59, no. 8, pp. 1664–1673, Aug. 2012. DOI: [10.1109/tuffc.2012.2372](https://doi.org/10.1109/tuffc.2012.2372).
- [18] M. F. Hamilton and D. T. Blackstock, *Nonlinear Acoustics*. Academic Press, 1998.
- [19] A. A. Haigh, B. E. Treeby, and E. C. McCreath, “Ultrasound Simulation on the Cell Broadband Engine Using the Westervelt Equation,” in *Algorithms and Architectures for Parallel Processing*, Springer Berlin Heidelberg, 2012, pp. 241–252. DOI: [10.1007/978-3-642-33078-0\\_18](https://doi.org/10.1007/978-3-642-33078-0_18).

# 5

## A new setup and first experiments

### 5.1. Introduction

The aim of shock tube experiments on Bethe-Zel'dovich-Thompson (BZT) fluid flows is to provide evidence of the existence of nonclassical gas dynamics by detecting and measuring the speed of propagation of expansion waves in a quiescent dense organic vapor. The train of waves may coalesce into a rarefaction shock wave, which is arguably the most exotic nonclassical phenomenon. However, proving that rarefaction waves accelerate would suffice as a proof of the existence of nonclassical gas dynamics.

The wave Mach number  $M_w$  is defined as the ratio between the speed of propagation of a wave and the local speed of sound in the quiescent fluid. If  $M_w > 1$ , i.e., if the wavespeed is supersonic, then the wave is a nonclassical RSW, while a  $M_w \leq 1$  would be associated to a classical expansion fan, or an upstream or double sonic expansion wave [1].

In this chapter, a novel experimental facility named the Asymmetric Shock Tube for Experiments on Rarefaction waves (ASTER) is described. Results of preliminary rarefaction wave experiments performed with the test fluid D<sub>6</sub> are analysed in detail. A novel procedure to measure the speed of sound in the fluid at rest using the ASTER is also presented. Such challenging speed of sound measurements, especially at thermodynamic conditions at which nonclassical gasdynamics is expected, can be used to improve the thermodynamic modelling of the fluids of interest.

## 5.2. Design and working principle

The ASTER is a Ludwig-type tube designed to verify nonclassical gasdynamic effects in the dense vapours of organic fluids. The working principle of the ASTER is the same as that of the FAST (Section 3.3). However, the ASTER is simpler, smaller and makes use of the experience gained by trying to solve the many issues that affected the FAST over many years. A major difficulty with the FAST was its large size. Also, the FAST employed a very complex and fault-prone fast opening valve (FOV) which moreover has a significantly longer opening time if compared with a diaphragm. Since the shock formation distance is directly proportional to the opening time of the barrier element [2], the FAST required a long charge tube ( $\approx 9$  m). On the contrary, the ASTER is fitted with a glass-disk diaphragm that can open almost instantaneously, thus requiring a much shorter charge tube (CT).

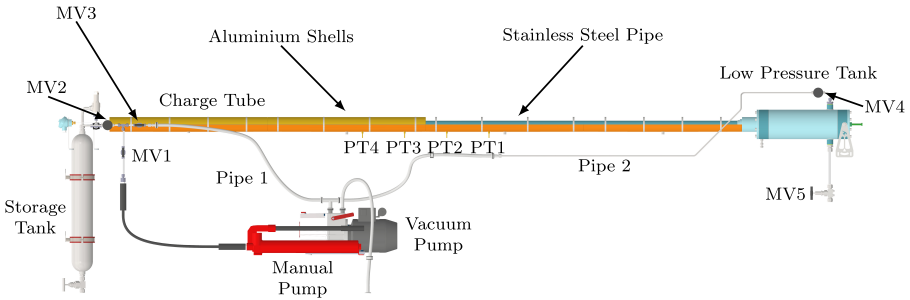


Figure 5.1: Schematic of of the ASTER setup.

Figures 5.1 and 5.2 show a schematic of the ASTER and a picture of the realized setup. The setup consists of a 3 m long stainless steel (316Ti) CT with an outside diameter  $D$  of 17.5 mm and thickness  $t$  of 2.35 mm. The radial dimension of the CT is similar to that in the FAST. Eight semi-cylindrical aluminium shells, each of length 750 mm, outside diameter of 35 mm and thickness of 17.5 mm, covers the stainless steel tube to favour a uniform temperature distribution along the setup (refer to Section 3.3.4).

The CT houses the hot, high pressure vapours of the working fluid  $D_6$  in case of nonclassical gasdynamic experiments. The working fluid is injected through the inlet port located on the left of the CT, see Fig. 5.3. The fluid is supplied by means of a HiForce HP110 hydraulic manual pump (see Fig. 5.10) which has a total volume of 1 L, a stroke length of 250 mm, and is capable of achieving pressures of up to 700 bar. The pump and the CT are connected via manual valves MV1 and MV2.

The other end of the CT is connected to the Low Pressure Tank (LPT), a



Figure 5.2: Picture of the ASTER setup.

1.1 litre stainless steel cylinder with a length of 345 mm, an outside diameter of 69.5 mm, and a thickness of 4 mm. The CT and the LPT are connected via a nozzle section. The nozzle creates a throat area to choke the flow, thereby preventing flow disturbances in the LPT from travelling upstream into the CT. A glass-disk placed at the exit of the nozzle separates the CT and the LPT. The LPT is kept at vacuum conditions in the beginning of the test; therefore, unlike the CT, its temperature homogeneity is not a requirement. For this reason, the LPT is not covered with aluminium shells.

Prior to the experiments, the setup is vacuumed to a minimum of 0.02 bar with the help of a Pfeiffer (Type Duo 5M) vacuum pump to remove any impurity in the setup. The vacuum pump is connected to the CT via Pipe 1 and manual valves MV2 and MV3, and to the LPT via Pipe 2 and manual valve MV4 (see Fig. 5.1). Once the setup is vacuumed, the fluid is filled into the CT using the hand pump where it is heated to the desired temperature and pressure (see Section 5.3.3). When the desired experimental conditions are reached, the glass disk is broken with a metal pin. The high pressure vapour contained in the CT expands into the LPT resulting in a rarefaction wave that propagates into the CT in the opposite direction of the flow. If the fluid states in the CT are in the nonclassical gasdynamic region [3], then this propagating wave should steepen into a rarefaction shock wave (RSW). The wave propagation speed can be measured with a time-of-flight method (see Section 5.3.4) using pressure transducers located along the CT.

After the completion of the experiment, the setup is allowed to cool down. The  $D_6$  that condenses in the LPT is extracted by opening manual valve MV5 at the bottom of the LPT, see Figure 5.1. A metallic filter placed within the LPT at the mouth of the outlet pipe ensures that glass pieces do not enter the outlet and block the flow of liquid  $D_6$ . The fluid collected in the CT is removed when the setup is heated and vacuumed during the next experiments.

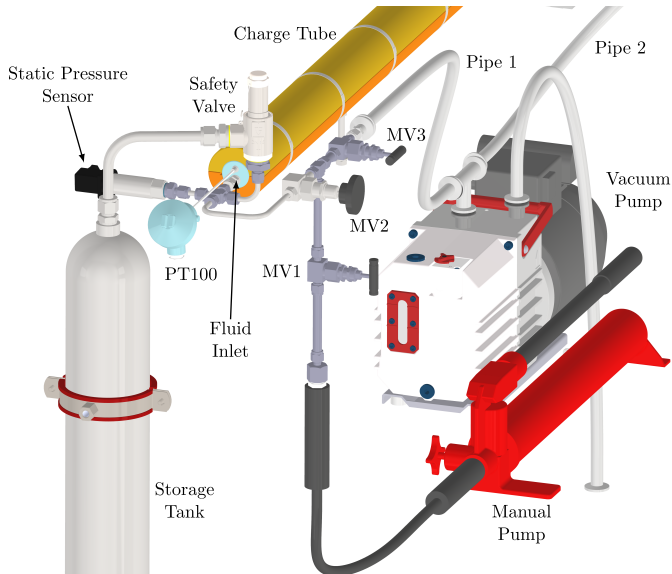


Figure 5.3: Close-up of the inlet-side end of the ASTER.

### 5.2.1. Diaphragm and rupture mechanism

Owing to the experiences gained with the FOV, the opening mechanism of the FAST, a diaphragm was chosen as a barrier element in the ASTER due to its simplicity and envisaged reliability. The disadvantage with respect to the FOV is that the LPT must be opened after every experiment to remove the debris and replace the diaphragm. Conventional shock tube designs make use of metallic diaphragms, often made of aluminium or copper, or of materials such as Mylar<sup>®</sup> (see Refs. [4]–[7]). Usually, diaphragms are designed to rupture spontaneously once a certain bursting pressure difference is exceeded. The thickness of the diaphragms is chosen based on calculations such that the diaphragm breaks at the desired pressure. A study of the diaphragm opening process by Rothkopf [2] showed that a thicker diaphragm capable of withstanding higher pressures also features a longer opening time. The authors studied the opening characteristics of several diaphragms made of different materials that were scored to facilitate the rupturing process. The results indicated that the opening of the diaphragm into petals along the score was neither simultaneous nor symmetric, although aluminium diaphragms performed better than those made of brass or copper. An incomplete opening of the diaphragm has a strong impact on the formation of a shock wave, as shown in the work of Gaetani *et al.* [8]. For these reasons and due to the relatively low pressure difference

typical of nonclassical gasdynamic experiments, it was decided to use a glass-disk diaphragm as a barrier element in the ASTER and to cause its rupture with an actuated mechanism. The benefits of using a glass-disk over conventional diaphragms are two-fold. Firstly, the compressive and tensile strengths of glass are sufficiently high to handle the range of pressures encountered in BZT experiments. Secondly, once a crack is initiated, the breaking of glass is almost instantaneous, and a complete opening can be achieved.

A 3.3 mm thick borosilicate glass-disk of diameter 50 mm is placed inside the LPT at the exit of the nozzle. The breaking of the glass-disk is achieved by means of the breaking mechanism shown in Figs. 5.4 and 5.5. The breaking pin consists of six drill bits of 8.5 mm diameter attached to a 320 mm long stainless steel rod that is mounted on a base of length 140 mm. The end of the base protrudes outside of the LPT. Two Kalrez<sup>®</sup> O-rings on the base ensure that the working fluid does not leak during experiments. To initiate an experiment, the end of the breaking pin is hit with a hammer such that the glass shatters in the shortest possible time. Once the experiment is finished, the end plate of the LPT is opened to remove the broken glass and a new glass-disk is placed. Although this mechanism requires opening the ASTER after each use, it allows for a quick and complete opening of the nozzle. It takes approximately half an hour to open the LPT, clean and replace the glass disk. This is still much less time than what was required with the FAST, where it took almost a whole day for the setup to cool, allowing the  $D_6$  to condense and run back into the Heated Fluid Tank (HFT) for reuse.

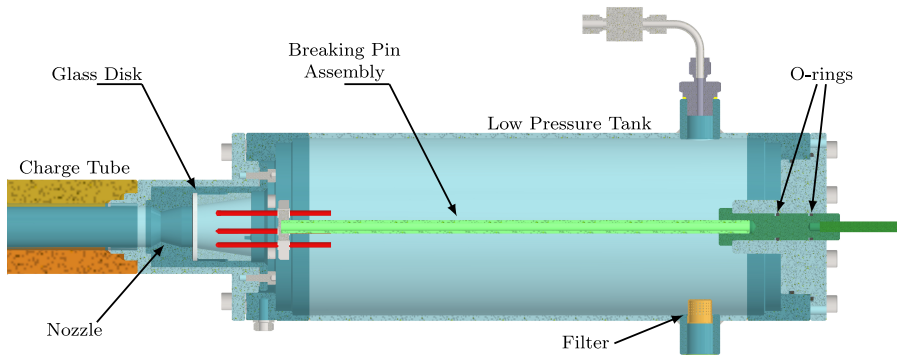


Figure 5.4: Cross-section view of the LPT showing the glass disk and the breaking pin assembly.



Figure 5.5: Photograph of the breaking pin assembly attached to the LPT end plate.

### 5.2.2. Instrumentation, data acquisition and control

5

The data is acquired using a National Instruments (NI) DAQ system. Lab-View, running on a computer connected to the DAQ, is used for monitoring and programming the control.

The data acquisition and monitoring for the experiment is achieved using a NI cDAQ 9189 chassis, which allows for a combination of different NI modules to measure digital and analog input/output (I/O) signals. The NI modules used for data acquisition in the ASTER, along with the instrument they are connected to, are listed in Table 5.1. The code containing the data acquisition and control algorithms is implemented into the *ASTER\_Manager* program, and is shown in Fig. 5.6.

The heating of the charge tube is achieved through two 1250 W glass-silk

Model	Type	Range	Channels	Instrument(s)
NI9264	Voltage Output	0 - 10V	16	Thyristors
NI9222	Voltage Input	0 - 10V	4	Dynamic pressure sensors
NI9203	Current Input	4 - 20mA	8	Static pressure sensor
NI9214	Temperature Input	-	16	Thermocouples
NI9217	Temperature Input	-	4	PT100

Table 5.1: Input or output modules installed in the National Instruments CompactDAQ 9189 chassis.



Figure 5.6: Graphical user interface of the *ASTER\_vi* LabView program, providing the operator with experiment data, monitoring and control information.

5



Figure 5.7: Thermocouple attached to the aluminum shell in the ASTER. The thermocouples are placed within a heat resistant fabric sheath to prevent any damage to the heating blankets.

heating jackets each with a 25 mm layer of insulation. The CT assembly is placed on sliding supports to allow for its thermal expansion at high temperatures, which is approximately 20 mm at 400 °C. The thermal energy supply to the facility is regulated using a PID control implemented in the *ASTER\_Manager* program. The voltage to the heating elements is supplied by RKC single-phase thyristors (THV-1PZ-020-5\*NN-6).

Temperature is the only controlled variable. The temperatures along the

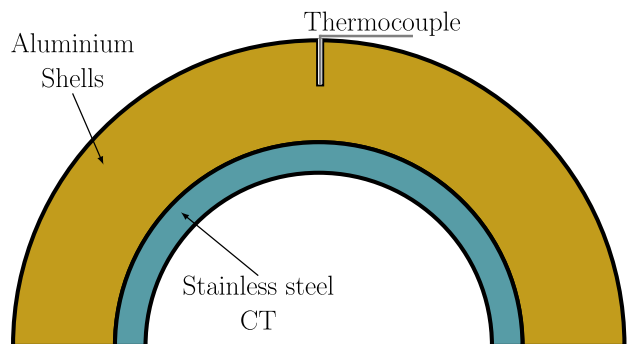


Figure 5.8: Schematic of the half-section view of the ASTER CT cross-section showing the placement of the thermocouple inside the aluminium shell.

## 5

CT are measured using eight 1 mm thick K-type thermocouples (TCs) placed equidistantly in the aluminium shells. The tips of the TCs are housed inside grooves drilled into the shells such that they lie within a few millimeters of the contact surface between the aluminium and the stainless steel. This ensures that the TCs provide a good estimate of the temperature at the surface of the CT and are not affected by the local wall temperature close to the blankets (see Figs. 5.7 and 5.8). Each blanket covers four TCs, and the average temperature of these four TCs is used as the process variable for the PID control of the corresponding blanket. A schematic of the temperature control system is shown in Fig. 5.9.

The LPT is heated using a 300 W glass-silk jacket with a 25 mm insulation layer. The blanket only partially covers the LPT to make way for piping connections at the end of the vessel. A built-in PT100 measures the temperature of the blanket, which is used as the process variable to control the LPT's temperature. The vessel is heated to the same setpoint as the CT in order to minimise temperature gradients across the nozzle.

PT100 sensors are located in the thermal blankets covering the CT too, but their measurements are used only for monitoring purposes and are not a part of the control system. The temperature of the working fluid inside the CT is measured using a PT100 placed at the inlet-side end, as shown in Fig. 5.3. To prevent the leaking of the working fluid through the probe connections, the PT100 is not placed in direct contact with the fluid. Instead, it is housed in a 135 mm long stainless steel thermowell that protrudes into the CT and is welded onto the CT endplate. The thermocouples and the PT100 sensor in contact with the fluid are calibrated with the Fluke 9100S dry-well calibrator with a rated accuracy of  $\pm 0.5$  K.

The static pressure of the fluid in the CT is measured by a Druck UNIK 5000 ref. X5072-TB-A2-CA-H1-PA sensor with a specified accuracy of  $\pm 0.1\%$

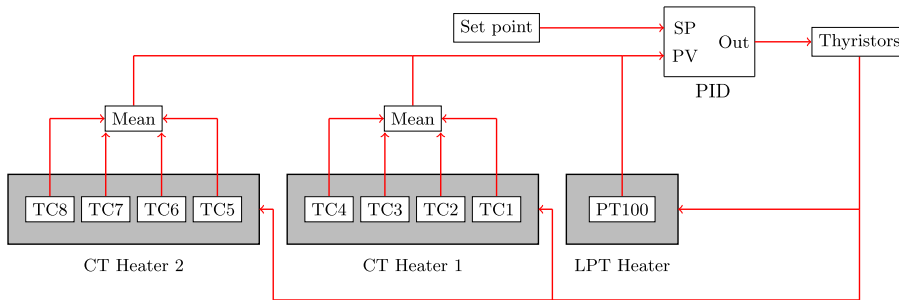


Figure 5.9: Schematic of the temperature control logic. PV and SP in the PID block stand for process variable and set point, respectively.

over the full range of 16 bar. This sensor, however, is rated for a maximum temperature of only 80 °C and is therefore mounted on the inlet pipe connecting MV-2 and the CT (see Fig. 5.3), away from direct contact with the hot vapour. The voltage for this sensor is supplied using the RS IPS2303 multiple output linear DC power supply. A safety release valve rated for 16 bar is also fitted at the location to prevent any unexpected surge in the fluid pressure. The outlet of the safety valve is connected to a collection tank with a volume of 4 liters to store the escaped fluid.

Four dynamic pressure transmitters PT1-PT4 (Kulite XTEH-10L-190SM-300PSI-A) are flush mounted along the CT at distances of 1.2, 1.4, 1.6 and 1.8 m from the nozzle throat, respectively (see Fig. 5.1). These sensors have a full scale of 21 bar and a frequency of 250 kHz, and can withstand temperatures up to 500 °C. The sensors suffer from significant drift of the calibration constant with temperature, but are suitable for recording fast-changing fluid pressure like those occurring in a shock tube. The signals are scaled after each experiment using the more accurate measurement from the static pressure transmitter. The 5-100 mV signals of the dynamic pressure sensors are amplified using a custom-built amplifier with a gain of 120 and are connected to the NI9222 module.

## 5.3. Experiments

### 5.3.1. Leak-tightness Characterization

The presence of oxygen and moisture dissolved in the working fluid or adsorbed on the containment metal are known to promote decomposition at high temperatures [9]. It is, therefore, of utmost importance that leakages in the setup, especially at low-pressure conditions when air can enter the CT, are avoided.

A series of leak tests were performed with air as the test fluid to assess the leak rate of the facility. The tightness of the setup is characterized using the average leak rate, defined as  $LR = V\Delta P \Delta t^{-1}$ , where  $V$  is the volume of the setup ( $\sim 0.0032 \text{ m}^3$ ), and  $\Delta p$  is the rise/drop in pressure measured after a time interval of  $\Delta t$ .

At vacuum conditions, a LR of  $2.2 \times 10^{-4} \text{ mbar}\cdot\text{l}\cdot\text{s}^{-1}$  was measured (air leaking into the system). Leakage tests at superatmospheric pressures conducted at different temperatures by filling the setup with air were consistently below  $5 \times 10^{-4} \text{ mbar}\cdot\text{l}\cdot\text{s}^{-1}$  (air escaping the setup). A similar leak-tightness characterization conducted on the FAST yielded a leak rate of  $5 \times 10^{-4} \text{ mbar}\cdot\text{l}\cdot\text{s}^{-1}$  under vacuum conditions and  $5 \times 10^{-2} \text{ mbar}\cdot\text{l}\cdot\text{s}^{-1}$  under superatmospheric conditions. Despite having leak-rates higher than that measured in the ASTER, no appreciable change in the composition of  $\text{D}_6$  was observed in the FAST up to temperatures of  $300 \text{ }^\circ\text{C}$ . Therefore, the leak-tightness of the ASTER is deemed satisfactory for the intended experiments.

## 5

### 5.3.2. Working Fluid Preparation

Siloxane  $\text{D}_6$  was chosen as the working fluid for experiments due to its high thermal stability, low levels of both flammability and toxicity for humans, and the larger size of the nonclassical thermodynamic region predicted by state-of-the-art thermodynamic models [10] compared to other fluids made of complex molecules. The fluid was produced by Dow Corning and is certified to be 97.4% pure [11]. Unfortunately, it was not possible to procure  $\text{D}_6$  of a higher degree of purity at the time of the experiments. The primary properties of the pure fluid are summarized in Table 5.2 and the composition of the fluid sample according to the analysis of the supplier is shown in Table 5.3.

It is important that moisture dissolved in the fluid is removed prior to heating since its presence can adversely affect the thermal stability of the fluid [9]. Dissolved water is removed by letting the fluid sit in a container with  $3 \text{ \AA}$  molecular sieve desiccants for several days. The presence of incondensable gases in the CT can also adversely affect the outcome of the experiments. This

Fluid name	CAS Number	MW (kg/kmol)	$P_c$ (bar)	$T_c$ ( $^\circ\text{C}$ )	$\nu_c$ ( $\text{m}^3/\text{kg}$ )
$\text{D}_6$	540-97-6	444.92	372.6	9.61	0.0036

Table 5.2: Relevant thermophysical properties of the working fluid  $\text{D}_6$  [10]. MW is the molecular weight,  $P_c$ ,  $T_c$ , and  $\nu_c$  are the critical pressure, temperature and specific volume respectively.

is because these gases have sound speeds much higher than that of  $D_6$  which would reduce the accuracy of both sound speed and wavespeed measurements. Since the CT is open and exposed to the atmosphere in between tests, such gases can get adsorbed onto the inner walls of the stainless steel pipe. They are therefore removed by vacuuming the CT multiple times as it is heated to the desired temperature prior to filling the CT with  $D_6$ .

### 5.3.3. Start-up Procedure

Before conducting an experiment, valves MV-1,-4 and -5 (see Figs. 5.1 and 5.3) are closed and the CT and LPT are vacuumed to remove residual gases present in the setup. The CT is heated to the desired setpoint temperature. The vacuuming of the setup is repeated at different temperatures to remove gases that are released as the setup heats up. The CT and the LPT are then isolated by closing valves MV-2,-3 and -4. The setup is now ready to be filled with the working fluid.

The procedure of filling the CT with the required amount of the working fluid  $D_6$  is referred to as *charging*. Unlike the FAST, the ASTER contains no external tank to heat the fluid to the necessary initial conditions before filling the CT with the vapours of the fluid. Here, heating of the liquid is done directly in the CT. A shortcoming of the design of the ASTER is that, once the glass disk is placed inside the LPT and the setup is sealed, there is no outlet port to release the pressure in the setup or to evacuate liquid  $D_6$ , except for a safety release valve in case of over-pressure conditions. Thus, it is important that the correct quantity of the fluid required to reach the chosen initial conditions is filled into the CT prior to the experiments.

Since the fluid is filled with a pump, the flow is discontinuous thus making

Component	CAS Number	MW (kg/kmol)	Mole fraction (%)
$D_6$	540-97-6	444.92	97.374
$D_5$	541-02-6	370.77	1.667
$D_7$	107-50-6	519.07	0.458
$D_4$	541-05-9	222.46	0.066
$D_3$	556-67-2	296.64	0.039

Table 5.3: Composition of the  $D_6$  supply based on the analysis provided by the manufacturer.



Figure 5.10: Manual pump used for charging the CT; the measuring jar is connected to the pump through the inlet port.

## 5

it impossible to measure the volume of the injected fluid using a flow meter. This volume is instead measured with the help of a measuring jar attached to the inlet port of the pump. The hand pump and the measuring jar setup are shown in Fig. 5.10.

To estimate the volume of the fluid pumped into the CT, the density of liquid  $D_6$  is first estimated by measuring the weight of the liquid at different volumes. Also, the density of fluid at the desired experimental conditions is computed using the best available thermodynamic model of the fluid [12]. Given that the internal volume of the CT is known, the volume of liquid  $D_6$  that needs to be filled in the tube is calculated as,

$$V_{\text{liq}} = \frac{V_{\text{CT}} \cdot \rho_{\text{CT}}}{\rho_{\text{liq}}} \quad (5.1)$$

where the subscripts liq and CT denote liquid and charge tube respectively.  $V_{\text{liq}}$  provides an initial estimate of the minimum volume of  $D_6$  needed for the experiment.

Before the CT is charged, the pump cylinder is completely filled with  $D_6$ , a sufficient amount is added to the measuring jar and the initial level in the jar is recorded. The fluid is then pumped with valve MV-1 closed so that  $D_6$  in the tubing is slightly pressurized. MV-1 is then opened such that the fluid now fills the manifold connecting valves MV-1 to MV-3. The level of the fluid in the measuring jar drops slightly, and this new level is recorded. MV-2 is now opened thereby allowing  $D_6$  to be siphoned into the CT that is in vacuum conditions. If the temperature of the CT is higher than the boiling point of  $D_6$  (250 °C at 1 bar), then the pressure in the CT rapidly increases due to the evaporating fluid. The volume of fluid that has entered the CT is estimated by recording the new level of the fluid in the jar. If this volume is lower than

that estimated using Eq. (5.1), then the remaining fluid is pumped into the CT using the hand pump. Once the CT is filled with sufficient  $D_6$ , MV-2 is closed and the experiment can be conducted.

#### 5.3.4. Finite-amplitude Wave Speed Measurements

A series of rarefaction tests were performed in  $D_6$  with the aim of measuring the speed of propagation of the wave and estimating the local value of the fundamental derivative of gasdynamics  $\Gamma$ . The initial thermodynamic state in the charge tube was set at different temperatures and pressures for which gas dynamic phenomena are expected to range from non-ideal to nonclassical.

The speed of the propagating wave in the CT is measured with the so-called *time-of-flight (ToF) method*. The pressure drop across the expansion wave is measured by the pressure sensors PT1 to PT4 placed 20 cm apart from each other. The wave speed  $w$  is then calculated as

$$w = \frac{L_T}{\Delta t}, \quad (5.2)$$

where  $L_T$  is the distance between any sensor pair at temperature  $T$ , and  $\Delta t$  is the time difference between the instants at which the head of the wave arrives at the sensor pairs. The distance  $L_T$  accounts for the thermal expansion of the metal of the charge tube and is estimated as

$$L_T = L_{T_0}(1 + \alpha(T - T_0)) \quad (5.3)$$

where  $L_{T_0}$  is the reference length between any two sensor pairs, and  $\alpha = 17.52 \times 10^{-6} / \text{K}$  is the thermal expansion coefficient of stainless steel 316Ti. To accurately estimate the wavespeed, it is necessary to also measure the reference length  $L_{T_0}$  accurately. However, this is challenging for two reasons: first, the sensors are located at the bottom of the CT, and second, the heads of the sensors themselves are situated deep within the aluminum shells. Distance  $L_T$  is therefore evaluated by measuring the propagation speed of a small amplitude wave in air. Such a wave, which is devoid of any nonlinear effects, propagates at the local speed of sound in air for which accurate data are available in the literature (see Refs. [13]–[16]). Therefore, by measuring the delay in the time of arrival,  $\Delta t$ , of an acoustic wave at the different pressure sensor pairs, the distance  $L_{T_0}$  between them can be found with Eq. (5.2) as

$$L_{T_0} = c_{\text{air}} \cdot \Delta t. \quad (5.4)$$

This measurement was conducted in dry air at 7.78 bar and 37 °C, and the local speed of sound in these conditions was estimated using the reference mul-

tiparameter EoS model for air [17]. Table 5.4 shows the computed distances between sensor pairs.

The pressure signals are smoothed using a gaussian-weighted moving average to reduce the noise. This is followed by the identification of the relevant section of the smoothed signal over which the method can be applied. The moment when the head of the wave crosses the sensor,  $t_{\text{head}}$ , is determined by identifying the time when the pressure deviates from the CT pressure by more than 15 mbar. This deviation is sufficient to exceed the residual signal noise level. The time when the tail of the wave occurs,  $t_{\text{tail}}$ , is chosen as the expected time when the head of the wave reaches the end of the CT from the first sensor. To compute this time, the speed of sound,  $c$ , as predicted by the thermodynamic model at the experimental initial conditions is used. Therefore, it follows that

$$t_{\text{tail}} = t_{\text{head}} + \frac{\Delta x}{c}, \quad (5.5)$$

where  $\Delta x$  is the distance between PT1 and the end of the CT ( $\approx 1.8$  m). The relevant section of the signal then spans from  $P_{\text{head}}$  to  $P_{\text{tail}}$ .

### Uncertainty Analysis

The uncertainty associated with the wave speed estimation  $u(w)$  (Eq. (5.2)) includes contributions from the separation distance  $u(L_T)$  and from the uncertainty related to the time interval  $u(\Delta t)$  for the shock to pass over the transducers. Assuming that the individual contributions of the sensors are unrelated, the overall uncertainty in the wavespeed is given by,

$$u(w) = \sqrt{\left(\frac{\partial w}{\partial L_T} u(L_T)\right)^2 + \left(\frac{\partial w}{\partial \Delta t} u(\Delta t)\right)^2}. \quad (5.6)$$

	$c_{\text{model}}$ (m/s)	$l_{12}$ (m)	$l_{23}$ (m)	$l_{34}$ (m)
$L$	351.99	0.200625	0.200625	0.198865

Table 5.4: Distances between the Kulite sensors computed using speed of sound measurements in air; the subscripts stand for the corresponding sensor pairs.

The uncertainty in the separation distance  $L_T$  can be written as,

$$u(L_T) = u_{L,\alpha} + u_{\text{loc}}, \quad (5.7)$$

where  $u_{L,\alpha}$  is the uncertainty due to thermal expansion arising from the uncertainty in temperature and the value of the thermal expansion coefficient  $\alpha$ , and  $u_{\text{loc}}$  is the uncertainty in the location of the centres of the holes made for the pressure sensors in the tube. It can also happen that the location of the maximum response of the pressure sensor and its geometric centre are not coincident [18], [19]. In this case, the orientation of the pressure sensor can influence wavespeed measurements and can introduce uncertainty. Though the distance between these two points was not directly measured, this uncertainty is already included in the distance measurements shown in Table 5.4.

The standard uncertainty in the distance between sensor pairs is estimated using a uniform probability distribution having a half-width of  $u_{\text{loc}} = 0.001$  m. The uncertainty due to thermal expansion, deriving from Eq. (5.3), is written as

$$u_{L,\alpha} = \sqrt{\left(\frac{\partial L}{\partial T}u(T)\right)^2 + \left(\frac{\partial L}{\partial \alpha}u(\alpha)\right)^2}. \quad (5.8)$$

The total uncertainty  $u(L_T)$  is then,

$$u(L_T) = \sqrt{\left(\frac{\partial L}{\partial T}u(T)\right)^2 + \left(\frac{\partial L}{\partial \alpha}u(\alpha)\right)^2} + 0.001, \quad (5.9)$$

where  $u(T)$  is the uncertainty in the temperature (mentioned in Section 5.2.2) and  $u(\alpha)$  the uncertainty in the thermal expansion coefficient. The value of  $u(\alpha)$  is taken to be 5% based on a review of the available data for the measured expansion coefficients of stainless steel 316Ti [18]. The uncertainty in the wave arrival times at the location of the pressure transducers is estimated using a normal probability distribution with a width equal to the sampling frequency of the sensors, which results in  $u(\Delta t) = 4 \cdot 10^{-6}/2$  s.

### Thermodynamic State of the Quiescent Fluid

The most suitable fluid thermodynamic state for a shock tube experiment would be one in which the Mach number  $M_w$  of the propagating RSW is maximum, as proposed by Guardone *et al.* [20]. In that study, the authors determined  $M_w$  using three different thermodynamic models, including the state-of-the-art multiparameter EoS [10], and estimated it to vary between

1.023 and 1.072. However, these thermodynamic models suffer from large uncertainties, especially in the region where nonclassical gasdynamic effects can be expected [21]. For example, values of the speed of sound in  $D_6$  estimated using the multiparameter EoS have been verified with experimental data only in the liquid phase due to a lack of availability of measurements in the gas phase [22]. Even these data suffer from uncertainties of up to 30% [10]. Although recent soundspeed measurements performed by the author of this dissertation in the nonclassical gasdynamic region, see Chapter 6, have achieved an accuracy of 0.22%, these results have not yet been incorporated in the thermodynamic model of the fluid. Since  $\Gamma$  is a quantity derived from sound speed, the uncertainty in its prediction is also very high.

Despite such large uncertainties, the initial conditions of the experiments are chosen based on the predictions of the multiparameter EoS [10], [12]. Table 5.5 shows the initial conditions along with the predicted thermodynamic properties of the rarefaction experiments performed using  $D_6$  in the ASTER. The location of these initial conditions in the  $P-v$  plane is shown in Fig. 5.11. Prior to performing experiments in the possible BZT region, tests were also conducted with the fluid in mildly non-ideal gasdynamic states to demonstrate the correct operation of the setup and to validate the time-of-flight (ToF) procedure to measure wavespeed.

5

Test No.	$P_0$ (bar)	$T_0$ (°C)	$\Gamma_{\text{model}}$ (-)	$Z$ (-)	$c_{\text{model}}$ (m/s)
1	2.66	349.8	0.86	0.86	93.35
2	2.89	300.3	0.73	0.78	80.64
3	5.85	357.6	0.59	0.68	72.76
4	8.87	370.9	0.096	0.48	48.18
5	8.96	369.6	-0.052	0.46	43.08
6	9.33	372.1	-0.013	0.43	39.8
7	9.37	370.7	6	0.21	42.5
8	9.4	371.97	0.023	0.41	36.55

Table 5.5: Thermodynamic conditions of the initial states of the rarefaction experiments.  $\Gamma$ ,  $Z$  and  $c$  are estimated using the multiparameter EoS model [17]. For test 7, the model predicts that the fluid is in the liquid state, hence a  $\Gamma$  of 6.

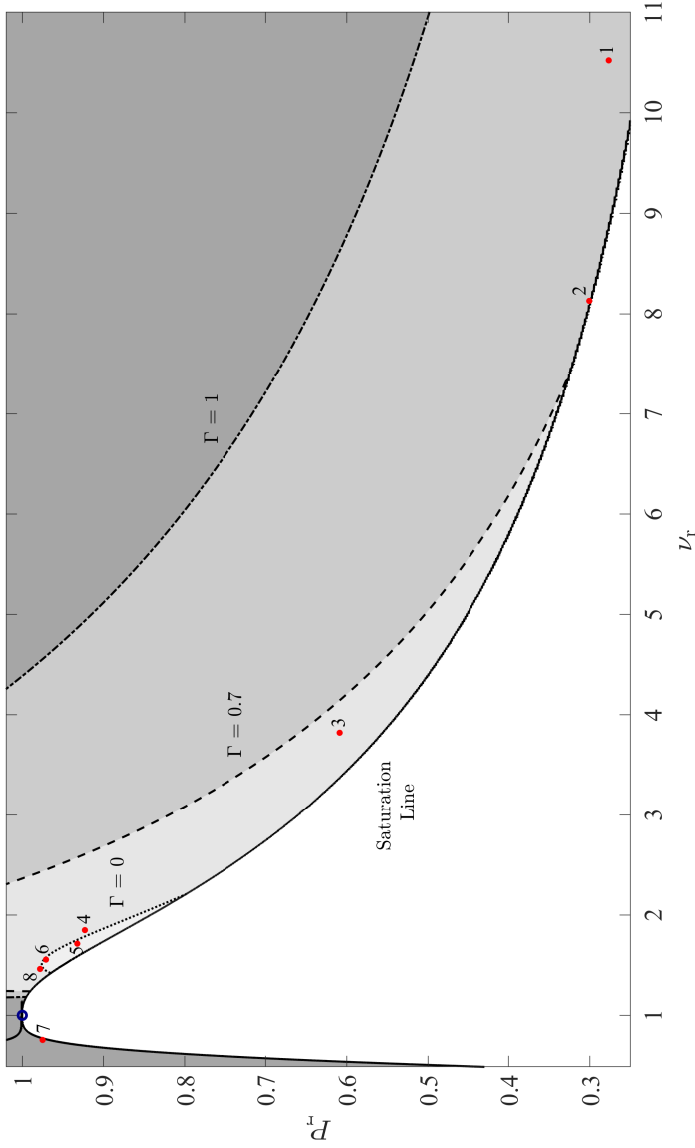


Figure 5.11:  $P_r$ - $0_r$  diagram of D6. (●) Thermodynamic states at which rarefaction tests were performed, see Table 5.5. (—) Vapour-liquid equilibrium (VLE) line; (○) critical point.

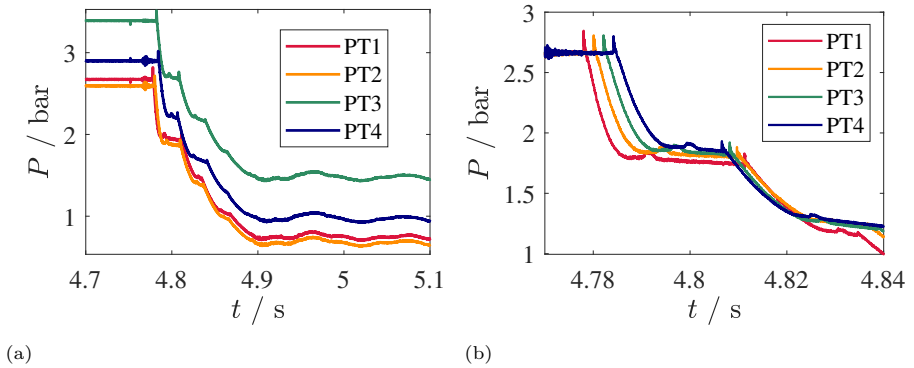


Figure 5.12: Test No. 1, see Table 5.5: pressure recorded by the high-frequency Kulite pressure sensors (PT1 to PT4 in Figure 5.1). (a) Raw signals. Significant drift of the signals can be observed. (b) Pressure signals scaled using the static pressure measurement (see *Static Pressure Sensor* in Figure 5.3).

## 5

### Expansion with the fluid initially in a mildly non-ideal thermodynamic state

The mildly non-ideal gasdynamic region includes fluid states that feature values of the fundamental derivative  $\Gamma$  between 0.7 and 1. In this gasdynamic regime, all flow variables exhibit similar changes as in a fluid where  $\Gamma > 1$ , except for the sound speed, which decreases across a compression and increases across an expansion. However, flows in this gasdynamic region share qualitative similarities with those evolving in ideal gases and can therefore be referred to as *classical*.

The pressure recordings from Test 1 (refer to Table 5.5 and Fig. 5.11) are shown in Fig. 5.12. Despite being scaled at the beginning of the experiments, the fast-response Kulite sensors suffer from significant drift in the offset. This can be seen in Fig. 5.12a: PT3 measures 0.5 bar above the static pressure of 2.66 bar measured by the static pressure sensor providing the value identifying the thermodynamic state of the fluid in the CT. In order to apply the ToF method, these signals are scaled using the static pressure sensor reading so as to obtain the same value at the instant of the opening of the diaphragm. The corrected signals are shown in Fig. 5.12b.

The pressure signals also contain significant noise that arises from the electrical interference with the cables of the heating blankets. Furthermore, in Fig. 5.12b, a distinct peak is evident at the wave's leading edge. This peak is attributed to the temporary compression of the glass disk resulting from the impact of the hammer, which is subsequently transferred to the dense vapors of the fluid just before the disk shatters. This noise is removed through the procedure described in Section 5.3.4. The signal window of the filtered pressure

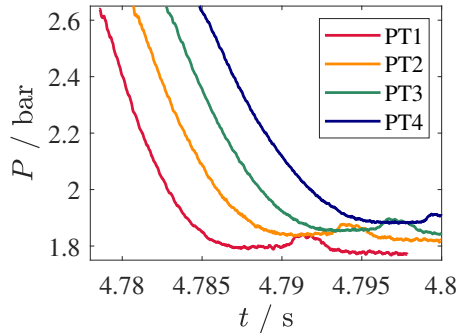


Figure 5.13: Relevant signal window of the filtered pressure recordings from Test No. 1 (see Table 5.5). This portion of the pressure recording is used to compute the wavespeed using the time-of-flight method.

recordings is shown in Fig. 5.13. The time-of-flight (ToF) method is applied to these signals to estimate the wavespeed. Figures 5.14a and 5.14b show the wave propagation speed determined using the ToF method for Test 1 using sensor pairs PT1-PT2 and PT1-PT4, respectively. To limit noise, a zero-phase, sixth order Butterworth digital filter is applied to the estimated wavespeed values. The plots also display the wavespeed for a shock-free isentropic expansion for comparison. The wavespeed values are computed according to Eq. (5.10) using the multiparameter EoS.

The model-estimated wavespeed decreases monotonically as the pressure across the wave drops, as expected under these fluid thermodynamic conditions. The same trend is observed in the measured wavespeed. Interestingly, the wavespeeds estimated using non-adjacent sensor pairs (PT1 and PT4) exhibit a smaller deviation from the theoretical value than those obtained from adjacent sensors (PT1 and PT2). The reason for this discrepancy is still being investigated at the time of writing. Additionally, despite the use of a filter, residual oscillations persist in the signal and are observed in the computed wavespeeds.

A significant deviation from the theoretical wavespeed value can be observed in Fig. 5.14c for the wavespeed estimated using sensors PT2 and PT3. One possible reason for this deviation could be the presence of local temperature gradients along the CT inner surface between these sensors. PT2 and PT3 are located on either side of the junction between the two thermal blankets covering the CT. Local cold spots may be expected in this region.

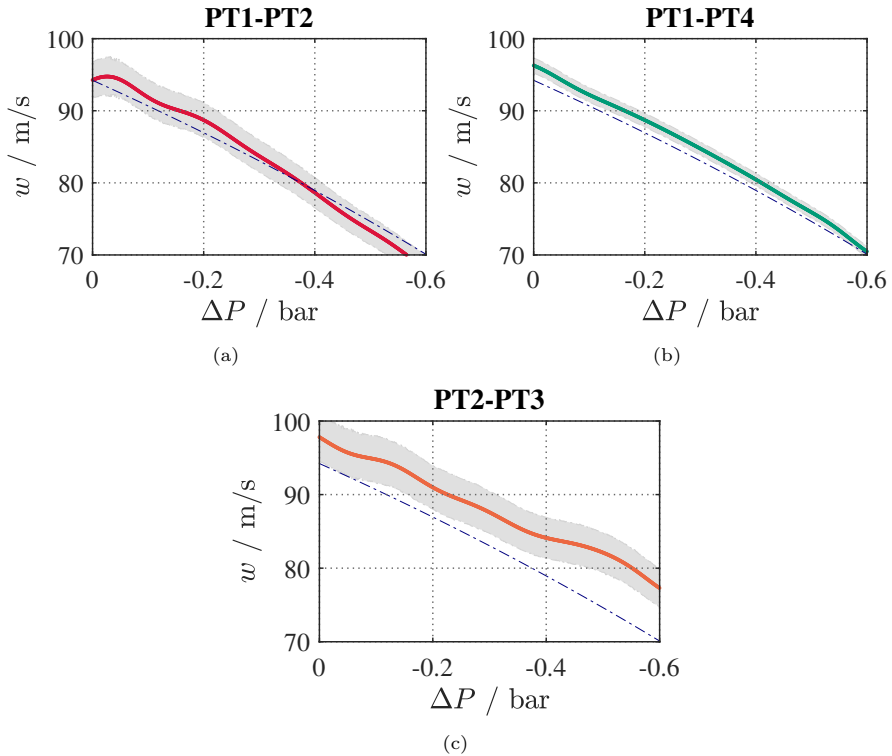


Figure 5.14: Wavespeed estimates obtained with the time-of-flight method using the pressure signals of sensors (a) PT1 and PT2 (b) PT1 and PT4 and (c) PT2 and PT3 (pressure intervals of 15 mbar). Data are taken from Test 1 (see Table 5.5). The blue dashed line represents the wavespeed calculated using a multiparameter equation of state thermodynamic model for  $D_6$  [10] and Eq. (5.10) which is valid for an isentropic shock-free expansion flow. Uncertainty bands on the wavespeed are shown in grey.

### Expansion with the fluid initially in a dense vapour thermodynamic state in proximity of the vapor-liquid critical point

Figure 5.15 shows the sections of the pressure signal used to estimate the wavespeed using the time-of-flight method applied to data acquired during Test No. 7 (see Table 5.5). Compared to the pressure signals of Test No. 1 under mildly non-ideal thermodynamic conditions (see Fig. 5.13), the pressure recordings exhibit a steeper and a larger drop. Additionally, the signals display an abrupt change of the pressure gradient occurring close to the head of the wave. A similar variation was observed in the signals recorded during ideal-gas experiments performed with the FAST facility, as discussed in Section 3.3.2. However, in the ASTER, this abrupt change of the pressure gradient appears

only in the pressure signals obtained during experiments performed in the dense-vapour thermodynamic conditions. This suggests that this signal feature is possibly related to a gasdynamic effect rather than one caused by an interaction of the fluid with a mechanical component, such as the breaking pin or a geometric irregularity of the CT, as was suspected in case of the FAST experiments.

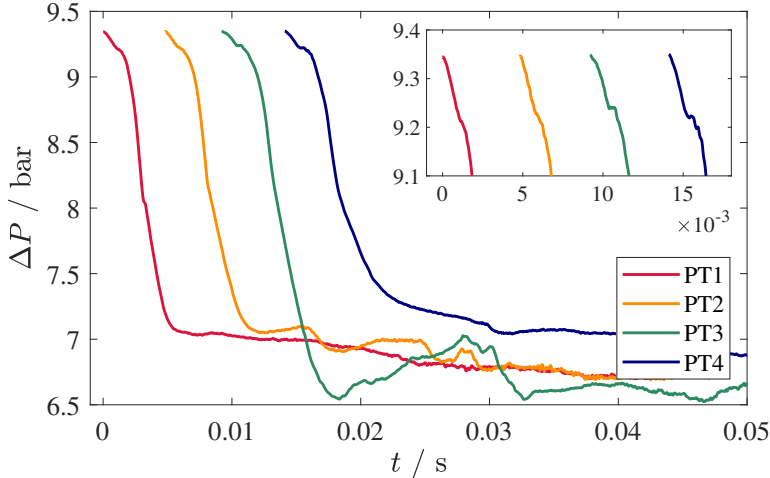


Figure 5.15: Relevant signal window of the filtered pressure recordings from Test No. 7 (see Table 5.5). This portion of the pressure recording is used to compute the wavespeed using the time-of-flight method. (Inset) Close-up of the head of the wave showing an abrupt change in the pressure gradient.

The initial thermodynamic state of the fluid for Test No. 7 was chosen to have a slightly higher pressure than that of states within the nonclassical gasdynamic region in the  $P - v$  plane, as predicted by the state-of-the-art multiparameter EoS model.  $\Gamma$  is predicted to be lower than zero for states defined by a narrow range of pressures and temperatures (approximately  $358 < T < 372$  °C and  $7.4 < P < 9.3$  bar for  $D_6$ ). However, as discussed in Section 2.5, the admissibility region for rarefaction shocks, the so-called rarefaction shock region (RSR), extends beyond states in which  $\Gamma < 0$ .

Instead of attempting to initiate an expansion wave from a thermodynamic state within the  $\Gamma < 0$  region, which is challenging to achieve and maintain, it is relatively easier to reach thermodynamic conditions within the larger RSR. This can maximise the chances of observing a RSW in the flow. The flow-field would therefore feature a rarefaction that starts from a thermodynamic state for which  $\Gamma > 0$ , proceeds through fluid states characterized by negative values of  $\Gamma$  thus displaying nonclassical gasdynamic features, and further evolves to

fluid states for which  $\Gamma$  is positive, thus forming a so-called mixed wave flow field, see [23]. This flow field corresponds to the isentropic expansion from point 1 to point 4 as displayed in the  $P - v$  diagram of Fig. 2.6.

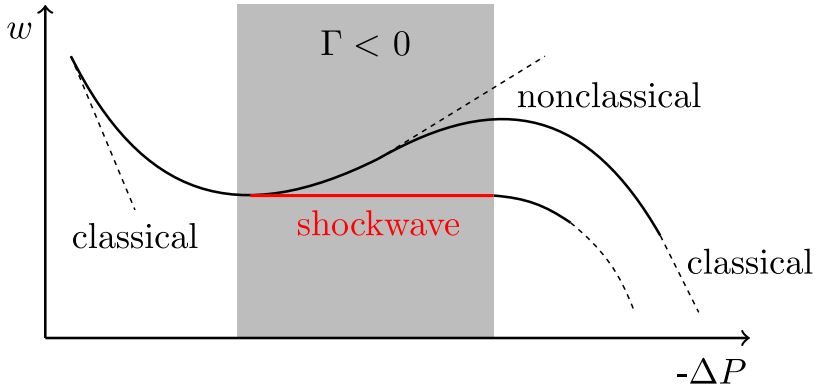


Figure 5.16: Schematic representation of the variation in wavespeed with pressure drop across a wave undergoing an unsteady expansion through a region of negative  $\Gamma$ .

5

The relationship between the wavespeed  $w$  and the pressure drop  $-\Delta P$  across a nonclassical mixed-wave expansion is qualitatively represented in Fig. 5.16. Two cases are depicted: one is related to an isentropic rarefaction whereby no shockwave forms, and the other in which a rarefaction shockwave (RSW) coalesces as a result of expansion waves propagating at increasing speeds throughout the medium. In the isentropic flow case, the wavespeed decreases with an associated pressure drop if the fluid states feature  $\Gamma > 0$ , and increases if the fluid states are characterized by  $\Gamma < 0$ . If a RSW is formed, the wavespeed initially decreases if the fluid states are in the positive- $\Gamma$  domain but remains constant once a shockwave is formed, since the shock moves at a constant supersonic speed. Once the fluid expands to a state in which  $\Gamma$  is again positive, the wavespeed continues to decrease with  $-\Delta P$  in the classical sense.

The opening time of the glass disk is expected to be similar to that of a diaphragm, which is less than 1ms [24]–[26]. Studies have shown that even if the diaphragm does not open completely, a single normal shock is already formed at a distance of about 20 times the length of throat diameter  $D$  from the diaphragm location [8]. Given that the first pressure sensor PT1 is located  $60D$  away from the nozzle, see Fig. 5.1, it is possible that a fully developed RSW can be observed at this location, assuming the quiescent fluid is in a thermodynamic state featuring  $\Gamma < 0$ .

Figures 5.17a and 5.17b show the variation in estimated wavespeed with pressure drop, computed using sensor pairs PT1-PT2 and PT1-PT4, respec-

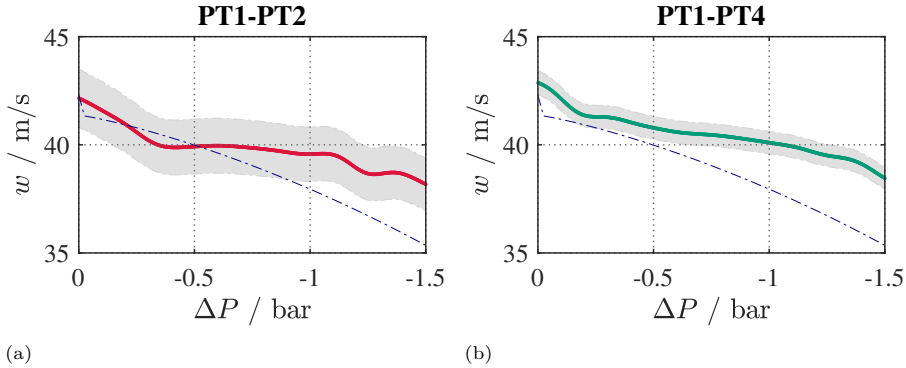


Figure 5.17: Wavespeed estimates obtained with the time-of-flight method using the pressure signals of sensors (a) PT1 and PT2 (b) PT1 and PT4 (pressure intervals of 15 mbar). Data are taken from Test 1 (see Table 5.5). The blue dashed line represents the wavespeed calculated using a multiparameter equation of state thermodynamic model for  $D_6$  [10] and Eq. (5.10) which is valid for an isentropic shock-free expansion flow. Uncertainty bands on the wavespeed are shown in grey.

tively. Consistent with the variation of  $w$  with  $\Delta P$  shown in Fig. 5.16, the wavespeed initially decreases with decreasing  $\Delta P$  since the initial conditions are predicted to be in the  $\Gamma > 0$  region. Close to a  $\Delta P$  of approximately -0.5 bar, the wavespeed remains nearly constant and independent of  $\Delta P$ , indicating the possible presence of a RSW in the flow. This behaviour extends until a  $\Delta P$  of approximately -1 bar, after which the wavespeed continues to decrease with pressure drop. For  $\Delta P > -1$  bar, the flow no longer features negative- $\Gamma$  values, and the expansion is again “classical”.

Such regions of relative flatness and independence from  $\Delta P$  are more clearly visible in Fig. 5.17a than in Fig. 5.17b. For the wavespeed computed using sensors PT1-PT4, the slope of  $w$  is still lower in the range of  $\Delta P$  between approximately -0.2 bar and -1.1 bar than in other regions, but it is not as flat as observed in Fig. 5.17a. However, unlike the monotonic decrease in the wavespeeds observed in Figs. 5.14a and 5.14b, the wavespeed estimated using PT1-PT4 exhibits weak dependence on pressure for values of  $\Delta P$  between -0.2 bar and -1 bar, thereby demonstrating strong non-ideal characteristics.

### 5.3.5. Estimation of $\Gamma$

The fundamental derivative of gas dynamics,  $\Gamma$ , is related to the local wave speed, density, and sound speed through [27]

$$\Gamma = \mathcal{Z} \left. \frac{dw}{dp} \right|_s. \quad (5.10)$$

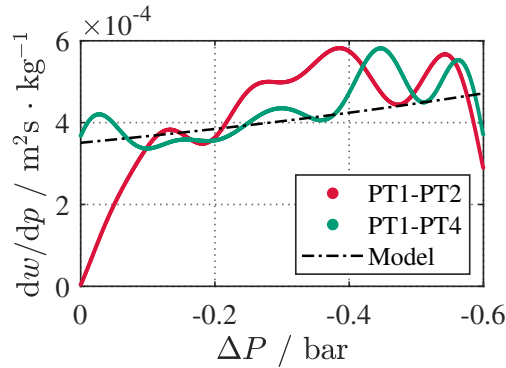


Figure 5.18: Derivative of wavespeed with respect to pressure drop for sensor pairs PT1-PT2 and PT1-PT4 for Test 1.

## 5

Here,  $Z = \rho c$  is the *acoustic impedance*. The value of  $dw/dp$  can be obtained by numerically differentiating the wave speed evaluated using the Time-of-Flight (ToF) method. To obtain an estimate of  $\Gamma$ , knowledge of the local values of  $\rho$  and  $c$  is also necessary. Since these quantities are not directly measured in the CT, it is not possible to obtain the value of  $\Gamma$  as a function of the pressure drop across the wave. Instead, the experimental value of  $dw/dp$  is compared with that obtained using the thermodynamic model of the fluid. Since both  $\rho$  and  $c$  are positive quantities, the sign of  $dw/dp$  is also the sign of  $\Gamma$ . Equation 5.10 is valid only along an isentrope, since  $dw/dp = 0$  across a rarefaction shock wave. Thus, if the estimated value of  $dw/dp$  is constant and zero, this can indicate the presence of a nonclassical shock in the flow-field.

Figure 5.18 displays the derivative of the wavespeed, which is computed using adjacent (PT1-PT2) and non-adjacent sensor pairs (PT1-PT4) with respect to the pressure drop for Test No. 1 (refer to Table 5.5). This derivative is estimated using central differences for the interior points and single-sided differences at the boundaries. The figure also shows the value of  $dw/dp$  computed using the multiparameter EoS model. The oscillations of the values of  $dw/dp$  are most likely residual low wavenumber oscillations which fall below the cutoff wavenumber of the filter and are then amplified by differentiation. Similar to what is observed in Figs. 5.14a and 5.14b, the estimate of  $dw/dp$  from PT1-PT4 is less affected by oscillations and shows better accordance with the values predicted by the thermodynamic model. Despite these oscillations, the experimental values and the values computed with the help of the thermodynamic model are in satisfactory agreement. It can also be observed that  $dw/dp$  is positive and increases with the pressure drop associated with the wave, thereby reaffirming that the expansion is evolving in a fluid whose states are in the mildly non-ideal gasdynamic region.

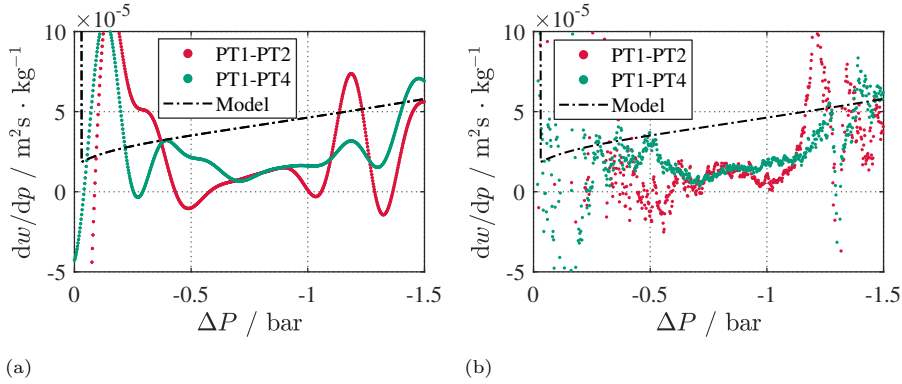


Figure 5.19: Derivative of wavespeed with respect to the pressure drop obtained from the signals recorded by sensor pairs PT1-PT2 and PT1-PT4 for Test No. 7. The derivatives are computed using (a) filtered wavespeed measurements and (b) unfiltered wavespeed measurements. The estimation of the wavespeed derivative obtained with the help of the thermodynamic model is shown as a black dashed line.

Figure 5.19 displays the derivative of the wavespeed, computed using sensor pairs PT1-PT2 and PT1-PT4, with respect to the pressure drop across the wave for Test 7 performed in the dense-vapour region of  $D_6$  (see Table 5.5). Oscillations similar to those observed in Fig. 5.18 arise due to the filtering of the wavespeed signal, especially close to the head and tail of the wave. Nonetheless,  $dw/dp$  increases with decreasing  $\Delta P$  until it reaches approximately -0.5 bar (as expected if  $\Gamma > 0$ ). For  $-0.5 \leq \Delta P \leq -1$  bar, it displays a region of near-constant value, consistent with the observations made in Fig. 5.17. Beyond  $\Delta P \approx -1$  bar,  $dw/dp$  once again increases to follow the trend of the model data.

Figure 5.19b shows the derivative estimated using the unfiltered wavespeed signals from the two sensor pairs.  $dw/dp$  is almost constant and close to 0 for  $\Delta P$  values between -0.5 bar and -1 bar. Since according to theory,  $dw/dp$  and  $\Gamma$  are constant and zero across a RSW, these values of  $dw/dp$  obtained from measurements shown in Figs. 5.19a and 5.19b suggest the occurrence of non-classical gasdynamic effects, and even possibly the propagation of a rarefaction shock wave. For all other values of  $\Delta P$ , the values of  $dw/dp$  obtained from the measurements closely follows the predictions of the model indicating that the flow evolves with the fluid in states belonging to the positive- $\Gamma$  domain.

Although here for brevity only results of a single experiment starting with the fluid in a dense-vapour thermodynamic state is presented, other test results with the fluid in similar states (in or near the predicted negative- $\Gamma$  region) are reported in Appendix A, namely those pertaining to Test No. 4 to 8, see Table 5.5. All these tests led to values of  $dw/dp$  obtained from measurements

that are almost constant and close to zero. It can therefore be inferred that these observed nonclassical gasdynamic phenomena are associated with the non-ideal thermodynamic property variation of dense vapor flows of complex organic molecules, which, apart from some uncertainties that still demand for further investigation, are largely in agreement with the theory of nonclassical gasdynamics.

### 5.3.6. Sound speed measurements

The ASTER was primarily designed and built to measure rarefaction waves and provide the first proof of the existence of nonclassical gasdynamics and possibly rarefaction shockwaves. However, the versatility of the setup also permits the measurement of the local speed of sound in the quiescent fluid, which, especially at elevated temperatures and pressures, is challenging, and experimental data are scarce or unavailable for the vast majority of complex organic compounds. Sound speed measurements are useful not only as auxiliary information for verifying the formation of rarefaction shockwaves but also for improving state-of-the-art thermodynamic models which rely on extensive, accurate thermodynamic data for robust fluid property modeling.

A small-amplitude wave propagating in a quiescent fluid travels at the local speed of sound and is not affected by nonlinear effects. Measuring the speed of this wave allows to estimate the local sound speed. To generate a small-amplitude wave using the ASTER, one approach is to fill both the CT and the LPT with dense vapors of  $D_6$ , ensuring only a slight pressure difference across the glass disk. Once the disk is broken, a wave of small amplitude corresponding to the pressure difference between the CT and the LPT would propagate into the CT. The speed of this wave can be computed using the time-of-flight method discussed in Section 5.3.4. However, this method requires a large amount of fluid for each test, with no option to reuse it due to contamination from air, moisture, and glass particles. Moreover, using a glass disk necessitates opening the setup after every test to clean and replace the disk, leading to increased downtime between experiments and exposing the inner surfaces to contaminants.

A better method that allows to avoid such difficulties consists in using a metallic disk having a diameter of 50 mm and a thickness of 3 mm in place of the glass disk, and in generating a small amplitude wave by just hitting the metallic disk. This method allows for repeated measurements of the speed of sound without the need of opening the CT. To ensure that the metallic disk is not damaged, the breaking-pin mechanism was also modified. The six sharp drill bits used for breaking the glass disk are removed and replaced with a rod featuring a blunt edge, as shown in Fig. 5.20.

To perform a measurement, the end of the breaking-pin is gently struck

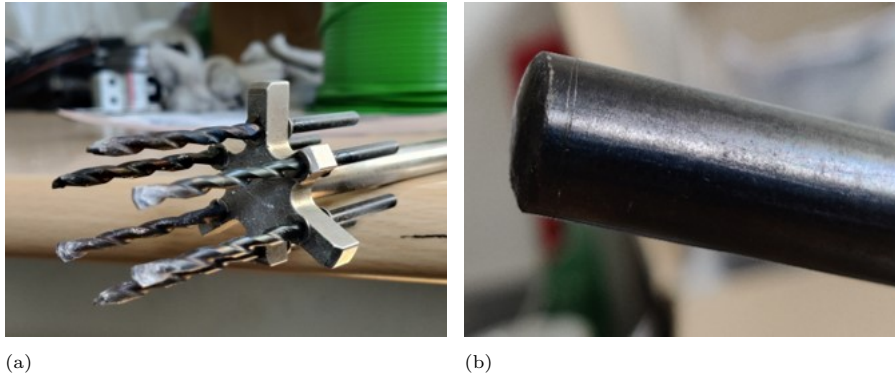


Figure 5.20: (a) Six 8 mm drill bits at the head of the breaking-pin rod used to shatter the glass-disk (b) Modified excitation system showing blunt edge of the rod that is used during sound speed measurements.

with a hammer, as done for the rarefaction tests, but with less force. This generates a weak, small-amplitude wave in the CT that travels back and forth as it reflects off the end-walls of the CT and the metallic disk. These pressure variations are recorded using Kulite pressure sensors and are used to calculate the local speed of sound.

Similar to rarefaction tests, the local sound speed in the fluid can be estimated using equation Eq. (5.2). The only difference is that the time difference between the arrival of the wave at any two sensors,  $\Delta t$ , is computed using cross-correlation instead. The cross-correlation (CC) technique has the advantage of being less sensitive to noise and utilizing all the information contained in the signals to produce a maximum value at the time delay between the two signals [28].

Figure 5.21a displays an interval of the pressure signals recorded by the Kulite sensors during a sound speed measurement test in  $D_6$  at 3.12 bar and 309.5 °C. Each peak in the figure corresponds to the propagation of a weak wave along the CT generated by a light hammer strike on the metal disk at intervals of approximately 2 seconds. The natural decay of the waves due to viscous effects is made evident by the decreasing amplitude following each peak. Figure 5.21b provides a close-up of one of the wave packets, namely the one occurring at  $\approx 5.7$  sec. The first quartet of pressure signals with the highest amplitude corresponds to the wave propagating from the disk as a result of the hammer strike, while each of the subsequent quartets correspond to reflected waves as they travel back and forth within the CT. Therefore, the order of the pressure signals in Fig. 5.21b is reversed for every quartet.

A series of experiments was conducted at different temperatures and pressures to measure the local speed of sound in  $D_6$ . The thermodynamic states

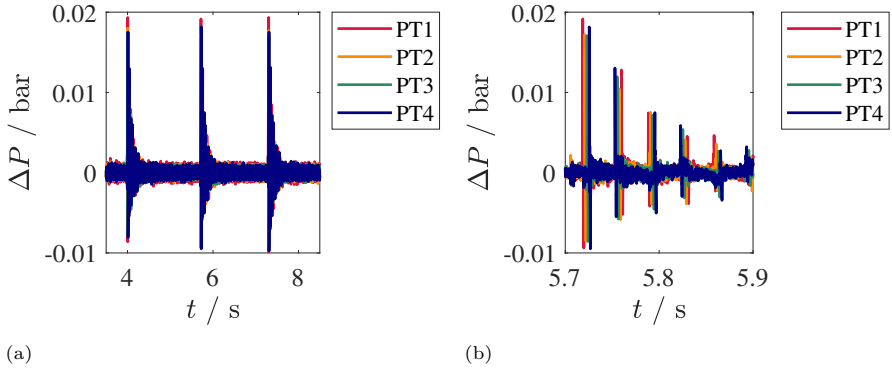


Figure 5.21: (a) Exemplary pressure recordings of the propagation of acoustic waves along the CT during a speed of sound measurement test using  $D_6$  as working fluid. The quiescent fluid is at  $P = 3.12$  bar and  $T = 309.5$  °C Each peak represents a small-amplitude wave generated by a light hammer strike of the metallic disk. (b) Close-up of one wave packet showing the pressure signals of the initial and the reflected waves.

## 5

at which the sound speed was measured are displayed in a  $P_r$ - $T_r$  diagram in Fig. 5.22, together with the VLE line, the critical point and the negative- $\Gamma$  region. The values of the sound speed measurements performed at those thermodynamic states are listed in Table 5.6. The uncertainty in the speed of sound measurement  $u(c)$  that arises from the uncertainties in pressure  $u(P)$  and in temperature  $u(T)$ , discussed in Section 5.2.2, is estimated as

$$u(c) = \sqrt{\left(\left.\frac{\partial c}{\partial P}\right|_{T_0} u(P)\right)^2 + \left(\left.\frac{\partial c}{\partial T}\right|_{P_0} u(T)\right)^2}. \quad (5.11)$$

The deviation (DEV) between the experimentally measured sound speed values  $c_{\text{exp}}$  and those predicted by the thermodynamic model  $c_{\text{model}}$  [12], [30], defined as,

$$DEV = 100 \cdot \left(\frac{c_{\text{exp}} - c_{\text{model}}}{c_{\text{model}}}\right), \quad (5.12)$$

is also reported in Table 5.6. At low pressures (i.e., in Tests No. 1 to 4), the thermodynamic model consistently underestimates the speed of sound by between 2.6% and 2.8%. Anticipating the results presented in Chapter 6, the experimental speeds of sound measured in the OVAR in similar conditions were up to 1.5 % higher than that predicted by the thermodynamic model. The incorrect estimation of the sound speed by the thermodynamic model likely arises from the large uncertainties present in the estimation of the ideal-gas

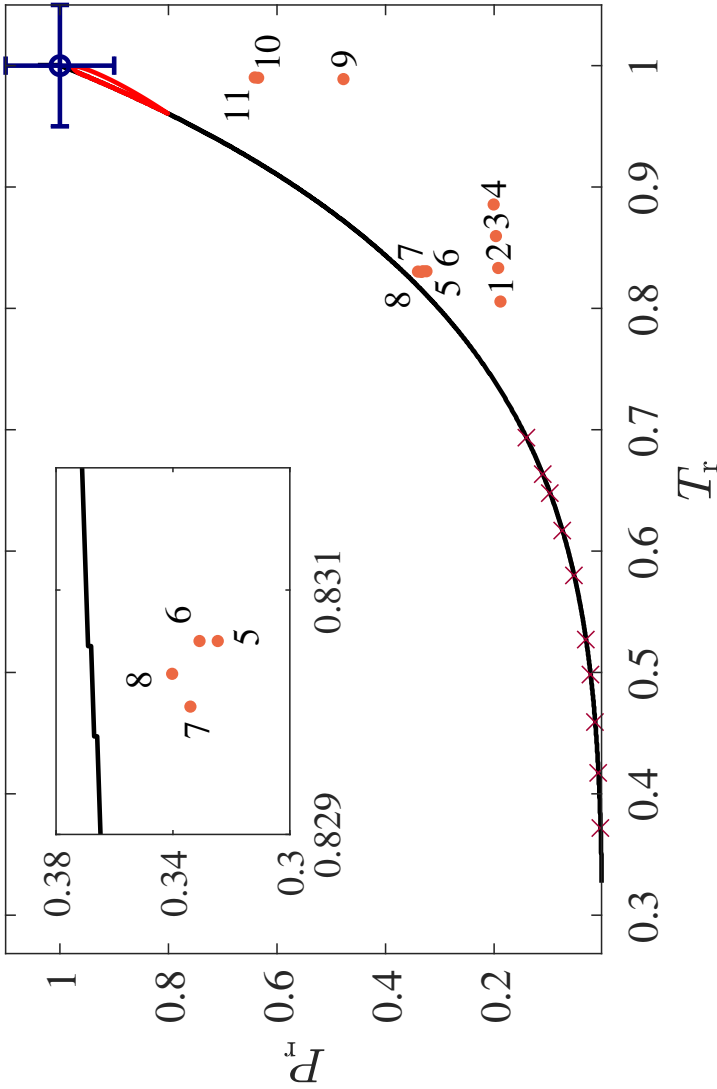


Figure 5.22:  $P$ - $T$  diagram of D6. (•) Thermodynamic states at which the speed of sound was measured, see Table 5.6. (—) Vapor-liquid equilibrium (VLE) line; (—)  $T = 0$  line; (⊙) critical point and its associated uncertainties. (Inset) Close-up of fluid states in Tests 5 to 8. Lines and data for the critical point are obtained with the multiparameter EoS model documented in [10]. (x) The only available experimental VLE data [29] that were fitted for the development of the thermodynamic model are also shown.

heat capacity  $c_{p,0}$  of  $D_6$  that is used as an input for the model (data obtained from the work of Nannan *et al.* [31]).

In Tests 5 to 8, the deviation between  $c_{\text{exp}}$  and  $c_{\text{model}}$  increases to between 6.5% and 8%. This deviation further increases to approximately 8.5% in Tests 10 and 11, with the exception of Test 9. The increase in deviation is associated with a decrease in the value of  $\Gamma$ , which highlights the shortcomings of the thermodynamic model in accurately predicting the speeds of sound in  $D_6$  under thermodynamic states where strong non-ideal or nonclassical gasdynamic effects can be expected.

In addition to the large uncertainties in the ideal-gas heat capacity  $c_{p,0}$  of  $D_6$ , there is an additional error arising from the incorrect prediction of  $P$ - $v$ - $T$  data and the vapor-liquid equilibrium (VLE) curve in these particular states. For example, the construction of the VLE or saturation line in the multiparameter equation of state (EoS) model involves fitting experimental data to the Wagner-Ambrose equation and extrapolating it up to the critical point (refer to Fig. 5.22). However, due to the scarcity of experimental data

## 5

No.	$P$ (bar)	$T$ (°C)	$Z$ (-)	$\Gamma$ (-)	$c_{\text{exp}}$ (m/s)	$u(c)$ (m/s)	DEV (%)
1	1.81	300.2	0.87	0.86	98.72	0.85	2.72
2	1.85	310.5	0.88	0.87	95.16	0.26	2.66
3	1.89	320.2	0.88	0.88	96.59	0.74	2.68
4	1.93	330.1	0.89	0.88	98.06	0.69	2.84
5	3.12	309.5	0.78	0.72	87.1	1.04	6.62
6	3.18	309.5	0.78	0.72	86.38	1.05	6.61
7	3.21	309.3	0.77	0.71	86.55	1.07	7.4
8	3.27	309.4	0.77	0.70	86.42	1.08	7.79
9	4.59	368.5	0.78	0.77	88.41	0.67	3.35
10	6.1	368.9	0.69	0.65	82.36	0.84	8.67
11	6.16	369	0.69	0.65	81.92	0.84	8.62

Table 5.6: Experimental values of speed of sound  $c$  in  $D_6$  as a function of temperature  $T$  and pressure  $P$ .  $u(c)$  and  $DEV$  denote the uncertainty in the wavespeed and the deviation between the experimentally measured and model predicted sound speed values, respectively. Thermodynamic states numbering correspond to the states indicated on Fig. 5.22.

available for the critical conditions of  $D_6$ , these values have been estimated based on those of lighter siloxanes. Colonna *et al.* [10] report uncertainties of 10% for the critical pressure, 5% for the critical temperature, and 25% for the critical density. These uncertainties, determined somewhat arbitrarily by DIPPR, are likely too large and may contribute to the challenges encountered in accurately predicting the fluid properties in these states.

The presence of impurities in the fluid can also contribute to the measurement of higher-than-predicted speeds of sound. There are two types of impurities: first, those that are already contained in the fluid sample (refer to Table 5.3), and the second from the decomposition of the fluid at higher temperatures releasing incondensable gases. It is possible to estimate the effect of such impurities on the predicted speed of sound by using the thermodynamic model for such mixtures.

Future experiments should be designed to cover a wider range of thermodynamic states and account for the presence of impurities. These new measurements would provide valuable data to refine the characterization of fluid properties of the working fluid and enhance the accuracy of its thermodynamic model. The following chapter presents the results from the first such measurements performed in the dense-vapor thermodynamic region of  $D_6$ .

## 5.4. Conclusions

A novel shock-tube facility for the study of nonclassical gasdynamic flows has been designed, realized and successfully commissioned at TU Delft. This facility, called the Asymmetric Shock Tube for Experiments on Rarefaction Waves (ASTER), is an evolution of a previous setup, the FAST, and is specifically designed to generate and detect rarefaction shock waves (RSWs) in fluids made of complex organic molecules. The fluid used for commissioning and first experiments is siloxane  $D_6$ . The ASTER can withstand pressures and temperatures of up to 15 bar and 400 °C. The triggering mechanism is either a glass disk equipped with a breaking mechanism for rarefaction shock waves, or a metal disk that generates an acoustic perturbation when hit, for sound speed measurements. The experiment conceived to detect nonclassical gasdynamic phenomena consists in determining whether a propagating rarefaction disturbance is supersonic by comparing it with the local speed of sound in the fluid. If this is the case, it can be argued that a rarefaction shock wave has formed.

A series of rarefaction tests were performed with  $D_6$  in thermodynamic states ranging from mildly non-ideal to the strongly non-ideal in the dense-vapour region. The wavespeed of the propagating rarefaction was estimated using a time-of-flight (ToF) method from recordings of fast-response pressure sensors. These wavespeed measurements were used to derive the value of the

fundamental derivative of gasdynamics,  $\Gamma$ .

Experiments conducted with the fluid in dense-vapor states have revealed a propagation pattern that qualitatively differs from tests performed at lower pressures and temperatures. Notably, the wave speed does not exhibit a monotonic decrease with the pressure drop across the wave. Instead, it remains constant within specific ranges of  $\Delta P$ , indicating the presence of a nonclassical RSW in the flow field. This behavior is also reflected in the variation of  $dw/dp$  with  $\Delta P$ , which represents the fundamental derivative  $\Gamma$ . The observed constant, near-zero value of  $dw/dp$  within ranges of  $\Delta P$  further supports the existence of a RSW. Additionally, an abrupt change in the pressure gradient near the leading edge of the wave is observed exclusively in the dense gas tests. While the underlying cause of this phenomenon remains undetermined, its occurrence solely in dense-vapor conditions implies that it is a gasdynamic phenomenon.

The availability of accurate sound speed data is important not only to verify the formation of RSWs but, more importantly, also for the improvement of state-of-the-art thermodynamic models for such organic compounds. The ASTER was modified by replacing the glass disk with a metallic disk to perform stand-alone measurements of sound speeds at various thermodynamic states. The results obtained from both types of measurements demonstrated that the experimental values of sound speed were consistently higher than the predictions of the thermodynamic model by approximately 2.5% to 2.8% for states with temperatures up to 330°C. Notably, this deviation increased significantly to up to 8.6% for states within the dense-vapor thermodynamic region, highlighting the presence of substantial uncertainties in the fluid's thermodynamic model. Consequently, further experimental measurements of sound speed are necessary to enhance and optimize the existing model.

A conclusive evidence for the existence of RSWs would be to observe the wavespeed increasing at lower pressures in a rarefaction wave, rather than simply observing the RSWs themselves. To achieve this, further experiments in the thermodynamic states encompassing the BZT region are required. The success of such gasdynamic experiments is also incumbent on the accuracy of the thermodynamic model that predicts the extent, in terms of pressure and temperature, of the BZT region. These models rely on the availability of accurate gasdynamic data which are scarce for complex organic molecules. Further measurements of the soundspeed, especially at high reduced pressures at temperatures, are therefore planned to help optimise and improve the thermodynamic models for siloxane D<sub>6</sub>, and eventually, for other complex organic molecules as well.

In order to conclusively prove the existence of nonclassical gasdynamic effects, a more thorough investigation of flows evolving in the dense-vapour thermodynamic regime is required. This involves both improving the ther-

hydrodynamic model and enhancing the ability to set precise initial conditions for experiments. The goal would be to calculate the state that maximizes the desired effect using an accurate model and replicate that state in the experimental setup. Additionally, it is also important to study the impact of impurities in the fluid sample on rarefaction propagation and sound speed, potentially purifying the sample if necessary. Investigating the presence of axial or radial temperature gradients in the ASTER and their influence on wave propagation through simulations and experimental studies is also required.



# Bibliography

- [1] N. R. Nannan, “Advancements in nonclassical gas dynamics,” Ph.D. dissertation, TU Delft, 2009.
- [2] E. M. Rothkopf, “Diaphragm opening process in shock tubes,” *Physics of Fluids*, vol. 17, no. 6, p. 1169, 1974. DOI: [10.1063/1.1694860](https://doi.org/10.1063/1.1694860).
- [3] N. R. Nannan, C. Sirianni, T. Mathijssen, A. Guardone, and P. Colonna, “The admissibility domain of rarefaction shock waves in the near-critical vapour–liquid equilibrium region of pure typical fluids,” *Journal of Fluid Mechanics*, vol. 795, pp. 241–261, Apr. 2016. DOI: [10.1017/jfm.2016.197](https://doi.org/10.1017/jfm.2016.197).
- [4] R. S. Tranter, K. Brezinsky, and D. Fulle, “Design of a high-pressure single pulse shock tube for chemical kinetic investigations,” *Review of Scientific Instruments*, vol. 72, no. 7, pp. 3046–3054, Jul. 2001. DOI: [10.1063/1.1379963](https://doi.org/10.1063/1.1379963).
- [5] L. Houas, G. Jourdan, L. Schwaederlé, R. Carrey, and F. Diaz, “A new large cross-section shock tube for studies of turbulent mixing induced by interfacial hydrodynamic instability,” *Shock Waves*, vol. 12, no. 5, pp. 431–434, Mar. 2003. DOI: [10.1007/s00193-002-0173-y](https://doi.org/10.1007/s00193-002-0173-y).
- [6] T. Furukawa, T. Aochi, and A. Sasoh, “Expansion Tube Operation with Thin Secondary Diaphragm,” *AIAA Journal*, vol. 45, no. 1, pp. 214–217, Jan. 2007. DOI: [10.2514/1.23846](https://doi.org/10.2514/1.23846).
- [7] G. K. Nambiar, M. Sriram, M. Dharanidhar, P. G. Nair, and S. R. Nagaraja, “Design and Fabrication of hand operated mini Shock Tube,” *IOP Conference Series: Materials Science and Engineering*, vol. 225, p. 012025, Aug. 2017. DOI: [10.1088/1757-899x/225/1/012025](https://doi.org/10.1088/1757-899x/225/1/012025).
- [8] P. Gaetani, A. Guardone, and G. Persico, “Shock tube flows past partially opened diaphragms,” *Journal of Fluid Mechanics*, vol. 602, pp. 267–286, Apr. 2008. DOI: [10.1017/s0022112008000815](https://doi.org/10.1017/s0022112008000815).
- [9] G. Angelino and C. Invernizzi, “Cyclic Methylsiloxanes as Working Fluids for Space Power Cycles,” *Journal of Solar Energy Engineering*, vol. 115, no. 3, pp. 130–137, Aug. 1993. DOI: [10.1115/1.2930039](https://doi.org/10.1115/1.2930039).
- [10] P. Colonna, N. R. Nannan, and A. Guardone, “Multiparameter equations of state for siloxanes: [(CH<sub>3</sub>)<sub>3</sub>Si-O<sub>1</sub>/2]<sub>2</sub>[O-Si-(CH<sub>3</sub>)<sub>2</sub>]<sub>i</sub>=1,...,3, and [O-Si-(CH<sub>3</sub>)<sub>2</sub>]<sub>6</sub>,” *Fluid Phase Equilibria*, vol. 263, no. 2, pp. 115–130, Feb. 2008. DOI: [10.1016/j.fluid.2007.10.001](https://doi.org/10.1016/j.fluid.2007.10.001).

- [11] D. Chemicals, *XIAMETER™ PMX-0246 Cyclohexasiloxane*.
- [12] P. Colonna, T. P. van der Stelt, and A. Guardone, *FluidProp (Version 3.1): A program for the estimation of thermophysical properties of fluids*, A computer program since 2004, 2019.
- [13] G. S. K. Wong, “Speed of sound in standard air,” *The Journal of the Acoustical Society of America*, vol. 79, no. 5, pp. 1359–1366, May 1986. DOI: [10.1121/1.393664](https://doi.org/10.1121/1.393664).
- [14] O. Cramer, “The variation of the specific heat ratio and the speed of sound in air with temperature, pressure, humidity, and CO<sub>2</sub> concentration,” *The Journal of the Acoustical Society of America*, vol. 93, no. 5, pp. 2510–2516, May 1993. DOI: [10.1121/1.405827](https://doi.org/10.1121/1.405827).
- [15] K. N. Huang, C. F. Huang, Y. C. Li, and M. S. Young, “High precision, fast ultrasonic thermometer based on measurement of the speed of sound in air,” *Review of Scientific Instruments*, vol. 73, no. 11, pp. 4022–4027, Nov. 2002. DOI: [10.1063/1.1510576](https://doi.org/10.1063/1.1510576).
- [16] A. Yavuz, “Measuring the speed of sound in air using smartphone applications,” *Physics Education*, vol. 50, no. 3, pp. 281–284, Apr. 2015. DOI: [10.1088/0031-9120/50/3/281](https://doi.org/10.1088/0031-9120/50/3/281).
- [17] E. W. Lemmon, I. H. Bell, M. L. Huber, and M. O. McLinden, *NIST Standard Reference Database 23: Reference Fluid Thermodynamic and Transport Properties-REFPROP, Version 10.0*, National Institute of Standards and Technology, 2018. DOI: <https://doi.org/10.18434/T4/1502528>.
- [18] D. Swyt, “Uncertainties in Dimensional Measurements Made at Non-standard Temperatures,” *Journal of Research of the National Institute of Standards and Technology*, no. 99, Jan. 1994.
- [19] A. Svete and J. Kutin, “Characterization of a newly developed diaphragmless shock tube for the primary dynamic calibration of pressure meters,” *Metrologia*, vol. 57, no. 5, p. 055 009, Sep. 2020. DOI: [10.1088/1681-7575/ab8f79](https://doi.org/10.1088/1681-7575/ab8f79).
- [20] A. Guardone, C. Zamfirescu, and P. Colonna, “Maximum intensity of rarefaction shock waves for dense gases,” *Journal of Fluid Mechanics*, vol. 642, pp. 127–146, Dec. 2009. DOI: [10.1017/s0022112009991716](https://doi.org/10.1017/s0022112009991716).
- [21] P. Colonna, N. R. Nannan, A. Guardone, and T. P. van der Stelt, “On the computation of the fundamental derivative of gas dynamics using equations of state,” *Fluid Phase Equilibria*, vol. 286, no. 1, pp. 43–54, Nov. 2009. DOI: [10.1016/j.fluid.2009.07.021](https://doi.org/10.1016/j.fluid.2009.07.021).
- [22] M. A. Javed, “Speed of Sound Measurement for Industrially Important Fluids with the Pulse-Echo Technique,” Ph.D. dissertation, Technical University of Berlin, Sep. 2020.

- [23] C. Zamfirescu, A. Guardone, and P. Colonna, “Admissibility region for rarefaction shock waves in dense gases,” *Journal of Fluid Mechanics*, vol. 599, pp. 363–381, Mar. 2008. DOI: [10.1017/s0022112008000207](https://doi.org/10.1017/s0022112008000207).
- [24] C. J. S. M. Simpson, “Effect on Shock Trajectory of the Opening Time of Diaphragms in a Shock Tube,” *Physics of Fluids*, vol. 10, no. 9, p. 1894, 1967. DOI: [10.1063/1.1762384](https://doi.org/10.1063/1.1762384).
- [25] J. E. Drewry and Z. A. Walenta, “Determination of diaphragm opening-times and use of diaphragm particle traps in a hypersonic shock tube,” National Aeronautics and Space Administration (NASA), Tech. Rep., Jun. 1965.
- [26] D. R. White, “Influence of diaphragm opening time on shock-tube flows,” *Journal of Fluid Mechanics*, vol. 4, no. 6, pp. 585–599, Nov. 1958. DOI: [10.1017/s0022112058000677](https://doi.org/10.1017/s0022112058000677).
- [27] P. A. Thompson, “A Fundamental Derivative in Gasdynamics,” *Physics of Fluids*, vol. 14, no. 9, p. 1843, 1971. DOI: [10.1063/1.1693693](https://doi.org/10.1063/1.1693693).
- [28] M. O. Khyam, S. S. Ge, X. Li, and M. R. Pickering, “Highly Accurate Time-of-Flight Measurement Technique Based on Phase-Correlation for Ultrasonic Ranging,” *IEEE Sensors Journal*, vol. 17, no. 2, pp. 434–443, Jan. 2017. DOI: [10.1109/jsen.2016.2631244](https://doi.org/10.1109/jsen.2016.2631244).
- [29] O. L. Flaningam, “Vapor pressures of poly(dimethylsiloxane) oligomers,” *Journal of Chemical & Engineering Data*, vol. 31, no. 3, pp. 266–272, Jul. 1986. DOI: [10.1021/je00045a002](https://doi.org/10.1021/je00045a002).
- [30] P. Colonna, N. R. Nannan, and A. Guardone, “Multiparameter equations of state for siloxanes:  $[(\text{CH}_3)_3\text{-Si-O}_{1/2}]_2\text{-[O-Si-(CH}_3)_2]_{i=1\dots 3}$ , and  $[\text{O-Si-(CH}_3)_2]_6$ ,” *Fluid Phase Equilibria*, vol. 263, no. 2, pp. 115–130, 2008. DOI: [10.1016/j.fluid.2006.04.015](https://doi.org/10.1016/j.fluid.2006.04.015).
- [31] N. R. Nannan, P. Colonna, C. M. Tracy, R. L. Rowley, and J. J. Hurly, “Ideal-gas heat capacities of dimethylsiloxanes from speed-of-sound measurements and ab initio calculations,” *Fluid Phase Equilibria*, vol. 257, no. 1, pp. 102–113, 2007. DOI: [10.1016/j.fluid.2007.04.028](https://doi.org/10.1016/j.fluid.2007.04.028).



# 6

## Speed of sound measurements in dense siloxane D6 vapour at temperatures up to 645 K by means of a novel cylindrical acoustic resonator

From:

B. Mercier *et al.*, “Speed of Sound Measurements in Dense Siloxane D<sub>6</sub> Vapor at Temperatures up to 645 K by Means of a New Prismatic Acoustic Resonator,” *Journal of Chemical & Engineering Data*, vol. 68, no. 3, pp. 561–573, Feb. 2023. DOI: [10.1021/acs.jced.2c00725](https://doi.org/10.1021/acs.jced.2c00725)

### 6.1. Introduction

Fluids formed by linear and cyclic siloxane molecules, or more precisely polydimethylsiloxane polymers, are widely employed as feedstock for the production of various types of silicone polymers, in the cosmetic industry, as solvents, and (mixed) as high-temperature heat transfer fluids. The most volatile among

these compounds are also used as working fluids in high-temperature organic Rankine cycle (ORC) power plants [2], [3] and recently in fundamental gas dynamics studies on non-ideal compressible fluid dynamics (NICFD), see, e.g., the introduction of Head [4] for an extensive review of the literature. Siloxanes are particularly suitable for these applications and for these scientific studies because: i) their thermodynamic properties match the requirements in terms of thermodynamic cycle and of related equipment, ii) they are thermally stable up to very high temperature (even in excess of 620 K in contact with stainless steel, if properly handled)[5]–[9], iii) they can be used as lubricants in the liquid phase, iv) their flammability is low (e.g., compared to hydrocarbons) and, v) their toxicity does not require special precautions, see, e.g., the safety data sheet of D<sub>6</sub> [10].

Among cyclic siloxanes, D<sub>6</sub> (dodecamethylcyclohexasiloxane, C<sub>12</sub>H<sub>36</sub>O<sub>6</sub>Si<sub>6</sub>) might be used as working fluid in highly miniaturized high-temperature ORC power plants [11]. Possibly more importantly, in the realm of scientific studies, D<sub>6</sub> is also particularly relevant in the niche field of nonclassical gasdynamics [12]. This branch of fluid mechanics is concerned with the study of compressible flows of dense vapours of fluids formed by complex organic molecules. For such fluids the theory predicts that classical nonlinear acoustic phenomena are inverted: for example rarefaction shock waves and compression fans are possible, as opposed to compression shockwaves and expansion fans [13]. Gasdynamics theory prescribes that for nonclassical phenomena to occur, a necessary condition is that the so-called fundamental derivative of gasdynamics

$$\Gamma = \frac{c^4}{2v^3} \left. \frac{\partial^2 v}{\partial p^2} \right|_s \quad (6.1)$$

is negative for some of the thermodynamic states that the fluid experiences throughout the flow, see, e.g., the studies of Zamfirescu *et al.* [14], Guardone *et al.* [15], and Nannan *et al.* [16] and Chandrasekaran *et al.* [17]. Here,  $c$  is the sound speed,  $v$  is the specific volume and  $p$  is the pressure. If there exist thermodynamic states in the dense vapour phase for which  $\Gamma < 0$ , such a fluid is termed a BZT fluid (from the initials of the three scientists who first argued about the possibility of nonclassical gas dynamic phenomena, namely Bethe, Zel'dovich, and Thompson) [18]–[20]. The proof for the existence of nonclassical gasdynamics has been pursued by several researchers, so far with inconclusive results [21], [22].

The Propulsion and Power group at the Delft University of Technology has researched NICFD and nonclassical gasdynamics for many years. In particular, D<sub>6</sub> was chosen as the working fluid for the realization of a Ludwig-tube-type experimental setup to generate and measure the nonclassical propagation of

waves in dense vapour of organic molecules [23], [24]. Also in this case, results were inconclusive and it can be argued that one of the main difficulties is the insufficient accuracy of the available thermodynamic models, which precludes the confident identification of experimental conditions leading to the generation of the wanted phenomena.

Compared to other organic fluids, very few measurements of thermodynamic properties are documented in the literature for siloxanes. Moreover, the more complex the siloxane molecule is, the fewer the measurements that are available. More in general, it can be argued that the more complex an organic molecule is, the more challenging it is to perform thermodynamic measurements to characterize the departure of properties from those of the ideal gas, given that they have to be performed at high temperatures and close to the thermal stability threshold. As a result, the current thermodynamic models for  $D_6$  are known to be comparatively inaccurate, especially for thermodynamic states at high reduced temperatures and pressures, and close to saturation, that is, the non-ideal thermodynamic states which make nonclassical gasdynamics possible.

Technical equations of state based on the Helmholtz energy formulation were initially developed for several linear and cyclic siloxanes, namely MM,  $MD_xM$  with  $x = 1\dots5$ ,  $D_4$ ,  $D_5$  and  $D_6$  [25]–[27]. The accuracy of these equations of state is however limited if compared to other classes of substances because of the scarcity of experimental data sets. Information about improvements of these multiparameter equations of state models based on additional highly accurate speed of sound measurements in the liquid phase was recently published [28]–[30]. However, these models were developed for all the mentioned siloxanes with the exception of  $D_6$ .

This study is therefore motivated by the need for improving thermodynamic models for  $D_6$  in general, and for speed of sound predictions of dense-vapour thermodynamics states in particular, in order to support experimental studies of nonclassical gasdynamics.

The speed of sound in fluids can currently be measured by means of three main techniques, with different outcomes in terms of accuracy and range of applications. The most direct method is based on the pulse-echo technique, which consists in measuring the duration of the travel of an acoustic wave through the medium over a known distance [31], [32]. This technique allows to reach an accuracy of the order of 0.01% for liquids but is not suited for vapours because their acoustic impedance is insufficient. Alternatively, the sound speed can be indirectly obtained from the modal behaviour of acoustic waves in a cavity. The speed of sound is computed from the measurement of the acoustic resonance frequency of the fluid in a resonator of known dimensions. The resonator can be cylindrical ([33]–[35]) or spherical ([36]–[38]). Spherical resonators allow to achieve lower uncertainties, typically of the order

of 0.01%, but values as low as  $\approx 1$  ppm can be achieved [37]. A comprehensive treatment of the theory of speed of sound measurements is provided by Meier [31]. Finally, the Brillouin scattering affecting the frequency of the light dispersed by molecules can also be used to correlate it with the local speed of sound through a fluid ([39]–[41]). The use of this method is rare, and the associated uncertainty is of the order of 1%. However, it is worth noting that it features the unique advantage that no energy is transferred to the fluid during the measurement. This characteristic can be very attractive, for example, if measurements are needed in extreme temperature conditions, or in thermodynamic conditions very close to the critical point. To the knowledge of the authors, the only published sound speed measurements data related to the dense vapour of complex organic compounds are reported by Timrot *et al.* [42]. The scarcity of this type of data is most likely due to the difficulty of performing sound speed measurements at high temperature, because of thermodynamic state control and sealing difficulties, instrument and actuator compatibility, and also because these states are close to the thermal stability threshold of the molecule.

The authors did not find any evidence of devices which can be used to measure the sound speed at the conditions of interest for nonclassical gas-dynamic studies, namely at temperatures up to 645 K and for a speed of sound value that can be as low as 50 m/s. A new apparatus had therefore to be designed, manufactured, and commissioned: the OVAR (Organic Vapour Acoustic Resonator). The OVAR is a cylindrical resonator with a square cross section. Despite it being known that this type of resonator cannot provide the highest level of accuracy, it offers many advantages if the needs of the study documented here are considered. The main advantage is that, for a given characteristic dimension, it is simple to manufacture in comparison to a spherical resonator. A second advantage of the cylindrical resonator is the possibility to use a larger acoustic excitation system which is required to generate a reasonable acoustic level in vapours. A square cross section for the acoustic cavity was chosen because according to the initial design an optical access should have equipped the device in order to measure also the density with an optical method based on Rayleigh Scattering [43].

Technical details of the resonator are presented in Section 6.2, followed by a description of the measurement procedure provided in Section 6.3. In addition to speed of sound measurements, the density at the experimental conditions have also been evaluated. An estimation of the uncertainties of both sound speed and density measurements is provided in Sections 6.3.3 and 6.3.5. Results are then compared with predictions of the iPRSV cubic equation of state model for  $D_6$ , and are discussed in Section 6.4.2. Section 6.5 completes this contribution with a summary of concluding remarks.

## 6.2. The acoustic resonator

The use of acoustic resonators for speed of sound measurements relies on the amplification of an acoustic signal inside a cavity filled with a fluid if the signal frequency matches a natural frequency of the cavity. For the OVAR, whose cavity is a rectangular cuboid of length  $l_0$  and square section of length  $h_0$ , the resonance frequencies are given as a function of the speed of sound  $c$  by

$$f_{k,m,n} = \frac{c}{2} \sqrt{\left(\frac{k}{l_0}\right)^2 + \left(\frac{m}{h_0}\right)^2 + \left(\frac{n}{h_0}\right)^2} \quad (6.2)$$

where  $k$ ,  $m$  and  $n$  are integers corresponding respectively to the mode numbers in the longitudinal and the two transversal directions. If  $l_0$  is significantly larger than  $h_0$ , this relation can be simplified as

$$f_k = k \frac{c}{2l_0} \quad (6.3)$$

for values of  $k$  such that the frequency of the longitudinal mode is significantly smaller than that of the first radial mode. The length to width ratio of the OVAR cavity is 7.1. Equation (6.3) is therefore valid for  $k \leq 6$ . The frequency  $f_{7,0,0}$  is indeed only 14 % lower than  $f_{0,1,0}$ , which means that both modes may overlap.

### 6.2.1. General layout

The OVAR is made of two main components as shown in Fig. 6.1, the cavity and the syringe. The syringe is used to inject a known volume of fluid into the cavity. In addition, it is equipped with four valves to isolate zones that need to be evacuated via Port 1 or Port 2. Fig. 6.1 also depicts the three main sensors of the setup, namely a K-Type thermocouple sensor T that measures the temperature inside the resonator near the center of the cavity, and two pressures sensors P1 and P2 to perform fluctuation and accurate time-averaged measurements.

#### Cavity

The cavity (Fig. 6.2) is milled out of a stainless steel 316L block. It is closed on the top by a stainless steel plate and terminated at both ends by two end-plates ensuring that there are sharp corners on each edge, so that the cavity shape resembles as much as possible that of a perfect cuboid. The cavity may also be equipped with optical accesses, but the openings were sealed for the purpose of

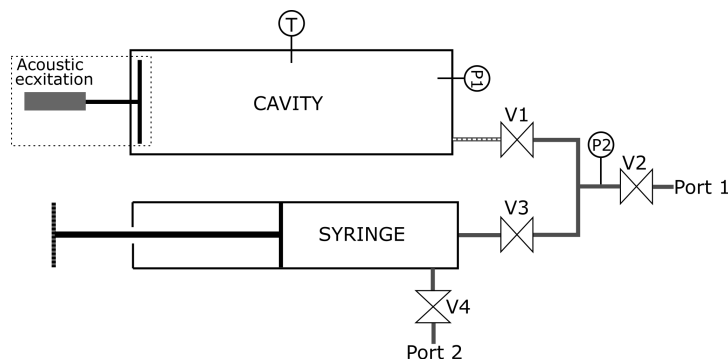


Figure 6.1: General layout of the OVAR setup.

the first experimental campaign, as indicated in Fig. 6.2. The measured length of the cavity is  $l_0 = 284 \text{ mm} \pm 0.2 \text{ mm}$ , and its cross section is a  $40 \pm 0.05 \text{ mm}$  square. The volume of the cavity at 293 K is  $454 \text{ cm}^3 \pm 1.5 \text{ cm}^3$ , which leads to a total volume of  $461 \text{ cm}^3 \pm 1.5 \text{ cm}^3$  including the dead volumes behind the piston and at the corners of the cavity. This volume increases with temperature due to the thermal expansion coefficient  $\alpha = (1.7 \times 10^{-5} \pm 3\%) \text{ K}^{-1}$ , from ambient to the maximum operating temperature. The effect of the pressure onto the volume is however negligible because, for a pressure of 1 MPa, the strain is  $3 \times 10^{-3}\%$  in the transverse directions, and  $4 \times 10^{-4}\%$  in the longitudinal direction.

### Syringe

The fluid is injected into the cavity with the help of a hand-pump, namely a syringe. It is driven by rotating a handle controlling a screw of pitch  $1.5 \text{ mm} \pm 0.0003 \text{ mm}$ . The inside diameter of the cylinder is  $30 \text{ mm} \pm 0.05 \text{ mm}$ . The displacement is therefore  $1.060 \text{ cm}^3 \pm 0.003 \text{ cm}^3$  per turn. The total volume of the syringe is approximately  $100 \text{ cm}^3$ .

### 6.2.2. Instrumentation

The instrumentation consists of three sensors. The pressure is measured by a DRUCK UNIK 5000 ref. X5072-TB-A2-CA-H1-PA silicon sensor (P2 in Fig. 6.1) rated for a maximum pressure of 16 bar with an uncertainty of  $\pm 0.1\%$  of the full scale, *i.e.*,  $\pm 16 \text{ mbar}$ , with respect to the best fit line. After calibration it appeared that the actual uncertainty of the sensor is the addition of a  $\pm 4 \text{ mbar}$  bias and  $0.1\%$  random error considering a day to day calibration of the offset based on atmospheric pressure. This sensor cannot withstand high temperature, thus it is mounted on the pipe between the syringe and the

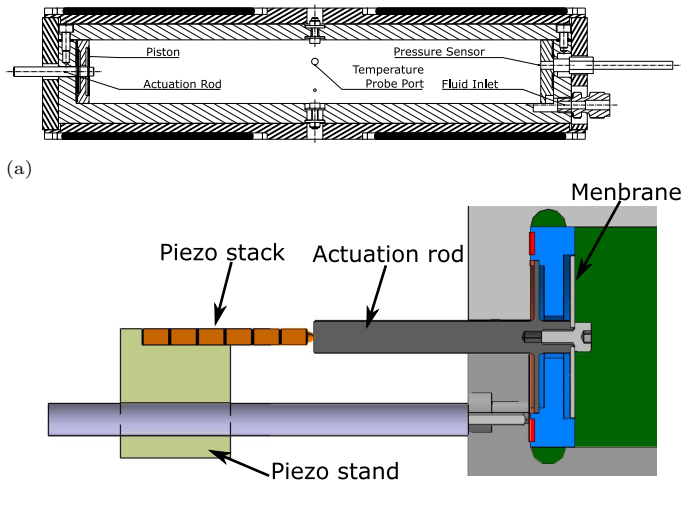


Figure 6.2: (a) Longitudinal cross-section of the resonator showing the stainless steel cavity, the aluminium shell and the heating elements (in black) (b) A more detailed cross-sectional view of the excitation system.

resonator. The 4-20 mA output is converted into voltage by a precision 250  $\Omega$  resistor, and digitized by a NI 9215 A/D converter.

The second pressure sensor is a Kulite XTEH-10L-190SM-300PSI-A (21 bar maximum pressure). It is a high frequency and high temperature pressure sensor flush mounted to the inside of the cavity (P1 in Fig. 6.1) to measure the acoustic pressure. The output is a 5-100 mV signal amplified by a custom +40 dB amplifier and also acquired with the NI 9215 module. The accuracy of this sensor is poor due to a significant drift of the calibration constant with the temperature. Therefore, it cannot be used to measure the absolute pressure inside the cavity, but it is suitable to provide the shape of the resonance curve which does not need to be converted into pressure units to determine the resonance frequency.

The temperature is measured by a calibrated K-type thermocouple mounted on a custom probe that fits in the M5 thread referred to as Temperature Probe Port in Fig. 6.2. The tip of the thermocouple protrudes inside the cavity to ensure that the reading corresponds to the temperature of the bulk flow, and that it is not affected by the local wall temperature. This thermocouple is connected to a NI 9210 thermometer. The thermocouple was calibrated with the Fluke 9100 dry-well calibrator whose rated uncertainty is  $\pm 0.5$  K.

### 6.2.3. Acoustic excitation

Acoustic excitation is a challenge because of the high temperature conditions affecting the entire resonator. It was therefore decided to move the actuation system away from hot parts and to connect it to an actuation rod made of stainless steel as indicated in Fig. 6.2. The rod is in contact on one end with the actuator, a 100V / 32.5  $\mu\text{m}$  Thorlabs piezo stack (reference PK3JUP1), and on the other end is connected to a disk made of stainless steel, which acts as a piston and is flush-mounted with free edges in the cavity. This piston has a thickness of 0.8 mm, a diameter of 30 mm, and a first natural frequency at approximately 3.4 kHz, which is high enough to prevent any coupling considering the frequency of interest in this resonator. The rod is attached to the cavity by means of a membrane that acts as a sealing element as well as a spring. The design of this membrane required much care because such membrane must be strong enough to withstand the pressure difference between the cavity and ambient pressure, and it must simultaneously be flexible enough to be compatible with the piezo stack in terms of forces. A thickness of 0.8 mm with a free diameter of 26 mm was found to be an acceptable combination for a maximum pressure of 10 bar. The first natural mode of the actuation system is 2.7 kHz which is also one order of magnitude larger than the frequencies of interest. If driven with the Thorlabs MDT694B amplifier, the maximum achievable excitation frequency is close to 500 Hz (-3 dB). The input signal for the amplifier is provided by an ELC GF467AF function generator controlled via the RS-232 protocol.

As a side note, the authors indicate that it would be difficult to realize an excitation system capable of withstanding pressures significantly higher than 10 bar with this approach. However, the pressure limitation could be overcome with a new technique. It consists in transferring energy to the fluid as heat instead of as work by sending modulated light to an absorbent surface according to the method proposed by Suchenek *et al.* [44].

### 6.2.4. Thermal control

The temperature homogeneity along the cavity is enhanced by a shell made of 10 mm thick plates of aluminium surrounding the stainless steel walls of the cavity. The shell is fitted with four pockets (two on the top, two on the bottom) holding four heating elements. The heating elements are mica heaters with an individual nominal power of 400 W at 240 V. They are supplied with a 93 V DC tension providing a total heating power of 256 W. The temperature of each heater is monitored individually with a thermocouple located near the center of the heater within the aluminium plate, close to the interface with the stainless steel cavity. A PID (Proportional-Integral-Derivative) controller implemented in a LabVIEW program, which also controls the resonator, gen-

erates a PWM (Pulse-Width Modulation) signal with a one second period that drives MOSFET transistors via the solid state relays of the NI-9485 module. When stabilised, the temperature is controlled within  $\pm 0.05$  K.

The resonator is covered by a 30 mm-thick insulation blanket that reduces heat fluxes toward the ambient air, and across the aluminium shells. Residual heat fluxes still exist from the heating elements to the two longitudinal ends of the resonator. A consequence is that the cavity wall temperature is not expected to be perfectly uniform. A finite element thermal analysis of the resonator was performed to estimate these variations in temperature. A uniform heat flux was imposed at the interface between the mica heaters and the aluminium plate. Thermal properties of the different materials were obtained from databases for the metals and from the manufacturer specifications for the insulation material. The convection coefficient between the outer surface and the atmosphere was chosen to fit the measured surface temperature. The thermal analysis put into evidence the possibility that cold spots may occur on the inner wall of the cavity. These surfaces are nearly 1.5 K colder than the area directly facing the positions of the four heaters. This phenomenon may become significant if the thermodynamic state for which the speed of sound measurement is planned is close to the dew point because local condensation may occur. Sufficiently far from conditions of local condensation, the homogeneity of the fluid can be achieved if the heat transfer through the fluid is largely due to natural convection and conduction is minimal. Such conditions of convection dominance can be verified by means of the Rayleigh number  $Ra$  defined as

$$Ra = \frac{g\beta\Delta TL_c^3\rho^2}{\mu^2}Pr, \quad (6.4)$$

where  $g$  is the acceleration due to gravity,  $\beta$ ,  $\rho$ ,  $\mu$  and  $Pr$  are the isobaric thermal expansion coefficient, the density, the dynamic viscosity, and the Prandtl number of the fluid;  $\Delta T$  and  $L_c$  are the characteristic temperature difference and characteristic length of the considered configuration. The so-called critical Rayleigh number is of the order of  $10^3$ , whereby higher values indicate the dominance of convection. If the fluid is siloxane D<sub>6</sub>, its thermodynamic properties can be estimated by means, for example, of an in-house server software implementing various thermodynamic and transport properties models for pure fluids and mixtures [45]. In particular, the iPRSV cubic equation of state [46] was employed to calculate thermodynamic properties, and the Chung et al. model [47] for transport properties. The Rayleigh number was computed for various experimental conditions with  $L_c = 0.04$  m and  $\Delta T = 1$  K and, as expected, its value is lower for low values of pressure  $p$  and high temperature  $T$  because in such thermodynamic states density is lower and viscosity higher.

For  $p = 1$  bar and  $T = 650$  K,  $Ra = 5 \times 10^5$ , thus a much larger value if compared to the critical Rayleigh number. Natural convection is therefore the dominant heat transfer mechanism within the fluid, indicating that the fluid temperature can be considered as homogeneous, and the thermal boundary layer can be neglected.  $Ra$  becomes as large as  $10^8$  for  $p = 8$  bar and  $T = 650$  K.

It can be concluded that, if the working fluid is siloxane  $D_6$ , or other similar siloxanes, the temperature measured by the thermocouple protruding inside the cavity can be considered as an accurate value contributing to the identification of the thermodynamic state of the fluid inside the cavity. This temperature is however always slightly lower than the set point temperature of the heaters due to cold spots occurring on surfaces not subjected to active heating.

## 6.3. Experimental method

### 6.3.1. Fluid characteristics and purification

Before the  $D_6$  sound speed measurement campaign, siloxanes  $D_4$  and  $D_5$  were utilized to calibrate the measurement system, given that high accuracy speed of sound experimental data at moderate temperatures in the vapour phase of these fluid are reported [48]. Both fluids were produced by Tokyo Chemical Industry and certified to be 99.9% pure. The experimental campaign aimed at obtaining dense vapor sound speed values for siloxane  $D_6$  was based on fluid samples obtained from Dow Corning. The purification level that can be obtained for  $D_6$  is lower and equal to 97.4%. According to the supplied gas chromatography analysis, the samples also contain 1.7% of  $D_5$ , 0.5% of  $D_7$  and traces of lighter siloxanes and water. The main properties of these siloxanes are summarized in Table 6.1.

Dehydration, thus extraction of dissolved water molecules, is mandatory because water can adversely affect the thermal stability of organic fluids [8]. All the three fluid samples were dehydrated by keeping beads of 3Å molecular sieves immersed in the samples for several days.

Gases dissolved in the fluid are also detrimental with respect to the thermal stability of the fluid molecules and the accuracy of speed of sound measurements. To mitigate this issue, vacuum degassing of the fluid samples was adopted, namely the fluid samples are left under vacuum in a large vessel for at least 12 hours and then the vacuum pump is operated to extract the incondensable substances from the vessel. This process was repeated every time a fluid sample was brought to high temperature because it was found that a detectable amount of incondensable gases are produced, most likely due to the thermal decomposition of siloxanes when kept at high temperature for a

long period of time. If light gases are not extracted, they cause a day to day increase of the measured speed of sound because they are released during the next heating.

	D <sub>4</sub>	D <sub>5</sub>	D <sub>6</sub>
CAS Number	556-67-2	541-02-6	540-97-6
Boiling temperature at 1 atm (K)	448	484	518
Molecular Mass $M$ (g/mol)	296.6	370.1	444.9
Density $\rho$ at 1 atm, 298 K (kg/m <sup>3</sup> )	950	954	963

Table 6.1: Main properties of the three cyclic siloxanes involved in the measurement campaign [25], [26].

Other possible products of thermal decomposition which were also observed were visible black particles, possibly black carbon conglomerates forming after several hours of exposure of the fluid to high temperature. No quantitative measurements of the concentration of these particles were carried out, but it seemed that they only appeared when approaching temperatures of 630 K and above, without significantly affecting the value of the measured speed of sound. The thermal stability threshold of cyclic siloxanes in stainless steel of approximately 630 K is in agreement with previous findings [6].

### 6.3.2. Measurement procedure

Before starting any experiment, the cavity is connected to the vacuum pump through Port 1, valves V2 and V1 are open and the pump actuated (see Fig. 6.1). V2 is then closed and the heating system is turned on to reach the desired temperature setpoint. The pressure rises slightly with the temperature because residual siloxanes from the previous experiments evaporate; the vacuum pump is therefore used also to extract these residual vapours. At the same time, the syringe is filled with the desired quantity of purified fluid via port 2. The pressure of the syringe is then set to vacuum conditions by connecting the vacuum pump to Port 2.

When the temperature has reached the setpoint, valve V1 is closed, and V3 is opened. The syringe is again connected to the vacuum pump through Port 1, and vacuum is set. V2 is closed, and the fluid is pushed with the syringe to fill the pipes. Valve V1 is then opened and the desired amount of fluid can be injected by rotating the syringe handle with the desired angle. A temperature

drop of the fluid inside the cavity is instantaneously observed. Speed of sound measurements can only start after the temperature has stabilized again and reached the setpoint. The measurements are repeated at least three times for each configuration, which together with constant temperature and pressure, ensures that steady state is reached.

Siloxane D<sub>4</sub>, D<sub>5</sub> and D<sub>6</sub> were all tested in the resonator, therefore care was taken to avoid fluid contamination. To this end, if the tested fluid is the same as the one used for the previous measurement, the syringe is used to push more fluid into the resonator in order to reach a new thermodynamic state. If the fluid previously used was different, then the entire system is flushed and the procedure is repeated with fresh fluid. This cleaning procedure is repeated until the speed of sound remains constant after the fluid is replaced. This condition indicates that there is no significant traces of contaminants, and is generally reached after three to four iterations.

A further precaution during the operation of the resonator concerns the fluid injection. The mass of injected fluid is a function of the fluid density inside the syringe, and hence of the fluid temperature. Though the outer surface temperature of the syringe is monitored, it is critical to never transfer hot fluid from the cavity to the syringe to avoid any rapid increase in temperature of the fluid stored inside the syringe which can not be captured by the temperature sensor. Successive speed of sound measurements were therefore always conducted by increasing the fluid density in the cavity. If, for any reason, fluid needed to be extracted, a long delay was imposed to ensure that the temperature inside the syringe had reached ambient temperature.

## 6

### 6.3.3. Estimation of the speed of sound

The speed of sound is determined from the frequency of the acoustic resonance of the cavity filled with the fluid using Eq. (6.3) with the cavity length corrected for thermal expansion. The frequency response of the cavity was scanned by sending a sinusoidal signal to the piezoelectric actuator and by measuring the acoustic response with the Kulite pressure sensor. The range of emitted frequencies was chosen to encompass the entire resonance peak of the second longitudinal mode, typically over a range of 5 Hz to 7 Hz and with steps of  $df = 0.33$  Hz. The excitation is started approximately 0.5 s before the beginning of the recording to provide enough time for the resonance to reach its maximum amplitude. The recording time is  $1/df = 3$  s for consistency with the next post-processing step. Once the scanning is done, the resonance of the cavity is described by a collection of records as shown in Fig. 6.3.

It was observed that the actuation frequency differs slightly from that prescribed to the signal generator because of a bias due to controlling this device with serial communication. The next step is therefore to identify more pre-

cisely the excitation frequencies, and the amplitude of the pressure signal  $p(t)$  at each excitation frequency. Frequency identification was performed in the frequency domain using the Fast Fourier Transform  $P(f)$  of the signal  $p(t)$ . The frequency resolution of the Fourier transform was improved by a factor of three by means of so-called zero-padding, thus  $df/3 = 0.11$  Hz. The obtained resolution could be further improved by windowing the pressure signal with a Gaussian weighting and by fitting the peak in the FFT with a Gaussian function as explained by Gasior and Gonzalez [49]. Yet 0.11 Hz was found to be sufficient for the purpose of this study. The rms value  $p_{\text{ext}}^{\text{rms}}$  of the pressure signal at the excitation frequency is obtained following Parseval's theorem as

$$p_{\text{ext}}^{\text{rms}} = \sum_k P(f_k)df, \quad (6.5)$$

where  $f_k$  is the  $k^{\text{th}}$  frequency which is an index identifying the range of the peak corresponding to the excitation frequency in  $P(f)$ . Figure 6.3 shows an exemplary result obtained by applying this method to the recording of one scan of the cavity resonance.

The final step consists in determining the resonance frequency of the cavity from the individual records. A common practice is to fit the envelope of the resonance peak formed by the previously determined points with a Lorentzian curve. However, a more robust, time-effective and sufficiently accurate method was devised, given the relatively large uncertainty of the measurement system. The resonance frequency is determined by averaging the peak frequencies within the corresponding record, weighted by their amplitudes. Only the records with an amplitude of at least half of the maximum amplitude were considered. The result is a barycentric frequency close to the frequency at which the maximum acoustic pressure would have been measured (this point is shown by a black dot in Fig. 6.3).

The obtained frequency is not exactly the resonance frequency because it is influenced by all the sources of energy dissipation, see the detailed study of Liu *et al.* [35] A better estimation of the resonance frequency is generally obtained by adding the full width at half maximum (FWHM) of the resonance peak to the central frequency of the peak. However, the observed FWHM value is at least an order of magnitude larger than that expected from the source of errors summarized by Liu *et al.* [35] and this can be explained as follows:

- Errors may arise from interactions between the fluid and the cavity shell. Zhang *et al.* [50] proposed a model to estimate the effect of this interaction for a resonator with a circular cross-section. This model is applied to the OVAR by approximating the cross-section of the OVAR to be circular with the same cross-sectional area as the actual square cylinder. This results in a perturbation of the peak frequency of the order of

0.01%. This perturbation is small because of the large difference between the speed of sound in D<sub>6</sub> vapour and in stainless steel.

- Frequency shifts can be introduced by the interaction between the acoustic modes and the vibrational relaxation of the molecule, however this is not relevant in the frequency range that is considered in this resonator.
- Perturbation due to wave propagation in the inlet duct is also expected to be weak because the duct diameter is only 0.8 mm and is filled with liquid D<sub>6</sub>, which implies the existence of a reflective boundary at the liquid/vapour interface.
- Thermoviscous dissipation also affects the frequency response of the cavity. Its effect can also be estimated following Zhang *et al.* [50]. However, since the correction reported by Zhang *et al.* is for a cavity of circular cross-section, it is calculated also in this case for an equivalent cavity of diameter  $a = 51$  mm with perimeter equal to that of the 40 mm × 40 mm square cavity. For longitudinal modes, the viscous perturbation  $\Delta f_v/f_0$  and the thermal perturbation  $\Delta f_T/f_0$  are

$$\frac{\Delta f_v}{f_0} = \frac{1}{2a} \sqrt{\frac{\eta}{2\pi\rho f_0}} \quad \text{and} \quad (6.6)$$

$$\frac{\Delta f_T}{f_0} = \frac{C_p/C_v - 1}{2a} \sqrt{\frac{\lambda}{\pi\rho C_p f_0}} \left(1 + \frac{2a}{l_0}\right), \quad (6.7)$$

where  $\eta$  is the dynamic viscosity,  $\lambda$  is the thermal conductivity, and  $C_p$  and  $C_v$  are the specific heat at constant-pressure and constant-volume respectively. These properties for D<sub>6</sub> have been estimated, albeit with fairly large uncertainty, by means of an in-house program [45] implementing a Helmholtz multiparameter equation of state model [26] ( $C_p$  and  $C_v$ ) and the Chung *et al.* model [47] ( $\eta$  and  $\lambda$ ). Noting that the uncertainty associated with these property values cannot be easily quantified,  $\Delta f_v/f_0 = 1.4 \times 10^{-4}$ ,  $\Delta f_T/f_0 = 1.8 \times 10^{-4}$  at  $T = 630$  K and  $p = 2.55$  bar, with  $C_p = 1992$  J/kg · K,  $C_v = 1957$  J/kg · K,  $\eta = 1.1 \times 10^{-5}$  Pa · s,  $\lambda = 3 \times 10^{-2}$  W/m · K,  $f_0 = 338$  Hz.

The dominant perturbation therefore arises from the viscous and thermal boundary layers. Two more sources of dissipation specific to this resonator could not be evaluated, namely, the viscous dissipation occurring at the gap between the piston and the cavity wall, and the dissipation due to phase change at the interface between vapour and liquid in the inlet pipe. It is however unlikely that their effect is two orders of magnitude larger than that of thermoviscous dissipation at the walls. All added together, the broadening of the

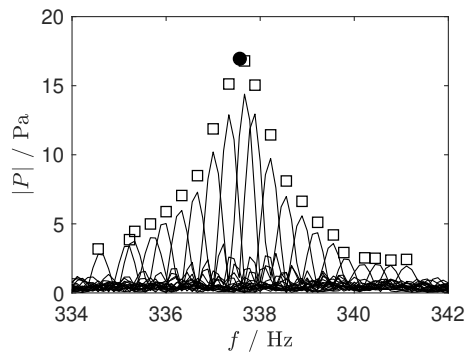


Figure 6.3: Fourier transforms of the recordings for the estimation of the resonance frequency in  $D_6$  at a 2.55 bar and 629.8 K.  $\square$  maxima of each individual Fourier transforms (amplitude is divided by 3),  $\bullet$  maximum of the resonance peak (amplitude divided by 3).

FWHM due to wave dissipation mechanisms should not exceed 0.1 Hz. As a consequence, the nearly 2 Hz FWHM that can be observed in Fig. 6.3 must be the result of another perturbation. It is conjectured that this somewhat large FWHM is due to albeit small variations of temperature within the cavity. This statement is supported by the observation that the FWHM tends to decrease if the resonator is kept at rest for a longer period of time, or if it is operated at a higher density, which causes better mixing of the fluid due to buoyancy. These variations introduce disturbances in local sound speed and in local flow velocity in the cavity due to natural convection. However, because the cavity is closed, the average velocity in any cross-section of the cavity must be zero following the continuity constraint. Also, the temperature fluctuations are small enough to assume that their effect on sound speed is linear, thus the bulk sound speed within the resonator is that associated with the average temperature. As a consequence, these fluctuations in temperature are not expected to cause any bias in the peak frequency of the resonance despite locally disturbing the wave fronts, causing some broadening of the spectrum. This was confirmed by the experimental observation that keeping the resonator at steady-state for a long time does not cause a sizable change of the measured central frequency of the resonance peak. Based on this remark, and considering that exposure of the fluid at high temperature increases the amount of thermal decomposition products, thus affecting the purity of the fluid sample, it can be argued that the obtained FWHM is acceptable and there is no need to wait until a further homogenization of the temperature. It is therefore assumed that the frequency of maximum pressure fluctuation coincides with the resonance frequency.

### 6.3.4. Calibration of the resonator

The linear relation between the speed of sound and the resonant frequency of the cavity is described by Eq. (6.3) for a perfect cavity; however, this equation is not expected to accurately model the actual resonator whose geometry is made of three coupled cavities. The main cavity is connected to two residual cavities: one that is situated behind the piston (see Fig. 6.2) and one at the fluid inlet. It was therefore decided to determine a correction for Eq. (6.3) by a calibration of the resonator. This process rests upon the comparison of the measured speeds of sound with reference measurements available in the literature. Despite no data being available for siloxane D<sub>6</sub>, accurate sound speed measurements are reported in the literature by Nannan *et al.* [48] for D<sub>4</sub> and D<sub>5</sub> at conditions of pressure and temperature matching with the capabilities of the OVAR. The thermodynamic states selected for calibration are summarized in Table 6.3. A sufficient high-purity amount of both D<sub>4</sub> and D<sub>5</sub> from the same batch of fluid that was used for the experiments documented by Nannan *et al.* [48] was still available in the laboratory and was used for calibration. Importantly, the possibility of performing this type of calibration with the same fluids allows to mitigate the influence of a possibly relevant source of error, namely the rather large amount of impurities in the D<sub>6</sub> samples used for the measurement campaign. Sourcing siloxanes with a higher level of purity proved to be impossible as of the time of the documented experiments. Performing a calibration with more conventional and well-characterised fluids such as CO<sub>2</sub> was considered as an alternative. However, the resonant frequencies associated with fluids made of simpler molecules at high temperature are out of the range of the excitation capability of the apparatus. In addition to the correction of systematic biases due to the geometry of the resonator, performing this calibration also allowed to point out random variations in the sound speed measurements, and therefore makes it possible to determine an uncertainty base for the statistics of the observed errors.

The calibration was performed in two stages. A first set of measurements using D<sub>5</sub> and D<sub>4</sub> as working fluids was performed before the D<sub>6</sub> experimental campaign. A second set of calibration measurements with D<sub>4</sub> was executed following all the D<sub>6</sub> sound speed measurements in order to assess a possible time-drift of the resonator properties. For each of the thermodynamic states listed in Table 6.3, the speed of sound  $c$  measured with the OVAR was corrected for the small difference in pressure  $dp$  and in temperature  $dT$  with respect to the reference values with

$$c_{\text{cor}} = c + \Delta p \left. \frac{\partial c}{\partial p} \right|_T + \Delta T \left. \frac{\partial c}{\partial T} \right|_p \quad (6.8)$$

where the partial derivatives of the speed of sound are computed using an in-house program [45] implementing the multiparameter equation of state model of  $D_6$  documented by Colonna *et al.* [26]. Deviations between the temperatures and pressures determining the thermodynamic state of the fluid in the cavity and the reference values were within  $\pm 0.1$  K and  $\pm 0.5$  mbar. The inaccuracy of the thermodynamic model is not expected to play any significant role in the calibration process given the small magnitude of these corrections.

The same partial derivatives of the speed of sound are also used to estimate the effect of the pressure uncertainty  $u(p)$  and of the temperature uncertainty  $u(T)$  discussed in section 6.2.2 on the sound speed uncertainty  $u(c)$  following

$$u(c) = \sqrt{\left(u(p) \frac{\partial c}{\partial p} \Big|_T\right)^2 + \left(u(T) \frac{\partial c}{\partial T} \Big|_p\right)^2}. \quad (6.9)$$

Deviations between the measured speed of sound and the reference values are listed in Table 6.3 and displayed in Fig. 6.4. Deviations of approximately  $-1.2\%$  observed for  $D_5$  before the  $D_6$  measurement campaign are consistent with those close to  $-1.1\%$  observed for  $D_4$  after the  $D_6$  measurement campaign. However speed of sound values measured in  $D_4$  before the  $D_6$  test campaign were approximately  $0.2\%$  higher than those measured after the test campaign, which is statistically significant. This is most probably the result of the presence of a small amount of non-condensable gases in the fluid sample, either because air leaked inward before the charging procedure or because of the imperfect degassing of the fluid sample before the measurement campaign. The sensitivity of speed of sound to the presence of light gases is large because of the much higher value of their speed of sound. The influence of these impurities is more pronounced if the thermodynamic state is at low density. For example, if a measurement in  $D_4$  at 1.4 bar and 500 K is considered, an error of  $0.2\%$  would be caused by a small amount of air featuring a partial pressure of 7 mbar. This small amount of air may not be detected because of the  $\pm 4$  mbar offset of the sensor. For this reason, test points 7 to 15 in Fig. 6.4 were discarded as far as the computation of the calibration constant is concerned. The average error based on all other measurements is  $-1.12\%$  with a standard deviation of  $0.109\%$ . A value of  $0.03\%$  must be added as this is due to the sum of the errors caused by thermoviscous dissipation and by interactions with the shell of the resonator. Table 6.2 summarizes the breakdown of the uncertainties. The speed of sound  $c$  is therefore expressed in terms of the measured speed of sound  $c_{\text{EXP}}$  as

$$c = (1.012 \pm 0.0014) c_{\text{EXP}}. \quad (6.10)$$

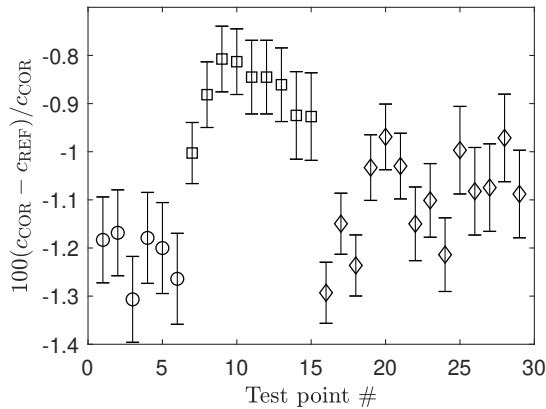


Figure 6.4: Deviation between measured sound speed values and reference values of Nannan *et al.* [48] Error bars show  $1\sigma$  uncertainty from pressure and temperature uncertainties.  $\circ$ : D5,  $\square$ : D4 before D6 test campaign,  $\diamond$ : D4 after D6 test campaign.

## 6

### 6.3.5. Estimation of the density

The use of a custom made syringe for injecting the fluid also allows to evaluate the volume and the mass of the fluid introduced into the cavity, whose volume is known, and thus the density of the vapour corresponding to the set thermodynamic state in the cavity. Assuming that the pipes are initially empty, the inner volume of the pipes must be subtracted from the total volume of fluid displaced by the syringe to determine the amount of fluid introduced in the cavity. Under this assumption, the error introduced by relative changes in density during the measurement of an isotherm was measured to be  $\pm 0.15 \text{ kg/m}^3$  and corresponds to the uncertainty of  $\pm 1/16$  turn associated the reading of the position of the handle that controls the piston in the syringe on which the estimation of the mass of liquid introduced into the cavity is based. In addition, errors with respect to the estimation of the cavity volume arise from i) the uncertain dimensions ( $\pm 0.33\%$ ), ii) the thermal expansion uncertainties which can be evaluated as  $\pm 1.5 \times 10^{-6} \cdot (T - 293)$ , and, iii) the uncertainty related to the syringe volume displacement ( $\pm 0.35\%$ ).

However, a further day to day variation between repeated measurements at the same temperature and pressure of up to  $\pm 1 \text{ kg/m}^3$  was observed. This source of error was later identified to result from the presence of liquid D<sub>6</sub> in the pipe connecting the pressure sensor to the inlet because the vacuum pump was not able to remove it completely, probably due to the effect of capillary

	Temperature	Pressure	Density	Soundspeed
Calibration	0.5 K	0.1 %		0.11 %
Bias		0.004 bar	0.03 kg·m <sup>-3</sup>	
Mass injection			0.15 kg·m <sup>-3</sup>	
Syringe displacement			0.35 %	
Cavity volume			0.33 %	
Thermal expansion			1.5·10 <sup>-4</sup> (T - 293)	
$\Delta f_v / f_0$				0.01 %
$\Delta f_T / f_0$				0.01 %
Shell interaction				0.01 %

Table 6.2: Sources and corresponding values of uncertainty affecting the measured quantities.

forces.

The density estimation is therefore affected by an unknown offset which changes every time the cavity is emptied, thus every time measurements along a new isotherm are performed. This bias could be mitigated provided that the offset can be estimated. This can be done since all measurements were performed along isotherms starting from low density conditions at which the compressibility factor is larger than 0.95; hence the departure of the thermodynamic properties from those of the ideal gas is very small and the existing equation of state models are expected to be accurate. It was therefore decided to estimate the offset as the average of the difference between the measured density and the one estimated with the iPRSV cubic equation of state[46] for the three measurement conditions at lowest pressure along each isotherm. The error introduced by this correction cannot be accurately quantified because no density measurement is documented in the literature. An estimate of magnitude of this random error can nevertheless be given based on the accuracy of the equation of state model of siloxane D<sub>5</sub>, which was initially devised within the same study as that of D<sub>6</sub> [26] and it was recently compared to a more accurate update of the model [30]. Thol *et al.* [30] report an uncertainty of the order of 0.2% for the vapour density at low pressure. This would imply that the density estimates obtained with the thermodynamic model for D<sub>6</sub> are affected by an additional error of 0.03 kg/m<sup>3</sup> for the isotherm at the lowest temperature of 544 K, and the error is even less at higher temperature. This

Fluid	$T / \text{K}$	$p / \text{bar}$	$c / \text{m/s}$	$u(c) \times 10^4 / \text{m/s}$
D <sub>4</sub>	495.00	1.43	109.7	283
	495.00	1.60	108.4	105
	495.00	2.25	103.4	31.8
D <sub>5</sub>	510.00	0.928	100.8	5.9
	510.00	1.03	99.89	82.5
	510.00	1.11	99.98	120

Table 6.3: Thermodynamic states and reference speeds of sound selected for the calibration of the OVAR. Values are taken from the work of Nannan *et al.* [48]

potential error is added to the uncertainty budget for density whose components are summarized in Table 6.2.

## 6

## 6.4. Measurements

### 6.4.1. Thermodynamic states

The thermodynamic states at which the speed of sound was measured are reported in Fig. 6.5. They cover eight isotherms ranging from 544 K to 644 K, hence reduced temperature  $T_r = T/T_c$  from  $T_r = 0.859$  to  $T_r = 0.997$ . The pressure was varied between approximately 1 bar up to approximately 90% of the dew pressure. All thermodynamic states feature a value of the compressibility factor  $Z = pv/RT$  between 0.95 and 0.44, therefore they all feature a rather large departure from the ideal gas state.

### 6.4.2. Comparison with sound speed and density values computed by means of a cubic equation of state

The obtained measurements are compared with speed of sound and density values calculated with a thermodynamic model formed by the iPRSV cubic equation of state[46]

$$p(T, v) = \frac{RT}{v - b} - \frac{a}{v^2 + 2vb - b^2}, \quad (6.11)$$

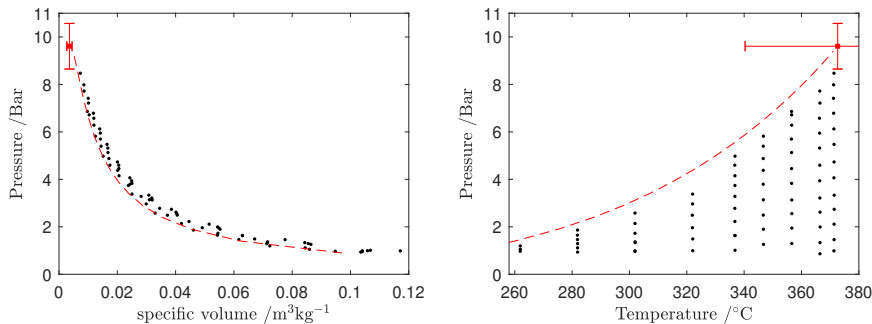


Figure 6.5: Thermodynamic states in the vapor phase ( $\cdot$ ) at which the speed of sound was measured in the  $p$ - $v$  and  $p$ - $T$  diagram of  $D_6$ . The dew line computed with the iPRSV thermodynamic model ( $---$ ) and the critical point estimate ( $\blacksquare$ ) together with the associated uncertainties are also indicated.

where  $v = 1/\rho$  is the specific volume, and  $a$  and  $b$  are fluid-specific coefficients and complemented with a temperature-dependent polynomial expression for the isobaric ideal-gas heat capacity [48]. This model was chosen because the more complex multiparameter model [26] is fitted on points generated with this cubic equation of state as far as the vapour phase is concerned, due to the lack of any experimental data in this thermodynamic region. The iPRSV model is also implemented in an in-house program for the calculation of fluid thermophysical properties [45] which was used for all computations.

### Density

Discrepancies between the density calculated with the iPRSV equation of state and density measurements corrected with the method described in section 6.3.5 are displayed in Fig. 6.6. A first remark about the results reported in this Figure is that, for isotherms with  $T > 595$  K ( $T_r > 0.92$ ), the relative difference lies within 0.0% and 1.5% for values of the normalised pressure  $p/p^{\text{sat}}$  up to approximately 0.6. This fairly good agreement can be expected because it is a constraint of the density correction method. However, the fact that the difference between calculated and experimental value remains almost constant over this range of pressure has two consequential implications. First, as expected the model predicts well the variation of density with the variation of pressure at moderate  $p/p^{\text{sat}}$ . Second, and consequently, the hypothesis that the equation of state provides relatively accurate estimates of the vapor density for isotherms with  $T > 595$  K is valid, and the corresponding density measurements can be considered as reliable.

For isotherms with  $T \leq 595$  K, the relative difference between the measured density and that calculated with the equation of state becomes larger. This can

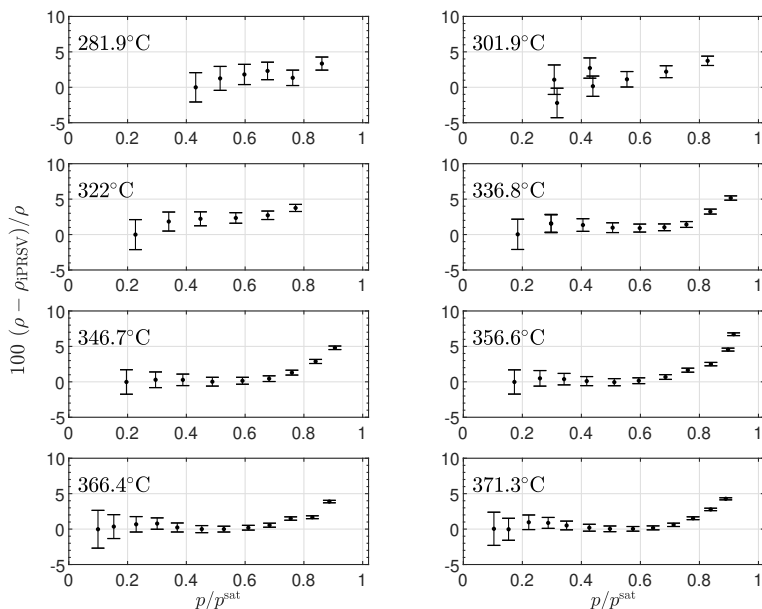


Figure 6.6: Relative deviation in density between the experimental measurements and the density estimates computed with a cubic equation of state [45], [46] against pressure normalised by the saturation vapour pressure at the given temperature.

be partially explained by the larger relative uncertainties in the measurement of the density at those conditions.

Above  $p/p^{\text{sat}} = 0.7$ , the equation of state estimate is increasingly different from the measured density: the value calculated with the equation of state is lower than the measured value by as much as 5% at  $p/p^{\text{sat}} = 0.9$  and this difference may increase at pressures that are closer to the dew pressure.

One possible explanation for this deviation is the inaccurate estimation of the saturated vapor density, which is possibly overestimated by  $\approx 10\%$  (see Fig. 6.6). This error may be the consequence of the lack of experimental data for the vapor-liquid critical point, which have been estimated starting from the critical point values of lighter siloxanes [26]. Colonna *et al.* [26] reported uncertainties that were defined arbitrarily by the DIPPR as 10% for the pressure, 5% for the temperature and 25% for the specific volume. These uncertainties are possibly exaggerated, but they illustrate the issues caused by the lack of experimental information for this fluid.

### Speed of sound

Differences between speed of sound measurements and values calculated with the the iPRSV model[46] are reported in Fig. 6.7. For all isotherms, the speed of sound calculated with the model is lower by approximately 1% to 1.5% at the lowest pressure, which is a significant difference if compared to the typical uncertainty of speed of sound estimations. At those conditions, the model predicts that the ideal gas departure implies a reduction of 4% to 6% of the speed of sound from ideal gas values over the range of tested temperatures. Experimental measurements therefore show that the thermodynamic model overestimates the ideal gas departure, even in the dilute vapour region. This deviation may be the result of the large uncertainty affecting the estimation of the ideal gas heat capacity of  $D_6$  used as an input for the thermodynamic model (data were taken from the work of Nannan *et al.* [48]). It could also be argued that impurities in the fluid impact speed of sound measurements. However, the  $D_5$  and  $D_7$  traces in the tested fluid sample are estimated to alter the ideal gas speed of sound by just 0.1%.

Figure 6.7 shows that the discrepancy between measured and calculated values remains within the same order of magnitude for all isotherms, with a maximum close to  $p/p^{\text{sat}} = 0.6$ . A different trend is however observed for the three isotherms at higher temperature for  $p/p^{\text{sat}} > 0.6$ . In particular, at  $T = 629.8$  K and maximum  $p/p^{\text{sat}}$ , the thermodynamic model predicts the speed of sound quite accurately, but it increasingly underestimates its value with increasing temperature, resulting in a deviation of 4.5% at  $T = 644.5$  K. In other words, the model accurately captures the ideal gas departure at  $T = 629.8$  K and  $p/p^{\text{sat}} = 0.9$ , but it overestimates all the values of ideal gas departure along the  $T = 644.5$  K isotherm, leading to an underestimation of the speed of sound. This observation is relevant with respect to the possibility that  $D_6$  is a BZT fluid because these thermodynamic states at high reduced temperatures and pressures close to saturation correspond to states for which the thermodynamic model predicts that the value of the fundamental derivative of gas dynamics  $\Gamma$  becomes negative. However, these measurements were performed at constant temperature, and  $\Gamma$  depends on the variation of speed of sound at constant entropy, therefore no information can be drawn from these measurements alone.

## 6.5. Conclusions

Measuring thermodynamic properties of complex organic molecules in the dense vapour phase is very challenging because measurements must be performed at high temperatures and close to the thermal stability limit of these molecules in contact with suitable containing materials. This possibly explains

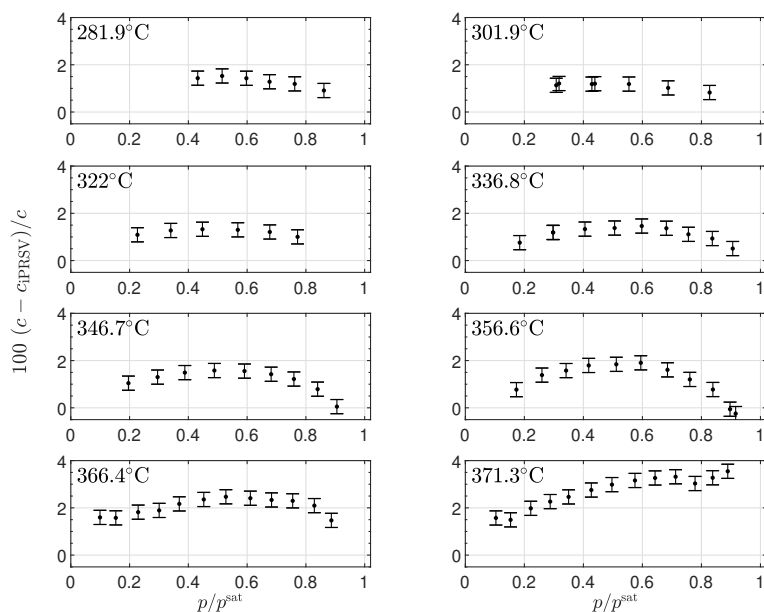


Figure 6.7: Relative deviation between speed of sound measurements along isotherms and values calculated with the iPRS cubic equation of state [45], [46] plotted against the pressure normalised by the value of the saturation pressure at the given temperature.

why data of this type are extremely rare and none is known to the authors for organic molecules with a high degree of complexity. Among the property measurements that are most useful for the development of thermodynamic property models of fluids, sound speed stands out because it provides a direct relation to heat capacities, which are difficult to measure directly. If measured for dense vapour thermodynamic states, the speed of sound provides information also on the departure of properties from those that are related by the ideal gas assumption.

Moreover, knowing the value of the speed of sound is fundamentally important in gas dynamics in general and, for states whose relations among properties depart significantly from those of the ideal gas, in non-ideal compressible fluid dynamics (NICFD), a relatively novel branch of fluid mechanics. Siloxane D<sub>6</sub>, being a sufficiently complex organic molecule is predicted to exhibit so-called nonclassical gasdynamic behavior in the dense vapour phase, and this is the main reason that motivated this experimental study.

The outcome of the investigation documented in this article can be summarized as follows:

- The possibility of measuring the speed of sound of fluids formed by complex organic molecules at dense vapour states has been demonstrated. For this purpose, a new cylindrical resonator has been designed, realized and successfully commissioned;
- The first measurement campaign has been carried out. The speed of sound and, in addition, the density of siloxane D<sub>6</sub> have been measured along eight isotherms (temperatures between 555 K and 645 K) in the dense vapour phase for states with  $0.44 < Z < 0.95$  and starting from states very close to saturation. The uncertainties of such measurements has been estimated to be 0.14% for the sound speed and between  $0.2 \text{ kg}\cdot\text{m}^{-3}$  and  $1.2 \text{ kg}\cdot\text{m}^{-3}$  for the density.
- The measured values have been compared with values calculated with the iPRSV cubic equation of state model as available at the time of the measurements in order to verify the consistency of the experimental data and highlight the limitations of currently available models. It was thus shown that the model correctly predicts the density given the temperature and the pressure for states characterized by a pressure ratio  $p/p^{\text{sat}}$  up to 0.7. However, the model underestimates the density by as much as 5% for  $p/p^{\text{sat}} \approx 0.9$ . iPRSV speed of sound predictions however all lie within  $-2\%$  and  $0\%$  of the measured value, except for the states along the isotherm at the highest temperature (645 K), for which model predictions differ from measured values by as much as  $-4\%$ ; this deviation may be reduced by performing critical point and dew line measurements at high reduced temperature  $T_r$ .

- The measurement accuracy can be improved with some modifications to the resonator body. First, the shape of the cavity should be modified to be a circular cross-section. This change could be achieved without significantly modifying the current resonator for instance by adding a circular tube which has the length of the cavity and the diameter of the acoustic excitation system. This improvement is three-folds: the acoustic actuator shape would match that of the cavity, thus stronger acoustic waves would be generated; the volume to area ratio would be more favourable, thus boundary layer losses would be weaker; the dead volume between the square cavity and the tube could be filled with a fluid such as pressurized air, or even liquid D<sub>6</sub>, to serve as a thermal bath and enhance the temperature homogeneity inside the cavity. A second modification would be the replacement of the current fluid injection port by a smaller capillary tube to reduce the uncertainty on the estimation of the density which is a function of the unknown amount of liquid fluid contained in the inlet pipe. Finally, a solution should be elaborated to ensure the complete bleeding of the various pipes, which was not found to be possible with the current setup.

# Bibliography

- [1] B. Mercier, N. B. Chandrasekaran, and P. Colonna, “Speed of Sound Measurements in Dense Siloxane D<sub>6</sub> Vapor at Temperatures up to 645 K by Means of a New Prismatic Acoustic Resonator,” *Journal of Chemical & Engineering Data*, vol. 68, no. 3, pp. 561–573, Feb. 2023. DOI: [10.1021/acs.jced.2c00725](https://doi.org/10.1021/acs.jced.2c00725).
- [2] A. Uusitalo, T. Turunen-Saaresti, J. Honkatukia, P. Colonna, and J. Larjola, “Siloxanes as working fluids for mini-ORC systems based on high-speed turbogenerator technology,” *Journal of Engineering for Gas Turbines and Power*, vol. 135, no. 4, p. 042305, 2013. DOI: [10.1115/1.4023115](https://doi.org/10.1115/1.4023115).
- [3] P. Colonna, E. Casati, C. Trapp, *et al.*, “Organic Rankine cycle power systems: From the concept to current technology, applications, and an outlook to the future,” *Journal of Engineering for Gas Turbines and Power*, vol. 137, no. 10, p. 100801, 2015. DOI: [10.1115/1.4029884](https://doi.org/10.1115/1.4029884).
- [4] A. J. Head, “Novel experiments for the investigation of non-ideal compressible fluid dynamics: The ORCHID and first results of optical measurements,” Ph.D. dissertation, Delft University of Technology, 2021. DOI: [10.4233/uuid:a3b03976-2df6-435c-b7df-1505718fcd3a](https://doi.org/10.4233/uuid:a3b03976-2df6-435c-b7df-1505718fcd3a).
- [5] G. Angelino and C. Invernizzi, “Cyclic methylsiloxanes as working fluids for space power cycles,” *Journal of Solar Energy Engineering*, vol. 115, no. 3, pp. 130–137, 1993. DOI: [doi.org/10.1115/1.2930039](https://doi.org/10.1115/1.2930039).
- [6] P. Colonna, “Fluidi di lavoro multi componenti per cicli termodinamici di potenza (Multicomponent working fluids for power cycles),” Ph.D. dissertation, Politecnico di Milano, Oct. 1996.
- [7] M. Preißinger and D. Brüggemann, “Thermal stability of hexamethyldisiloxane (MM) for high-temperature organic Rankine cycle (ORC),” *Energies*, vol. 9, no. 3, p. 183, 2016. DOI: [10.3390/en9030183](https://doi.org/10.3390/en9030183).
- [8] L. Keulen, S. Gallarini, C. Landolina, *et al.*, “Thermal stability of hexamethyldisiloxane and octamethyltrisiloxane,” *Energy*, vol. 165, pp. 868–876, 2018. DOI: [10.1016/j.energy.2018.08.057](https://doi.org/10.1016/j.energy.2018.08.057).
- [9] S. Chen, C. Liu, Q. Li, Y. Liu, L. Xin, and W. Yu, “A ReaxFF-based molecular dynamics study of the pyrolysis mechanism of hexamethyldisiloxane,” *Journal of Molecular Liquids*, vol. 356, p. 119026, 2022. DOI: [10.1016/j.molliq.2022.119026](https://doi.org/10.1016/j.molliq.2022.119026).

- [10] *Dodecamethylcyclohexasiloxane, safety data sheet SID4625.0*, Online, 2014.
- [11] F. Leverone, M. Pini, A. Cervone, and E. Gill, “Solar energy harvesting on-board small satellites,” *Renewable Energy*, vol. 159, pp. 954–972, 2020. DOI: <https://doi.org/10.1016/j.renene.2020.05.176>.
- [12] P. Colonna, A. Guardone, and N. R. Nannan, “Siloxanes: A new class of candidate Bethe-Zel’dovich-Thompson fluids,” *Physics of Fluids*, vol. 19, no. 8, p. 086102, 2007. DOI: [10.1063/1.2759533](https://doi.org/10.1063/1.2759533).
- [13] A. Kluwick, “Rarefaction shocks,” in *Handbook of shock waves*, G. Bendor, O. Igra, and T. Elperin, Eds. Elsevier, 2001, vol. 1, ch. 3.4, pp. 339–411.
- [14] C. Zamfirescu, A. Guardone, and P. Colonna, “Admissibility region for rarefaction shock waves in dense gases,” *Journal of Fluid Mechanics*, vol. 599, pp. 363–381, 2008. DOI: [10.1017/S0022112008000207](https://doi.org/10.1017/S0022112008000207).
- [15] A. Guardone, C. Zamfirescu, and P. Colonna, “Maximum intensity of rarefaction shock waves for dense gases,” *Journal of Fluid Mechanics*, vol. 642, pp. 127–146, 2010. DOI: [10.1017/S0022112009991716](https://doi.org/10.1017/S0022112009991716).
- [16] N. R. Nannan, C. Sirianni, T. Mathijssen, A. Guardone, and P. Colonna, “The admissibility domain of rarefaction shock waves in the near-critical vapour–liquid equilibrium region of pure typical fluids,” *Journal of Fluid Mechanics*, vol. 795, pp. 241–261, 2016. DOI: [10.1017/jfm.2016.197](https://doi.org/10.1017/jfm.2016.197).
- [17] N. B. Chandrasekaran, B. Mercier, and P. Colonna, “Nonlinear wave propagation in dense vapor of Bethe–Zel’dovich–Thompson fluids subjected to temperature gradients,” *Physics of Fluids*, vol. 33, no. 10, p. 107109, 2021. DOI: [10.1063/5.0063226](https://doi.org/10.1063/5.0063226).
- [18] H. A. Bethe, “On the theory of shock waves for an arbitrary equation of state,” in *Classic Papers in Shock Compression Science*, J. N. Johnson and R. Chéret, Eds., ser. High-pressure shock compression of condensed matter. New York, NY: Springer, 1998, pp. 421–495. DOI: [10.1007/978-1-4612-2218-7\\_11](https://doi.org/10.1007/978-1-4612-2218-7_11).
- [19] Y. B. Zeldovich, “Selected works of Yakov Borisovich Zeldovich,” in R. A. Sunyaev, Ed. Princeton University Press, 2014, vol. 1, ch. On the possibility of rarefaction shock waves, pp. 152–154, From Y. B. Zel’dovich, On the possibility of rarefaction shock waves, *Zh. Eksp. Teor. Fiz.*, 16, 4, 363–364, 1946. DOI: [10.1515/9781400862979.152](https://doi.org/10.1515/9781400862979.152).
- [20] P. A. Thompson, “A fundamental derivative in gasdynamics,” *Physics of Fluids*, vol. 14, no. 9, pp. 1843–1849, 1971. DOI: [10.1063/1.1693693](https://doi.org/10.1063/1.1693693).

- [21] A. A. Borisov, A. A. Borisov, S. S. Kutateladze, and V. E. Nakoryakov, "Rarefaction shock wave near the critical liquid-vapour point," *Journal of Fluid Mechanics*, vol. 126, pp. 59–73, 1983. DOI: [10.1017/S002211208300004X](https://doi.org/10.1017/S002211208300004X).
- [22] S. Ferguson, A. Guardone, and B. Argrow, "Construction and validation of a dense gas shock tube," *Journal of Thermophysics and Heat Transfer*, vol. 17, no. 3, pp. 326–333, 2003. DOI: [10.2514/2.6789](https://doi.org/10.2514/2.6789).
- [23] P. Colonna, A. Guardone, N. R. Nannan, and C. Zamfirescu, "Design of the dense gas flexible asymmetric shock tube," *Journal of Fluids Engineering*, vol. 130, no. 3, p. 034501, 2008. DOI: [10.1115/1.2844585](https://doi.org/10.1115/1.2844585).
- [24] T. Mathijssen, M. Gallo, E. Casati, *et al.*, "The flexible asymmetric shock tube (FAST) - a Ludwig tube facility for wave propagation measurements in high-temperature vapours of organic fluids," *Experiments in Fluids*, vol. 56, no. 10, 195, 2015. DOI: [10.1007/s00348-015-2060-1](https://doi.org/10.1007/s00348-015-2060-1).
- [25] P. Colonna, N. R. Nannan, A. Guardone, and E. W. Lemmon, "Multiparameter equations of state for selected siloxanes," *Fluid Phase Equilibria*, p. 19, 2006. DOI: [10.1016/j.fluid.2006.04.015](https://doi.org/10.1016/j.fluid.2006.04.015).
- [26] P. Colonna, N. R. Nannan, and A. Guardone, "Multiparameter equations of state for siloxanes:  $[(\text{CH}_3)_3\text{Si-O}_{1/2}]_2\text{-[O-Si-(CH}_3)_2]_{i=1\dots 3}$ , and  $[\text{O-Si-(CH}_3)_2]_6$ ," *Fluid Phase Equilibria*, vol. 263, no. 2, pp. 115–130, 2008. DOI: [10.1016/j.fluid.2006.04.015](https://doi.org/10.1016/j.fluid.2006.04.015).
- [27] R. N. Nannan and P. Colonna, "Improvement on multiparameter equations of state for dimethylsiloxanes by adopting more accurate ideal-gas isobaric heat capacities: Supplementary to P. Colonna, N. R. Nannan, A. Guardone, E. W. Lemmon, *Fluid Phase Equilib.* 244, 193 (2006)," *Fluid Phase Equilibria*, vol. 280, no. 1–2, pp. 151–152, 2009, Short Communication. DOI: [10.1016/j.fluid.2009.02.009](https://doi.org/10.1016/j.fluid.2009.02.009).
- [28] M. Thol, G. Rutkai, A. Köster, *et al.*, "Thermodynamic properties of octamethylcyclotetrasiloxane," *Journal of Chemical & Engineering Data*, vol. 61, no. 7, pp. 2580–2595, 2016, ISSN: 0021-9568, 1520-5134. DOI: [10.1021/acs.jced.6b00261](https://doi.org/10.1021/acs.jced.6b00261).
- [29] M. Thol, F. H. Dubberke, E. Baumhögger, J. Vrabec, and R. Span, "Speed of sound measurements and fundamental equations of state for octamethyltrisiloxane and decamethyltetrasiloxane," *Journal of Chemical & Engineering Data*, vol. 62, no. 9, pp. 2633–2648, 2017. DOI: [10.1021/acs.jced.7b00092](https://doi.org/10.1021/acs.jced.7b00092).

- [30] M. Thol, M. A. Javed, E. Baumhögger, R. Span, and J. Vrabec, “Thermodynamic properties of dodecamethylpentasiloxane, tetradecamethylhexasiloxane, and decamethylcyclopentasiloxane,” *Industrial & Engineering Chemistry Research*, vol. 58, no. 22, pp. 9617–9635, 2019. DOI: [10.1021/acs.iecr.9b00608](https://doi.org/10.1021/acs.iecr.9b00608).
- [31] K. Meier, “The pulse-echo method for high precision measurements of the speed of sound in fluids,” Postdoctoral thesis, Helmut-Schmidt-Universität / Universität der Bundeswehr Hamburg, Apr. 2006.
- [32] H. Gedanitz, M. J. Dávila, E. Baumhögger, and R. Span, “An apparatus for the determination of speeds of sound in fluids,” *The Journal of Chemical Thermodynamics*, vol. 42, no. 4, pp. 478–483, 2010. DOI: [10.1016/j.jct.2009.11.002](https://doi.org/10.1016/j.jct.2009.11.002).
- [33] K. A. Gillis, “Thermodynamic properties of two gaseous halogenated ethers from speed-of-sound measurements: Difluoromethoxydifluoromethane and 2-difluoromethoxy-1,1,1-trifluoroethane,” *International Journal of Thermophysics*, vol. 15, no. 5, pp. 821–847, 1994. DOI: [10.1007/BF01447097](https://doi.org/10.1007/BF01447097).
- [34] J. J. Hurly, J. W. Schmidt, S. J. Boyes, and M. R. Moldover, “Virial equation of state of helium, xenon, and helium-xenon mixtures from speed-of-sound and burnett  $p\rho T$  measurements,” *International Journal of Thermophysics*, vol. 18, no. 3, pp. 579–634, 1997. DOI: [10.1007/BF02575125](https://doi.org/10.1007/BF02575125).
- [35] Q. Liu, X. Feng, B. An, and Y. Duan, “Speed of sound measurements using a cylindrical resonator for gaseous carbon dioxide and propene,” *Journal of Chemical & Engineering Data*, vol. 59, no. 9, pp. 2788–2798, 2014. DOI: [10.1021/je500424b](https://doi.org/10.1021/je500424b).
- [36] M. R. Moldover, M. Waxman, and M. Greenspan, “Spherical acoustic resonators for temperature and thermophysical property measurements,” *High Temperature High Pressure*, vol. 11, p. 75, 1979.
- [37] M. R. Moldover, J. P. M. Trusler, T. J. Edwards, J. B. Mehl, and R. S. Davis, “Measurement of the universal gas-constant R using a spherical acoustic resonator,” *Journal of Research of the National Bureau of Standards*, vol. 93, no. 2, pp. 85–144, 1988.
- [38] J. P. M. Trusler and M. Zarari, “The speed of sound and derived thermodynamic properties of methane at temperatures between 275 K and 375 K and pressures up to 10 MPa,” *The Journal of Chemical Thermodynamics*, vol. 24, no. 9, pp. 973–991, 1992. DOI: [10.1016/S0021-9614\(05\)80008-4](https://doi.org/10.1016/S0021-9614(05)80008-4).

- [39] J. G. Hirschberg, J. D. Byrne, A. W. Wouters, and G. C. Boynton, "Speed of sound and temperature in the ocean by Brillouin scattering," *Applied Optics*, vol. 23, no. 15, pp. 2624–2628, 1984. DOI: [10.1364/AO.23.002624](https://doi.org/10.1364/AO.23.002624).
- [40] X. Zheng, Y. Zhang, and M. He, "Speed of sound measurement in ethyl tert-butyl ether and tert-amyl methyl ether by Brillouin light scattering," *Fluid Phase Equilibria*, vol. 418, pp. 108–118, 2016. DOI: [10.1016/j.fluid.2015.10.026](https://doi.org/10.1016/j.fluid.2015.10.026).
- [41] T. Zhan, J. Chen, X. Li, Q. Zhou, M. He, and Y. Zhang, "Speed of sound for ethanol in vicinity of the critical point from Rayleigh-Brillouin light scattering spectroscopy," *Fluid Phase Equilibria*, vol. 515, p. 112585, 2020. DOI: [10.1016/j.fluid.2020.112585](https://doi.org/10.1016/j.fluid.2020.112585).
- [42] D. L. Timrot, M. A. Serednitskaya, and N. N. Alekseev, "Experimental study of the speed of sound in Dowtherm vapor," *Journal of Engineering Physics*, vol. 33, no. 5, pp. 1311–1314, 1977. DOI: [10.1007/BF00860905](https://doi.org/10.1007/BF00860905).
- [43] B. Mercier, T. Castelain, E. Jondeau, and C. Bailly, "Density fluctuations measurement by Rayleigh scattering using a single photomultiplier," *AIAA Journal*, vol. 56, no. 4, pp. 1310–1316, 2018, ISSN: 0001-1452, 1533-385X. DOI: [10.2514/1.J056507](https://doi.org/10.2514/1.J056507).
- [44] M. Suchenek and T. Borowski, "Measuring sound speed in gas mixtures using a photoacoustic generator," *International Journal of Thermophysics*, vol. 39, no. 1, p. 11, 2018. DOI: [10.1007/s10765-017-2335-2](https://doi.org/10.1007/s10765-017-2335-2).
- [45] P. Colonna, T. P. van der Stelt, and A. Guardone, *FluidProp (Version 3.1): A program for the estimation of thermophysical properties of fluids*, A computer program since 2004, 2019.
- [46] T. P. van der Stelt, N. R. Nannan, and P. Colonna, "The iPRSV equation of state," *Fluid Phase Equilib.*, vol. 330, pp. 24–35, 2012. DOI: [10.1016/j.fluid.2012.06.007](https://doi.org/10.1016/j.fluid.2012.06.007).
- [47] T. H. Chung, M. Ajlan, L. L. Lee, and K. E. Starling, "Generalized multiparameter correlation for non-polar and polar fluid transport properties.," *Industrial & Engineering Chemistry Research*, vol. 27, no. 4, pp. 671–679, 1988. DOI: [10.1021/ie00076a024](https://doi.org/10.1021/ie00076a024).
- [48] N. R. Nannan, P. Colonna, C. M. Tracy, R. L. Rowley, and J. J. Hurly, "Ideal-gas heat capacities of dimethylsiloxanes from speed-of-sound measurements and ab initio calculations," *Fluid Phase Equilibria*, vol. 257, no. 1, pp. 102–113, 2007. DOI: [10.1016/j.fluid.2007.04.028](https://doi.org/10.1016/j.fluid.2007.04.028).

- [49] M. Gasior, “Improving FFT frequency measurement resolution by parabolic and Gaussian spectrum interpolation,” in *AIP conference proceedings*, vol. 732, Knoxville, Tennessee (USA): AIP, 2004, pp. 276–285. DOI: [10.1063/1.1831158](https://doi.org/10.1063/1.1831158).
- [50] J. T. Zhang, H. Lin, J. P. Sun, X. J. Feng, K. A. Gillis, and M. R. Moldover, “Cylindrical Acoustic Resonator for the Re-determination of the Boltzmann Constant,” *International Journal of Thermophysics*, vol. 31, no. 7, pp. 1273–1293, Jun. 2010. DOI: [10.1007/s10765-010-0754-4](https://doi.org/10.1007/s10765-010-0754-4).

# 7

## Conclusions and recommendations

### 7.1. Key findings

This thesis presents experimental efforts to verify nonclassical gasdynamic effects in the dense-vapour flows of Bethe-Zel'dovich-Thompson (BZT) fluids. The nonclassical gasdynamic region in the dense vapour phase of Bethe-Zel'dovich-Thompson (BZT) fluids, as explained in Chapter 1, is characterized by negative values of the fundamental derivative of gasdynamics  $\Gamma$ , a thermodynamic property which determines the variation of the convected soundspeed with pressure. Unconventional gasdynamic phenomena such as rarefaction shockwaves (RSW) and isentropic compression fans are theoretically admissible if the flow evolves with the fluid, even partially, in thermodynamic states featuring negative values of  $\Gamma$ .

The existence of nonclassical gas dynamics has been studied extensively in theory, as outlined in Chapter 2. However, there is a lack of experimental evidence to corroborate these predictions. Previous efforts to demonstrate the existence of nonclassical gasdynamic effects in BZT fluids have suffered from numerous difficulties, including the incorrect choice of the working fluid and thermal decomposition due to air and moisture dissolved in the fluid. A brief history of the various experimental attempts to date, including the most recent endeavour using the Flexible Asymmetric Shock Tube (FAST) facility at TU Delft, is presented in Chapter 3.

As part of this research, a study was conducted to investigate the effect of axial temperature gradients in a BZT fluid on nonlinear wave propagation. Such gradients, though unwanted, are often unavoidable in setups of large

sizes. Simulations of nonlinear wave propagation in a tube containing the BZT fluid siloxane  $D_6$  subjected to different axial temperature variations were studied using both analytical and numerical solutions. Fluid thermodynamic properties were calculated with the state-of-the-art multiparameter equation of state (EoS) model and viscous effects were considered. The main findings of this study are:

- In the presence of a non-uniform temperature distribution in the fluid, a minimum initial slope (in pressure) is required for a rarefaction wave propagating in this fluid to steepen into a RSW. The value of this minimum slope depends on the nature and magnitude of the variation of the axial temperature.
- Gradients in the axial temperature of the fluid also result in gradients in the local sound speed and density. These gradients in fluid properties also affect the steepening characteristics of propagating waves. The influence of these gradients is particularly noticeable in fluid states with  $\Gamma \approx 0$ , where they can cause waves to steepen in a manner opposite to what is expected based on the local value of  $\Gamma$ . For example, a rarefaction wave can steepen and a compression can relax when  $\Gamma > 0$ , and vice-versa when  $\Gamma < 0$ .
- Temperature gradients can enhance the steepening of a finite-amplitude rarefaction wave propagating in a BZT fluid featuring states for which  $\Gamma < 0$ . This can cause the wave to steepen into a RSW at a shorter distance from the wave origin than in a homogeneous medium. This suggests that the presence of temperature gradients in a test facility need not be necessarily detrimental to the outcome of nonclassical experiments. However, this enhancing effect diminishes with increasing initial wave slopes.
- In contrast, compression waves propagating in a BZT fluid with thermodynamic states where  $\Gamma > 0$  are less affected by temperature gradients. The distance at which shock formation occurs remains nearly constant and unchanged with respect to the homogeneous condition. The reason for this difference in behavior between compression and expansion waves is that the values of  $\Gamma$ ,  $\rho$ , and  $c$  are much more sensitive to temperature variations in the  $\Gamma < 0$  region than in the  $\Gamma > 0$  region.

A new test setup called the Asymmetric Shock Tube for Experiments on Rarefaction Waves (ASTER) was designed and developed to perform nonclassical gasdynamic experiments using  $D_6$  as the working fluid. The ASTER is a Ludwig-type shock tube setup that shares both the basic design features and the experimental aim of the FAST. Lessons learned through working with the

FAST were incorporated into the design of the ASTER, resulting in a more compact and simpler setup with a straightforward control system. Most importantly, the ASTER features a glass-disk barrier element that is resistant to high pressures and temperatures, can break almost instantaneously by means of a manually actuated pin, and is easy to replace. The ASTER was employed to perform rarefaction tests with the aim of measuring, for the first time, a nonclassical rarefaction shock wave (RSW). The speed of the propagating wave was estimated using a time-of-flight (ToF) method. If this wave propagation speed was higher than the local speed of sound in the working fluid, then the wave would be a RSW. A detailed description of the design, instrumentation and the working of the ASTER is presented in Chapter 5.

Compared to other simpler siloxanes, there is a lack of accurate measurements of sound speed in  $D_6$ , especially in the dense-vapour states close to the critical point. Sound speed measurements are useful not only for verifying the formation of RSWs, but also for improving state-of-the-art thermodynamic models that rely on extensive, accurate thermodynamic data to robustly model fluid properties. The speed of sound in  $D_6$  was estimated both during the rarefaction tests and by using the novel Organic Vapour Acoustic Resonator (OVAR) setup, described in Chapter 6. The OVAR is a square-cylindrical resonator that exploits the modal behavior of acoustics in an enclosed cavity. Although a spherical resonator provides higher accuracy, a square-cylindrical cross-section was found to be more suitable for the study described here due to its ease of construction and ability to house a larger excitation system that results in stronger acoustic levels in the vapours. The OVAR was also used to measure the density of the fluid in addition to the sound speed.

The following observations can be highlighted from the experimental campaigns:

- Rarefaction wave tests were performed in  $D_6$  ranging from the mildly non-ideal to the dense-vapour thermodynamic states. Wavespeed measurements with tests in which the fluid is in mildly non-ideal states show a classical variation with the pressure drop across a wave. Tests with the fluid in dense-vapour states, in contrast, show a clear deviation from this classical variation. The wavespeed displays a weaker variation with the pressure drop across the wave, when compared with the model predictions. This indicates the presence of strong non-ideal effects in the flow-field.
- A main feature of a nonclassical isentropic expansion is the increase in the wavespeed across such an expansion (see Fig. 5.16). This exotic variation of the wavespeed was not observed in any of the tests with the quiescent fluid in dense-vapour states. The current thermodynamic models for  $D_6$  are known to be inaccurate compared to other siloxanes,

especially for thermodynamic states close to the critical point and the saturation curve where nonclassical gasdynamics can be expected. Thus, even though the multiparameter EoS predicted negative values of  $\Gamma$  for the tests with the quiescent fluid in dense-vapour states, it is possible that the fluid was in states in which  $\Gamma$  was still positive.

- For tests in the dense-vapour states of  $D_6$  (Tests 4 to 8 in Table 5.5), the slope of the wavespeed vs  $\Delta P$  across the expansion is close to zero for certain ranges of  $\Delta P$ . Since the wavespeed is constant across a RSW (i.e., the slope of this curve is zero), this observation suggests the possible existence of a nonclassical RSW in the flow field.
- The value of the fundamental derivative  $\Gamma$  is estimated from wave speed measurements. This estimation corresponds to observations from wave speed versus  $\Delta P$  plots. In certain ranges of  $\Delta P$ , the value is close to zero and remains constant, suggesting the presence of BZT effects in those ranges. However, because this value is a derivative of the primary measured value, it is subject to large uncertainties.
- The soundspeed and density were measured along eight isotherms (between 282 °C and 372 °C) in the dense vapour states ( $0.44 < Z < 0.95$ ) using the OVAR setup. The experimental measurements were compared with values calculated with the iPRSV EoS model. The predictions of this model agreed with experimental measurements for pressure ratios of  $p/p^{\text{sat}} < 0.7$ , where  $p^{\text{sat}}$  is the saturation pressure of  $D_6$  at a given temperature. However, the deviation between these values increased to as much as 5% for  $p/p^{\text{sat}} \approx 0.9$ . The iPRSV soundspeed predictions, however, all lie within -2% and 0% of the measured value except for states along the highest isotherm, for which the deviation was  $\approx -4\%$ .

7

## 7.2. Recommendations

The results of this experimental work are promising in that they indicate the possible existence of nonclassical gasdynamic effects. However, many questions still remain unanswered. First and foremost, more and repeatable experiments are needed. Moreover, the possibility of fluid condensation must be ruled out, as well as of other possible perturbations, like temperature gradients in the quiescent fluid. Moreover, the range of pressures and temperatures in which a negative value of  $\Gamma$  can be expected is not known because the state-of-the-art thermodynamic model is insufficiently accurate. Whether the fluid undergoes thermal decomposition at high temperature is not fully clear, and, in that case, what is its impact on the experimental results.

Suggestions and possible future directions in which this research can head, are as follows:

1. Developing a more accurate thermodynamic model for  $D_6$

The properties of siloxane  $D_6$  in this research have been estimated using an in-house software implementing a multiparameter EoS. The accuracy of this thermodynamic model relies on precise experimental measurements, particularly under conditions where nonclassical effects are expected. However, compared to other siloxanes, there is a scarcity of such data available for  $D_6$ . Consequently, the accuracy of property estimations using this EoS is adversely affected.

For example, as described in Section 5.3.6, the VLE curve for  $D_6$  suffers from a significant uncertainty. This is mainly because experimental measurements of saturation pressure  $p_{\text{sat}}$  of  $D_6$  exist only up to 260 °C and the critical point has an associated uncertainty of 10% in pressure and 5% in temperature. These uncertainties, determined somewhat arbitrarily by DIPPR, are likely too large and may contribute to the challenges encountered in accurately predicting the fluid properties in states close to the critical point.

More accurate fluid property measurements are therefore necessary not just for the success of the envisaged rarefaction experiments, but to also develop a more accurate EoS for the fluid. The speed of sound measurements performed in the OVAR (see Chapter 6) are one such example. However, both the ASTER and the OVAR are not suitable for measuring properties such as the critical point or the VLE curve. This can be achieved for example through collaborations with other institutes that possess experimental setups suitable for such measurements.

2. Study of the effect of temperature gradients along the charge tube of the ASTER

One of the major contributions of this research work involved the analysis of the steepening characteristics of finite amplitude waves that propagate in a BZT fluid that is subjected to axial temperature gradients. The need for such a study stemmed from observations of temperature inhomogeneity along the FAST charge tube. As a consequence of this observation, aluminium shells were added to the charge tube of the ASTER to homogenize the axial temperature. However, the internal wall temperature of the ASTER was not measured prior to conducting experiments. The design of the ASTER already incorporated a 3 mm wide groove in the aluminium shells for measuring the temperature along the stainless steel wall using a thermocouple. However, this groove proved to be too narrow to slide a thermocouple along the tube, especially at high temperatures.

Knowledge of the inner wall temperature can help verify if the addition of aluminium shells was successful in homogenizing the axial temperature. It can also help identify cold spots and sites of possible local condensation of  $D_6$ , thus possibly solutions to this problem.

This study also focussed primarily on the longitudinal variation in temperature since this was along the direction of wave travel. The associated length scales also meant that the gradient in the axial direction was the most significant (the aspect ratios of charge tubes (CT) of the FAST and the ASTER are 450 and 200 respectively). In the ASTER, the fluid is directly heated in the CT. As the fluid evaporates, the top wall in contact with the hot vapours can have a slightly higher temperature when compared with the bottom wall that is in contact with liquid  $D_6$ . This creates a temperature gradient in the radial direction. Such gradients can result in variations in the sound speed and density, which in turn can distort the wavefront leading to a complex flow field in the CT. It is, therefore, useful to extend the study on temperature effects on the nonlinear steepening of waves to include two-dimensional variations in temperature and to understand the impact this can have on the formation of rarefaction shockwaves.

3. Explanation of the change in the pressure gradient close to the head of the wave in dense-gas tests

An interesting feature of the pressure signals obtained during rarefaction tests is the presence of an abrupt change in the pressure gradient close to the head of the wave. An initial hypothesis was that the breaking pin might temporarily block the flow close to the throat of the nozzle. However, this distortion was absent both during tests in ideal-gas and  $D_6$  in the mildly-ideal gasdynamic region. This suggests that this change in the gradient could be a gasdynamic effect. At the moment of writing, no explanation could be given for the existence of this step. Further investigations into the occurrence of this change, for example, using numerical simulations, can provide valuable insight into the behaviour of this fluid at conditions close to the critical point.

4. Improve fluid volume estimation while charging the setup.

When designing the ASTER, a primary objective was to keep the setup as simple and compact as possible. As a result, and unlike the FAST, the ASTER does not have an external tank with a precisely known volume in which the fluid is vaporized before filling the CT. Instead, a hand pump is used to fill the charge tube (CT), where the fluid is heated directly. While this eliminates the need for multiple components in the setup, it does not allow for direct measurement of the volume of liquid injected.

Knowledge of the fluid volume is crucial for successful experimentation, as achieving the experimental initial conditions relies on an accurate volume of the fluid being injected into the CT.

Future modifications to the ASTER can include a suitable flowmeter to measure the amount of fluid injected into the CT. Since the fluid is fed using a hand pump, this flowmeter must be suitable for discrete flow applications. A separate heating tank, like the Heated Fluid Tank (HFT) in the FAST, can also be designed and installed in the ASTER to enable charging the setup with a precise quantity of the working fluid.

5. Investigate the effect of thermal decomposition of the fluid.

One of the reasons for choosing a siloxane as the test fluid over other classes of compounds such as perfluorocarbons, which are also predicted to exhibit nonclassical behaviour, is the relatively high thermal stability, together with the fact that in case of decomposition no hazardous compound can be formed. Nonetheless, with the operating temperature of the experiment being close to the thermal stability limit of the fluid, it is possible that the fluid undergoes thermal degradation. The presence of oxygen and humidity in the setup can also negatively influence their thermal stability. Though care is taken, both in the ASTER and the OVAR, to remove oxygen and moisture in the setup as much as possible, residual traces of such impurities might still be present in them. As mentioned in Chapter 6, detectable amounts of incondensable gases were found during successive tests using the same fluid samples in the OVAR. This was observed during experiments as a small yet continuous increase in the pressure. Also, impurities in the form of black particles were found in the fluid after exposure to high temperatures for a long time. These are possibly carbon conglomerates which form as a result of chemical reactions. Such products seemed to appear only when the temperature approached 360 °C and higher. No further analysis was conducted to estimate the composition or the concentration of these particles or gases. Future experiments using the ASTER and the OVAR would benefit from a more accurate estimation of the thermal stability limit of D<sub>6</sub> in contact with stainless steel and its main degradation path.



# A

## Rarefaction experiments in the ASTER

**A.1.** Test 1:  $P_0 = 2.66$  bar,  $T_0 = 349.8$  °C,  $\Gamma_{\text{model}} = 0.87$

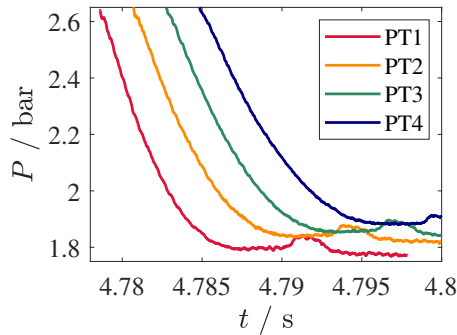


Figure A.1: Relevant portion of the pressure signal from Test 1 for computing the wavespeed using the time-of-flight method

The relevant portions of the pressure recordings from the four Kulite sensors that are used for computing the wavespeed using the ToF method (refer Section 5.3.4) are shown in Fig. A.1. This test was performed in the mildly non-ideal gasdynamic region ( $0.7 < \Gamma < 1$ ) of  $D_6$ . The corresponding wavespeed estimates are displayed in Figs. A.2a to A.2f and the variation of  $dw/dp$  with pressure drop across the wave are shown in Figs. A.3a to A.3f. Following the discussions presented in Section 5.3.4, it can be observed in Figs. A.2a to A.3f

## A

that the wavespeed and  $dw/dp$  closely follow the theoretical predictions as is expected in this thermodynamic region. Significant deviations are observed in the values obtained using sensor pairs PT2-PT3 and PT3-PT4, possibly due to the possible presence of temperature gradients. Figures A.3a to A.3f also show a linear regression line of the experimental  $dw/dp$  data. This fit shows a close accordance with the theoretical value for all sensor pairs. The value of  $dw/dp$  is positive, and increases with the pressure drop across the wave; thus, nonclassical effects are absent in the fluid. The oscillations observed in Figs. A.3a to A.3f arise from the filtering of the wavespeed data, needed to limit the impact of noise that is amplified as a result of the differentiation.

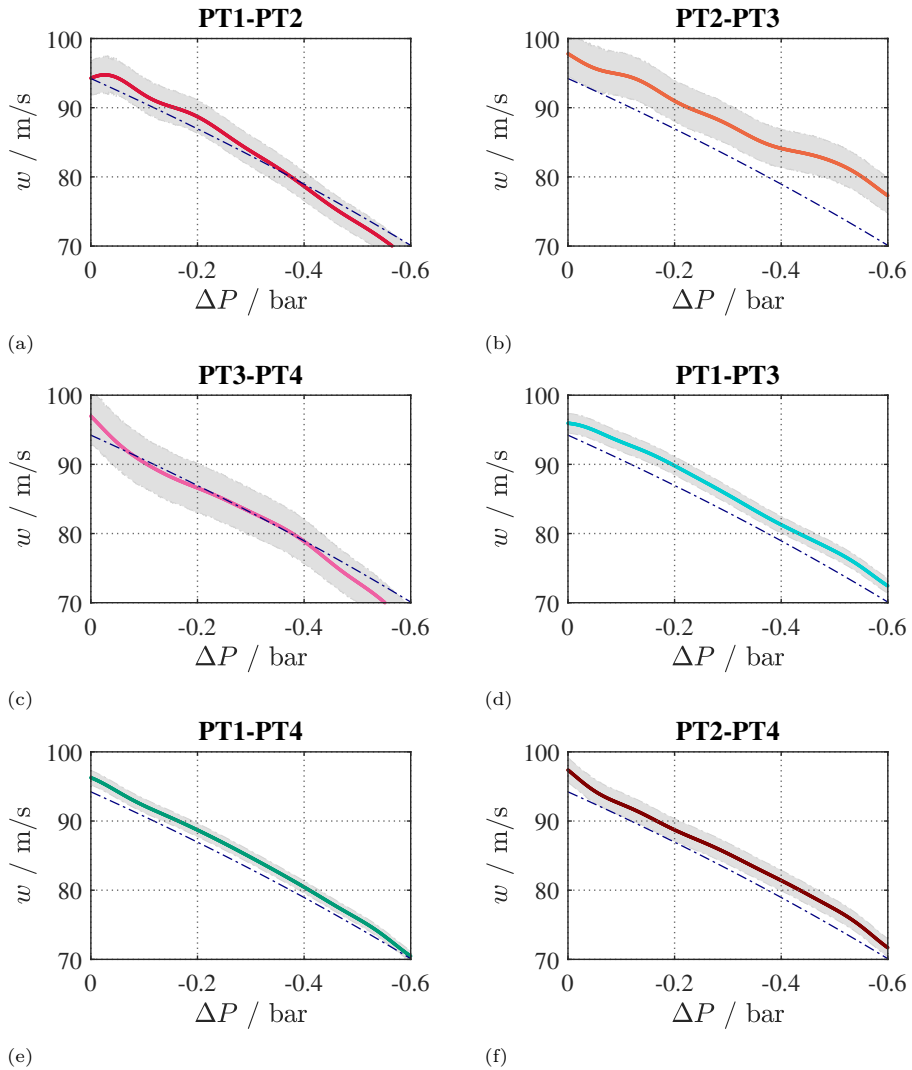


Figure A.2: Wavespeed measurements estimated using different sensor pairs from Test 1 (see Table 5.5). Each dot represents a time-of-flight estimation of the wavespeed at pressure intervals of 15 mbar. (---): theoretical isentropic wavespeed calculated using the thermodynamic model [1] for a shock-free flow. Uncertainty bands on the wavespeed are shown in grey.

A

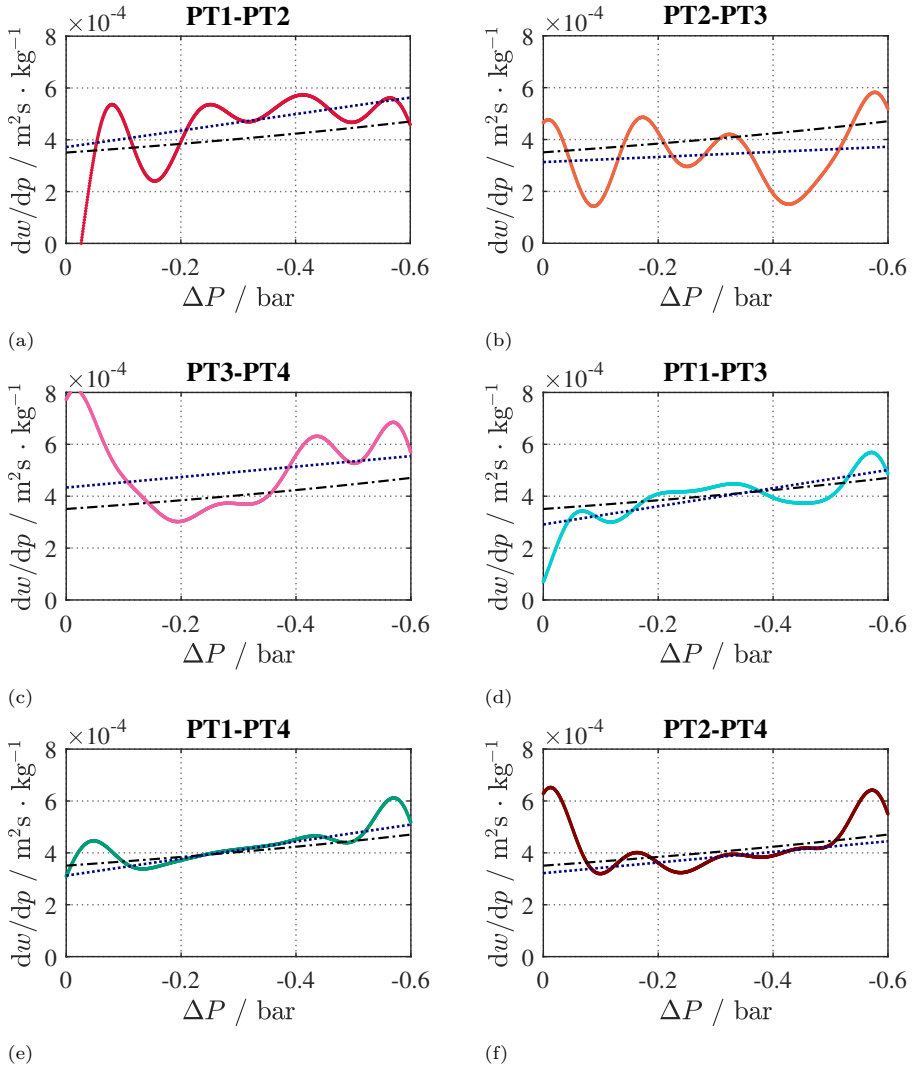


Figure A.3: Derivative of wavespeed with respect to pressure for different sensor pairs for Test 1. (---): prediction of the thermodynamic model. (.....): linear fit of experimental data

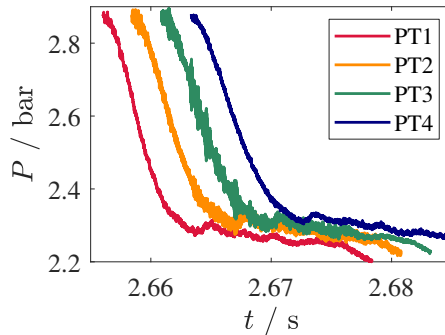
**A.2. Test 2:  $P_0 = 2.89$  bar,  $T_0 = 300.3$  °C,  $\Gamma_{\text{model}} = 0.74$** **A**

Figure A.4: Relevant portion of the pressure signal from Test 2 for computing the wavespeed using the time-of-flight method

The relevant portions of the pressure recordings from the four Kulite sensors that are used for computing the wavespeed using the ToF method (refer Section 5.3.4) are shown in Fig. A.4. The corresponding wavespeed estimates are displayed in Figs. A.5a to A.5f and the variation of  $dw/dp$  with pressure drop across the wave are shown in Figs. A.6a to A.6f. Significant noise can be observed in sensors PT2 and PT3. One possible explanation for this noise could be that the test was performed close to the saturation curve (see Fig. 5.11). Thus, any cold spot in the setup could have led to local condensation. As mentioned in Section 5.3.4, such a cold spot can be expected between sensors PT2 and PT3 due to a gap in the thermal blankets. Thus, it is possible that liquid  $D_6$  might have covered the sensors leading to an increased noise in the measurements.

The effect of this noise is evident in the estimates of wavespeed (Figs. A.5a to A.5f) and  $dw/dp$  (Figs. A.6a to A.6f). In the case of wavespeed, strong oscillations in the data are observed except for the case of the wavespeed estimated using sensors PT1-PT4 and PT2-PT4. The general trend in the variation of  $w$  with  $\Delta P$ , however, is similar to that obtained using the thermodynamic model. The variation of  $dw/dp$  with  $\Delta P$  is greatly affected by the noise that no meaningful conclusion can be made from Figs. A.6a to A.6d. Similar to the wavespeed data,  $dw/dp$  obtained using sensors PT1-PT4 and PT2-PT4 are less affected by noise and show that the estimation from the experimental data agrees with the theoretical prediction.

A

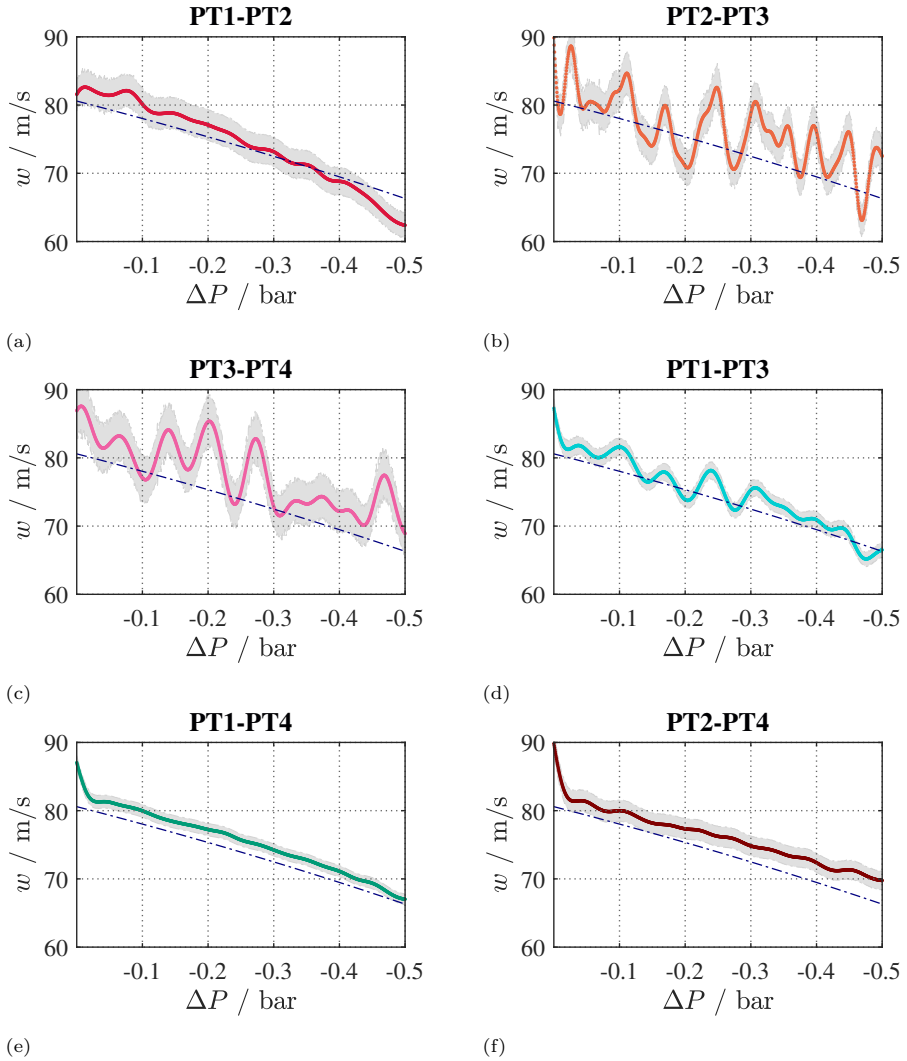


Figure A.5: Wavespeed measurements estimated using different sensor pairs from Test 2 (see Table 5.5). Each dot represents a time-of-flight estimation of the wavespeed at pressure intervals of 15 mbar. (---): theoretical isentropic wavespeed calculated using the thermodynamic model [1] for a shock-free flow. Uncertainty bands on the wavespeed are shown in grey.

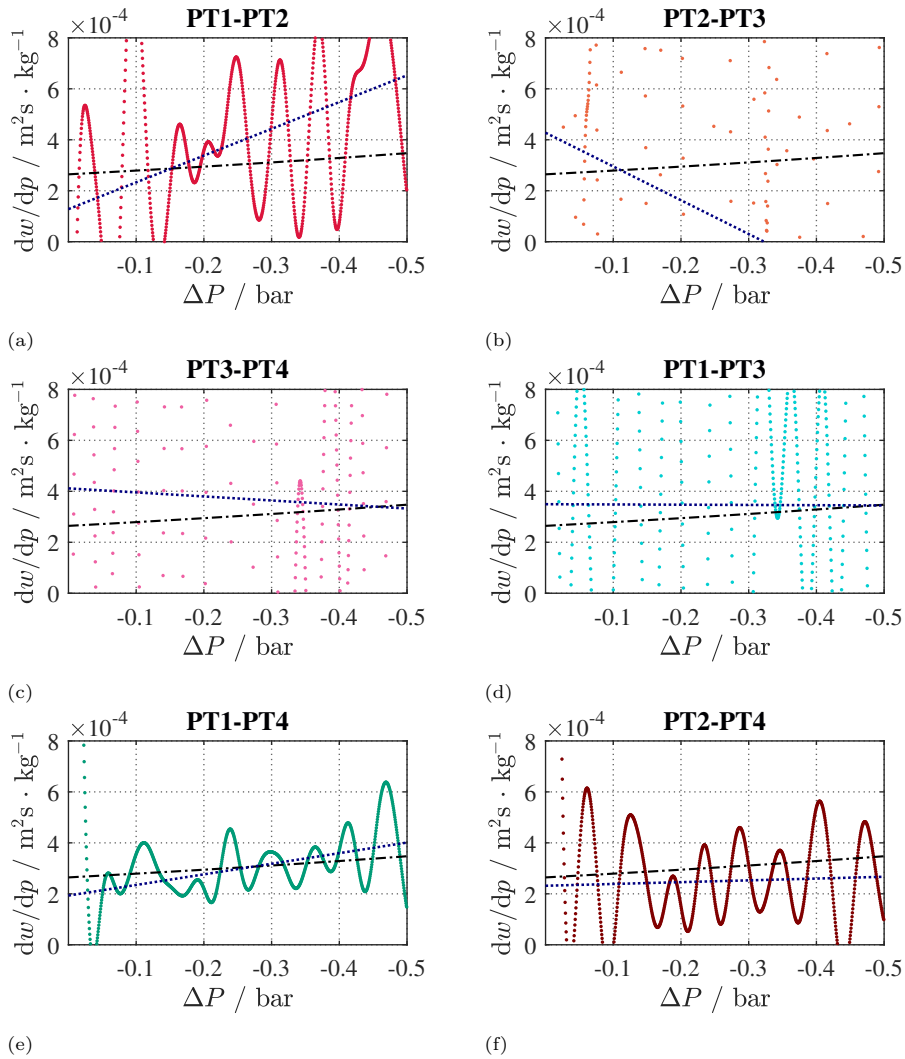


Figure A.6: Derivative of wavespeed with respect to pressure for different sensor pairs for Test 2. (---): prediction of the thermodynamic model. (.....): linear fit of experimental data

### A.3. Test 3: $P_0 = 5.85$ bar, $T_0 = 357.6$ °C, $\Gamma_{\text{model}} = 0.58$

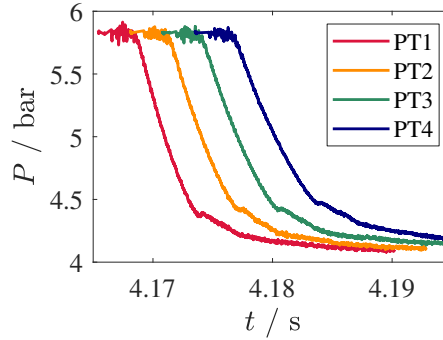


Figure A.7: Relevant portion of the pressure signal from Test 3 for computing the wavespeed using the time-of-flight method

The relevant portions of the pressure recordings from the four Kulite sensors that are used for computing the wavespeed using the ToF method (refer Section 5.3.4) are shown in Fig. A.7. With  $\Gamma_{\text{model}} = 0.58$ , this test is in the thermodynamic region where relatively strong non-ideal effects can be expected. This is already observed in Fig. A.7, where the pressure signals are steeper when compared to those from Test 1 (see Fig. A.1), which was performed in the “mildly non-ideal” region. Unlike the smooth variations in pressure observed in Tests 1 & 2, a kink is also seen close to the tail of the wave.

Figures A.8a to A.8f show the variation in  $w$  with  $\Delta P$  across the expansion wave. The estimated wavespeed differs significantly from the theoretical value and is seen to be less sensitive to the drop in pressure across the wave. This could indicate that the value of  $\Gamma$  in the flow is lower than what is predicted by the thermodynamic model. This is also observed in the variation of  $dw/dp$  with  $\Delta P$  shown in Figs. A.9a to A.9f. The value of the fundamental derivative at stagnation conditions ( $\Gamma = \Gamma_0$ ), obtained by extrapolating the linear fit of  $dw/dp$  to  $\Delta P = 0$ , shows that  $\Gamma_0$  from experiments is consistently lower than that provided by the model. This is possible, since there is scarce experimental data available for  $D_6$  at these thermodynamic conditions.

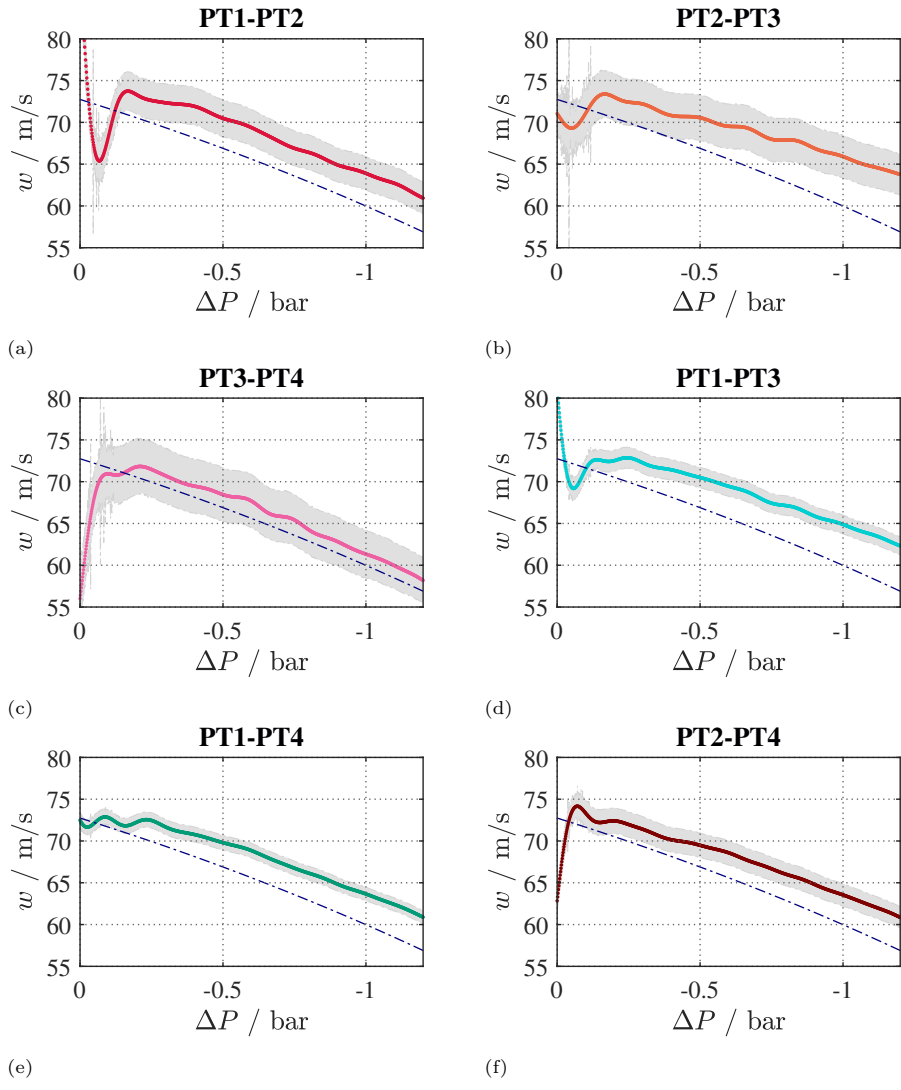


Figure A.8: Wavespeed measurements estimated using different sensor pairs from Test 3 (see Table 5.5). Each dot represents a time-of-flight estimation of the wavespeed at pressure intervals of 15 mbar. (-·-·-): theoretical isentropic wavespeed calculated using the thermodynamic model [1] for a shock-free flow. Uncertainty bands on the wavespeed are shown in grey.

A

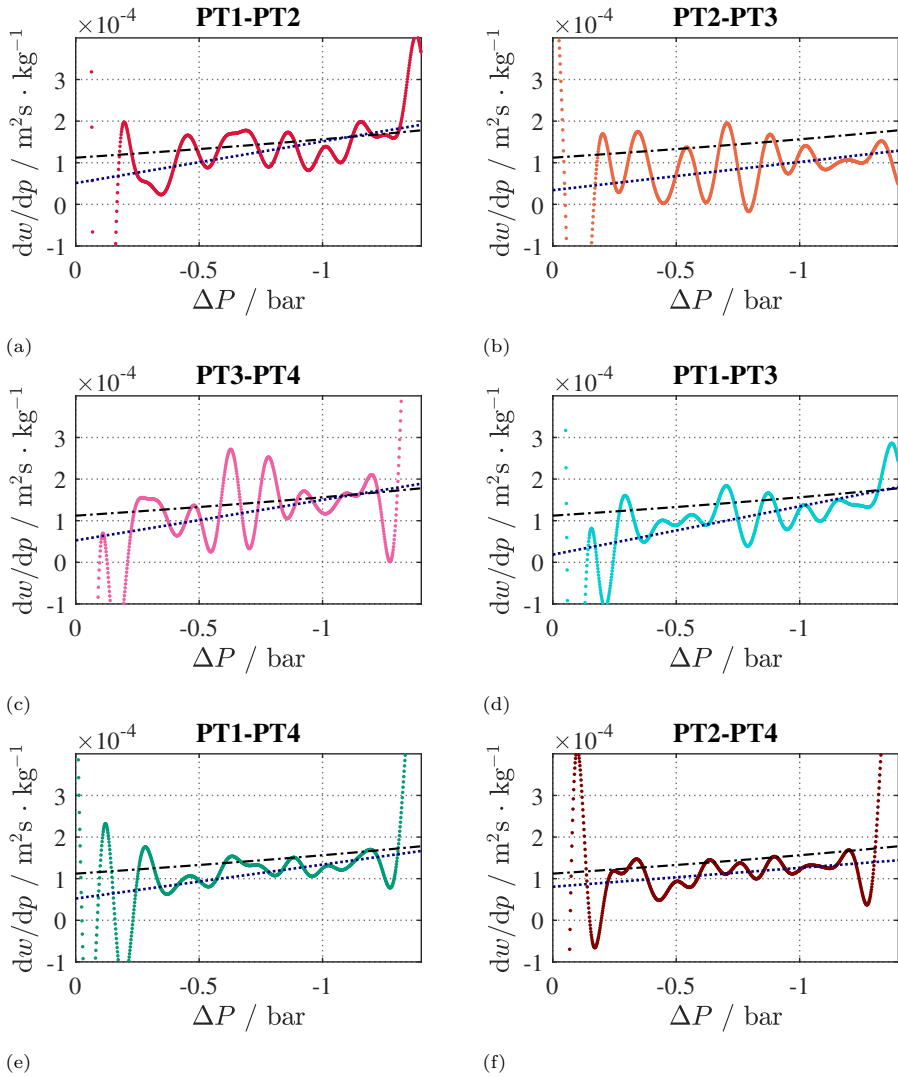


Figure A.9: Derivative of wavespeed with respect to pressure for different sensor pairs for Test 3. (---): prediction of the thermodynamic model. (.....): linear fit of experimental data

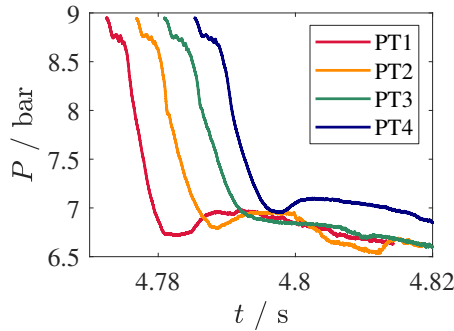
**A.4. Test 4:  $P_0 = 8.87$  bar,  $T_0 = 370.9$  °C,  $\Gamma_{\text{model}} = 0.096$** **A**

Figure A.10: Relevant portion of the pressure signal from Test 4 for computing the wavespeed using the time-of-flight method

The relevant portions of the pressure recordings from the four Kulite sensors that are used for computing the wavespeed using the ToF method (refer Section 5.3.4) are shown in Fig. A.10. Again, strong non-ideal effects can be observed in this figure with the pressure signals being much steeper than in the previous tests (see Figs. A.1, A.4 and A.7). Two kinks can now be observed, one close to the head of the wave and the other at  $P \approx 8$  bar. The reason for the presence of such kinks is not yet known but they are observed only during experiments in the dense-gas thermodynamic region.

Figures A.11a to A.11f show the variation in  $w$  with  $\Delta P$  across the expansion wave. The estimated wavespeed not only differs significantly from the theoretical value but also no longer smoothly varies along the wave. Though the wavespeed plots don't feature a horizontal line which would indicate the presence of a RSW in the flow (see the discussions of Section 5.3.4), it features several regions where the wavespeed varies only slightly with the drop in pressure. The wavespeed estimated using sensor pairs PT1-PT4 and PT2-PT4 show the highest degree of flatness, with the wavespeed varying by less than 3 m/s across the wave. Similar observations can be made from the variation of  $dw/dp$  with  $\Delta P$  shown in Figs. A.12a to A.12f. Except for Fig. A.12b and Fig. A.12c, the linear fits in all other charts are nearly horizontal with  $\Gamma_0$  being close to zero. This is typical of an expansion taking place close to the boundary of  $\Gamma < 0$  region, in the presence of strong non-ideal effects.

A

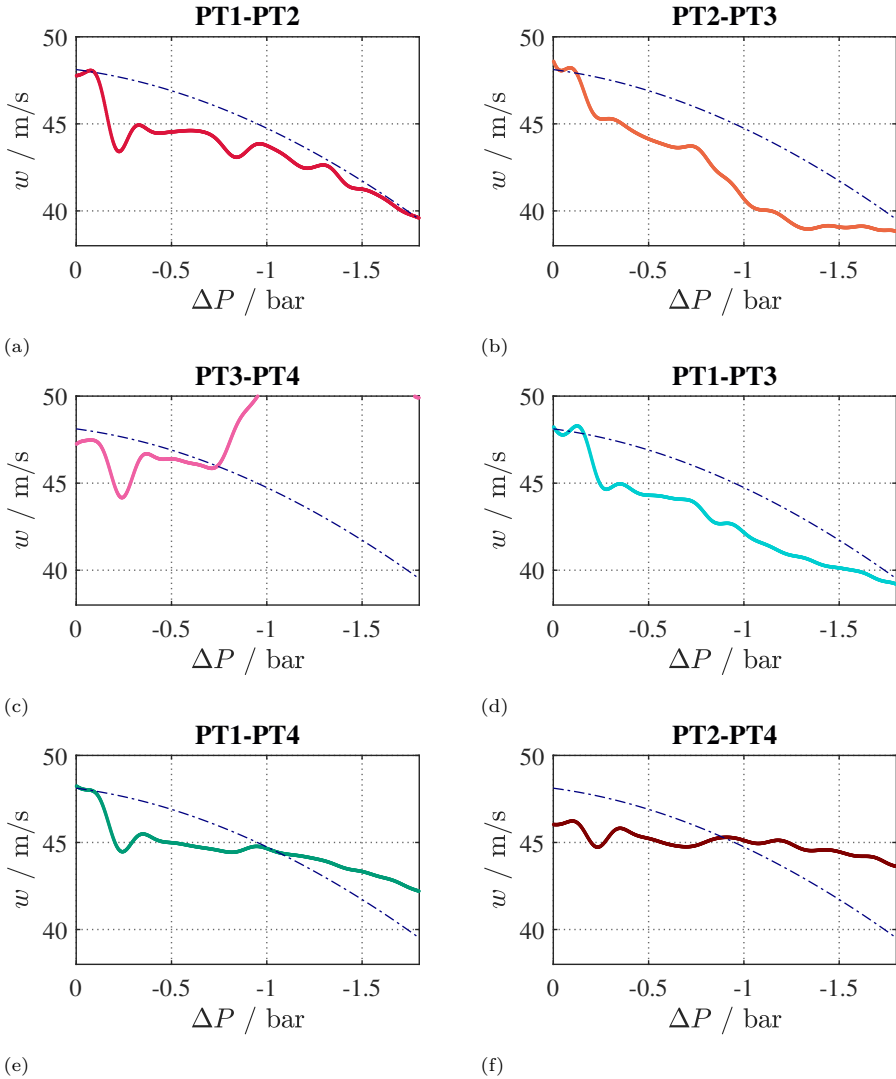


Figure A.11: Wavespeed measurements estimated using different sensor pairs from Test 4 (see Table 5.5). Each dot represents a time-of-flight estimation of the wavespeed at pressure intervals of 15 mbar. (---): theoretical isentropic wavespeed calculated using the thermodynamic model [1] for a shock-free flow. Uncertainty bands on the wavespeed are shown in grey.

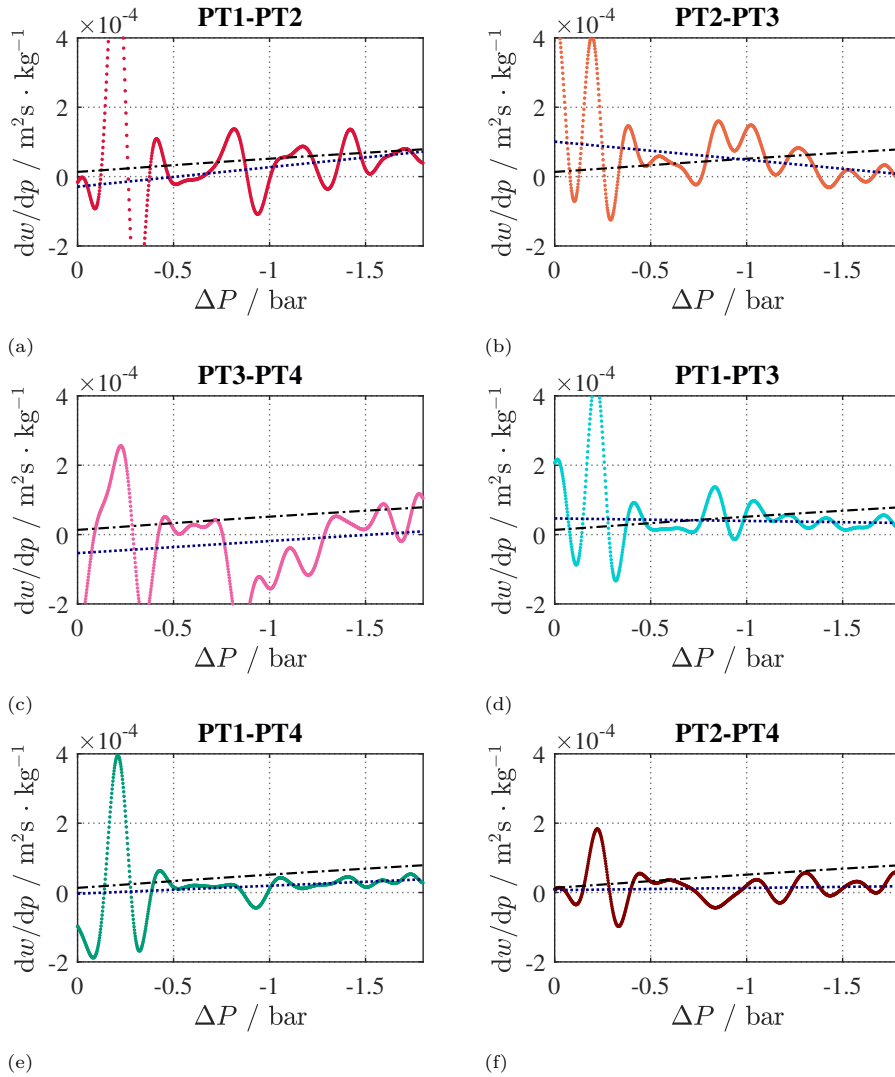


Figure A.12: Derivative of wavespeed with respect to pressure for different sensor pairs for Test 4. (---): prediction of the thermodynamic model. (.....): linear fit of experimental data

### A.5. Test 5: $P_0 = 8.96$ bar, $T_0 = 369.6$ °C, $\Gamma_{\text{model}} = -0.052$

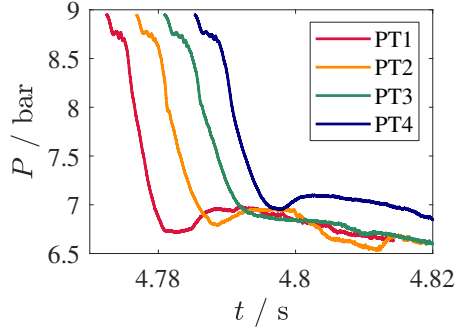


Figure A.13: Relevant portion of the pressure signal from Test 5 for computing the wavespeed using the time-of-flight method

The relevant portions of the pressure recordings from the four Kulite sensors used for computing the wavespeed using the ToF method (refer Section 5.3.4) are shown in Fig. A.13. The pressure signals are similar to the ones seen in Test 4 (Appendix A.4) performed in similar thermodynamic conditions. Figures A.14a to A.14f show the variation in  $w$  with  $\Delta P$  across the expansion wave. Unlike in Test 4, the wavespeed signals show a smoother variation with pressure. For values of  $\Delta P$  between -0.5 bar and -1 bar, the wavespeed displays regions of local flatness and, close to  $\Delta P = -1$  bar, even increases with the pressure drop. This can be seen in the wavespeed estimations from all the possible sensor pairs. These suggest the presence of a locally weak RSW followed by a nonclassical isentropic expansion.

Figures A.15a to A.15f show the variation of  $dw/dp$  with  $\Delta P$  across the wave. Here, unlike in the previous tests,  $dw/dp$  is computed using the unfiltered wavespeed measurements. It was observed during post-processing that while using an unfiltered wavespeed signal resulted in significant noise in the estimation of  $dw/dp$  in ideal-gas tests, this noise progressively decreased as the test conditions approached the nonclassical region. The use of unfiltered  $w$  data removes spurious oscillations making it easier to identify regions of flatness or a negative slope caused by nonclassical effects. For  $\Delta P$  between -0.5 bar and -1 bar,  $dw/dp$  either decreases or stays constant, thereby strongly suggesting the presence of nonclassical gasdynamic phenomena in the flow.

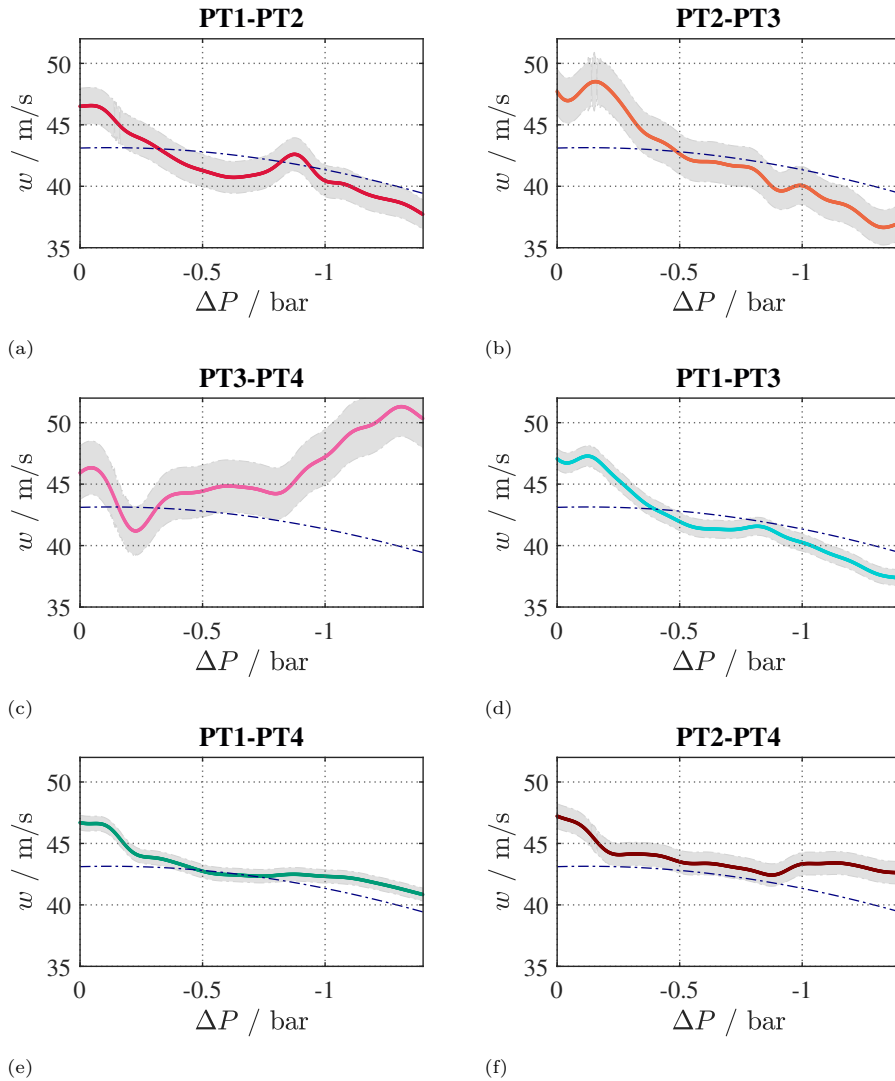


Figure A.14: Wavespeed measurements estimated using different sensor pairs from Test 5 (see Table 5.5). Each dot represents a time-of-flight estimation of the wavespeed at pressure intervals of 15 mbar. (---): theoretical isentropic wavespeed calculated using the thermodynamic model [1] for a shock-free flow. Uncertainty bands on the wavespeed are shown in grey.

A

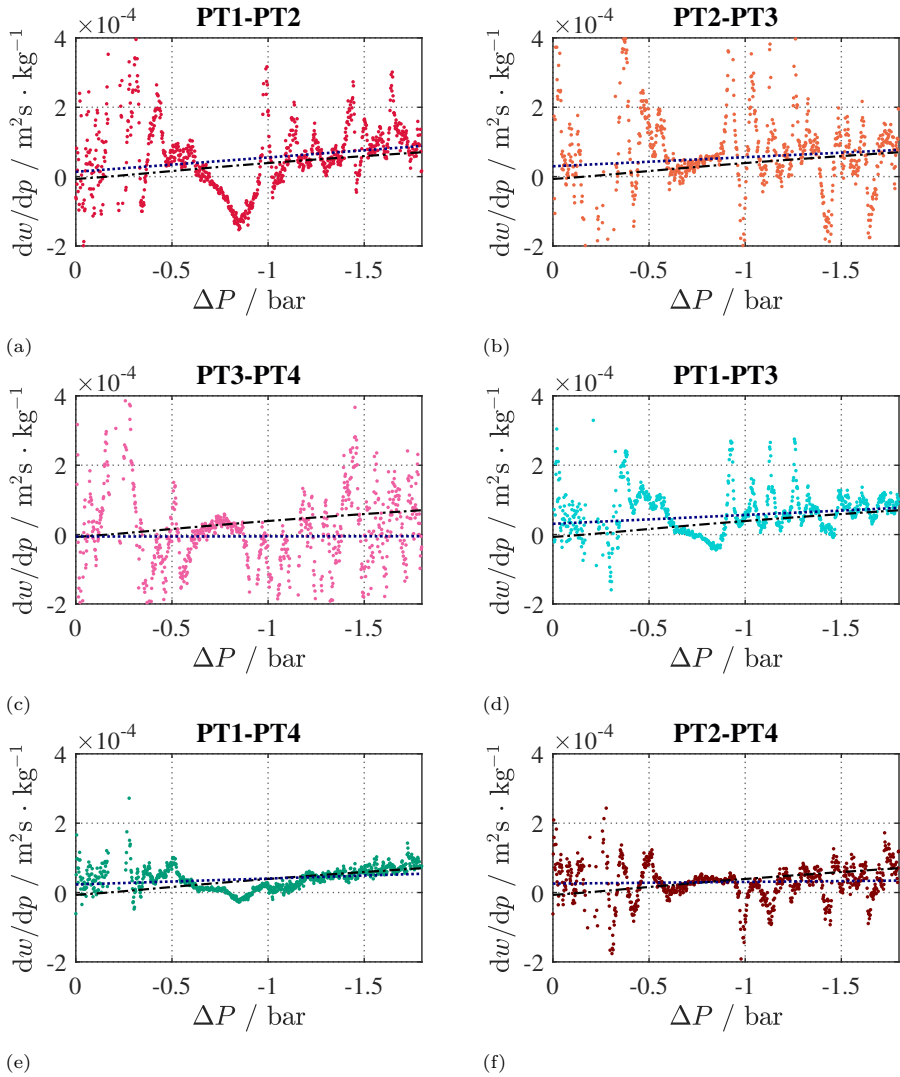


Figure A.15: Derivative of wavespeed with respect to pressure for different sensor pairs for Test 5. (---): prediction of the thermodynamic model. (····): linear fit of experimental data

## A.6. Test 6: $P_0 = 9.33$ bar, $T_0 = 372.1$ °C, $\Gamma_{\text{model}} = -0.013$

A

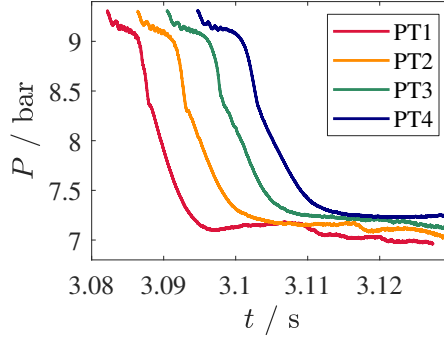


Figure A.16: Relevant portion of the pressure signal from Test 6 for computing the wavespeed using the time-of-flight method

The relevant portions of the pressure recordings from the four Kulite sensors used for computing the wavespeed using the ToF method (refer Section 5.3.4) are shown in Fig. A.16. The pressure signals are similar to the ones seen in Tests 4 & 5 (Appendices A.4 and A.5) performed in similar thermodynamic conditions. Figures A.17a to A.17f show the variation in  $w$  with  $\Delta P$  across the expansion wave. Though the wavespeed measurements show a trend similar to that seen in Tests 4 & 5, the region of flatness between  $\Delta P$  values of -0.5 bar and -1 bar is larger than in the previous cases. A reason for this enlarged region of flatness can be deduced from Fig. 5.11. The initial conditions of Test 6 are located close to the boundary of  $\Gamma = 0$  domain, higher in pressure than both Tests 4 & 5. Thus, an expansion starting from point 6 in Fig. 5.11 traverses through a larger number of thermodynamic states featuring  $\Gamma < 0$  than that from point 4 or 5. Thus, stronger nonclassical effects, including a larger RSW, can be expected in the flow in this case, which is also what is observed in the plots.

Figures A.18a to A.18f show the variation of  $dw/dp$  with  $\Delta P$  across the wave. Again,  $dw/dp$  is computed using the unfiltered wavespeed signals. Similar to what is observed in Figs. A.17a to A.17f,  $dw/dp$  is horizontal between  $\Delta P$  values of -0.5 bar and -1 bar indicating the presence of a RSW in the flow.

A

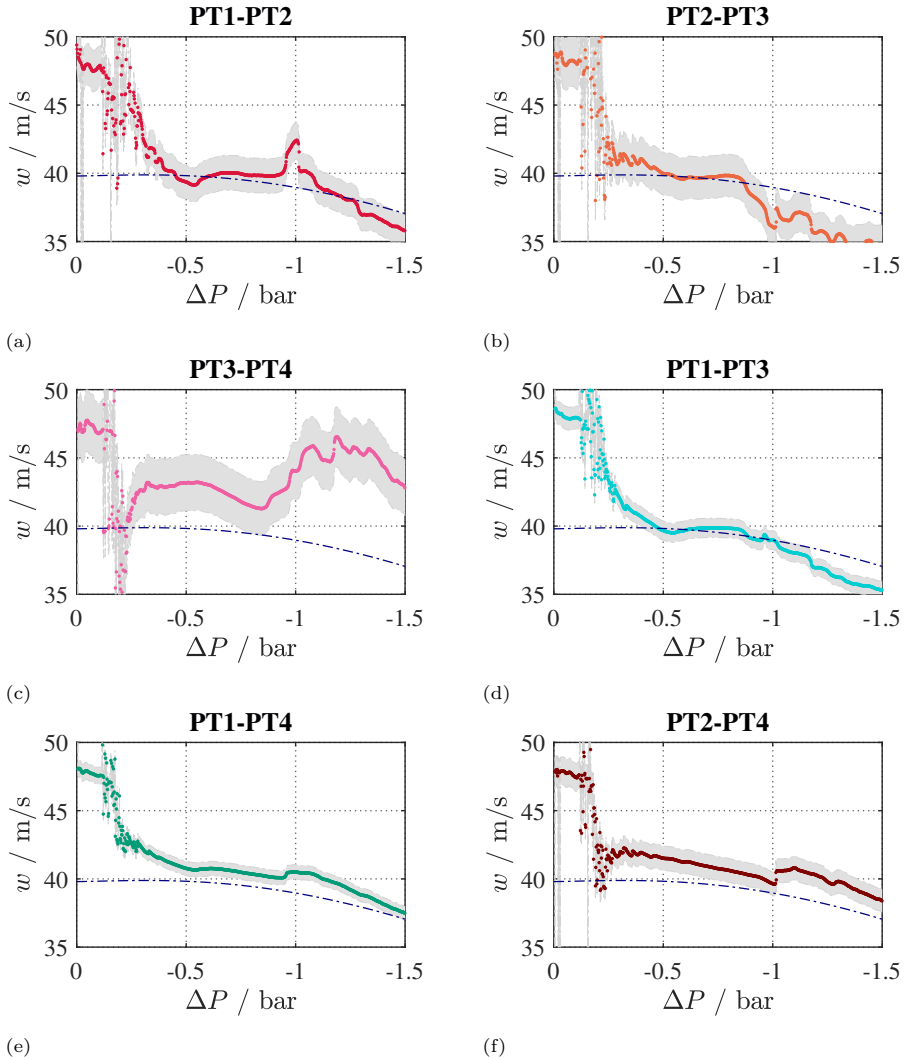


Figure A.17: Wavespeed measurements estimated using different sensor pairs from Test 6 (see Table 5.5). Each dot represents a time-of-flight estimation of the wavespeed at pressure intervals of 15 mbar. (---): theoretical isentropic wavespeed calculated using the thermodynamic model [1] for a shock-free flow. Uncertainty bands on the wavespeed are shown in grey.

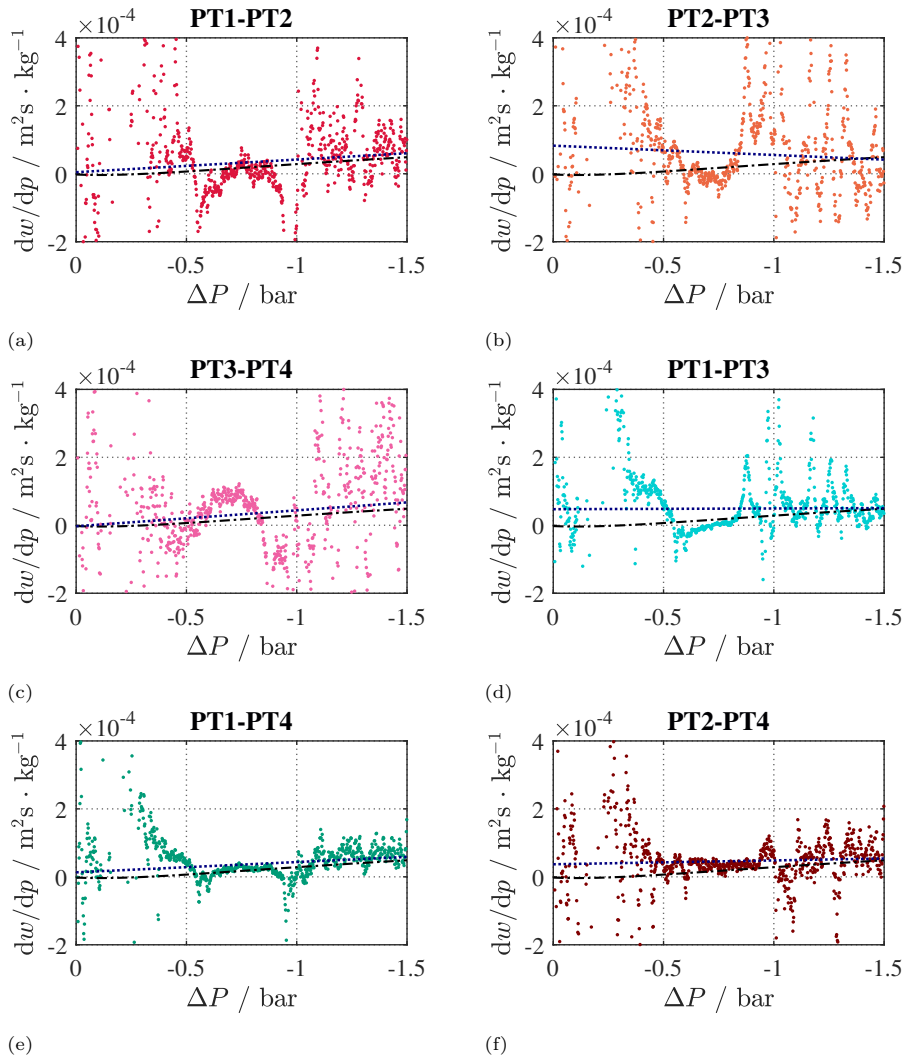


Figure A.18: Derivative of wavespeed with respect to pressure for different sensor pairs for Test 6. (---): prediction of the thermodynamic model. (.....): linear fit of experimental data

### A.7. Test 7: $P_0 = 9.37$ bar, $T_0 = 370.7$ °C, $\Gamma_{\text{model}} = 6$

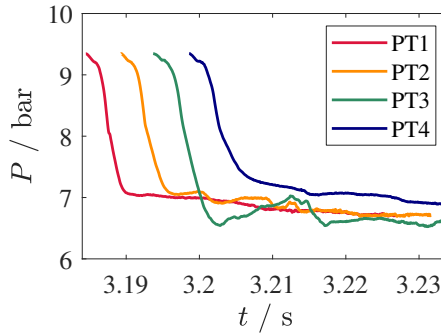


Figure A.19: Relevant portion of the pressure signal from Test 7 for computing the wavespeed using the time-of-flight method

The relevant portions of the pressure recordings from the four Kulite sensors used for computing the wavespeed using the ToF method (refer Section 5.3.4) are shown in Fig. A.19. Figures A.20a to A.20f show the variation in  $w$  with  $\Delta P$  across the expansion wave and Figs. A.21a to A.21f show the variation of  $dw/dp$  with  $\Delta P$  across the wave. A discussion of the results of this test can be found in Section 5.3.4.

It is worth noting that the thermodynamic model predicts the local value of  $\Gamma$  in the flow to be 6. This implies that the test was performed in the liquid region of  $D_6$  in the  $P - v$  plane (refer to Fig. 5.11), since the value of  $\Gamma$  in the gas-phase is, at maximum, equal to  $(\gamma + 1)/2$ . However, this prediction of the thermodynamic model is probably incorrect as large uncertainties are present in the estimates of the thermodynamic critical point and in the location of the saturation dome of  $D_6$  (see discussions of Section 5.3.6).

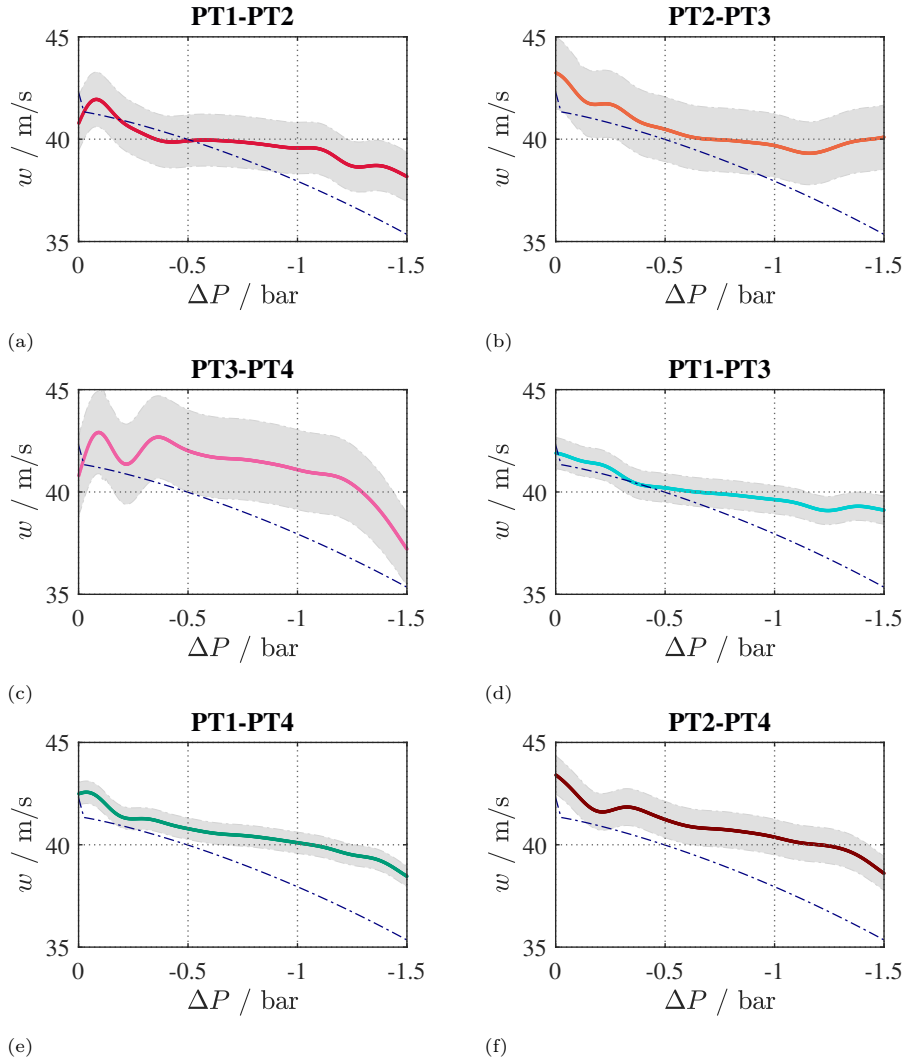


Figure A.20: Wavespeed measurements estimated using different sensor pairs from Test 7 (see Table 5.5). Each dot represents a time-of-flight estimation of the wavespeed at pressure intervals of 15 mbar. (---): theoretical isentropic wavespeed calculated using the thermodynamic model [1] for a shock-free flow. Uncertainty bands on the wavespeed are shown in grey.

A

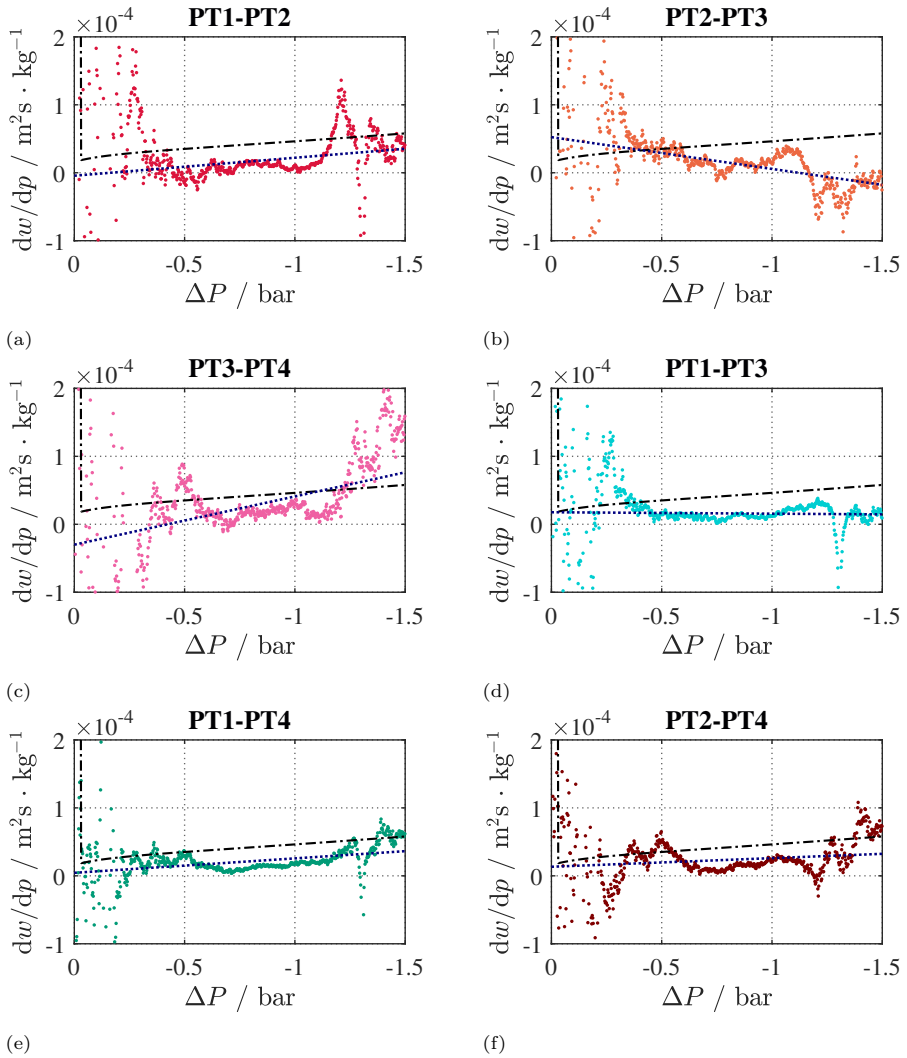


Figure A.21: Derivative of wavespeed with respect to pressure for different sensor pairs for Test 7. (---): prediction of the thermodynamic model. (.....): linear fit of experimental data

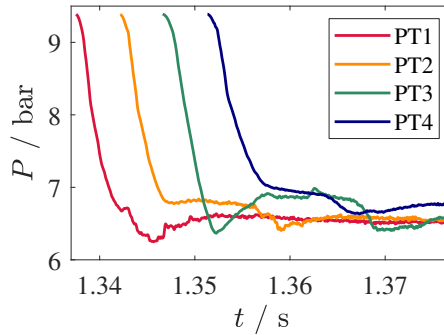
**A.8.** Test 8:  $P_0 = 9.4$  bar,  $T_0 = 372$  °C,  $\Gamma_{\text{model}} = 0.023$ **A**

Figure A.22: Relevant portion of the pressure signal from Test 8 for computing the wavespeed using the time-of-flight method

The relevant portions of the pressure recordings from the four Kulite sensors used for computing the wavespeed using the ToF method (refer Section 5.3.4) are shown in Fig. A.22. Unlike in the previous tests in the dense-gas thermodynamic region, no kink can be observed in the pressure signals. Figures A.23a to A.23f show the variation in  $w$  with  $\Delta P$  and Figs. A.24a to A.24f show the variation of  $dw/dp$  with  $\Delta P$  across the expansion wave. Both the wavespeed and  $dw/dp$  exhibit elements of nonclassical gasdynamic behaviour such as local regions of flatness across the wave. However, a clear indication of the presence of a RSW in the flow, similar to that observed in Appendices A.5 to A.7 is absent. Nonetheless, the wavespeed drops by less than 3 m/s across the wave, thereby suggesting that the expansion takes place in the vicinity of  $\Gamma = 0$  region of  $D_6$ .

A

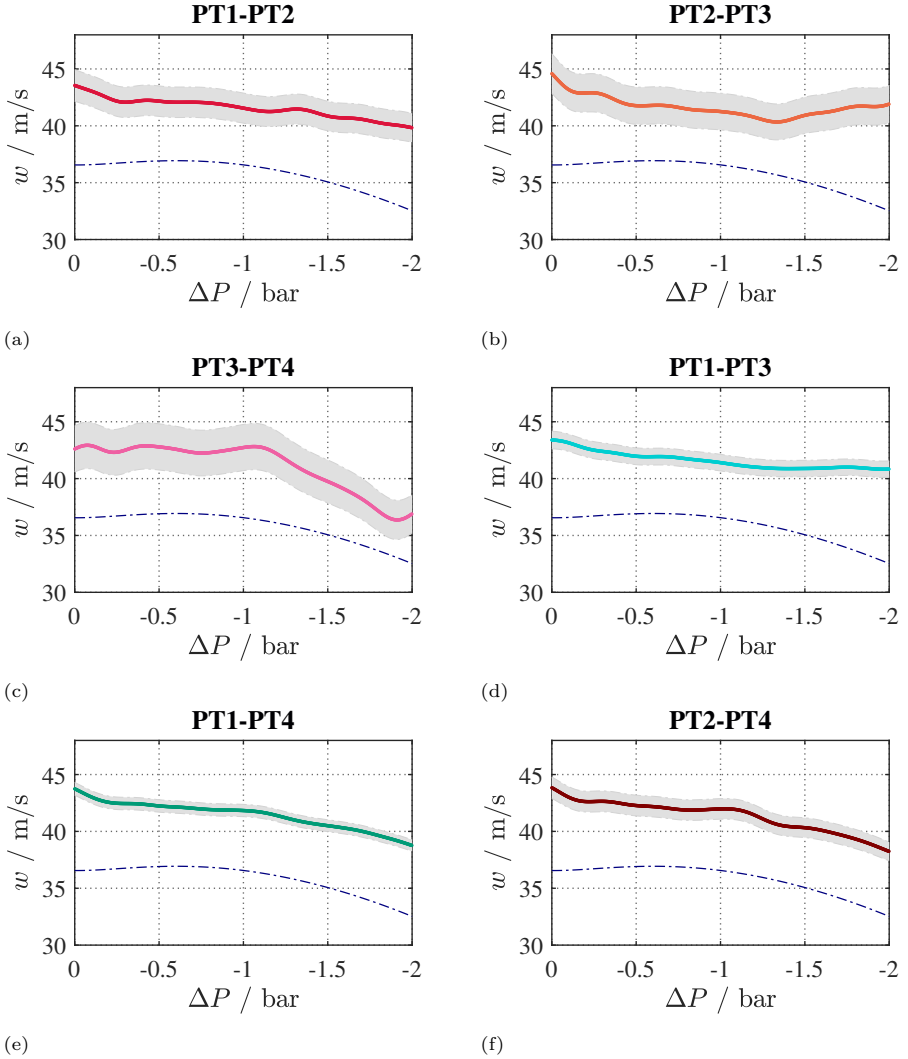


Figure A.23: Wavespeed measurements estimated using different sensor pairs from Test 8 (see Table 5.5). Each dot represents a time-of-flight estimation of the wavespeed at pressure intervals of 15 mbar. (---): theoretical isentropic wavespeed calculated using the thermodynamic model [1] for a shock-free flow. Uncertainty bands on the wavespeed are shown in grey.

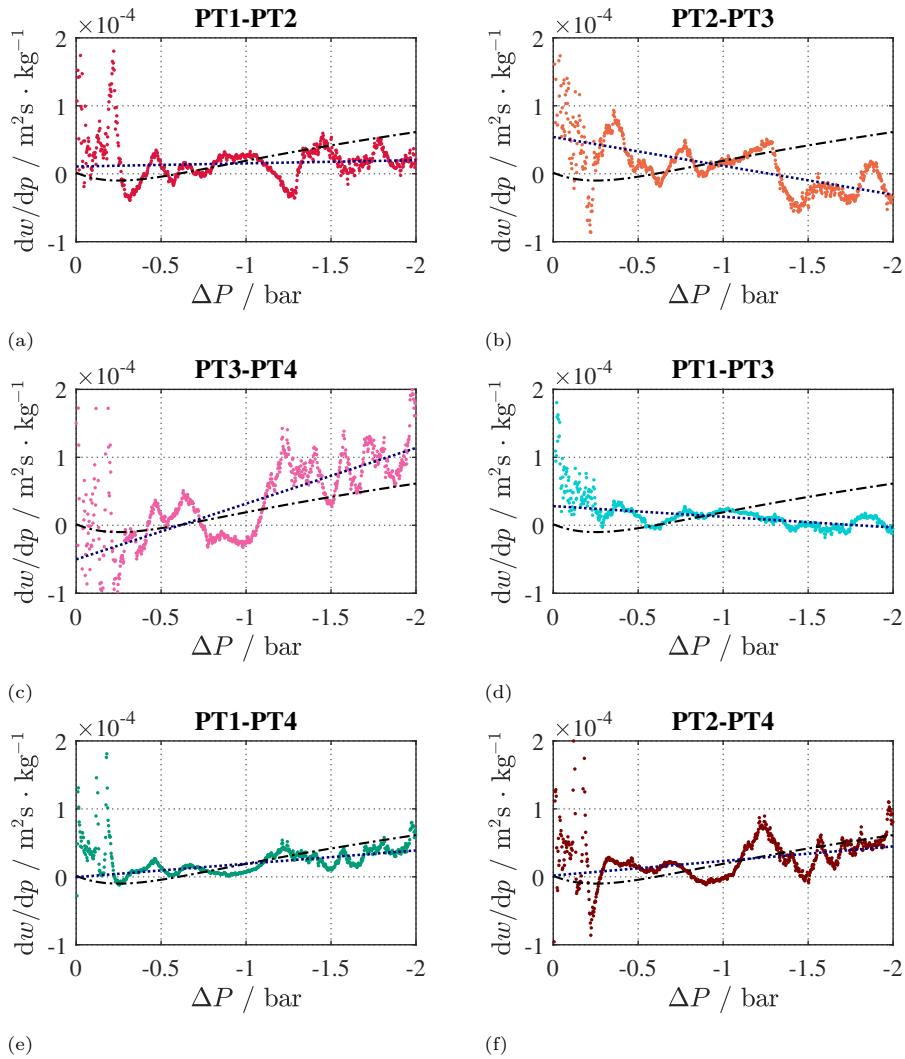


Figure A.24: Derivative of wavespeed with respect to pressure for different sensor pairs for Test 8. (---): prediction of the thermodynamic model. (.....): linear fit of experimental data



# Acknowledgements

It would be remiss of me to claim sole ownership of the work contained in this document. On the contrary, it is the product of collaboration with the incredible individuals that I've had the privilege to work with during my four years as a Ph.D. Their encouragement, feedback, and guidance have greatly enriched my experience and made this journey enjoyable and rewarding.

First and foremost, I extend my deepest gratitude to Prof. Piero Colonna for his unwavering support, guidance and encouragement throughout my Ph.D. Your positivity, even in challenging times, has been truly inspiring. I have learned valuable lessons from you that I am certain will benefit me both in my career and my life.

I would also like to express my heartfelt thanks to Bertrand, for his invaluable guidance and insights into the theoretical and experimental aspects of this research. Your intelligence and expertise were pivotal, especially during the challenges faced in the FAST lab. Thanks a lot for your contributions to the ASTER and the OVAR. Theo, I admire your attitude, enthusiasm, and dedication to what you do. Your exceptional technical skills were instrumental in realising the ASTER. I am delighted that you will remain in the university, and I eagerly look forward to our future discussions.

Furthermore, I would like to thank Chiara for her patience to read through my dissertation multiple times and share her feedback. I am excited to continue to work on this research with you. Teus, thanks much for your timely helps with issues with FluidProp and also to provide insights into the implementation of state equations.

I would like to express my gratitude to Leon Roessen and Steve van Herk from DEMO for their contributions to the design of the experimental setups. Steve, your dedication to making the designs ready under time constraints was remarkable. Jeroen and Niek, thank you for assembling and disassembling the FOV countless times in our pursuit to make it work. Although our efforts were ultimately unsuccessful, I gained valuable technical knowledge working with you both. Martijn, thank you for providing electrical assistance in the FAST. And Frank, your exceptional work in realizing the ASTER and the OVAR, as well as your continued technical assistance, is greatly appreciated. Thank you Adam, for your help in realising the ASTER.

I was lucky to have had amazing people to share my office with that has made this experience more bearable. Federica, Francesco I & II, Andrea, Gioele, Fabio, Dabo, Alessandro I & II, Evert, Matteo, Nitish, and Lorenzo: it

## A

was a pleasure to work, and also to avoid work, with you guys. Special thanks to Evert for translating my summary into Dutch. I should also mention the fantastic people I met from other groups: Hugo, Martijn, Fernanda, Livia, Tercio, Claudia, PJ, Blanca, Carmine, Jatinder, Cristina, Dylan, Rishikesh & Kaushal.

To my friends from my undergraduate days (Rakesh, Vignesh, Cindhu, Venky, Naveen and Ashwin) who made the transition to the Netherlands easier, I am thankful for your companionship, and for the unforgettable travels and moments I got to share with you.

Last but certainly not the least, I would like to express my heartfelt gratitude to my parents and my sister Nandhini for their unconditional love and encouragement throughout my PhD journey. Without their unwavering support, I would not have been able to achieve this milestone. I would also like to thank my extended family for their love and support. Special mention goes to Manga and Paapu for the unlimited entertainment they provide and for being so lovely. Your presence has brought much joy to my life and I am truly grateful for it.

## About the author

Nitish Barathwaj Chandrasekaran was born in 1993 in Chennai, India. Following the completion of his schooling there, he moved to Coimbatore in 2010 to pursue a B.Tech. in Aerospace Engineering at the Amrita School of Engineering. He subsequently shifted to the Netherlands to pursue a M.Sc. degree in Delft University of Technology, specializing in Flight Performance and Propulsion. During his study, he performed an internship at Rolls-Royce Aerospace GmbH in Berlin, Germany where he worked with the Transient Engine Performance Team to study lean burn combustion system control strategies for small and large civil gets to reduce harmful  $\text{NO}_x$  emissions.



In 2018, he started his Ph.D. at the Faculty of Aerospace Engineering in the Propulsion & Power Group under the supervision of Prof. Piero Colonna. His PhD focussed on studying high temperature flows of complex organic fluids using experimental and numerical methods. He is currently a post-doctoral researcher in the Propulsion & Power group, where he continues to perform research in the fields of nonclassical gasdynamics and thermodynamic modelling of industrial working fluids.



# List of Publications

4. B. Mercier, **N. B. Chandrasekaran**, P. Colonna, *Speed of Sound Measurements in Dense Siloxane  $D_6$  Vapor at Temperatures up to 645 K by Means of a New Prismatic Acoustic Resonator*, [Journal of Chemical & Engineering Data](#) **3**, p. 561-573 (2023).
3. **N. B. Chandrasekaran**, T. Michelis, B. Mercier, P. Colonna, *Preliminary Experiments in High Temperature Vapours of Organic Fluids in the Asymmetric Shock Tube for Experiments on Rarefaction Waves (ASTER)*, [Proceedings of the 4th International Seminar on Non-Ideal Compressible Fluid Dynamics for Propulsion and Power](#) **29**, p. 201-208 (2023).
2. **N. B. Chandrasekaran**, B. Mercier, P. Colonna, *Nonlinear wave propagation in dense vapor of Bethe-Zel'dovich-Thompson fluids subjected to temperature gradients*, [Physics of Fluids](#) **10**, 107109 (2021).
1. **N. B. Chandrasekaran**, B. Mercier, P. Colonna, *Formation of Rarefaction Shockwaves in Non-ideal Gases with Temperature Gradients*, [Proceedings of the 3rd International Seminar on Non-Ideal Compressible Fluid Dynamics for Propulsion and Power](#) **28**, p. 20-25 (2021).